THE UNIVERSITY *of* EDINBURGH

RETROSPECTIVE SEISMOLOGY BY SOURCE-RECEIVER INTERFEROMETRY

Elizabeth Entwistle

A Thesis Submitted for the Degree of Doctor of Philosophy

School of GeoSciences

The University of Edinburgh

2014

Author's Declaration

I declare that this thesis has been composed solely by myself and that it has not been submitted, either in whole or in part, in any previous application for a degree. Except where otherwise acknowledged, the work presented is entirely my own.

Elizabeth Entwistle

16^{th} December 2014

Abstract

Seismology is the study of earthquakes and the Earth's internal structure using seismic waves. Traditional seismology is constrained by the timing and location of seismic sources, and by the location of seismometers with which energy from the sources are recorded. Improvements in the global seismometer networks have reduced the latter constraint. Furthermore, recent advances into Seismic Interferometry (SI) have enabled detailed information about the Earth's interior to be obtained using ambient seismic noise, hence even in areas with low natural seismicity. The most common approach to SI is to use the cross-correlation of ambient noise recordings to construct an estimate of the Green's function between two seismometer locations. The Green's function estimate is then analysed or inverted for seismic properties of the Earth. This method of noise interferometry is now a popular approach in earthquake seismology as in some situations it renders active seismic sources (earthquakes or synthesised explosions) obsolete, as subsurface information can be obtained even in times of seismic quiescence.

This thesis investigates a different method: Source-Receiver Interferometry (SRI). SRI can be used to construct earthquake seismograms on seismometers that were not necessarily deployed when the earthquakes occurred - a form of 'retrospective seismology'. This might be useful if, for example, we wish to analyse old earthquakes with newly installed seismometers. The application of SRI involves evaluating two interferometric integrals. The first integral is evaluated using ambient noise interferometry: at least 6 months of noise data is cross-correlated to estimate the Green's functions between pairs of seismometers. These inter-receiver Green's functions are then used as the "propagators" for SRI. Their role is to project earthquake signals recorded on a backbone array of seismometers to the location of a target sensor at which a new, novel earthquake seismogram is to be constructed - a form of spatial redatuming. To spatially redatum the earthquake data, the second interferometric integral is evaluated using either processes of correlation (resulting in correlation-correlation SRI) or convolution (correlation-convolution SRI). The method used depends on the relative location of the target sensors with respect to both the backbone seismometer array and the earthquake epicentre. The SRI process is completed by integrating (summing) over all projected earthquake signals. To regularise the spatial distribution of the projected earthquake data and to invoke this second interferometric integral more precisely, the backbone seismometers are embedded within 2D spatial

Voronoi cells.

New seismograms for 87 earthquakes were reconstructed on up to eight target sensors, seven of which were deployed when the earthquakes occurred and are used to test the success of the method by comparing with the SRI results with the directly-recorded seismograms. The seismogram reconstructions on the eighth target sensor are truly novel. The SRI method was developed to operate over two length scales. The first focusses on relatively small length scales in which the inter-station distance between the eight target sensors and the backbone array seismometers is between $\sim$ 210 km and 540 km. Both correlation-correlation SRI and correlation-convolution SRI are used to reconstruct the earthquake seismograms on four of the same target sensors. Applying correlation-convolution SRI is shown to remove spurious signals associated with correlation-correlation SRI. Second, a significantly larger length scale is considered where a second set of target sensors are located up to 2420 km from a second backbone seismometer array. The correlation-correlation and correlation-convolution SRI methods are used in parallel to increase the spatial extent of the study. The quality of the SRI seismograms constructed is shown to depend on the quality of three components: 1) the SRI propagators constructed using ambient noise interferometry, 2) the earthquake signals recorded on the backbone seismometer array, and 3) the correlation (or convolution) functions that are summed in the second interferometric integral to construct the final SRI seismogram. The quality of each component is quantified by its signal-to-noise ratio and root-mean-square value, and criteria are proposed to obtain optimal earthquake seismogram reconstructions using SRI. SRI is most successful when the target sensors are located less than 540 km from the backbone array seismometers. Such SRI seismograms are being used to create a catalogue of new, 'virtual' earthquake seismograms that are available to complement real earthquake data for use in future earthquake seismology studies.

An alternative approach to noise interferometry is also considered: the recordings from just 15 earthquakes are used to perform multidimensional deconvolution (MDD) to estimate the Green's functions between pairs of seismometers. This is the first time such data has been used to perform MDD, which is valid in attenuating media and is thus theoretically more valid in earthquake seismology settings than correlational interferometry. The Green's functions estimated using MDD are compared with those same Green's functions estimated using ambient noise interferometry and the results are comparable on several occasions, despite using far fewer data for MDD. However, the quality of the results of MDD is significantly affected by the illumination of the

receiver array from the earthquake sources. A greater density of earthquakes that sufficiently illuminates all backbone array seismometers is required to obtain accurate Green's functions by MDD.

Acknowledgments

First and foremost I would like to thank Andrew Curtis and Brian Baptie for offering this project and for providing their full support and supervision over the last four years. Brian has been an invaluable source of help with the practical aspects of this project, helping me through the trials and complexities of working with real data. As principal supervisor, Andrew's enthusiasm for the project has never faltered, providing encouragement when I have been at my most doubtful, instilling a sense of determination that has enabled me to complete this research. I also offer my sincere gratitude to Andrew for his time and commitment over the last few months, when I have left him with countless chapter edits and revisions.

Funding for this PhD has been provided by the School of GeoSciences at the University of Edinburgh and the British Geological Survey, without whom, this project would not have been possible. All data throughout this PhD has been provided by the IRIS Data Management Center.

All members of the Edinburgh Interferometry Project, both students and sponsors, have always challenged and questioned my research, whilst also offering advice and experience. My special thanks go to Giovanni who has been available for many impromptu discussions over the last 6 months and has become an unofficial but highly valued third supervisor. My thanks also go to the IT team at Edinburgh and those at ECDF who have helped with numerous computing difficulties over the last 4 years.

I have been fortunate enough to be involved in many Geophysics fieldtrips during my time as a PhD student. All have been made even more enjoyable by Erica, with whom I share some of my most cherished PhD memories. Thank you.

The last 4 years would not have been the same without the friendship of my fellow Melville Terrace flatmates, both past and present! A special mention goes to Rachel, Tom M, Johannes and Matteo. Thank you also to all Grant Attic residents for your friendship and support over the years, especially to Sophie, Maddy, Gus, Mike, Tom R, Gill, Simon K, Matt H, Nick R and Darren, and to Jen, Nick J, Maddy, Tom M, Robyn, Mark, Rob, Matt C, Jamie, Rosie and Jack for many a cycle ride and outdoor adventure!

Finally, I thank my mum, who has always supported my decisions and made my education possible, and my sister, who has always offered help and advice. One final, single thank you goes to Andrew, for being a constant source of encouragement, support and inspiration when I have been unable to see the bigger picture.

Contents

Author's Declaration **iii**

Abstract **v**

Acknowledgments **ix**

Table of Contents **xi**

1 Introduction **1**

1.1 Seismic Interferometry 2

1.1.1 Inter-receiver interferometry 3

1.1.2 Inter-source interferometry 11

1.1.3 Source-receiver interferometry 13

1.2 Thesis Motivation, Objectives and Layout 14

1.3 Paper Plan 16

Bibliography 18

2 Theoretical Overview **29**

2.1 Outline 29

2.2 Inter-Receiver Interferometry 30

2.2.1 Acoustic reciprocity theorems 30

2.2.2 Acoustic Green's function representation 31

2.2.3 Inter-receiver interferometry by MDD 35

2.3 Inter-Source Interferometry 38

2.4 Source-Receiver Interferometry (SRI) 39

2.5 Summary 43

Bibliography 45

3 Practical Methodology and Data Processing **49**
3.1 Outline . . . 49
3.2 Inter-Receiver Interferometry Using Noise Data . . . 50
3.2.1 Data download . . . 50
3.2.2 Single station data preparation . . . 52
3.2.3 Green's function estimation . . . 53
3.2.4 Quality control . . . 54
3.3 A Review of the Estimated Green's Functions . . . 56
3.4 Inter-Receiver Interferometry by MDD . . . 63
3.4.1 Earthquake data preparation . . . 64
3.4.2 Constructing Γ and C . . . 65
3.4.3 Singular value decomposition . . . 65
3.4.4 Green's function estimation . . . 66
3.5 Summary and Look Ahead for Inter-Receiver Interferometry . . . 66
3.6 Source-Receiver Interferometry (SRI) . . . 68
3.6.1 Station criteria . . . 68
3.6.2 Processing . . . 69
3.6.3 Green's function estimation . . . 70
3.6.4 Inter-source interferometry . . . 70
3.6.5 Voronoi cells . . . 71
3.7 Justification of the Station Criteria for SRI . . . 75
3.7.1 Criteria 1-3 . . . 75
3.7.2 Criterion 4 . . . 75
3.7.3 Summary . . . 86
3.8 Chapter Summary . . . 86
Bibliography . . . 88

4 Correlation-Correlation SRI **91**
4.1 Outline . . . 91
4.2 Introduction . . . 92
4.3 Method . . . 93
4.4 Application at Exploration Seismology Scale . . . 94
4.4.1 Example 1 at a short scale . . . 94
4.5 Applications in Earthquake Seismology . . . 97
4.5.1 Data selection, processing and methodology . . . 98
4.5.2 Example 2 at an intermediate scale . . . 98
4.5.3 Example 3 at the largest scale . . . 100
4.6 Discussion . . . 103
4.7 Conclusion . . . 110
Bibliography . . . 112

5 Correlation-Convolution SRI **115**
5.1 Outline . . . 115
5.2 Introduction . . . 116
5.3 Application . . . 118
5.4 Results . . . 121
5.5 Discussion . . . 121
5.6 Conclusion . . . 130
Bibliography . . . 132

6 Multi-Scale Applications of SRI **133**
6.1 Outline . . . 133
6.2 Introduction . . . 134
6.3 Method . . . 136
6.4 Results . . . 138
6.4.1 SRI reconstructions using the East-West aligned array . . . 138
6.4.2 SRI reconstructions using the North-South aligned array . . . 149
6.5 Discussion . . . 161
6.5.1 West vs. East: The geological effects of the US . . . 162
6.5.2 Quantitative Analysis: SNR analyses of the components of SRI 172
Estimated Green's functions . . . 173
Earthquake recordings . . . 176
Correlation/Convolution Functions . . . 182
Summary . . . 188
6.6 Conclusion . . . 189
Bibliography . . . 192

7 Green's Function Estimation by MDD **193**
7.1 Outline . . . 193
7.2 Introduction . . . 194
7.3 Data and Methodology . . . 196
7.4 Results . . . 202
7.5 Discussion . . . 215
7.6 Conclusion . . . 225
Bibliography . . . 227

8 Conclusions and Further Work **229**
8.1 Methodology . . . 229
8.1.1 Experimental Design: The 'ideal' receiver geometry for SRI . 230
8.1.2 Source phase analysis . . . 234
8.2 The Success of SRI in Constructing Earthquake Seismograms Retrospectively . . . 235
8.3 Multidimensional Deconvolution (MDD) . . . 243
8.3.1 Further work . . . 244
8.4 Summary . . . 245
Bibliography . . . 247

Appendices **249**

A Earthquake List **251**

B RMS and SNR Analyses of Event Recordings **257**
B.1 Introduction 257
B.2 Earthquakes recorded on the East-West aligned array 257
B.3 Earthquakes recorded on the North-South aligned array 259

CHAPTER 1

Introduction

Seismology is the study of earthquakes and the Earth's internal structure using seismic waves. Seismic waves typically originate from active sources, such as earthquakes or man-made explosions, and are recorded on seismometer networks. In earthquake seismology this seismogram data is thus sensitive to the paths of energy propagation between earthquake hypocentres and seismometer locations and one has to rely on source occurrence and location before subsurface Earth properties can be determined. The deployment of large seismometer networks worldwide and the use of "passive" seismic waves (e.g. ocean swell-, wind- or industrial noise-generated seismic waves that are excited constantly in space and time and propagate as "surface waves" along the surface of the Earth) have gone some way to reducing these spatial constraints imposed on seismogram data. Furthermore, recent advances in the field of seismic or wavefield interferometry (sometimes referred to as Green's function estimation) create new data types that are sensitive to a variety of different spatial volumes using the same seismometer networks and seismic source distributions. This thesis uses passive wavefields and methods of seismic interferometry to construct new earthquake seismograms, at a time after an earthquake has occurred and after all the energy from that event has dissipated. This renders possible the concept of 'retrospective seismology'.

1.1 Seismic Interferometry

Seismic interferometry refers broadly to processes of cross-correlation, convolution or deconvolution that estimate the Green's function between two receivers (inter-receiver interferometry), two sources (inter-source interferometry), or a source and a receiver (source-receiver interferometry). Inter-receiver interferometry (Weaver and Lobkis, 2001; Campillo and Paul, 2003; Wapenaar, 2003, 2004; van Manen et al., 2005, 2006; Wapenaar and Fokkema, 2006) allows one to construct the seismic signals that would have been recorded at one receiver location if an energy source had been fired at the location of the other receiver (the so-called "virtual source" location), whilst inter-source interferometry (Hong and Menke, 2006; Curtis et al., 2009; Tonegawa and Nishida, 2010; Poliannikov et al., 2012) allows one to construct the response from one of the sources that would have been recorded at the location of the other source (i.e. as if a "virtual receiver" had been active at the location of the other source). Source-receiver interferometry (SRI) acts quite differently to the other two interferometric methods and allows one to construct the seismic response between a source and a receiver, without ever having recorded that seismic response on the receiver directly (Curtis and Halliday, 2010; Halliday and Curtis, 2010). Since their inception these methods have been widely used in exploration seismology (e.g., Schuster (2001); Schuster et al. (2004); Bakulin and Calvert (2004); Xiao et al. (2006); Halliday et al. (2007, 2010, 2012)), and earthquake seismology (e.g., Shapiro and Campillo (2004); Roux et al. (2005); Sabra et al. (2005a,b); Shapiro et al. (2005); Stehly et al. (2007, 2008); Wang et al. (2008); Bensen et al. (2008); Brenguier et al. (2008); Curtis et al. (2009); Nicolson et al. (2012); Curtis et al. (2012)). They have also been significantly advanced and trialled in a number of other fields including acoustics and ultrasonics (Cassereau and Fink, 1993; Roux and Fink, 2003; Weaver and Lobkis, 2001; Derode et al., 2003a,b), helioseismology (Rickett and Claerbout, 1999), structural engineering (Snieder and Safak, 2006), medical diagnostics (Sabra et al., 2007) and electromagnetics (Slob et al., 2007; Slob and Wapenaar, 2007).

Here we introduce the underlying concepts of each method and review some of the key literature in exploration and earthquake seismology. The theoretical derivations of all interferometric methods are left to Chapter 2.

1.1.1 Inter-receiver interferometry

The first work in wavefield interferometry began in 1968 when Claerbout postulated that the reflection response of a horizontally layered medium can be synthesised from the autocorrelation of its transmission response.(Claerbout, 1968). This method is now more widely known as inter-receiver interferometry. Two possible geometries required to perform inter-receiver interferometry are shown in Figure 1.1: sources at locations such as $\mathbf{x}'$ on boundary S' are recorded on receivers at locations $\mathbf{x_A}$ and $\mathbf{x_B}$ and (A) cross-correlated, or (B) convolved. Integration (summation) over all source locations constructs the response that would have been recorded at $\mathbf{x_A}$ if an impulsive source had been fired from the location of $\mathbf{x_B}$, thus turning the receiver at $\mathbf{x_B}$ into a "virtual source" (Weaver and Lobkis, 2001; Campillo and Paul, 2003; Wapenaar, 2003, 2004; van Manen et al., 2005, 2006; Wapenaar and Fokkema, 2006). For the correlation approach to interferometry (as in Figure 1.1A) we assume the medium inside V' to be lossless (Wapenaar and Fokkema, 2006). Convolution-type interferometry (as in Figure 1.1B) does not have an underlying assumption of zero attenuation and is thus more suited to real data applications.

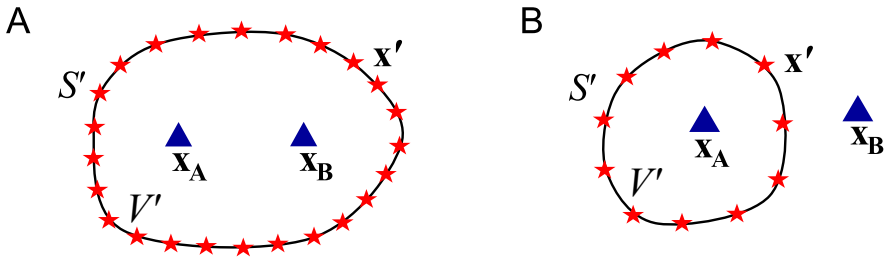

Figure 1.1: Schematic source and receiver geometries for inter-receiver interferometry. Stars are sources, triangles are receivers. The responses from each source at locations such as $\mathbf{x}'$ on boundary S' are recorded on receivers $\mathbf{x_A}$ and $\mathbf{x_B}$ and (A) cross-correlated or (B) convolved. In both cases the results of all cross-correlations or convolutions are summed (integrated over S') to obtain an approximation of the Green's function between the receivers at $\mathbf{x_A}$ and $\mathbf{x_B}$.

Cross-correlation

First we focus on inter-receiver interferometry via processes of cross-correlation. The method has been widely used in exploration seismology - a field in seismology that primarily involves imaging the subsurface to identify areas of significant geologic structure that are subsequently of economic interest. *Controlled-source seismic*

interferometry, so called as it uses *active* seismic sources for Green's function estimation, has led to interesting discoveries within this field of seismology. Its first practical application in an exploration environment was by Bakulin and Calvert (2004): borehole receivers recorded the down-going wavefield that propagated from surface sources through a complex overburden, and the reflected signal from a deep target. Cross-correlations of these wavefields and summations over all source locations constructed the reflection response of a virtual source located in the borehole, free of overburden distortions. The surface sources were thus redatumed (projected) to virtual source locations in boreholes - locations physically occupied by receivers. Here the authors pioneered the Virtual Source Method (VSM) to eliminate propagation distortions of complex, inhomogeneous overburdens that are often responsible for a number of seismic imaging/4D problems.

Schuster (2001) and Schuster et al. (2004) developed a similar *interferometric redatuming* concept using methods of stationary phase. Consider the illustrations in Figure 1.2: (A) The signals from the subsurface source (explosion) are recorded on the surface receiver at $\mathbf{x_A}$. (B) The reflection response from this source involving the subsurface scatterer (circle) is recorded at receiver $\mathbf{x_B}$. It is assumed that receiver $\mathbf{x_A}$ is located at the exact specular reflection point of the ray drawn in (B), such that the branch of the ray in (A) coincides with the first branch of the ray in (B). (C) Cross-correlation of the direct wave in (A) with the reflected wave in (B) leaves the traveltime of the reflection response only, and the subsurface source is redatumed (repositioned) to the location of surface receiver $\mathbf{x_A}$.

In practice, subsurface source locations and specular reflection points are typically unknown, but Schuster et al. (2004) show how interferometric redatuming is still possible if one considers multiple unknown sources at depth. All one requires is for one of the sources to emit the specular ray that propagates via receiver $\mathbf{x_A}$ and the scatterer. Cross-correlations of all direct and reflected waves at the two receiver locations constructs a set of impulse responses, the traveltime curve of which is stationary for the source that emits the specular ray. All cross-correlations are then summed: the main contribution to this summation comes from sources within the Fresnel zone, which is located around the source location where the traveltime curve is stationary, whilst all other source contributions interfere destructively. This estimates the impulse response that represents the reflection response from a source at receiver $\mathbf{x_A}$ recorded on the receiver $\mathbf{x_B}$. The subsurface source that emits the specular ray has thus been redatumed (repositioned) to the location of surface receiver $\mathbf{x_A}$, without ever

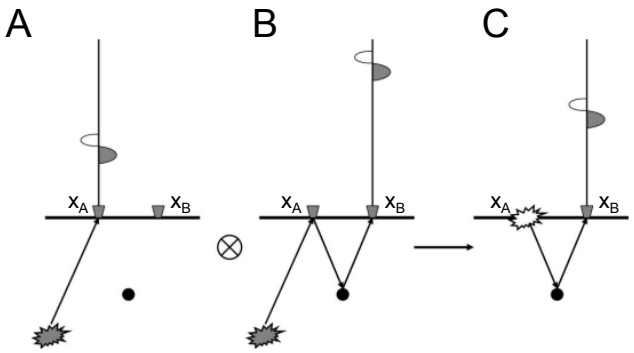

Figure 1.2: The basic principle of reflected-wave interferometry (Schuster, 2001, 2009) (adapted from Wapenaar et al. (2010)). (A) The subsurface source (explosion) is recorded at surface receiver $\mathbf{x_A}$. (B) The second surface receiver at $\mathbf{x_B}$ retrieves a reflected wave from the subsurface scatterer (circle). (C) Cross-correlation of the wavefield recorded at $\mathbf{x_A}$ with the wavefield recorded at $\mathbf{x_B}$ eliminates the common propagation path between the source and the receiver at $\mathbf{x_A}$. The result is an estimate of the reflection response of a source at the location of $\mathbf{x_A}$ recorded at $\mathbf{x_B}$. The receiver at $\mathbf{x_A}$ thus becomes a virtual source location.

knowing the exact locations of any of the sources or the velocity model of the medium. This work was the beginning of many advances into interferometric redatuming in exploration seismology and many possible interferometric transformations between surface data are discussed by Schuster (2009)

The method of stationary phase has also been widely developed by Snieder (2004) and Snieder et al. (2006). The authors use the cross-correlations of multiply scattered waves to estimate the Green's function between two receiver locations. They show that waves radiating from secondary sources (scatterers) located close to the receiver line interfere constructively, whilst those waves radiating from scatterers further away from the receivers interfere destructively. This relaxes the global requirement that all normal modes of the system are uncorrelated and carry the same amount of energy (equipartitioning) as one only requires scattered waves to propagate approximately isotropically near the receivers in order to estimate the Green's function between the receiver pair. Furthermore, Snieder et al. (2006) show that surface sources located around the stationary phase regions of the source boundary contribute the most to the governing interferometric integrals. Thus, sources occupying the stationary phase points alone are responsible for the emergence of the Green's function.

These studies into seismic interferometry by methods of stationary phase have paved the way for seismic interferometry in practical, real-data applications. Instead of measuring the response from all sources at locations $\mathbf{x}'$ on boundary S', one only needs

to measure those responses propagating from regions around the boundary that provide a stationary phase contribution to the interferometric integral. Thus, the number of observations made and the number of cross-correlations performed is significantly reduced.

The active seismic sources used in exploration seismology are typically replaced with ambient seismic sources in earthquake seismology. These passive sources include ocean swell, the wind and industrial noise, and all excite seismic waves that propagate as surface waves, diminishing in amplitude with depth into the Earth. These passive waves are typically referred to as ambient seismic noise. Coda waves are a second type of passive seismic wave. The seismic coda refers to the later wave arrivals on a seismogram that are usually discarded in seismology due to their low amplitudes, which often resemble background noise, and to their complexity which has previously made them difficult to interpret. They are generated by the multiple scattering of existing seismic waves (e.g. from past earthquakes) in complex, inhomogeneous media. Both of these passive wave types also obviate the need to measure many individual responses from full boundaries of sources as they are generated constantly in space and time (with varying strength). Furthermore, ambient seismic noise and coda waves have since adopted their own methods of interferometry and their applications in earthquake seismology are discussed below.

Coda-wave interferometry

After travelling through a heterogeneous, strongly-scattering medium, the later arriving seismic waves (the seismic coda) recorded at a receiver station have repeatedly sampled the medium through multiple-scattering (Figure 1.3). This scattering creates the diffusive wavefields necessary to construct a spatially averaged correlation and thus an estimate of the Green's function between two receivers.

Campillo and Paul (2003) provided the first practical application of coda-wave interferometry. The authors performed cross-correlations of the seismic coda from 101 earthquakes that occurred off the coast of Mexico to estimate the Rayleigh and Love wave components of the actual Green's tensor between two receivers on the Earth's surface. The strongly scattered nature of coda waves makes them highly sensitive to small perturbations in the medium compared to the ballistic arrivals that propagate directly between a source and receiver (Gret, 2003). This has made coda waves an attractive tool to monitor small temporal changes in a laboratory setting (Snieder et al.,

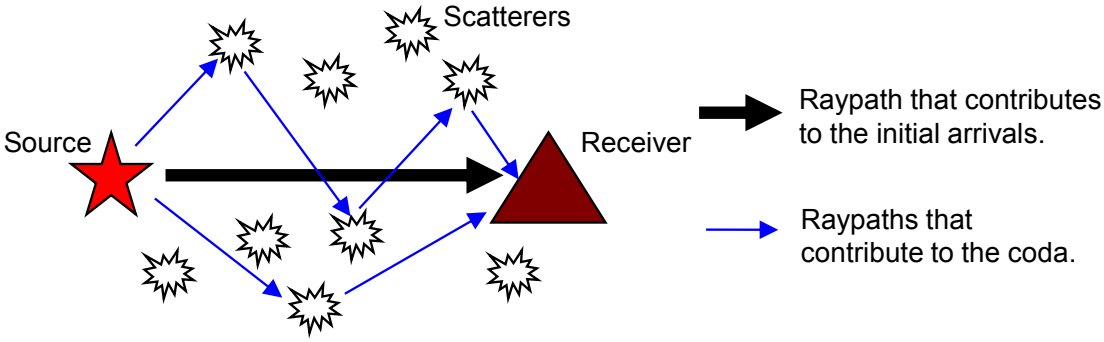

Figure 1.3: A schematic diagram to illustrate difference in path length, and hence traveltime, of the seismic coda caused by multiple scattering compared to initial arrivals.

2002), in fault zones (Wang et al., 2008; Takagi et al., 2012), and more commonly in volcanic settings (Snieder and Hagerty, 2004; Gret et al., 2005; Pandolfi et al., 2006; De Angelis, 2009; Zaccarelli et al., 2009).

Ambient noise interferometry

Ambient seismic noise typically refers to low frequency seismic energy, sources of which include the oceans, wind, industrial noise and the constant "ringing" of the Earth in response to teleseismic earthquakes ("Earth hum"). When recorded over long periods of time, these ambient field fluctuations may be considered to be a diffusive or random field, and cross-correlations of such fields have been found to result in a reasonable estimate of the Green's function (Lobkis and Weaver, 2001). The cross-correlation of mutually uncorrelated noise sources thus provides a non-invasive method to extract the surface wave response between two receivers (Shapiro and Campillo, 2004; Shapiro et al., 2005; Sabra et al., 2005b; Stehly et al., 2007, 2008). Such Rayleigh wave Green's functions do not depend on source location and phase, and are highly sensitive to the region connecting the two receivers. Ambient noise interferometry thus lends itself to the construction of tomographic models with high spatial resolution (Shapiro et al., 2005; Sabra et al., 2005a; Lin et al., 2007; Nicolson et al., 2012, 2014).

Ambient noise interferometry is also commonly used in the monitoring of active volcanoes (e.g. Sens-Schoenfelder and Wegler (2006); Brenguier et al. (2008); Baptie (2010)): continuous ambient noise data recorded on receivers located close to volcanic centres are cross-correlated to construct surface wave estimates between receiver pairs.

These Rayleigh wave Green's functions contain not only the ballistic arrivals, but also reflected and scattered waves that are extremely sensitive to small changes in Earth properties. Comparisons of these Green's functions over time thus identify small changes in the strain properties of the medium sampled by the surface waves, thereby detecting changes in subsurface properties that may lead to potentially hazardous eruptions. The property typically evaluated is seismic velocity and the small changes usually exist far into the coda of the passively estimated Green's functions, not in the direct surface wave arrivals. The application of ambient noise interferometry is occasionally favoured over coda-wave interferometry as it does not require a repeatable source, which can be expensive and can result in temporally irregular measurements in practical field applications (Sens-Schoenfelder and Wegler, 2006).

Albeit less common, ambient noise interferometry has also been shown to construct body wave estimates between receiver locations (Roux et al., 2005; Miyazawa et al., 2008; Lewis and Gerstoft, 2012; Poli et al., 2012a,b; Lin et al., 2013). The first work into P-wave estimation was by Roux et al. (2005). The authors used cross-correlations of ambient seismic noise recorded on a dense, temporary seismic network in the Parkfield area, California, to demonstrate the presence of both Rayleigh waves and P-waves in the estimated Green's functions. Roux et al. (2005) explain the presence of body waves as a consequence of heterogeneities in the Earth's upper crust that convert microseism-induced Rayleigh waves to body waves.

All examples introduced so far have utilised correlation-type interferometry pertaining to the geometry shown in Figure 1.1A, where sources at locations $\mathbf{x}'$ surround the two receivers at locations $\mathbf{x_A}$ and $\mathbf{x_B}$. When the dissipation throughout the medium is significant however, correlation-type interferometry requires sources to be located throughout the whole volume V', not just on a surrounding boundary. This follows from processes of time-reversal (complex conjugation) in correlation-type interferometry, which cannot be applied in attenuative media unless all of the lost energy is projected back into the medium (from sources distributed homogeneously throughout the whole medium). Slob et al. (2007), Slob and Wapenaar (2007) and Wapenaar (2007) propose convolution-type interferometry as an alternative approach to correlation. This method requires one of the receivers to be located outside of volume V', as in Figure 1.1B.

Convolution

Convolution-type interferometry was first trialled in electromagnetics (Slob et al., 2007; Slob and Wapenaar, 2007) as it was observed that when applying ground penetrating radar (GPR) to the shallow subsurface, some energy was always converted to heat. When these losses were significant, spurious arrivals were present in the estimated Green's functions estimated by processes of cross-correlation. Convolution interferometry was thus introduced for electromagnetic wavefields in lossy media, but with the possibility of extending the theory to acoustic and elastic wavefields.

Halliday and Curtis (2009) provided the first example of convolution-type interferometry in seismology. They observed that when using scattered surface waves in attenuating elastic media, terms associated with the cross-correlation of scattered wavefields in the governing theoretical equations were responsible for constructing estimates of the Green's functions between two observation points that deviated from the true estimate of the Green's function. These terms contain non-physical arrivals that should mutually cancel in lossless media, but do not when the source boundary is incomplete or when the medium is attenuating. Attenuation introduces amplitude imbalances into the mutually cancelling terms and as a result, non-physical arrivals are constructed in the final correlation Green's functions. Halliday and Curtis (2009) show that non-physical arrivals do not exist in the mutually cancelling terms in the equations governing convolution-type interferometry. Convolution interferometry thus provides a suitable alternative to correlation interferometry when the medium is strongly attenuating or when the source aperture is limited (Halliday and Curtis, 2009).

Deconvolution

Finally, we consider interferometry by deconvolution. One of the main differences between correlation interferometry and the deconvolution approach is that correlation interferometry estimates the Green's function between two measurement locations, whereas deconvolution does not. Instead, deconvolution constructs a wavefield that, for $t = 0$, vanishes at the virtual source location. This is described as a "clamped boundary condition" by Vasconcelos and Snieder (2008a,b), who provide extensive reviews of interferometry by 1D deconvolution.

Interferometry by deconvolution was first used by Snieder and Safak (2006) to extract the building response of the Millikan Library in Pasadena, California. The

authors deconvolved the motion recorded at different levels within the building and used the deconvolved wavefields to determine the shear velocity and attenuation in the building. Mehta et al. (2007) used 1D deconvolution to determine properties of the near-surface. The authors deconvolved earthquake signals recorded on receivers located at different depths throughout boreholes with those same signals recorded on the surface. These deconvolved waves exhibit upwards and downwards propagating waves that were used to determine P- and S-wave velocities near the surface. Furthermore, a comparison of the amplitudes of the up- and down-going waves at the same depth would allow the quality factor (a measure of attenuation) to be estimated.

The 1D deconvolution approach to interferometry is extended to two and three dimensions by multidimensional deconvolution (MDD). The geometry required for MDD is similar to that for convolution-type interferometry and is shown here in Figure 1.4: receivers $\mathbf{x}$ on boundary S surround an individual receiver at $\mathbf{x_B}$; a source at $\mathbf{x_S}$ lies outside of the volume V. The response from the source at $\mathbf{x_S}$ is recorded on $\mathbf{x}$ ($G(\mathbf{x}, \mathbf{x_S})$) and on $\mathbf{x_B}$ ($G(\mathbf{x_B}, \mathbf{x_S})$). The unknown that we want to resolve by MDD is the Green's function between $\mathbf{x}$ and $\mathbf{x_B}$ ($G(\mathbf{x_B}, \mathbf{x})$). This represents the response that would be recorded at receiver $\mathbf{x_B}$ if an impulsive source were fired from the location of $\mathbf{x}$, thus turning the receiver at $\mathbf{x}$ into a virtual source. $G(\mathbf{x_B}, \mathbf{x})$ is estimated by inverting the Green's function $G(\mathbf{x}, \mathbf{x_S})$ using methods of least squares (van der Neut et al., 2010; Wapenaar et al., 2011a; van der Neut et al., 2011) or singular value decomposition (Minato et al., 2011; van Dalen et al., 2014), for example.

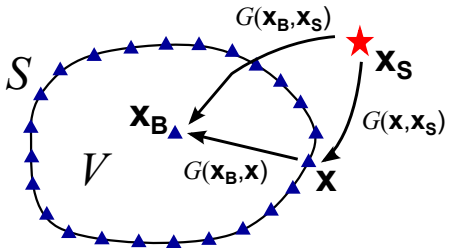

Figure 1.4: A schematic diagram illustrating one possible geometry required to perform multidimensional deconvolution (MDD). Key as in Figure 1.1. The rays represent full responses, including primary and multiple scattering due to inhomogeneities inside and outside S. Terms such as $G(\mathbf{x}, \mathbf{x_S})$ represent the Green's function between, in this case, the source at $\mathbf{x_S}$ and the receiver at $\mathbf{x}$.

MDD does not rely on a regular source distribution but it does require a regular array of receivers on which the source energy is recorded. Unlike correlation-type interferometry, MDD is valid in media with and without losses. This makes MDD

an attractive alternative to correlation-type interferometry. MDD typically involves the separation of the observed wavefields into their up-going and down-going components, which requires both pressure and particle velocity data (e.g. Wapenaar et al. (2008a, 2011b)). If backscattered energy is assumed to be weak across the receiver boundary S however, we show in Chapter 7 how the full observed wavefields at $\mathbf{x}$ and $\mathbf{x_B}$ can be used instead of the up- and down-going components (Wapenaar et al., 2011a).

The MDD method was first trialled in numerical examples using both controlled-source electromagnetic (CSEM) data (Wapenaar et al., 2008a) and passive seismic data (Wapenaar et al., 2008b). MDD has since been used in other numerical examples to redatum controlled free-surface source seismic data to downhole receivers (van der Neut et al., 2011), and to estimate the surface waves between pairs of seismometers from within the USArray seismometer network (Wapenaar et al., 2011a). In the latter study, the authors synthesise (model) ambient seismic noise in the Atlantic Ocean that propagates towards an array of seismometers aligned North-South in the centre of the United States. The noise wavefields recorded on the array are not separated into their directional components in this example as it is assumed that the energy propagates from this one direction only (from East to West). The authors show how surface waves estimated using MDD are significantly more accurate than those estimated by correlation interferometry alone. This follows from a better focussing of the virtual sources (at the locations of the array seismometers) in space and time when using MDD. Recently, Nakata et al. (2014) provided the first application of MDD on a real earthquake dataset to estimate PP, PS and SS reflected plane waves, using the separation of the wavefields to perform MDD. For a concise review of interferometry by MDD and a systematic comparison with interferometry by cross-correlation, see Wapenaar et al. (2011b).

So far we have reviewed inter-receiver interferometry by processes of correlation, convolution and deconvolution. All methods have been shown to estimate the Green's functions between pairs of receivers. Next we consider inter-source interferometry to estimate the Green's functions between pairs of sources.

1.1.2 Inter-source interferometry

Figure 1.5 illustrates two possible geometries for inter-source interferometry, obtained by applying the theory of source-receiver reciprocity to the geometries in Figure 1.1 and thus to the equations governing inter-receiver interferometry (see Chapter 2). Integrating (summing) over all receiver locations estimates the Green's function

between the two sources as if a "virtual receiver" had been active at the location of one of the sources (Hong and Menke, 2006; Curtis et al., 2009; Tonegawa and Nishida, 2010; Poliannikov et al., 2012). As for inter-receiver interferometry, any correlation-type interferometric processes assume zero attenuation. Thus, in Figure 1.5A the medium inside V is assumed lossless.

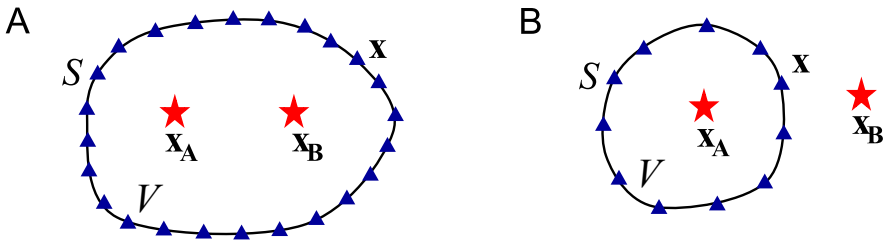

Figure 1.5: Schematic source and receiver geometries for inter-source interferometry. Key as in Figure 1.1. The responses from sources at locations $\mathbf{x_A}$ and $\mathbf{x_B}$ are recorded on each receiver $\mathbf{x}$ on boundary S and (A) cross-correlated or (B) convolved. In both cases the results of all cross-correlations or convolutions are summed (integrated over S) to obtain an approximation of the Green's function between the sources at $\mathbf{x_A}$ and $\mathbf{x_B}$.

Hong and Menke (2006) were the first to use spatial reciprocity to redatum receiver arrays to regions of seismicity at depth along a fault plane. The authors created seismic records at event locations by stacking the original station records of an event obtained on receivers within a surface array. These stacked waveforms then represented an observation at the event location for synchronised impulses at the station locations. For each pair of events along the fault plane, stacked waveforms were cross-correlated to estimate the Green's function between that event pair. The Green's functions were then used to construct tomographic maps of shear velocity and to image the fault zone.

The method first became known as "inter-source interferometry" when Curtis et al. (2009) extracted surface waves between two earthquake locations, thus turning one earthquake source into a virtual seismometer. The authors applied this method and the concept of stationary phase to show that earthquake responses constructed on virtual receivers were consistent with those recorded by instrumental seismometers.

The first study to extract body waves between two earthquake sources was by Tonegawa and Nishida (2010). Direct P- and S-waves extracted between two earthquakes at depths of 300 km - 500 km emphasised the potential of inter-source interferometry to reveal new seismological features in the Earth's deep interior.

The method of inter-source interferometry thus has the potential to be applied in a number of tectonic settings as a tool for remotely observing changes in the elastic properties of the subsurface. Importantly, the method offers the possibility to explore new geographical areas which have previously been inaccessible, due to extreme weather, terrain etc., or areas where receiver coverage is sparse. The literature reviewed herein has used correlation-type inter-source interferometry as in Figure 1.5A; however, convolution inter-source interferometry is equally as applicable if the source and receiver geometry pertains to that in Figure 1.5B.

1.1.3 Source-receiver interferometry

Source-receiver interferometry (SRI) is a third interferometric method that can be derived either directly from representation theorems (Curtis and Halliday, 2010; Halliday and Curtis, 2010), or by combining the theories of inter-receiver and inter-source interferometry (Curtis, 2009; Curtis et al., 2012). The result is that a Green's function between a source and a receiver can be constructed from data recorded from a set of other sources on a boundary of other receivers. Processes of correlation and/or convolution can be used to perform SRI, and three possible geometries are shown in Figure 1.6 pertaining to (A) correlation-correlation SRI, (B) correlation-convolution SRI, and (C) convolution-convolution SRI. These three forms of SRI are derived and described in full by Curtis and Halliday (2010). Alternatively, we propose processes of deconvolution to construct two additional forms of SRI - deconvolution-correlation SRI and deconvolution-convolution SRI. These two forms of SRI require MDD as introduced above and will be discussed in more detail in Chapter 8.

Full boundaries of sources and receivers are not required to construct accurate Green's function estimates between $\mathbf{s}$ and $\mathbf{r}$. Instead, invoking the stationary phase approach as described earlier one only requires those sources and receivers that lie approximately around the stationary phase regions of boundaries S' and S. These regions are highlighted schematically in Figure 1.6A by the grey shaded lines. This significantly reduces the number of direct observations that need to be recorded and thus the number of correlations/convolutions/deconvolutions performed.

SRI has led to the development of new algorithms for imaging (Halliday and Curtis, 2010; Vasconcelos et al., 2010; Poliannikov, 2011; Poliannikov et al., 2012; Vasconcelos and Rickett, 2013; Ravasi and Curtis, 2013a,b; Vasconcelos, 2013; Ravasi et al., 2014), noise removal (Halliday et al., 2007, 2010; Duguid et al., 2011), methods to correct for errors in inter-receiver and inter-source interferometry (King and Curtis,

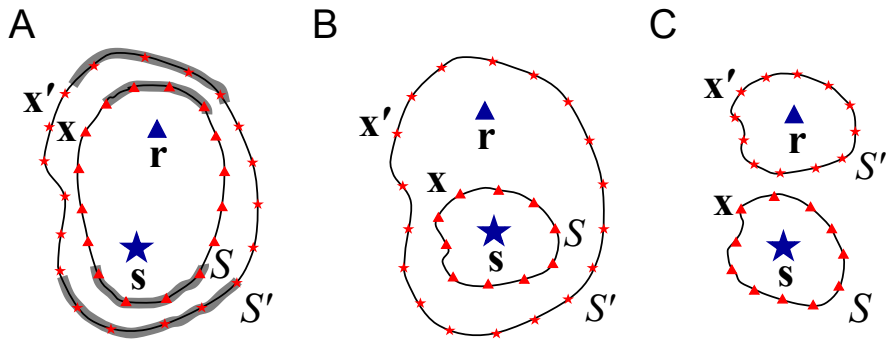

Figure 1.6: Three possible source and receiver geometries for source-receiver interferometry (SRI) pertaining to (A) correlation-correlation SRI, (B) correlation-convolution SRI, and (C) convolution-convolution SRI. Key as in Figure 1.1. The grey shaded regions in (A) highlight schematically the stationary phase regions of the boundaries S and S'.

2012; Meles and Curtis, 2014a) and methods to analyse and synthesise scattered wavefields (Loer et al., 2014a,b; Meles and Curtis, 2014b). All of these methods involve using SRI for some form of spatial redatuming of recorded data.

Recently however, Curtis et al. (2012) showed that SRI can also be used for a type of temporal redatuming: using recordings of earthquake sources made on a backbone seismometer array, seismograms of the same source events can be constructed on receivers that were not deployed at the time of the event. Thus 'retrospective' seismology is possible whereby one obtains virtual seismograms of an energy source at the location of a new seismometer, chosen retrospectively after that source was activated and after all energy from it has dissipated. One can thus use the benefit of hindsight of the source location or magnitude estimates to decide at which new locations to construct a new seismogram.

Curtis et al. (2012) demonstrated this idea by reconstructing seismic signals from two earthquakes in New Zealand on a set of temporary seismometers, some of which were not actively recording data when the earthquakes occurred. The new seismograms obtained were used to estimate seismic velocities in the vicinity of the seismometers and in principle provide independent information about the source phase.

1.2 Thesis Motivation, Objectives and Layout

The ability of source-receiver interferometry (SRI) to both spatially and temporally redatum earthquake seismogram data may lead to significant implications within earthquake seismology: in the days following a large earthquake, temporary

seismometers might be deployed closer to the earthquake epicentre to measure subsequent seismic activity in the area. Had these temporary seismometers been deployed at the time of the main event, properties of that earthquake would be better constrained. Using a backbone array of seismometers that did record the earthquake energy, in principle one can spatially and temporally redatum the energy fluctuations from the main event onto the set of temporary seismometers.

The initial work by Curtis et al. (2012) showed that SRI was able to construct earthquake seismograms retrospectively on 5 new seismometer locations (herein referred to as 'target sensors'). The authors tested the method on a relatively small length scale in which earthquake seismogram data was redatumed over distances < 100 km from a backbone array seismometers to the locations of the 5 target sensors. However, the successes and limitations of the method in other real, practical applications are still unknown. Here we aim to bring to light the constraints that larger scale applications may impose on the method.

The primary objectives of this thesis have thus been to:

- Develop a set of spatial criteria for the application of source-receiver interferometry (SRI) that links the spatial extent of backbone arrays of seismometers to earthquake epicentres and to the locations of seismometers (target sensors) at which we wish to construct the new earthquake seismograms.
- Use these spatial criteria to devise a robust methodology to invoke correlation-correlation SRI on multiple length scales using ambient seismic noise and earthquake seismogram data.
- Adapt this methodology to invoke correlation-convolution SRI.
- Apply the SRI methodologies to construct earthquake seismograms of past events retrospectively on target sensors that were not necessarily deployed when the events occurred.
- Determine the successes and limitations of both correlation-correlation SRI and correlation-convolution SRI using earthquake data that sample multiple earthquake magnitude scales and a number of inter-station length scales.
- Consider multidimensional deconvolution (MDD) as an alternative method to Green's function estimation when Earth properties limit the theoretical

application of correlation-type interferometry, and assess the potential of MDD in SRI.

These objectives have been addressed in six chapters that are a compilation of three unpublished papers. Chapter 2 introduces the theory behind correlation-correlation SRI and correlation-convolution SRI and how the theories are adapted for practical application in earthquake seismology. Chapter 3 provides a detailed description of the SRI methodologies developed and trialled throughout this PhD. Chapters 4 and 5 then provide examples of both correlation-correlation SRI and correlation-convolution SRI, respectively, invoking the theories and methodologies described in Chapters 2 and 3 to construct earthquake seismograms retrospectively. This is the first time correlation-convolution SRI has been used for both spatial and temporal redatuming of earthquake seismogram data. Chapter 6 provides a quantitative analysis of the SRI methods by constructing the seismograms of 87 earthquakes. This chapter is designed to determine the successes and limitations of the SRI methodologies when required to perform over multiple length and earthquake magnitude scales. Finally, in Chapter 7 we use multidimensional deconvolution (MDD) as an alternative approach to noise interferometry to estimate inter-receiver Green's functions between pairs of seismometers located at varying inter-station distances throughout the United States. We compare the results of MDD with those of noise interferometry. This study is preliminary, but it provides one of the first applications of MDD using real earthquake data, without separating the up- and down-going wavefield components.

1.3 Paper Plan

The individual chapters of this thesis are compiled/in preparation for publication as follows:

- Chapters 4 and 5: Combined, these two chapters have formed the basis of *"Constructing new seismograms from old earthquakes: Retrospective seismology at multiple length scales"*, which has been submitted to the Journal of Geophysical Research (JGR). Co-authors: Andrew Curtis, Erica Galetti, Brian Baptie and Giovanni Meles. The relevant sections of Chapters 2 and 3 have been incorporated within the paper to provide full reviews of correlation-correlation SRI and correlation-convolution SRI.

- Chapter 6: In preparation. This paper will provide an extensive review of SRI, discussing the successes and limitations of the method in earthquake seismology.
- Chapter 7: This chapter provides a preliminary analysis of Green's function estimation by MDD. Before publication, this chapter will be extended to include more earthquake data and larger seismometer arrays in order to present a comprehensive analysis of MDD. Source-receiver interferometry by MDD will also be trialled.

In invoking this multi-paper format for the thesis, a significant amount of repetition is present throughout. Where possible however attempts have been made to cross-reference the relevant theory and methodologies introduced and described in Chapters 2 and 3, respectively.

Bibliography

Bakulin, A., and R. Calvert (2004), Virtual source: new method for imaging and 4D below complex overburden, 74th Annual International Meeting, 23(1), 2477–2480, SEG Technical Program Expanded Abstracts.

Baptie, B. (2010), Lava dome collapse detected using passive seismic interferometry, Geophysical Research Letters, 37, doi:{10.1029/2010GL042489}.

Bensen, G. D., M. H. Ritzwoller, and N. M. Shapiro (2008), Broadband ambient noise surface wave tomography across the United States, Journal of Geophysical Research - Solid Earth, 113(B5), doi:{10.1029/2007JB005248}.

Brenguier, F., N. Shapiro, M. Campillo, V. Ferrazzini, Z. Duputel, O. Coutant, and A. Nercessian (2008), Towards forecasting volcanic eruptions using seismic noise, Nature Geoscience, 1(2), 126–130, doi:{10.1038/ngeo104}.

Campillo, M., and A. Paul (2003), Long-Range Correlations in the Diffuse Seismic Coda, Science, 299, 547–549, doi:{10.1126/science.1078551}.

Cassereau, D., and M. Fink (1993), Focusing with plane time-reversal mirrors - an efficient alternative to closed cavities, Journal of the Acoustical Society of America, 94(4), 2373–2386, doi:{10.1121/1.407457}.

Claerbout, J. (1968), Sythensis of a layered medium from its acoustic transmission response, Geophysics, 33(2), 264–&, doi:{10.1190/1.1439927}.

Curtis, A. (2009), Source-receiver seismic interferometry, chap. 733, pp. 3655–3659, Society of Exploration Geophysicists, doi:{10.1190/1.3255626}.

Curtis, A., and D. Halliday (2010), Source-receiver wave field interferometry, Physical Review E, 81(4, 2), doi:{10.1103/PhysRevE.81.046601}.

Curtis, A., H. Nicolson, D. Halliday, J. Trampert, and B. Baptie (2009), Virtual seismometers in the subsurface of the Earth from seismic interferometry, Nature Geoscience, 2(10), 700–704, doi:{10.1038/NGEO615}.

Curtis, A., Y. Behr, E. Entwistle, E. Galetti, J. Townend, and S. Bannister (2012), The benefit of hindsight in observational science: Retrospective seismological observations, Earth and Planetary Science Letters, 345, doi:{DI10.1016/j.epsl.2012.06.008}.

De Angelis, S. (2009), Seismic source displacement by coda wave interferometry at soufriÃÍre hills volcano, montserrat, wi, Natural Hazards and Earth System Science, 9(4), 1341–1347, doi:10.5194/nhess-9-1341-2009.

Derode, A., E. Larose, M. Campillo, and M. Fink (2003a), How to estimate the Green's function of a heterogeneous medium between two passive sensors? Application to acoustic waves, Applied Physics Letters, 83(15), 3054–3056, doi:{http://dx.doi.org/10.1063/1.1617373}.

Derode, A., E. Larose, M. Tanter, J. de Rosny, A. Tourin, M. Campillo, and M. Fink (2003b), Recovering the Green's function from field-field correlations in an open scattering medium (L), Journal of the Acoustical Society of America, 113(6), 2973–2976, doi:{10.1121/1.1570436}.

Duguid, C., D. Halliday, and A. Curtis (2011), Source-receiver interferometry for seismic wavefield construction and ground-roll removal, The Leading Edge, 30(8), 838–843, doi:{10.1190/1.3626489}.

Gret, A. (2003), Time-Lapse Monitoring with Coda Wave Iinterferometry, Ph.D. thesis, Center for Wave Phenomena, Colorado School of Mines, 1500 Illinois Street, Golden, Colorado 80401.

Gret, A., R. Snieder, R. Aster, and P. Kyle (2005), Monitoring rapid temporal change in a volcano with coda wave interferometry, Geophysical Research Letters, 32, doi:{10.1029/2004GL021143}.

Halliday, D., and A. Curtis (2009), Seismic interferometry of scattered surface waves in attenuative media, Geophysical Journal International, 178(1), 419–446, doi:{10.1111/j.1365-246X.2009.04153.x}.

Halliday, D., and A. Curtis (2010), An interferometric theory of source-receiver scattering and imaging, Geophysics, 75(6), SA95–SA103, doi:{10.1190/1.3486453}.

Halliday, D., A. Curtis, and K. Wapenaar (2012), Generalized PP plus PS=SS from seismic interferometry, Geophysical Journal International, 189(2), 1015–1024, doi:{10.1111/j.1365-246X.2012.05396.x}.

Halliday, D. F., A. Curtis, J. O. A. Robertsson, and D.-J. van Manen (2007), Interferometric surface-wave isolation and removal, Geophysics, 72(5), A69–A73, doi:{10.1190/1.2761967}.

Halliday, D. F., A. Curtis, P. Vermeer, C. Strobbia, A. Glushchenko, D. van Manen, and J. O. A. Robertsson (2010), Interferometric ground-roll removal: Attenuation of scattered surface waves in single-sensor data, Geophysics, 75(2), SA15–SA25, doi:{10.1190/1.3360948}.

Hong, T.-K., and W. Menke (2006), Tomographic investigation of the wear along the San Jacinto fault, southern California, Physics of the Earth and Planetary Interiors, 155(3-4), 236–248, doi:{10.1016/j.pepi.2005.12.005}.

King, S., and A. Curtis (2012), Suppressing nonphysical reflections in Green's function estimates using source-receiver interferometry, Geophysics, 77(1), Q15–Q25, doi:{10.1190/GEO2011-0300.1}.

Lewis, M. A., and P. Gerstoft (2012), Shear wave anisotropy from cross-correlation of seismic noise in the Parkfield pilot hole, Geophysical Journal International, 188(2), 626–630, doi:{10.1111/j.1365-246X.2011.05285.x}.

Lin, F., M. H. Ritzwoller, J. Townend, S. Bannister, and M. K. Savage (2007), Ambient noise Rayleigh wave tomography of new Zealand, Geophysical Journal International, 170(2), 649–666, doi:{10.1111/j.1365-246X.2007.03414.x}.

Lin, F.-C., V. C. Tsai, B. Schmandt, Z. Duputel, and Z. Zhan (2013), Extracting seismic core phases with array interferometry, Geophysical Research Letters, 40(6), 1049–1053, doi:{10.1002/grl.50237}.

Lobkis, O., and R. Weaver (2001), On the emergence of the Green's function in the correlations of a diffuse field, Journal of the Acoustical Society of America, 110, 3011–3017, doi:{10.1121/1.1417528}.

Loer, K., G. A. Meles, A. Curtis, and I. Vasconcelos (2014a), Diffracted and pseudo-physical waves from spatially limited arrays using source-receiver interferometry (SRI), Geophysical Journal International, 196(2), 1043–1059, doi:{10.1093/gji/ggt435}.

Loer, K., G. Meles, and A. Curtis (2014b), Automated identification of multiply diffracted waves and their ordered scattering paths, submitted, JASA.

Mehta, K., R. Snieder, and V. Graizer (2007), Extraction of near-surface properties for a lossy layered medium using the propagator matrix, Geophysical Journal International, 169(1), 271–280, doi:{10.1111/j.1365-246X.2006.03303.x}.

Meles, G. A., and A. Curtis (2014a), Discriminating physical and non-physical diffracted energy in sourceâĂŞreceiver interferometry, Geophysical Journal International, doi:10.1093/gji/ggu054.

Meles, G. A., and A. Curtis (2014b), Fingerprinting ordered diffractions in multiply diffracted waves, Geophysical Journal International, 198(3), 1701–1713, doi:10.1093/gji/ggu195.

Minato, S., T. Matsuoka, T. Tsuji, D. Draganov, J. Hunziker, and K. Wapenaar (2011), Seismic interferometry using multidimensional deconvolution and crosscorrelation for crosswell seismic reflection data without borehole sources, Geophysics, 76(1), SA19–SA34, doi:{10.1190/1.3511357}.

Miyazawa, M., R. Snieder, and A. Venkataraman (2008), Application of seismic interferometry to extract P- and S-wave propagation and observation of shear-wave splitting from noise data at Cold Lake, Alberta, Canada, Geophysics, 73(4), D35–D40, doi:{10.1190/1.2937172}.

Nakata, N., R. Snieder, and M. Behm (2014), Body-wave interferometry using regional earthquakes with multidimensional deconvolution after wavefield decomposition at free surface, Geophysical Journal International, 199(2), 1125–1137, doi:10.1093/gji/ggu316.

Nicolson, H., A. Curtis, B. Baptie, and E. Galetti (2012), Seismic interferometry and ambient noise tomography in the British Isles, Proceedings of the Geologists Association, 123(1), 74–86, doi:{10.1016/j.pgeola.2011.04.002}.

Nicolson, H., A. Curtis, and B. Baptie (2014), Rayleigh wave tomography of the British Isles from ambient seismic noise, Geophysical Journal International, 198(2), 637–655, doi:{10.1093/gji/ggu071}.

Pandolfi, D., C. Bean, and G. Saccorotti (2006), Coda wave interferometric detection of seismic velocity changes associated with the 1999 M=3.6 event at Mt. Vesuvius, Geophysical Research Letters, 33(6), doi:{10.1029/2005GL025355}.

Poli, P., M. Campillo, H. Pedersen, and L. W. Grp (2012a), Body-Wave Imaging of Earth's Mantle Discontinuities from Ambient Seismic Noise, Science, 338(6110), 1063–1065, doi:{10.1126/science.1228194}.

Poli, P., H. A. Pedersen, M. Campillo, and P. L. W. Grp (2012b), Emergence of body waves from cross-correlation of short period seismic noise, Geophysical Journal International, 188(2), 549–558, doi:{10.1111/j.1365-246X.2011.05271.x}.

Poliannikov, O. V. (2011), Retrieving reflections by source-receiver wavefield interferometry, Geophysics, 76(1), SA1–SA8, doi:{10.1190/1.3524241}.

Poliannikov, O. V., S. Rondenay, and L. Chen (2012), Interferometric imaging of the underside of a subducting crust, Geophysical Journal International, 189(1), 681–690, doi:{10.1111/j.1365-246X.2012.05389.x}.

Ravasi, M., and A. Curtis (2013a), Nonlinear scattering based imaging in elastic media: Theory, theorems, and imaging conditions, Geophysics, 78(3), S137–S155, doi:{10.1190/GEO2012-0286.1}.

Ravasi, M., and A. Curtis (2013b), Elastic imaging with exact wavefield extrapolation for application to ocean-bottom 4C seismic data, Geophysics, 78(6), S265–S284, doi:{10.1190/GEO2013-0152.1}.

Ravasi, M., I. Vasconcelos, and A. Curtis (2014), Beyond conventional migration: non-linear elastic subsalt imaging with transmissions and two-sided illumination, Geophyscial Journal International, 198(2), 1173–1185, doi:{10.1093/gji/ggu192}.

Rickett, J., and J. Claerbout (1999), Acoustic daylight imaging via spectral factorization: Helioseismology and reservoir monitoring, The Leading Edge, 18(1), 1675–1678.

Roux, P., and M. Fink (2003), Green's function estimation using secondary sources in a shallow water environment, Journal of the Acoustical Society of America, 113(3), 1406–1416, doi:{10.1121/1.1542645}.

Roux, P., K. Sabra, P. Gerstoft, W. Kuperman, and M. Fehler (2005), P-waves from cross-correlation of seismic noise, Geophysical Research Letters, 32(19), doi:{10.1029/2005GL023803}.

Sabra, K., P. Gerstoft, P. Roux, W. Kuperman, and M. Fehler (2005a), Extracting time-domain Green's function estimates from ambient seismic noise, Geophysical Research Letters, 32, doi:{10.1029/2004GL021862}.

Sabra, K., S. Conti, P. Roux, and W. Kuperman (2007), Passive in vivo elastography from skeletal muscle noise, Applied Physics Letters, 90(19), doi:{10.1063/1.2737358}.

Sabra, K. G., P. Gerstoft, W. A. Roux, P .and Kuperman, and M. C. Fehler (2005b), Surface wave tomography from microseisms in Southern California, Geophysical Research Letters, 32(14), doi:{10.1029/2005GL023155}.

Schuster, G. (2001), Theory of daylight/interferometric imaging: Tutorial, 63rd Conference and Technical Exhibition, EAGE, Extended Abstracts, A32.

Schuster, G. (2009), Seismic Interferometry, Cambridge University Press.

Schuster, G., J. Yu, J. Sheng, and J. Rickett (2004), Interferometric daylight seismic imaging, Geophysical Journal International, 157, 838–852, doi:{10.1111/j.1365-246X.2004.02251.x}.

Sens-Schoenfelder, C., and U. Wegler (2006), Passive image interferometry and seasonal variations of seismic velocities at Merapi Volcano, Indonesia, Geophysical Research Letters, 33, doi:{10.1029/2006GL027797}.

Shapiro, N. M., and M. Campillo (2004), Emergence of broadband Rayleigh waves from correlations of the ambient seismic noise, Geophysical Research Letters, 31(7), doi:{10.1029/2004GL019491}.

Shapiro, N. M., M. Campillo, L. Stehly, and M. H. Ritzwoller (2005), High-resolution surface-wave tomography from ambient seismic noise, Science, 307(5715), 1615–1618, doi:{10.1126/science.1108339}.

Slob, E., and K. Wapenaar (2007), Electromagnetic Green's functions retrieval by cross-correlation and cross-convolution in media with losses, Geophysical Research Letters, 34(5), doi:{10.1029/2006GL029097}.

Slob, E., D. Draganov, and K. Wapenaar (2007), Interferometric electromagnetic Green's functions representations using propagation invariants, Geophysical Journal International, 169(1), 60–80, doi:{10.1111/j.1365-246X.2006.03296.x}.

Snieder, R. (2004), Extracting the Green's function from the correlation of coda waves: A derivation based on stationary phase, Physical Review E, 69(4, 2), doi:{10.1103/PhysRevE.69.046610}.

Snieder, R., and M. Hagerty (2004), Monitoring change in volcanic interiors using coda wave interferometry: Application to Arenal Volcano, Costa Rica, Geophysical Research Letters, 31(9), doi:{10.1029/2004GL019670}.

Snieder, R., and E. Safak (2006), Extracting the building response using seismic interferometry: Theory and application to the Millikan Library in Pasadena, California, Bulletin of the Seismological Society of America, 96(2), 586–598, doi:{10.1785/0120050109}.

Snieder, R., A. Gret, H. Douma, and J. Scales (2002), Coda wave interferometry for estimating nonlinear behavior in seismic velocity, Science, 295(5563), 2253–2255, doi:{10.1126/science.1070015}.

Snieder, R., K. Wapenaar, and K. Larner (2006), Spurious multiples in seismic interferometry of primaries, Geophysics, 71(4, S), SI111–SI124, doi:{10.1190/1.2211507}, 75th Annual International Meeting of the Society-of-Exploration-Geophysicists, Houston, TX, NOV 06-11, 2005.

Stehly, L., M. Campillo, and N. M. Shapiro (2007), Traveltime measurements from noise correlation: stability and detection of instrumental time-shifts, Geophysical Journal International, 171(1), 223–230, doi:{10.1111/j.1365-246X.2007.03492.x}.

Stehly, L., M. Campillo, B. Froment, and R. Weaver (2008), Reconstructing Green's function by correlation of the coda of the correlation (C(3)) of ambient seismic noise, Journal of Geophysical Research - Solid Earth, 113(B11), doi:{10.1029/2008JB005693}.

Takagi, R., T. Okada, H. Nakahara, N. Umino, and A. Hasegawa (2012), Coseismic velocity change in and around the focal region of the 2008 Iwate-Miyagi Nairiku earthquake, Journal of Geophysical Research - Solid Earth, 117, doi:{10.1029/2012JB009252}.

Tonegawa, T., and K. Nishida (2010), Inter-source body wave propagations derived from seismic interferometry, Geophysical Journal International, 183(2), 861–868, doi:{10.1111/j.1365-246X.2010.04753.x}.

van Dalen, K. N., K. Wapenaar, and D. F. Halliday (2014), Surface wave retrieval in layered media using seismic interferometry by multidimensional deconvolution, Geophysical Journal International, 196(1), 230–242, doi:{10.1093/gji/ggt389}.

van der Neut, J., E. Ruigrok, D. Draganov, and K. Wapenaar (2010), Retrieving the earth's reflection response by multi-dimensional deconvolution of ambient seismic noise, EAGE, Extended Abstracts, pp. P406–1–P406–4.

van der Neut, J., J. Thorbecke, K. Mehta, E. Slob, and K. Wapenaar (2011), Controlled-source interferometric redatuming by crosscorrelation and multidimensional deconvolution in elastic media, Geophysics, 76(4), SA63–SA76, doi:{10.1190/1.3580633}.

van Manen, D.-J., J. Robertsson, and A. Curtis (2005), Modeling of wave propagation in inhomogeneous media, Physical Review Letters, 94(16), doi:{10.1103/PhysRevLett.94.164301}.

van Manen, D.-J., A. Curtis, and J. Robertsson (2006), Interferometric modeling of wave propagation in inhomogeneous elastic media using time reversal and reciprocity, Geophysics, 71(4, S), SI47–SI60, doi:{10.1190/1.2213218}, 75th Annual International Meeting of the Society-of-Exploration-Geophysicists, Houston, TX, NOV 06-11, 2005.

Vasconcelos, I. (2013), Source-receiver, reverse-time imaging of dual-source, vector-acoustic seismic data, Geophysics, 78(2), WA123–WA145, doi:{10.1190/GEO2012-0300.1}.

Vasconcelos, I., and J. Rickett (2013), Broadband extended images by joint inversion of multiple blended wavefields, Geophysics, 78(2), WA147–WA158, doi:{10.1190/GEO2012-0475.1}.

Vasconcelos, I., and R. Snieder (2008a), Interferometry by deconvolution: Part 1 - Theory for acoustic waves and numerical examples, Geophysics, 73(3), S115–S128, doi:{10.1190/1.2904554}.

Vasconcelos, I., and R. Snieder (2008b), Interferometry by deconvolution: Part 2 - Theory for elastic waves and application to drill-bit seismic imaging, Geophysics, 73(3), S129–S141, doi:{10.1190/1.2904985}.

Vasconcelos, I., P. Sava, and H. Douma (2010), Nonlinear extended images via image-domain interferometry, Geophysics, 75(6), SA105–SA115, doi:{10.1190/1.3494083}.

Wang, B., P. Zhu, Y. Chen, F. Niu, and B. Wang (2008), Continuous subsurface velocity measurement with coda wave interferometry, Journal of Geophsical Research - Solid Earth, 113(B12), doi:{10.1029/2007JB005023}.

Wapenaar, K. (2003), Synthesis of an inhomogeneous medium from its acoustic transmission response, Geophysics, 68(5), 1756–1759, doi:{10.1190/1.1620649}.

Wapenaar, K. (2004), Retrieving the elastodynamic Green's function of an arbitrary inhomogeneous medium by cross correlation, Physical Review Letters, 93(25), doi:{10.1103/PhysRevLett.93.254301}.

Wapenaar, K. (2007), General representations for wavefield modeling and inversion in geophysics, Geophysics, 72(5, S), SM5–SM17, doi:{10.1190/1.2750646}.

Wapenaar, K., and J. Fokkema (2006), Green's function representations for seismic interferometry, Geophysics, 71, SI33–SI46, doi:{10.1190/1.2213955}.

Wapenaar, K., E. Slob, and R. Snieder (2008a), Seismic and electromagnetic controlled-source interferometry in dissipative media, Geophysical Prospecting, 56, 419–434, doi:{10.1190/1.2976118}.

Wapenaar, K., J. van der Neut, and E. Ruigrok (2008b), Passive seismic interferometry by multidimensional deconvolution, Geophysics, 73(6), A51–A56, doi:{10.1190/1.2976118}.

Wapenaar, K., E. Slob, R. Snieder, and A. Curtis (2010), Tutorial on seismic interferometry: Part 2-Underlying theory and new advances, Geophysics, 75(5), A211–A227, doi:{10.1190/1.3463440}.

Wapenaar, K., E. Ruigrok, J. van der Neut, and D. Draganov (2011a), Improved surface-wave retrieval from ambient seismic noise by multi-dimensional deconvolution, Geophysical Research Letters, 38, doi:{10.1029/2010GL045523}.

Wapenaar, K., J. van der Neut, E. Ruigrok, D. Draganov, J. Hunziker, E. Slob, J. Thorbecke, and R. Snieder (2011b), Seismic interferometry by crosscorrelation and by multidimensional deconvolution: a systematic comparison, Geophysical

Journal International, 185(3), 1335–1364, doi:{10.1111/j.1365-246X.2011.05007.x}.

Weaver, R., and O. Lobkis (2001), Ultrasonics without a source: Thermal fluctuation correlations at MHz frequencies, Physical Review Letters, 87(13), doi:{10.1103/PhysRevLett.87.134301}.

Xiao, X., M. Zhou, and G. T. Schuster (2006), Salt-flank delineation by interferometric imaging of transmitted P- to S-waves, Geophysics, 71(4, S), SI197–SI207, doi:{10.1190/1.2209550}, 75th Annual International Meeting of the Soceity-of-Exploration-Geophysicists, Houston, TX, NOV 06-11, 2005.

Zaccarelli, L., D. Pandolfi, F. Bianco, G. Saccorotti, C. Bean, and E. Del Pezzo (2009), Temporal changes in seismic wave propagation towards the end of the 2002 Mt Etna eruption, Geophysical Journal International, 178(3), 1779–1788, doi:{10.1111/j.1365-246X.2009.04219.x}.

CHAPTER 2

Theoretical Overview

2.1 Outline

The term "Seismic Interferometry" (SI) encompasses three types of interferometry: inter-receiver interferometry, inter-source interferometry, and source-receiver interferometry.

Here we introduce the underlying theory of all three methods including the governing equations. For inter-receiver interferometry, we start from first principles using reciprocity theorems of both the correlation type and convolution type to yield acoustic Green's function representations (Wapenaar, 2003). We then introduce the key equations governing Green's function estimation by ambient noise interferometry (Shapiro and Campillo, 2004) and multidimensional deconvolution (MDD) (Wapenaar et al., 2008a). Both methods will be discussed with an earthquake seismology focus. To derive equivalent theory for inter-source interferometry, we apply source-receiver reciprocity to the derived inter-receiver interferometric integrals (Curtis et al., 2009).

Source-receiver interferometry (SRI) can be derived either directly from representation theorems (Curtis and Halliday, 2010; Halliday and Curtis, 2010), or by combining the theories of inter-receiver and inter-source interferometry (Curtis et al., 2012). We define the exact formula for correlation-correlation SRI, so called as it is derived from two correlation-type reciprocity theorems. We then simplify the exact formula for practical applications in earthquake seismology and incorporate information about the source phase into the derivations. Simplified formulae for correlation-convolution SRI, derived from one correlation-type reciprocity theorem

and one convolution-type reciprocity theorem, are also introduced. Schematic illustrations outlining the required source and receiver geometries for both SRI methods are provided.

2.2 Inter-Receiver Interferometry

2.2.1 Acoustic reciprocity theorems

In 2003, Kees Wapenaar proved Claerbout's conjecture for 3D acoustic media. This proof is unique in that it does not rely on the assumption that the wavefields are diffuse, but uses reciprocity theorems to relate two independent acoustic states (e.g., two independent seismic experiments), that could occur in one and the same domain, i.e., the medium parameters in the two independent experiments are chosen to be identical (De Hoop, 1988; Wapenaar, 2003). These reciprocity theorems can be of either correlation-type or convolution-type.

Wapenaar and Fokkema (2006) provide a concise derivation of the acoustic reciprocity theorem: Acoustic wavefields characterised by acoustic pressure $p(\mathbf{x}, t)$ and particle velocity $v_i(\mathbf{x}, t)$ are used such that they obey the equation of motion

$$j\omega\rho v_i + \partial_i p = f_i \tag{2.1}$$

and the stress-strain relation,

$$j\omega\kappa p + \partial_i v_i = q \tag{2.2}$$

where $j = \sqrt{-1}$, ∂_i represents the partial derivative in the $\mathbf{x}_i$-direction, $\rho(\mathbf{x})$ and $\kappa(\mathbf{x})$ are the mass density and the compressibility of the medium, respectively, $f_i(\mathbf{x}, \omega)$ is the external volume force density and $q(\mathbf{x}, \omega)$ is the source distribution in terms of volume injection rate density at location $\mathbf{x}$ and angular frequency ω (Wapenaar and Fokkema, 2006). The interaction quantity (De Hoop, 1988) is also defined:

$$\partial_i\{p_A v_{i,B} - v_{i,A} p_B\} \tag{2.3}$$

where subscripts A and B refer to the two independent acoustic states. Substituting the equation of motion and the stress-strain relation for both states A and B into the interaction quantity, integrating over a spatial domain D enclosed within a boundary ∂D with outward pointing normal $n = (n_1, n_2, n_3)$ and applying Gauss' Theorem to convert the volume integral to a surface integral, one can obtain a relationship that relates the pressure source and the velocity field in the two independent states. This relationship is the reciprocity theorem of the *convolution-type* and is defined as

$$\int_D \{p_A q_B - v_{i,A} f_{i,B} - q_A p_B + f_{i,A} v_{i,B}\} d^3\mathbf{x} = \oint_{\partial D} \{p_A v_{i,B} - \hat{v}_{i,A} \hat{p}_B\} d^2\mathbf{x} \quad (2.4)$$

To obtain the reciprocity theorem of the correlation-type the principal of time-reversal is applied. Since time-reversal is equivalent to complex conjugation in the frequency domain (denoted *), p^* and -v_i^* obey the same equations as above for p and v_i, but with source terms f_i^* and $-q^*$. Making these substitutions in state A only, the reciprocity theorem of the *correlation-type* is obtained:

$$\int_D \{p_A^* q_B + v_{i,A}^* f_{i,B} + q_A^* p_B + f_{i,A}^* v_{i,B}\} d^3\mathbf{x} = \oint_{\partial D} \{p_A^* v_{i,B} + v_{i,A}^* p_B\} n_i d^2\mathbf{x} \quad (2.5)$$

where products such as $p_A^* q_B$ in the frequency domain are equivalent to correlation in the time domain.

2.2.2 Acoustic Green's function representation

Consider the geometry in Figure 2.1A where two receivers at $\mathbf{x_A}$ and $\mathbf{x_B}$ are surrounded by impulsive sources of volume injection rate at positions $\mathbf{x}'$ on boundary S'.

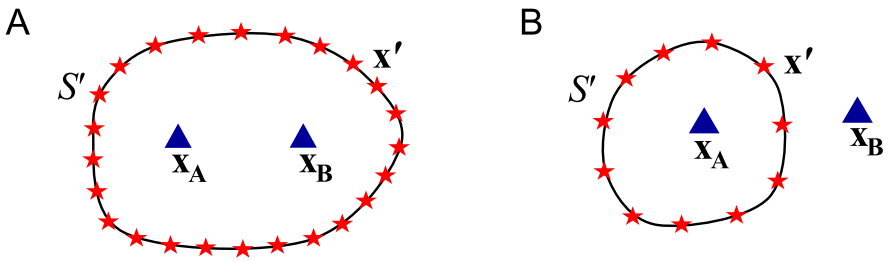

Figure 2.1: Schematic source and receiver geometries for inter-receiver interferometry. Stars are sources, triangles are receivers. The responses from each source at locations such as $\mathbf{x}'$ on boundary S' are recorded on receivers $\mathbf{x_A}$ and $\mathbf{x_B}$ which are then (A) cross-correlated or (B) convolved. In both cases the results of all cross-correlations or convolutions are summed (integrated over S') to obtain an approximation of the Green's function between the receivers at $\mathbf{x_A}$ and $\mathbf{x_B}$.

First, we express the wavefields in states A and B above in terms of Green's functions, i.e. for state A

$$p_A(\mathbf{x_A}, \omega) = G(\mathbf{x_A}, \mathbf{x}', \omega) \tag{2.6}$$

and

$$v_{i,A}(\mathbf{x_A}, \omega) = \frac{-1}{j\omega\rho(\mathbf{x_A})}\partial_{i'}G(\mathbf{x_A}, \mathbf{x}', \omega), \tag{2.7}$$

where G and $\partial_{i'}Gn_{i'}$ are the responses of monopole and dipole sources at locations $\mathbf{x}'$, and terms such as $G(\mathbf{x_A}, \mathbf{x}')$ are the Green's functions, in this case between $\mathbf{x}'$ and $\mathbf{x_A}$, i.e., the response recorded at $\mathbf{x_A}$ from an impulsive source at the location of $\mathbf{x}'$.

Applying the reciprocity theorem of the convolution type (Equation (2.4)), Wapenaar and Fokkema (2006) show how one can construct the well-known source-receiver reciprocity relation for the acoustic Green's function:

$$G(\mathbf{x_B}, \mathbf{x_A}, \omega) = G(\mathbf{x_A}, \mathbf{x_B}, \omega). \tag{2.8}$$

Applying the reciprocity theorem of the correlation type and source-receiver reciprocity yields the acoustic homogeneous Green's function

$$G(\mathbf{x_A}, \mathbf{x_B}, \omega) + G^*(\mathbf{x_A}, \mathbf{x_B}, \omega) = \int_{S'} \frac{-1}{j\omega\rho(\mathbf{x}')} \Big(G^*(\mathbf{x_B}, \mathbf{x}', \omega)\partial_{i'} G(\mathbf{x_A}, \mathbf{x}', \omega) - (\partial_{i'} G^*(\mathbf{x_B}, \mathbf{x}', \omega)) G(\mathbf{x_A}, \mathbf{x}', \omega) \Big) n_{i'} d^2\mathbf{x}' \quad (2.9)$$

Boundary S' is arbitrary as long as it encloses $\mathbf{x_A}$ and $\mathbf{x_B}$, and $G(\mathbf{x_A}, \mathbf{x_B}, \omega)$ contains direct and scattered (primaries and multiples) wave contributions from inhomogeneities inside and outside of S'. $G(\mathbf{x_A}, \mathbf{x_B}, \omega) + G^*(\mathbf{x_A}, \mathbf{x_B}, \omega)$ is the homogeneous Green's function, where, as defined above, $G(\mathbf{x_A}, \mathbf{x_B}, \omega)$ represents the response recorded at $\mathbf{x_A}$ from an impulsive source at the location of $\mathbf{x_B}$, and $G^*(\mathbf{x_A}, \mathbf{x_B}, \omega)$ transforms to that same Green's function but extending in the negative time direction. Applying Equation (2.9) to the geometry outlined in Figure 2.1A thus turns the receiver at $\mathbf{x_B}$ into a "virtual" source.

If the boundary S' only surrounds one receiver as in Figure 2.1B then a similar set of operations are carried out to estimate $G(\mathbf{x_A}, \mathbf{x_B}, \omega)$, but instead of using correlation in this case the boundary source recordings must be convolved (Wapenaar and Fokkema, 2006):

$$G(\mathbf{x_A}, \mathbf{x_B}, \omega) = \int_{S'} \frac{-1}{j\omega\rho(\mathbf{x}')} \Big(G(\mathbf{x_A}, \mathbf{x}', \omega)\partial_{i'} G(\mathbf{x_B}, \mathbf{x}', \omega) - \big(\partial_{i'} G(\mathbf{x_A}, \mathbf{x}', \omega)\big) G(\mathbf{x_B}, \mathbf{x}', \omega) \Big) n_{i'} d^2\mathbf{x}' \quad (2.10)$$

where, as in Equation (2.9) terms such as $G(\mathbf{x_A}, \mathbf{x}', \omega)$ are the Fourier transforms of causal time-domain Green's functions $G(\mathbf{x_A}, \mathbf{x}', t)$.

For simplicity Equations (2.9) and (2.10) are described above for wave propagation in any lossless arbitrary inhomogeneous fluid (acoustic) medium, thus ignoring the elastic nature of seismic waves. For the exact elastodynamic Green's function representation see Wapenaar and Fokkema (2006). In practical applications of Equations (2.9) and (2.10) acoustic (or elastic) assumptions are often violated (e.g. boundary S' is incomplete). We thus need to address the following impracticalities:

1. There are two correlation (or convolution) products that must be evaluated separately,

2. Monopole and dipole sources are assumed at all positions $\mathbf{x}'$ on S', and

3. Sources are assumed to be impulsive.

By considering separately the waves propagating inward and outward from sources $\mathbf{x}'$ on S', Wapenaar and Fokkema (2006) show that Equation (2.9) can be reduced to just one correlation product:

$$G(\mathbf{x_A}, \mathbf{x_B}, \omega) + G^*(\mathbf{x_A}, \mathbf{x_B}, \omega) = \frac{2}{j\omega\rho} \int_{S'} \big(\partial_{i'} G^*(\mathbf{x_B}, \mathbf{x}', \omega)\big) G(\mathbf{x_A}, \mathbf{x}', \omega) n_{i'} d^2\mathbf{x}' \quad (2.11)$$

When only monopoles are available, approximations are made to the dipoles by assuming S' is a sphere of large radius, such that

$$n_{i'} \partial_{i'} G \approx -j\frac{\omega}{c} G \quad (2.12)$$

and Equation (2.11) can thus be re-written in the form

$$G(\mathbf{x_A}, \mathbf{x_B}, \omega) + G^*(\mathbf{x_A}, \mathbf{x_B}, \omega) \approx \frac{2}{\rho c} \int_{S'} G^*(\mathbf{x_B}, \mathbf{x}', \omega) G(\mathbf{x_A}, \mathbf{x}', \omega) d^2\mathbf{x}' \quad (2.13)$$

where c is the propagation velocity of the medium outside of S'. Finally, to obviate the need to measure each source on S' separately, we replace the impulsive point sources at $\mathbf{x}'$ with a boundary of mutually uncorrelated noise sources, whereafter it can be shown that Equation (2.13) reduces to

$$\Big[G(\mathbf{x_A}, \mathbf{x_B}, \omega) + G^*(\mathbf{x_A}, \mathbf{x_B}, \omega)\Big] S(\omega) \approx \frac{2}{\rho c} \langle p^*_{obs}(\mathbf{x_B}, \omega) p_{obs}(\mathbf{x_A}, \omega) \rangle \quad (2.14)$$

where $S(\omega)$ is the power spectrum of the noise sources, $p_{obs}(\mathbf{x_A}, \omega)$ is the observed wavefield at $\mathbf{x_A}$ due to noise sources acting simultaneously on S', and $\langle \cdot \rangle$ denotes a spatial ensemble average (Wapenaar and Fokkema, 2006). Equation (2.14) is thus well suited for the practical application of seismic interferometry and is now commonly

applied in earthquake seismology studies to estimate the surface wave Green's function between two observation locations.

We shall use noise interferometry as in Equation (2.14) throughout Chapters 4 to 6 to estimate the Green's functions between pairs of seismometers deployed throughout the United States. However, we also provide an alternative approach to Green's function estimation in Chapter 7: some of the same Green's functions constructed using noise interferometry are also constructed using multidimensional deconvolution (MDD). Thus, we dedicate the next section to the theory of inter-receiver interferometry by MDD.

2.2.3 Inter-receiver interferometry by MDD

We now introduce the theory of multidimensional deconvolution (MDD) for Green's function estimation using real earthquake data. An illustration outlining the source and receiver geometry required for MDD is shown in Figure 2.2 for earthquake sources at locations such as $\mathbf{x_{S}}_i$.

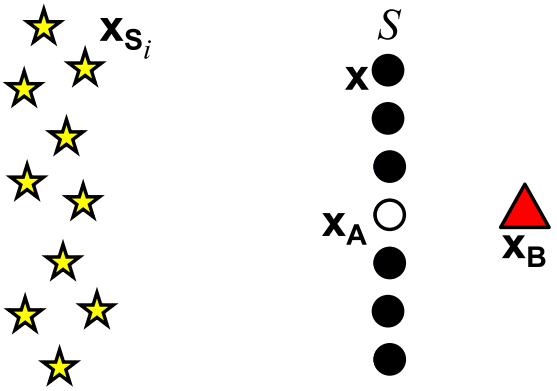

Figure 2.2: An illustration outlining the geometry required to perform MDD in an earthquake seismology setting. The aim is to construct the Green's function $G(\mathbf{x_B}, \mathbf{x_A})$ between the receiver at the location of $\mathbf{x_B}$ (triangle) and a receiver at the location of $\mathbf{x_A}$ (unfilled circle) on the receiver boundary S. This requires: 1) the point-spread function Γ, which is constructed between the seismometer at $\mathbf{x_A}$ on S and each receiver $\mathbf{x}$ also on S (all circles), and 2) the correlation function C, which is constructed between the receiver at $\mathbf{x_B}$ and each receiver $\mathbf{x}$ on S. Γ and C are constructed by cross-correlating the earthquake signals recorded on the appropriate receivers and summing over all earthquake sources. The earthquake signals originate at locations such as $\mathbf{x_{S}}_i$, that are on the opposite side of the receiver boundary S to the receiver at $\mathbf{x_B}$.

.

The aim is to construct an estimate of the Green's function $G(\mathbf{x_B}, \mathbf{x})$ between a receiver at the location of $\mathbf{x_B}$ and a receiver located at $\mathbf{x}$ (for $\mathbf{x} = \mathbf{x_A}$) on the boundary S. To construct G using MDD, Wapenaar and van der Neut (2010); Wapenaar et al. (2011a,b) and van der Neut et al. (2011) show that two components are required: the point-spread function Γ and the correlation function C. Both components are constructed by processes of cross-correlation. First consider Γ, constructed between receivers located at positions $\mathbf{x}$ on the receiver boundary S, and receiver $\mathbf{x_A}$, also located on boundary S. Earthquake signals propagating from locations such as $\mathbf{x_{S_i}}$ are recorded on $\mathbf{x}$ and $\mathbf{x_A}$ and cross-correlated, such that

$$\Gamma(\mathbf{x}, \mathbf{x_A}, t) = \sum_i u(\mathbf{x}, \mathbf{x_{S_i}}, t) * u(\mathbf{x_A}, \mathbf{x_{S_i}}, -t) \tag{2.15}$$

where

$$u(\mathbf{x}, \mathbf{x_{S_i}}, t) = G(\mathbf{x}, \mathbf{x_{S_i}}, t) * s_i(t) \tag{2.16}$$

and represents the observations recorded on $\mathbf{x}$ from an earthquake source at the location of $\mathbf{x_{S_i}}$ with source function $s_i(t)$. Equation (2.15) is thus a summation over all earthquake sources, $*$ represents convolution but time-reversing one of the two convolved signals turns the convolution into cross-correlation.

The correlation function C is constructed between the receiver at $\mathbf{x_A}$ and the receiver at $\mathbf{x_B}$, which does not lie on the receiver boundary S and is on the opposite side of S to the earthquake sources. C is constructed using processes of cross-correlation and summation as above:

$$C(\mathbf{x_B}, \mathbf{x_A}, t) = \sum_i u(\mathbf{x_B}, \mathbf{x_{S_i}}, t) * u(\mathbf{x_A}, \mathbf{x_{S_i}}, -t) \tag{2.17}$$

It has been shown (Wapenaar and van der Neut, 2010; Wapenaar et al., 2011a) that the correlation function $C(\mathbf{x_B}, \mathbf{x_A})$, the point-spread function $\Gamma(\mathbf{x}, \mathbf{x_A})$ and the dipole Green's function $G(\mathbf{x_B}, \mathbf{x})$ are mutually related through an approximation to the

convolutional representation theorem in Equation (2.10) as follows:

$$C(\mathbf{x_B}, \mathbf{x_A}, t) = \int_S G(\mathbf{x_B}, \mathbf{x}, t) * \Gamma(\mathbf{x}, \mathbf{x_A}, t) d\mathbf{x} \tag{2.18}$$

where the integration is taken over all receivers at locations $\mathbf{x}$ on the receiver boundary S. Thus, the correlation function is proportional to the Green's function with its source smeared in space and time by the point-spread function.

In order to solve Equation (2.18) to estimate G, we must invert $\mathbf{\Gamma}$, where $\mathbf{\Gamma}$ is the matrix notation of the point-spread function transformed into the frequency domain, and is usually ill-conditioned. There are two possible methods to perform and stabilise this inversion: the first involves adding a small constant ϵ to the diagonal of $\mathbf{\Gamma}$ (Wapenaar et al., 2008b,a; van der Neut et al., 2010; Wapenaar et al., 2011b), whilst the second method is to apply singular value decomposition (Minato et al., 2011; van Dalen et al., 2014), and this is the method we adopt herein. Transforming C and Γ into the frequency domain, Equation (2.18) becomes a matrix equation for each frequency component:

$$\mathbf{C} = \mathbf{G\Gamma} \tag{2.19}$$

where $\mathbf{\Gamma}$ can be decomposed using singular value decomposition as follows:

$$\mathbf{\Gamma} = \mathbf{V}_r \mathbf{\Delta}_r \mathbf{U}_r^\dagger \tag{2.20}$$

where r is the number of non-zero singular values, $\mathbf{V}_r$ is an Nxr matrix (where N is the number of seismometers within the backbone array), the columns of which are composed of the r-eigenvectors of $\mathbf{\Gamma}(\mathbf{\Gamma}^\dagger)$ having non-zero eigenvalues, $\mathbf{\Delta}_r^{-1}$ is an rxr diagonal matrix whose diagonal components are non-zero singular values, $\mathbf{U}_r$ is an Nxr matrix, the columns of which are composed of the r-eigenvectors of $(\mathbf{\Gamma})^\dagger\mathbf{\Gamma}$ having non-zero eigenvalues, and the dagger symbol † indicates the complex conjugate transpose. Taking the pseudoinverse of $\mathbf{\Gamma}$

$$\mathbf{\Gamma^{-1}} \approx \mathbf{U}_r \mathbf{\Delta}_r^{-1} \mathbf{V}_r^\dagger, \tag{2.21}$$

the solution of Equation (2.19) becomes

$$\mathbf{G} \approx \mathbf{C}\boldsymbol{\Gamma}^{-1} \tag{2.22}$$

When using real data, the inversion of the point-spread function $\boldsymbol{\Gamma}$ will be an ill-posed problem. Singular value decomposition thus defines the number of singular values to be included in the inversion, which in turn stabilises the process. The singular values represent the energy of the system (in this case, the energy in the cross-correlated earthquake data that comprise $\boldsymbol{\Gamma}$) and they take different values for each frequency component. For MDD, it has been shown that it is better to exclude the smallest singular values from the inversion (Minato et al., 2011). We thus find the global maximum singular value over all frequencies and define a tolerance value to be a percentage of this global maximum. All singular values that are greater than this tolerance value are included in the inversion. All singular values that are smaller than this tolerance value are set to zero and thus excluded from the inversion.

This approach to Green's function estimation will be performed in Chapter 7 and the results will be compared to those estimated using noise interferometry as in Equation (2.14). For detailed derivations of the equations governing MDD and for a systematic comparison with seismic interferometry by cross-correlation, see Wapenaar et al. (2011a).

2.3 Inter-Source Interferometry

Let us now consider the geometry outlined in Figure 2.3A for performing inter-source interferometry by cross-correlation. Applying the source-receiver reciprocity relation in Equation (2.8) to Equation (2.13) for receivers located at positions $\mathbf{x} = \mathbf{x}'$ on boundary $S = S'$, we obtain the inter-source interferometric integral:

$$G(\mathbf{x_B}, \mathbf{x_A}, \omega) + G^*(\mathbf{x_B}, \mathbf{x_A}, \omega) \approx \frac{2}{\rho c} \int_S G^*(\mathbf{x}, \mathbf{x_B}, \omega) G(\mathbf{x}, \mathbf{x_A}, \omega) d^2\mathbf{x} \tag{2.23}$$

Thus, integrating over all receiver positions $\mathbf{x}$ on S extracts an estimate of the Green's function between the two sources, turning the source at $\mathbf{x_B}$ into a "virtual" receiver that records the response from the source at $\mathbf{x}_A$.

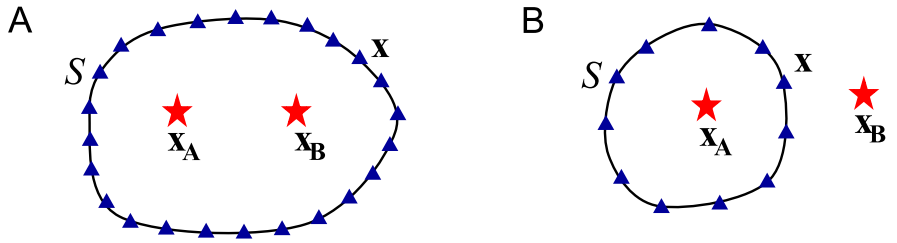

Figure 2.3: Schematic source and receiver geometries for inter-source interferometry. Key as in Figure 2.1. By applying source-receiver reciprocity to the illustrations in Figure 2.1, the responses from sources at $\mathbf{x_A}$ and $\mathbf{x_B}$ are recorded by each receiver at locations such as $\mathbf{x}$ on boundary S and (A) cross-correlated or (B) convolved. In both cases the results of all cross-correlations or convolutions are summed (integrated over S) to obtain an approximation of the Green's function between the sources at $\mathbf{x_A}$ and $\mathbf{x_B}$.

Similarly to the inter-receiver case, inter-source interferometry also takes a convolutional form when the boundary S only surrounds one source as in Figure 2.3B. We will use the approximate convolutional relation:

$$G(\mathbf{x_B}, \mathbf{x_A}, \omega) \approx \frac{2}{\rho c} \int_S G(\mathbf{x}, \mathbf{x_B}, \omega) G(\mathbf{x}, \mathbf{x_A}, \omega) d^2\mathbf{x} \tag{2.24}$$

2.4 Source-Receiver Interferometry (SRI)

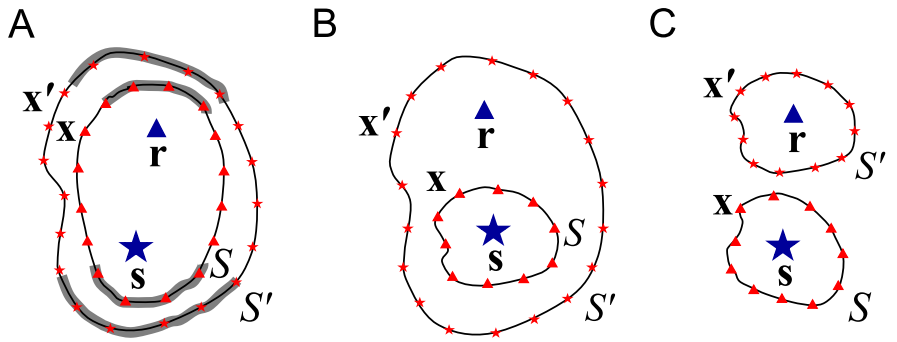

Figure 2.4: Distributions of sources (stars) and receivers (triangles) for application of source-receiver interferometry using (A) two correlation-type reciprocity theorems, (B) one correlation-type reciprocity theorem and one convolution-type reciprocity theorem, and (C) two convolution-type reciprocity theorems (Curtis and Halliday, 2010). The grey shaded regions in (A) are schematic representations of the stationary phase regions of boundaries S and S' (Snieder, 2004).

The three canonical source-receiver geometries for SRI are shown above in Figure 2.4 (Curtis and Halliday, 2010). In Figure 2.4A, a source $\mathbf{s}$ and receiver $\mathbf{r}$ are surrounded by a boundary of receivers $\mathbf{x}$ on S and a boundary of sources $\mathbf{x}'$ on S'. For wave propagation in an acoustic medium we then obtain the exact SRI formula

$$
\begin{aligned}
&G(\mathbf{r},\mathbf{s}) + G^*(\mathbf{r},\mathbf{s}) = \\
&\frac{-1}{j\omega\rho}\int_S \Bigg\{ \Bigg[\frac{-1}{j\omega\rho}\int_{S'} \big\{ G^*(\mathbf{r},\mathbf{x}')n_{i'}\partial_{i'}G(\mathbf{x},\mathbf{x}') \\
&\qquad\qquad - n_{i'}\partial_{i'}G^*(\mathbf{r},\mathbf{x}')G(\mathbf{x},\mathbf{x}')\big\} dS' \Bigg] n_i\partial_i G(\mathbf{x},\mathbf{s}) \\
&\quad -n_i\partial_i \Bigg[\frac{-1}{j\omega\rho}\int_{S'} \big\{ G^*(\mathbf{r},\mathbf{x}')n_{i'}\partial_{i'}G(\mathbf{x},\mathbf{x}') \\
&\qquad\qquad - n_{i'}\partial_{i'}G^*(\mathbf{r},\mathbf{x}')G(\mathbf{x},\mathbf{x}')\big\} dS' \Bigg] G(\mathbf{x},\mathbf{s}) \Bigg\} dS
\end{aligned}
\tag{2.25}
$$

where $G(\mathbf{r},\mathbf{s})$ is the Green's function in the frequency domain representing the pressure at $\mathbf{r}$ due to a volume injection-rate density source at $\mathbf{s}$. Equation (2.25) represents the exact interferometric formula for correlation-correlation SRI, so called as it is derived from two correlation-type reciprocity theorems (Curtis and Halliday, 2010). For the equivalent exact SRI equation in elastic media see Curtis and Halliday (2010).

Assuming high-frequency propagation, locally planar wavefronts, and that Somerfield radiation conditions hold on both S and S', Curtis and Halliday (2010) approximate dipole sources to monopole sources as in Equation (2.12), and Equation (2.25) is reduced to a form far better suited to practical applications of SRI:

$$
G(\mathbf{r},\mathbf{s}) + G^*(\mathbf{r},\mathbf{s}) \approx \frac{4k^2}{(\omega\rho)^2}\int_S\int_{S'} G^*(\mathbf{r},\mathbf{x}')G(\mathbf{x},\mathbf{x}')G(\mathbf{x},\mathbf{s})dS'dS \tag{2.26}
$$

Alternatively, one can split Equation (2.26) into two separate integrals to be evaluated independently (Curtis et al., 2012)

$$
G_H(\mathbf{r},\mathbf{s}) \cong \frac{2jk}{\omega\rho}\int_S G^*(\mathbf{x},\mathbf{s})G(\mathbf{x},\mathbf{r})d\mathbf{x} \tag{2.27}
$$

where

$$G_H(\mathbf{x},\mathbf{r}) \cong \frac{2jk}{\omega\rho}\int_{S'} G^*(\mathbf{r},\mathbf{x}')G(\mathbf{x},\mathbf{x}')d\mathbf{x}' \tag{2.28}$$

Equation (2.28) is a representation of inter-receiver interferometry (equivalent to Equation (2.13)) and, in practice, is applied first. $G_H(\mathbf{x},\mathbf{r}) = G(\mathbf{x},\mathbf{r}) + G^*(\mathbf{x},\mathbf{r})$ is the homogeneous Green's function, where $G(\mathbf{x},\mathbf{r})$ represents the response at $\mathbf{x}$ from a virtual source at $\mathbf{r}$, and $G^*(\mathbf{x},\mathbf{r})$ is the time-reversal of this Green's function. $G(\mathbf{x},\mathbf{r})$ can therefore be estimated by taking the positive time part of $G_H(\mathbf{x},\mathbf{r})$. Herein we refer to these inter-receiver Green's functions as the 'propagators' for SRI as (in the application of Equation (2.27)) they project the source signals recorded on the receiver boundary S to the location of the receiver at $\mathbf{r}$.

Equation (2.27) is a representation of inter-source interferometry (equivalent to Equation (2.23)). Substituting the SRI propagators $G(\mathbf{x},\mathbf{r})$ into Equation (2.27) we obtain the homogeneous Green's function $G_H(\mathbf{r},\mathbf{s}) = G(\mathbf{r},\mathbf{s}) + G^*(\mathbf{r},\mathbf{s})$. Thus, one is able to construct the response at $\mathbf{r}$ from a source at $\mathbf{s}$, without ever recording $\mathbf{s}$ on $\mathbf{r}$ directly.

In the case represented by Figure 2.4B, convolution should be used in place of correlation in Equation (2.27):

$$G(\mathbf{r},\mathbf{s}) \cong \frac{2jk}{\omega\rho}\int_{S} G(\mathbf{x},\mathbf{s})G(\mathbf{x},\mathbf{r})d\mathbf{x} \tag{2.29}$$

Equation (2.29) thus represents the practical application of correlation-convolution SRI, so called because the exact SRI formula is derived from one reciprocity theorem of the correlation-type and one reciprocity theorem of the convolution type (Curtis and Halliday, 2010).

Invoking the stationary phase approximation (Snieder, 2004) reduces the number of direct measurements that need to be made during practical applications of SRI: under the assumption that the amplitude of the integrands in Equations (2.27) and (2.28) vary smoothly, only those sources and receivers that lie around regions of boundaries S' and S at which the integrands become approximately stationary with respect to locations on the boundaries contribute significantly to the integrals. A schematic representation of these stationary phase regions is given by the grey shaded regions in Figure 2.4A. Furthermore, the controlled sources on boundary S'

can be replaced by mutually uncorrelated noise sources. This reduces the integral in Equation (2.28) to a summation over space- and time-averaged observations made at $\mathbf{x}$ and $\mathbf{r}$. Equation (2.28) then takes on the form of Equation (2.14) and the SRI propagators are constructed using noise interferometry. Applying Equation (2.14) in place of Equation (2.28) has become very attractive in earthquake seismology as it eliminates the need to measure the response from all sources on a boundary S' individually, and thus studies no longer need to depend on suitably located earthquakes or other sources (Shapiro and Campillo, 2004; Shapiro et al., 2005; Sabra et al., 2005).

Finally, the energy released from an earthquake source has a characteristic source time signature $T(\omega)$. Thus, boundary receivers at locations $\mathbf{x}$ record not just $G(\mathbf{x}, \mathbf{s})$, but $TG(\mathbf{x}, \mathbf{s})$. Furthermore, $T(\omega)$ need not be associated with a point source, but can be linked to a rupture sequence along a fault plane F. Such rupture sequences R recorded on boundary receivers at locations $\mathbf{x}$ can be described by integrating over all source positions $\mathbf{s}$:

$$R(\mathbf{x}, F) = \int_{\mathbf{s}\in F} T(\mathbf{s})G(\mathbf{x}, \mathbf{s})d\mathbf{s} \tag{2.30}$$

Thus, pre-multiplying Equation (2.27) by $T^*(\mathbf{s})$, integrating over sources $\mathbf{s}$ on fault plane F, and applying source-receiver reciprocity gives

$$\begin{aligned}\int_{\mathbf{s}\in F} T^*(\mathbf{s})G_H(\mathbf{r}, \mathbf{s})d\mathbf{s} &\cong \frac{2jk}{\omega\rho}\int_{\mathbf{s}\in F}\int_S \big[T(\mathbf{s})G(\mathbf{x}, \mathbf{s})\big]^* G(\mathbf{x}, \mathbf{r})d\mathbf{s}d\mathbf{x} \\ &\cong \frac{2jk}{\omega\rho}\int_S R^*(\mathbf{x}, F)G(\mathbf{x}, \mathbf{r})d\mathbf{x}\end{aligned} \tag{2.31}$$

where $T^*G_H = T^*G + T^*G^*$. At positive times we obtain $T^*G(\mathbf{r}, \mathbf{s})$. This is not the true response of the earthquake source $\mathbf{s}$ at receiver $\mathbf{r}$ as G is convolved with the time-reverse of the source time signature T. However, at negative times we obtain $T^*G^*(\mathbf{r}, \mathbf{s})$ which, after time-reversal (complex conjugation), gives $TG(\mathbf{r}, \mathbf{s})$. Thus, when following correlation-correlation SRI we should use only the acausal parts of the reconstructed signal to correctly represent the response from an earthquake source on a receiver at $\mathbf{r}$. A similar analysis for correlation-convolution SRI in Equation (2.29)

shows that the correct seismogram is created by inserting $R(\mathbf{x}, F)$ in place of $G(\mathbf{x}, \mathbf{s})$ in Equation (2.31) and applying source-receiver reciprocity to give

$$\int_{\mathbf{s}\in F} T(\mathbf{s})G(\mathbf{r}, \mathbf{s})d\mathbf{s} \cong \frac{2jk}{\omega\rho} \int_S \int_{\mathbf{s}\in F} T(\mathbf{s})G(\mathbf{x}, \mathbf{s})G(\mathbf{x}, \mathbf{r})d\mathbf{s}d\mathbf{x}$$

$$\cong \frac{2jk}{\omega\rho} \int_S R(\mathbf{x}, F)G(\mathbf{x}, \mathbf{r})d\mathbf{x} \tag{2.32}$$

Thus, convolution interferometry on the right of Equation (2.32) constructs the desired one-sided estimate of $R(\mathbf{r}, F)$ in Equation (2.30) directly, without the need for time-reversal (complex conjugation).

Here we do not consider the third type of SRI: convolution-convolution SRI, the canonical geometry of which is shown in Figure 2.4C. Since the source boundary S' is required to surround the receiver at $\mathbf{r}$ only, convolution-convolution SRI does not lend itself to practical applications in earthquake seismology when using noise interferometry as in Equation (2.14) to construct the SRI propagators. In Equation (2.14) we assume the noise field to be equipartitioned and thus recorded isotropically on the receiver at $\mathbf{r}$ and on the receivers at locations $\mathbf{x}$ on boundary S. This is achieved when mutually uncorrelated noise sources are located approximately on a closed, surrounding source boundary S' as in Figure 2.4A or Figure 2.4B. For full derivations of the SRI formulae pertaining to convolution-convolution SRI see Curtis and Halliday (2010).

2.5 Summary

To summarise, we will use the equations derived herein in each Chapter as follows:

- Chapter 3: Practical Methodology and Data Processing. This describes the practical aspects of invoking: 1) MDD as in Equation (2.22) using Equations (2.15) and (2.17) to construct the MDD components Γ and C, respectively, and Equation (2.21) to perform the matrix inversion of $\mathbf{\Gamma}$ by singular value decomposition, and 2) SRI using Equations (2.31) and (2.32) and noise interferometry as in Equation (2.14) to construct the SRI propagators.

- Chapter 4: Correlation-correlation SRI. An application of SRI as in Equation (2.31) using noise interferometry as in Equation (2.14) to construct the SRI propagators.

- Chapter 5: Correlation-convolution SRI. An application of SRI as in Equation (2.32) using noise interferometry as in Equation (2.14) to construct the SRI propagators.

- Chapter 6: SRI on multiple length and magnitude scales. Several applications of SRI as in Equations (2.31) and (2.32) using noise interferometry as in Equation (2.14) to construct the SRI propagators.

- Chapter 7: Green's function estimation by MDD. Application of MDD to estimate $\mathbf{G}$ as in Equation (2.22) using Equations (2.15) and (2.17) to construct the MDD components Γ and C, respectively, and Equation (2.21) to perform the matrix inversion of $\mathbf{\Gamma}$ by singular value decomposition.

Bibliography

Curtis, A., and D. Halliday (2010), Source-receiver wave field interferometry, Physical Review E, 81(4, 2), doi:{10.1103/PhysRevE.81.046601}.

Curtis, A., H. Nicolson, D. Halliday, J. Trampert, and B. Baptie (2009), Virtual seismometers in the subsurface of the Earth from seismic interferometry, Nature Geoscience, 2(10), 700–704, doi:{10.1038/NGEO615}.

Curtis, A., Y. Behr, E. Entwistle, E. Galetti, J. Townend, and S. Bannister (2012), The benefit of hindsight in observational science: Retrospective seismological observations, Earth and Planetary Science Letters, 345, doi:{DI10.1016/j.epsl.2012.06.008}.

De Hoop, A. (1988), Time-Domain Reciprocity Theorems For Acoustic-wave Fields In Fluids With Relaxation, Journal Of the Acoustical Society of America, 84, 1877 – 1882, doi:{10.1121/1.397152}.

Halliday, D., and A. Curtis (2010), An interferometric theory of source-receiver scattering and imaging, Geophysics, 75(6), SA95–SA103, doi:{10.1190/1.3486453}.

Minato, S., T. Matsuoka, T. Tsuji, D. Draganov, J. Hunziker, and K. Wapenaar (2011), Seismic interferometry using multidimensional deconvolution and crosscorrelation for crosswell seismic reflection data without borehole sources, Geophysics, 76(1), SA19–SA34, doi:{10.1190/1.3511357}.

Sabra, K., P. Gerstoft, P. Roux, W. Kuperman, and M. Fehler (2005), Extracting time-domain Green's function estimates from ambient seismic noise, Geophysical Research Letters, 32, doi:{10.1029/2004GL021862}.

Shapiro, N. M., and M. Campillo (2004), Emergence of broadband Rayleigh waves from correlations of the ambient seismic noise, Geophysical Research Letters, 31(7), doi:{10.1029/2004GL019491}.

Shapiro, N. M., M. Campillo, L. Stehly, and M. H. Ritzwoller (2005), High-resolution surface-wave tomography from ambient seismic noise, Science, 307(5715), 1615–1618, doi:{10.1126/science.1108339}.

Snieder, R. (2004), Extracting the Green's function from the correlation of coda waves: A derivation based on stationary phase, Physical Review E, 69(4, 2), doi:{10.1103/PhysRevE.69.046610}.

van Dalen, K. N., K. Wapenaar, and D. F. Halliday (2014), Surface wave retrieval in layered media using seismic interferometry by multidimensional deconvolution, Geophysical Journal International, 196(1), 230–242, doi:{10.1093/gji/ggt389}.

van der Neut, J., E. Ruigrok, D. Draganov, and K. Wapenaar (2010), Retrieving the earth's reflection response by multi-dimensional deconvolution of ambient seismic noise, EAGE, Extended Abstracts, pp. P406–1–P406–4.

van der Neut, J., J. Thorbecke, K. Mehta, E. Slob, and K. Wapenaar (2011), Controlled-source interferometric redatuming by crosscorrelation and multidimensional deconvolution in elastic media, Geophysics, 76(4), SA63–SA76, doi:{10.1190/1.3580633}.

Wapenaar, K. (2003), Synthesis of an inhomogeneous medium from its acoustic transmission response, Geophysics, 68(5), 1756–1759, doi:{10.1190/1.1620649}.

Wapenaar, K., and J. Fokkema (2006), Green's function representations for seismic interferometry, Geophysics, 71, SI33–SI46, doi:{10.1190/1.2213955}.

Wapenaar, K., and J. van der Neut (2010), A representation for Green's function retrieval by multidimensional deconvolution, Journal of the Acoustical Society of America, 128(6), EL366–EL371, doi:{10.1121/1.3509797}.

Wapenaar, K., J. van der Neut, and E. Ruigrok (2008a), Passive seismic interferometry by multidimensional deconvolution, Geophysics, 73(6), A51–A56, doi:{10.1190/1.2976118}.

Wapenaar, K., E. Slob, and R. Snieder (2008b), Seismic and electromagnetic controlled-source interferometry in dissipative media, Geophysical Prospecting, 56, 419–434, doi:{10.1190/1.2976118}.

Wapenaar, K., J. van der Neut, E. Ruigrok, D. Draganov, J. Hunziker, E. Slob, J. Thorbecke, and R. Snieder (2011a), Seismic interferometry by crosscorrelation and by multidimensional deconvolution: a systematic comparison, Geophysical Journal International, 185(3), 1335–1364, doi:{10.1111/j.1365-246X.2011.05007.x}.

Wapenaar, K., E. Ruigrok, J. van der Neut, and D. Draganov (2011b), Improved surface-wave retrieval from ambient seismic noise by multi-dimensional deconvolution, Geophysical Research Letters, 38, doi:{10.1029/2010GL045523}.

CHAPTER 3

Practical Methodology and Data Processing

3.1 Outline

This Chapter introduces the practical methodologies that have been developed, evaluated and applied throughout this PhD. We begin by looking at a simple methodology to perform inter-receiver interferometry between pairs of stations whose deployments coincide in time. This methodology uses cross-correlations of ambient seismic noise to estimate the Green's functions between the receiver pairs, thus providing a methodology for noise interferometry. A separate analysis is then performed to introduce the method of Green's function estimation by multidimensional deconvolution (MDD). A brief Summary is provided before discussing the methodology developed specifically to perform source-receiver interferometry (SRI) on earthquake datasets.

The SRI methodology has been tested using USArray seismometers deployed across the United States and real earthquakes that have occurred not only locally to the seismometers (within 2500 km) but also teleseismically, in some cases at epicentral distances greater than 10,000 km. We first use noise interferometry to construct the SRI propagators. Subsequent sections of the method are then automated to perform cross-correlations, Voronoi cell calculations and weighted-stack summations to evaluate the interferometric surface integrals.

3.2 Inter-Receiver Interferometry Using Noise Data

Here we develop a methodology to perform inter-receiver interferometry using cross-correlations of vertical component ambient seismic noise. The method follows processing techniques introduced by Bensen et al. (2007) and incorporates additional quality control checks designed to identify data with a high signal-to-noise ratio (SNR) and eliminate data whose SNR is poor. This method can be used to estimate Green's functions between any two stations whose deployment coincides by at least six months - here we use the period of six months as a general rule of thumb for when the background ambient noise level is low-to-moderate, e.g. for seismic stations located inland (Lin et al., 2007). For seismic stations located close to the coast where ambient noise levels are high however, inter-receiver Green's functions can be estimated from far fewer days of data, e.g. from as little as one month of ambient noise (Baptie, 2010). Ambient noise Green's functions offer the flexibility of not having to wait for an earthquake to occur in order to sample a (virtual) source-to-receiver path. Ambient noise Green's functions are thus being widely used in surface wave tomography studies where they have been shown to improve the resolution of seismic images compared to more traditional tomographic methods (e.g. Shapiro et al. (2005); Lin et al. (2007); Nicolson et al. (2012, 2014)). Herein we shall use them as the "propagators" in source-receiver interferometry, discussed in more detail in Section 3.6.

3.2.1 Data download

The installation dates of *all* 7,121 USArray stations are provided by IRIS (`http://www.iris.edu/earthscope/usarray/ALL-StationList.htm`). A search over all station installation dates determines the number of stations deployed in a given year. For example, currently, 989 stations are deployed and actively recording the seismic wavefields from all existing seismic sources, including earthquakes and ambient seismic noise. When available, up to one year of raw data (ambient seismic noise) from 1st January to 31st December, recorded on the vertical component, were downloaded. Since USArray stations are operational for $\sim$ two years, up to two years of ambient seismic noise data is downloaded for most stations. This raw data is downloaded in .SAC format using the IRIS web services request tool, IRISWS (`http://service.iris.edu/irisws/`), and retrieved data is one day in length. A 1000 s sample of noise data recorded on the vertical component of station SC25 on 24th December 2009 is shown Figure 3.1A.

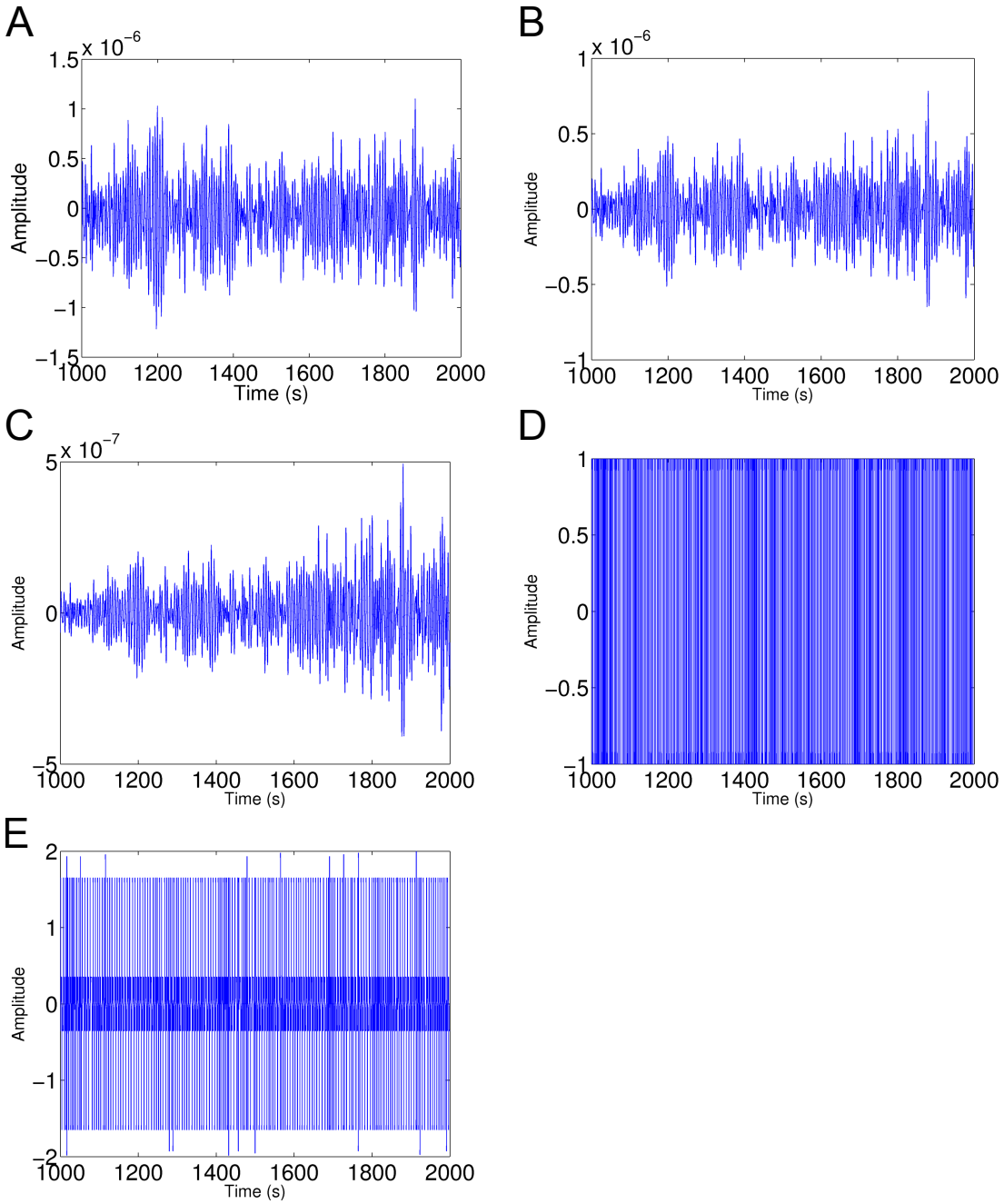

Figure 3.1: The 4 processing stages to be applied prior to inter-receiver interferometry for a 1000 s sample of raw data recorded at station SC25 on 24th December 2009. (A) Vertical component raw data as downloaded from the IRIS database, (B) the instrument response is removed from the raw data, (C) a bandpass filter with corner frequencies at 0.01 Hz and 1 Hz is applied, (D) 1-bit normalisation is applied, and (E) spectral whitening is applied.

3.2.2 Single station data preparation

After the raw data has been downloaded, data processing is carried out following the methods of Bensen et al. (2007), using Seismic Analysis Code (SAC) (`http://www.iris.edu/files/sac-manual/`). We consider four stages and an example plot is shown in Figure 3.1 for each stage (figures B-E).

Stage 1: Remove the Instrument Response

Day files are read into SAC and the mean and linear trend are removed, a cosine taper is applied to the edges of the traces, and the instrumental response is removed (see Figure 3.1B). The instrumental response files (RESP files) can be downloaded using the IRISWS request tool as described in Section 3.2.1. Using the TRANSFER function in SAC, the complete system response is calculated from these RESP files using EVALRESP routines which have been embedded into the TRANSFER function as an "instrument type". This allows the user to remove the complete system response by deconvolution using spectral division. The waveforms are then transformed, by convolution and spectral multiplication, to a new instrument type of either displacement, velocity or acceleration. Here we transform to velocity and specify a high pass filter at low frequencies using frequency limits of 0.02 Hz and 0.06 Hz. A full review of the TRANSFER function can be found at `http://seismolab.gso.uri.edu/~savage/sac/commands/transfer.html`.

Stage 2: Filter

The day files are filtered. Here we apply a bandpass filter with corner frequencies at 0.01 Hz and 1 Hz (see Figure 3.1C). This filter is kept as broad as possible at this stage to ensure that no important frequencies are lost. This benefits the archive of raw data we are creating as we are not limiting the use of the data to studies governed by certain frequencies. Instead, the data can easily be used in any earthquake seismology study and the users can apply additional filters as necessary.

Stage 3: Temporal Normalisation

Temporal normalisation is applied to the day files to reduce the effects of large amplitude signals on the cross-correlations. Such signals are caused by earthquakes,

non-stationary noise sources near to the station and instrumental irregularities (Bensen et al., 2007). We use the 1-bit normalization method which replaces all positive amplitudes with $+1$ and all negative amplitudes with -1 (see Figure 3.1D). This is described by Bensen et al. (2007) as "the most aggressive temporal normalization method" as it removes all amplitude information by keeping only the sign of the raw signal. Since the amplitude of ambient noise can vary by orders of magnitude, it is beneficial to use a method like this to stop the most energetic parts of the noise being over-weighted in the cross-correlation process (Shapiro and Campillo, 2004). This method has also been shown to improve the signal-to-noise ratio (SNR) of the data (Derode et al., 2003) and has been used successfully in a number of seismic studies to perform cross-correlations of ambient seismic noise (Shapiro and Campillo, 2004; Shapiro et al., 2005; Stehly et al., 2007; Nicolson et al., 2012, 2014).

Stage 4: Spectral Normalisation

Finally, spectral normalisation or 'whitening' is applied to the filtered, 1-bit normalised day files (see Figure 3.1E). This process acts to reduce the effects of the spectrally biased nature of ambient seismic noise: the frequency spectra of ambient noise is not flat but contains peaks correlating to Earth hum (> 50 s) and the primary (15 s) and secondary (7.5 s) microseisms. Shapiro et al. (2006) also identify an extra peak in the noise spectra at 26 s that corresponds to noise sources originating in the Gulf of Guinea. Those authors show that these persistent, monochromatic signals produce large amplitude arrivals in cross-correlations of ambient noise which can thus degrade dispersion measurements near 26 s period if not accounted for. Shapiro et al. (2006) offer a complex solution to this problem involving filtering the noise data specifically around the 26 s peak. Bensen et al. (2007) however show that spectral whitening is sufficient to reduce the effects of even the most persistent signals. Thus, using the WHITEN function in SAC, the complex noise spectrum of each day file is inversely weighted by a smooth version of its amplitude spectrum to produce a spectrally whitened waveform that can be used in future cross-correlations.

3.2.3 Green's function estimation

Here we discuss the steps involved in estimating the Green's functions between pairs of receivers through cross-correlations of ambient seismic noise as in Equation (2.14). The aim is to construct the response that would have been recorded at one of the

receiver locations if an impulsive source had been fired from the location of the second receiver. This turns one of the receivers in the receiver pair into a "virtual" source.

A search of all processed and normalised day files is carried out to determine the number of stations that have recorded at least six months of coincident ambient noise. From these stations, all inter-station pairs are determined and the inter-station distances are computed.

For a given station pair, at locations $\mathbf{x_A}$ and $\mathbf{x_B}$ say, all daily noise records are cross-correlated to construct a set of noise correlation Green's functions to which a second bandpass filter with corner frequencies at 0.02 Hz and 0.1 Hz (10 s - 50 s period) is applied. All daily correlation functions constructed between $\mathbf{x_A}$ and $\mathbf{x_B}$ are stacked (summed) to construct the estimated Green's function between that station pair. This summation acts to integrate over all (unknown) ambient source positions, and thus over all ambient field fluctuations recorded over time as in Equation (2.14). This constructs an estimate of the homogeneous Green's function $G_H(\mathbf{x}_A, \mathbf{x}_B)$, which is a two-sided function consisting of a causal part (at positive times) and an acausal part (at negative times). The causal part represents the response recorded on receiver $\mathbf{x}_A$ from an impulsive source fired at the location of receiver $\mathbf{x}_B$, whilst the acausal part is another Green's function estimate starting at time zero but extending in the negative time direction. Here, the acausal part of $G_H(\mathbf{x}_A, \mathbf{x}_B)$ is time-reversed and added to the causal part to construct $G(\mathbf{x}_A, \mathbf{x}_B)$ at positive times only which often improves the signal to noise ratio of the Green's function estimate.

These Green's function estimates, constructed using noise interferometry as in Equation (2.14), are used as the propagators in SRI (Equations (2.31) and (2.32)). Their role is to project earthquake recordings from one location to another. This spatial redatuming of the earthquake data constructs a new SRI seismogram at that new location. The quality of these Green's function estimates is thus important in constructing accurate SRI seismograms.

3.2.4 Quality control

Two quality control checks are carried out following the cross-correlation of the ambient seismic noise data. These checks are primarily used to calculate the signal-to-noise ratio (SNR) of: 1) each noise correlation function, and 2) each estimated Green's function. The SNR is defined as the ratio of the absolute maximum amplitude within the signal window to the root-mean-square (RMS)-value of a noise window. The signal

window spans a time period within which we expect a surface wave arrival, and the noise window is defined such that it follows this signal window temporally.

We use a prior estimate of the group velocity within our quality checking procedures. Bensen et al. (2008) calculate Rayleigh wave group and phase dispersion curves for USArray inter-station paths, and from their results we choose an average group velocity of 3.25 km/s for all station paths and frequencies used herein. Using this group velocity we calculate the surface wave arrival time τ that would be recorded if a seismic wave were to originate at one of the station locations and be recorded at the second station location. We thus define an approximate signal window within which we expect the surface wave to arrive: $[\tau_{min} : \tau_{max}]$ where $\tau_{min} = \tau - 250s$ and $\tau_{max} = \tau + 250s$.

SNR of Noise Correlation Functions

The first SNR check is carried out on all daily noise correlation functions. The minimum ($\tau - 250s$) and maximum ($\tau + 250s$) expected surface arrival times are used to define the signal windows for all station pairs, and 500 s noise windows are defined such that they follow these signal windows temporally. The SNR of each noise correlation function is calculated: the absolute maximum amplitude of the signal window is divided by the RMS value of the noise window. Daily correlation functions with a SNR value ≥ 4.8 are normalised (divided) by the RMS-value of their signal window whilst those with a SNR value between 2 and 4.8 are normalised by their absolute maximum amplitude. Daily correlation functions with a SNR value ≤ 2 are removed altogether.

SNR of Estimated Green's Functions

A second SNR check is carried out after the daily noise correlation functions have been stacked and the estimated Green's functions constructed. Estimated Green's functions with a SNR value ≥ 15 are normalised by the RMS-value of their signal window, whilst those with a SNR value between 3 and 15 are normalised by their absolute maximum amplitude. Estimated Green's functions with a SNR value ≤ 3 are removed.

All SNR limits were defined following a series of trial and error tests on many data files. For example, trial and error tests on the daily correlation functions identified a possible top SNR limit of between 4.5 and 5, with the majority of good-looking signals

having a SNR value greater than 5. However, to encompass those correlation functions whose signals were still strong in comparison to the background noise level (SNR values between 4.5 and 5), an intermediate value of 4.8 was chosen. For the majority of daily files with SNR values less than 4.8 the signal was not clearly discernible from the noise.

3.3 A Review of the Estimated Green's Functions

We now briefly illustrate some of the estimated Green's functions constructed using the methodology described above. Figure 3.2 shows the locations of a dense seismometer array in New Mexico. All seismometers are a part of the USArray Transportable Array (TA) (`http://www.usarray.org/researchers/obs/transportable`). Seismometers are named in (East-West) rows and (North-South) columns, such that all seismometers along a row start with the same letter (or number), i.e. 'V', 'W', 'X', ... , '5', '6', and all seismometers down a column end in the same sequence i.e. '20A', '21A', '22A', ... , '31A', '32A'. Some of these rows and columns have been highlighted in the array shown in Figure 3.2.

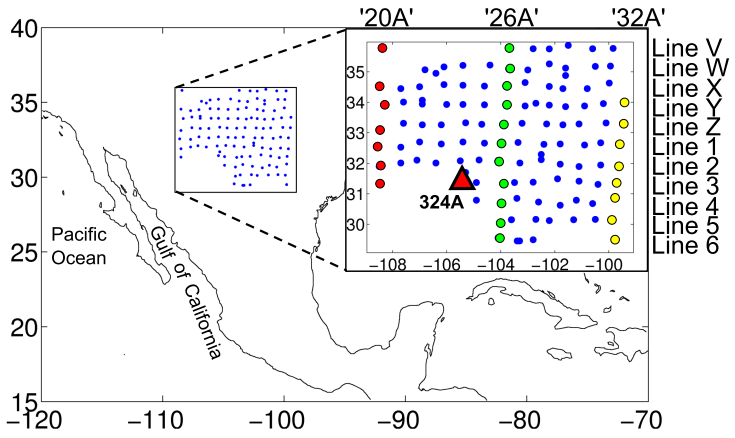

Figure 3.2: Seismometers from the USArray TA network. Estimated Green's functions have been constructed between receiver 324A (triangle) and all other seismometers (circles) using ambient noise interferometry as in Equation (2.14). Some particular North-South lines of seismometers have been highlighted for reference. Left North-South line: seismometers whose station name ends with the sequence '20A'. Central North-South line: station names that end with '26A'. Right North-South line: station names that end with '32A'. East-West lines of seismometers start with the same letter or number, from Line 'V' in the north of the array to Line '6' in the south.

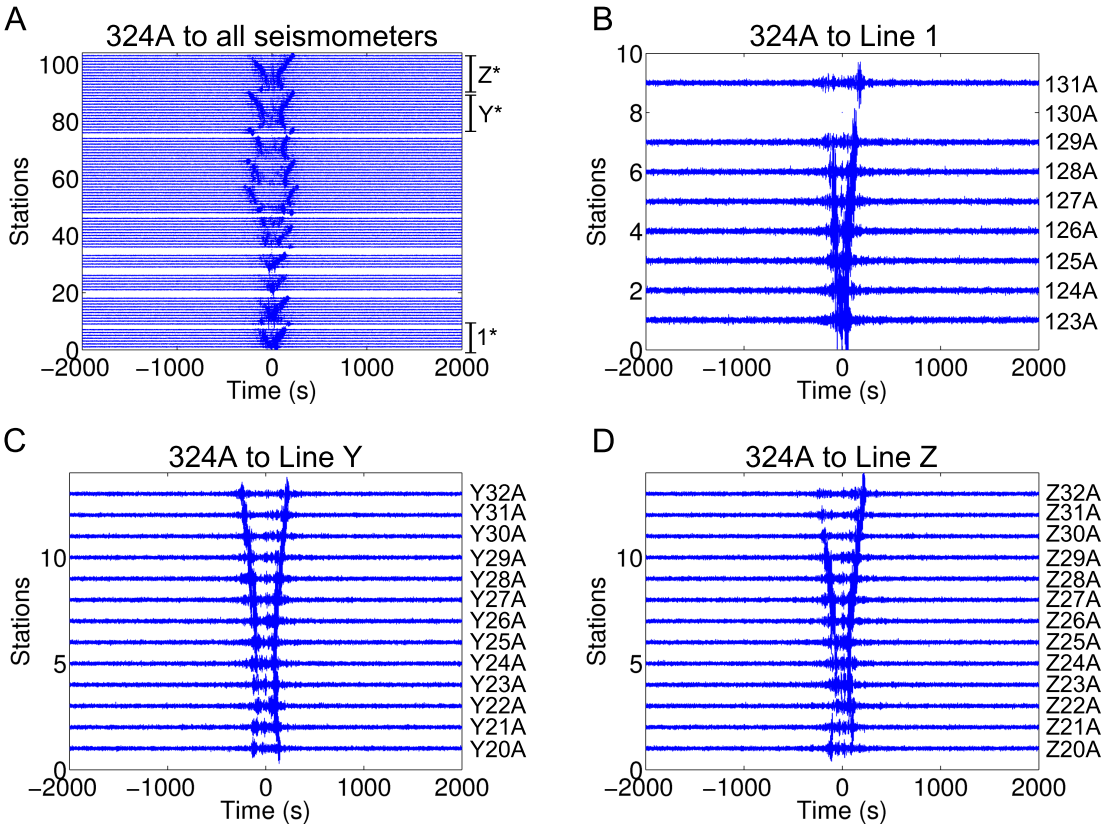

Figure 3.3: Estimated Green's functions constructed between seismometer 324A and (A) all seismometers within the array shown in Figure 3.2, (B) seismometers 123A - 131A, (C) seismometers Y20A - Y32A, and (D) seismometers Z20A - Z32A.

Figure 3.3 shows the estimated Green's functions constructed between seismometer 324A and a selection of seismometers from within the array. Where traces are missing, the SNR analyses described in Section 3.2.4 have eliminated those inter-receiver paths from the study. Figure 3.3A shows the estimated Green's functions between 324A and *all* of the seismometers within the array. The estimated Green's functions have been arranged alphabetically to compliment the naming convention of the USArray TA network. Thus, the first 9 traces at the bottom of Figure 3.3A represent the estimated Green's functions constructed between seismometer 324A and all seismometers along Line '1', whilst the top 13 traces are the estimated Green's functions between seismometer 324A and all seismometers along Line 'Z'.

The estimated Green's functions between 324A and Line 1 can be seen in more detail in Figure 3.3B and we observe that the Green's function estimate at seismometer 130A has been rejected by the quality control criteria. The estimated Green's functions appear to be well constructed, as the surface wave arrivals can be identified between

all station pairs. Furthermore, surface wave arrival times increase with distance from seismometer 324A. Both the causal and acausal parts of the estimated Green's functions are plotted and one observes almost equal amounts of energy on both parts with the exception of the constructions at 129A and 131A, in which the signals are mainly causal. This implies that there is a slight bias in the propagation of ambient noise across the array. In this case, more energy is propagating in the direction from seismometer 324A to 129A/131A (southwest to northeast), than from 129A/131A to 324A (northeast to southwest). We conclude that the ambient seismic noise is predominantly ocean-swell generated from the Gulf of California and further out in the Pacific Ocean.

Similarly, Figure 3.3C and Figure 3.3D show the estimated Green's functions between 324A and seismometers along rows Y and Z, respectively. Here we observe an appropriate moveout along each row of seismometers as the surface waves arrive earlier at seismometers closer to 324A (e.g. Y24A, Z24A) than at seismometers positioned further from 324A and towards the ends of the rows (e.g. Y20A, Z32A).

We now review the estimated Green's functions constructed over much larger length scales. The locations of seismometers used in this study are shown in Figure 3.4. Again, the seismometers within the array (circles) are a part of the USArray TA network and the naming convention is as described above. Here we focus on 5 North-South columns of seismometers from Line '24A' in the West to Line '28A' in the East, and two of these columns have been highlighted in the figure for reference.

We illustrate the estimated Green's functions constructed between the 8 receivers located outside of the dense array (triangles) and seismometers within the dense array (circles) in Figures 3.5 and 3.6. We review the average SNR and the average RMS values of the estimated Green's functions constructed between the array seismometers and each of the 8 receivers in Table 3.1. Here, the 8 receivers are listed under 'Station Name' and estimated Green's functions are constructed between each of these 8 receivers and the array seismometers located along the lines listed under 'Lines Used'. The quantities under 'Average RMS of Signal Window' are the average root-mean-square values of 500 s time windows (τ - 250 s, τ + 250 s) of the estimated Green's functions within which we expect the first surface waves to arrive. Since all estimated Green's functions have been normalised to their absolute maximum amplitude, the maximum RMS value we can obtain is 1.0. The quantities under 'Average SNR Values' refer to the average of the signal-to-noise ratios of the estimated Green's functions constructed between each receiver and each array seismometer. The SNR is

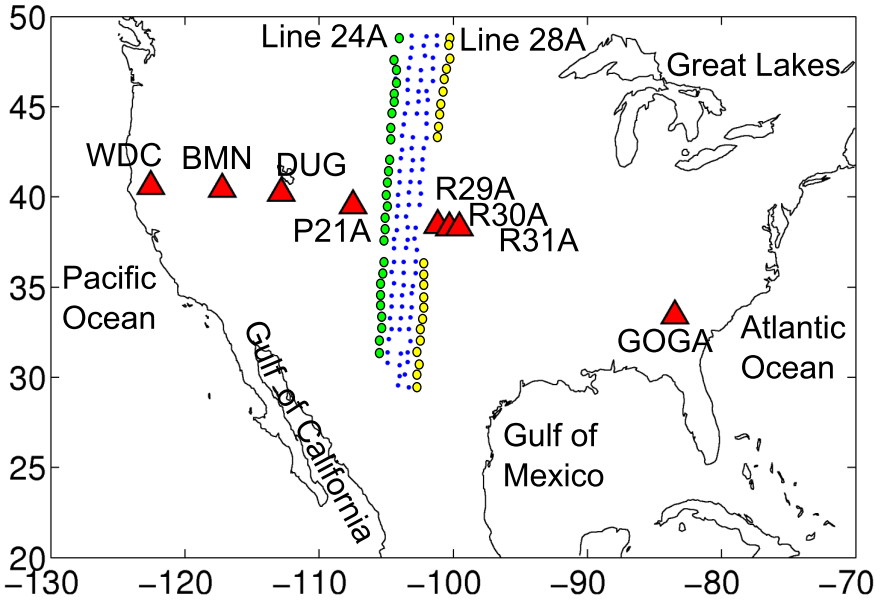

Figure 3.4: Seismometers from the USArray TA network (triangles and circles). Estimated Green's functions are constructed between each of the triangles and each of the circles using ambient noise interferometry as in Equation (2.14). North-South lines of seismometers within the main array have been highlighted for reference. Western line: seismometers whose station name ends with the sequence '24A'. Eastern line: station names that end with '28A'.

determined by taking the absolute maximum amplitude of the signal window defined previously and dividing it by the RMS of the 500 s noise window which directly follows the signal window temporally. Finally, under 'Average Distance' we list the average of the inter-station distances considered (between each receiver and each array seismometer).

In Figure 3.5 we construct the estimated Green's functions between seismometers along lines 24A and 25A of the array in Figure 3.4 with receivers WDC, BMN, DUG and P21A that lie to the West of the array. Using these same lines of array seismometers we are able to compare the quality of the estimated Green's functions constructed as the distance between the array seismometers and the receivers increases. In Figure 3.5A we observe the estimated Green's functions constructed between 55 array seismometers and WDC, which is located furthest from the array at an average distance of 1635 km. We observe the main surface wave arrivals across the array seismometers but the estimated Green's functions exhibit a low signal-to-noise ratio. The average SNR value for these estimated Green's functions is 6.94 and the average RMS value is 0.28. Thus, we observe that at this large distance from the array

Table 3.1: The average root-mean-square (RMS) values and signal-to-noise ratios (SNRs) of all estimated Green's functions constructed between receivers ('Station Name') and seismometers within an array ('Lines used'). See Figure 3.4 for a map of all station locations and Figures 3.5 and 3.6 for plots of the estimated Green's functions. 'Average Distance' is the average of inter-station distances considered

Station Name	Lines Used	Average RMS of Signal Window	Average SNR	Average Distance (km)
WDC	24A-25A	0.28	6.94	1635
BMN	24A-25A	0.28	6.92	1225
DUG	24A-25A	0.68	15.43	905
P21A	24A-25A	0.88	25.27	555
R29A	25A-26A	0.77	28.91	615
R30A	26A-27A	0.70	26.19	620
R31A	27A-28A	0.70	23.76	700
GOGA	24A-25A	0.31	6.19	2080

seismometers, the estimated Green's functions are relatively poorly constructed.

Figure 3.5B illustrates the estimated Green's functions constructed between the array seismometers and receiver BMN, which is located at an average distance of 1225 km from the array. We again observe that over these large inter-station distances, the estimated Green's functions are poorly constructed as the average signal-to-noise ratio is low (a value of 6.92) and the RMS of the signal is again 0.28 out of 1.0.

The estimated Green's functions constructed between the array seismometers and receiver DUG, which is located at an average distance of 905 km from the array, are shown in Figure 3.5C. Here we observe a slightly higher average SNR value of 15.43 and the average RMS value of the signal is 0.68 out of 1.0. We see that the main surface wave arrivals can be identified over the noise level and the moveout of these arrivals along the array is visible. For example, the surface wave arrival times are shorter for seismometers located within the centre of the array (around station 30), closer to receiver DUG, compared to those seismometers located towards the edges of the array (stations 1 and 57).

Finally, Figure 3.5D illustrates the estimated Green's functions constructed between the array seismometers and receiver P21A, located at an average distance of 555 km from the array. The surface wave arrivals can be clearly identified. Subsequently, the average SNR value is high at 25.27 and the average RMS value is 0.88 out of 1.0.

Thus we observe that as the distance over which the estimated Green's functions

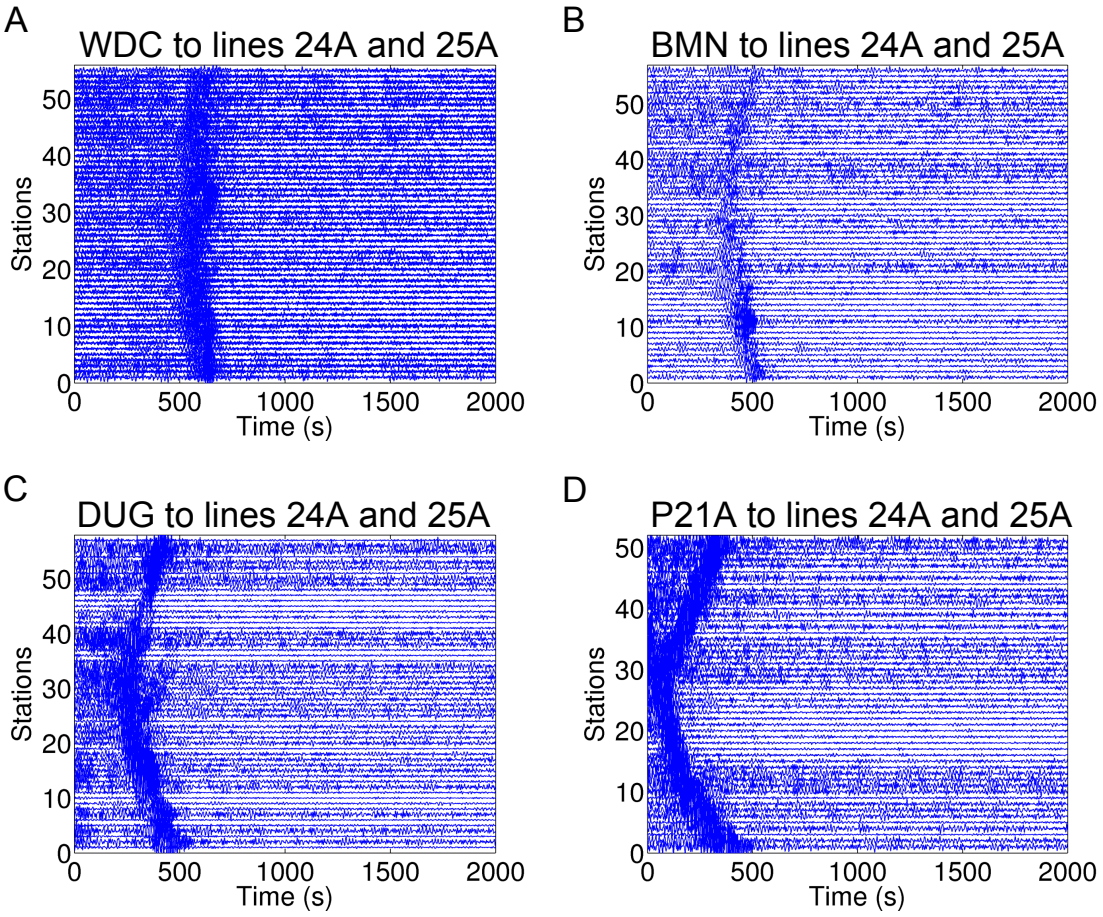

Figure 3.5: Estimated Green's functions constructed between seismometers along lines 24A and 25A of the USArray TA network with (A) receiver WDC, (B) receiver BMN, (C) receiver DUG and (D) receiver P21A. See Figure 3.4 for the locations of all seismometers. All seismograms are normalised by their absolute maximum amplitude for display purposes.

are constructed decreases, the quality of the estimated Green's functions increases. This is demonstrated quantitatively in Table 3.1 by the higher SNR and RMS values of the signal windows.

A similar analysis is performed for those receivers located to the East of the array in Figure 3.4. Here the estimated Green's functions are constructed between varying lines of array seismometers and these estimated Green's functions can be seen in Figure 3.6.

Figure 3.6A-C shows the estimated Green's functions constructed between seismometers from within 2-line combinations of seismometers located along lines 25A-28A of the array and receivers R29A, R30A and R31A, respectively. All array seismometers are located close to the three receivers (at an average distance of between

600 km and 700 km) and the estimated Green's functions are constructed successfully over these distances. The average SNR values can be seen in Table 3.1 and all values are high. Similarly, the average RMS values are also greater than 0.7.

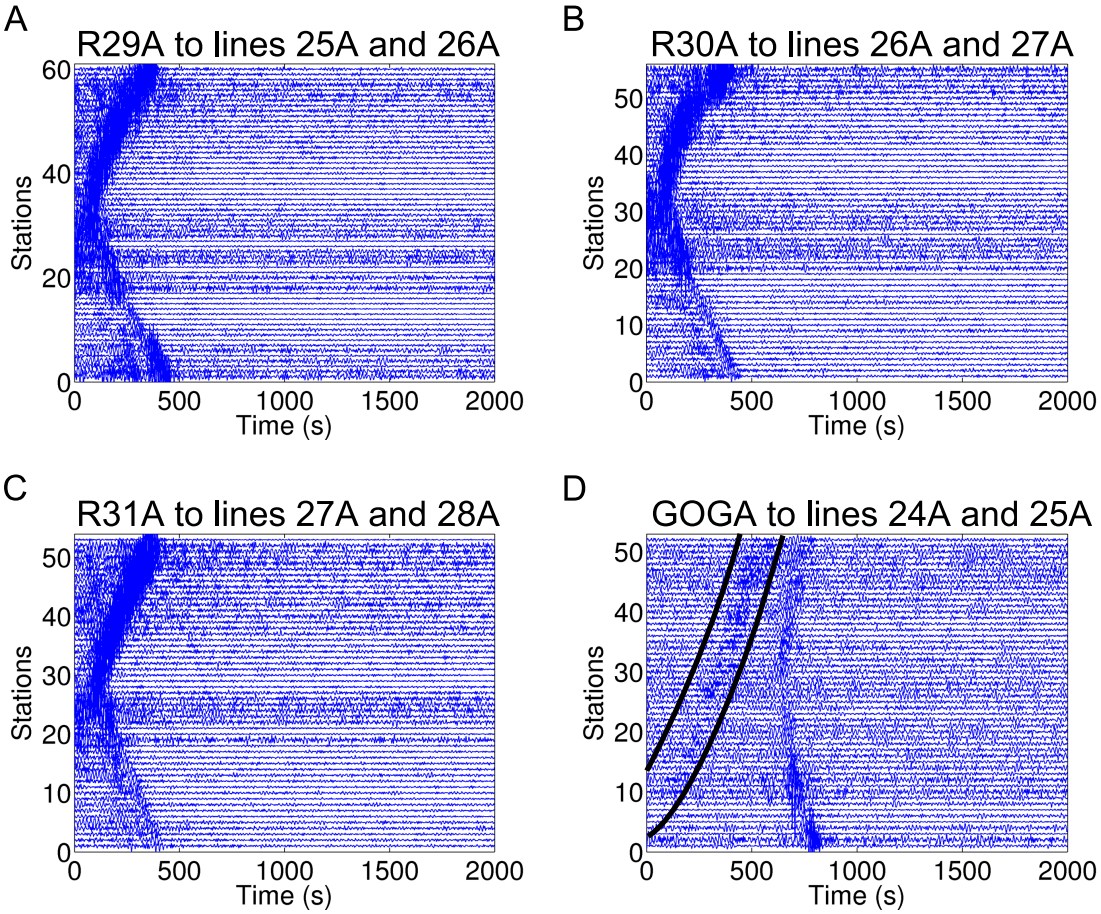

Figure 3.6: Estimated Green's functions constructed between (A) seismometers along lines 25A and 26A with receiver R29A, (B) seismometers along lines 26A and 27A with receiver R30A, (C) seismometers along lines 27A and 28A with receiver R31A, and (D) seismometers along lines 24A and 25A with receiver GOGA. See Figure 3.4 for the locations of all seismometers. The thick black lines in (D) outline the prominent non-physical arrivals that contaminate the estimated Green's functions.

In Figure 3.6D we observe the Green's functions constructed between array seismometers located along lines 24A and 25A and receiver GOGA, which is located at an average distance of 2080 km from the array seismometers. Here there is a clear decline in the quality of the estimated Green's functions and this is represented by the low SNR and RMS values (6.19 and 0.31, respectively). Furthermore, the estimated

Green's functions have been contaminated by non-physical arrivals, outlined by the thick black lines in Figure 3.6D. These spurious arrivals could be a consequence of a break down in the underlying assumptions of correlation-type interferometry: we assume an elastic, non-attenuative medium between the receiver pair which is unlikely to be valid over an average distance of 2080 km. We also assume the distribution of noise sources to be roughly homogeneous; however, these non-physical arrivals approach zero time at station 10 within the array. One way to obtain coherent non-physical arrivals before the first physical arrival is if the noise comes specifically from a direction oblique or perpendicular to the inter-receiver path. Hence, it may be that there is a stronger component of noise coming from the Gulf of Mexico or the Great Lakes, which causes these errors. In any case, as also seen for the furthest positioned receivers to the west of the array, we again observe that as the inter-station distances increase, the quality of the estimated Green's functions constructed over those distances decreases.

To conclude, it is important to check the quality of the inter-receiver Green's functions before they are used as propagators in source-receiver interferometry. If the estimated Green's functions have low SNR and RMS values, the results of source-receiver interferometry will be contaminated by noise and non-physical arrivals. This will be discussed more in later chapters, but it is important to note that herein we will place the most confidence in those estimated Green's functions constructed over shorter inter-station distances whose SNR and RMS values are higher than those Green's function estimates constructed over larger length scales.

3.4 Inter-Receiver Interferometry by MDD

Multidimensional deconvolution (MDD) is an alternative approach to Green's function estimation and, unlike ambient noise interferometry, it can be used in conjunction with real earthquake data to construct an estimate of the Green's function between two receiver locations. To perform MDD requires a spatially regular array of receivers at locations such as $\mathbf{x}$ on boundary S (our "backbone" array), a single receiver at $\mathbf{x_B}$ (our "target sensor") and a distribution of earthquake sources at locations such as $\mathbf{x_{S_i}}$, as illustrated in Figure 3.7. The earthquake sources need not be located on a fixed, regular boundary as we consider each source separately in Equations (2.15) and (2.17) rather than as an integration over a source boundary. To perform MDD accurately however, the energy that propagates from the sources must illuminate the Green's functions between the receiver boundary and the target sensor sufficiently. Furthermore, the

target sensor at $\mathbf{x_B}$ must be located on the opposite side of the receiver boundary S to the earthquake sources. The aim of MDD is to construct the estimated Green's function between a backbone receiver at $\mathbf{x_A}$ on S and the individual target sensor at $\mathbf{x_B}$.

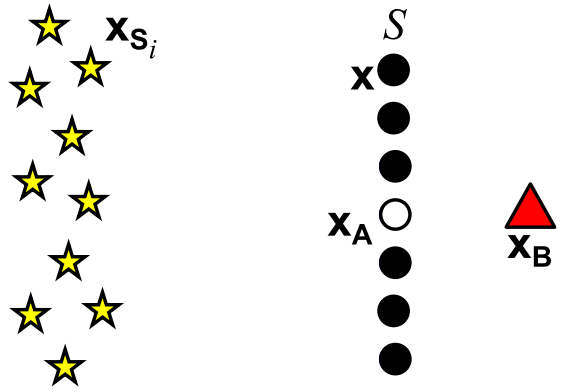

Figure 3.7: Schematic illustration of the geometry required to perform MDD in an earthquake seismology setting. The Green's function G is constructed as in Equation (2.22) between the target sensor at location $\mathbf{x_B}$ (triangle) and a backbone array seismometer at location $\mathbf{x_A}$ (unfilled circle) on the receiver boundary S. The earthquake signals originate at locations such as $\mathbf{x}_{\mathbf{S}_i}$, that are on the opposite side of S to the target sensor.

.

3.4.1 Earthquake data preparation

Earthquake data recorded on the backbone seismometers and on the target sensors are downloaded from the IRIS database using the web service request tool as described in Section 3.2.1. Data is down sampled to 4 samples per second. The data is then pre-processed similarly to the noise data downloaded for noise interferometry: the mean and linear trend are removed, a cosine taper is applied to the edges of the trace and the instrument response is removed. A bandpass filter is applied with corner frequencies at 0.01 Hz and 1 Hz, placing the earthquake records within the 1 s - 100 s period band.

The temporal normalisation of the earthquake data differs from that of the noise data. We place no constraint on the magnitudes of the earthquakes selected, thus the aim of temporal normalisation is to prevent large magnitude earthquakes from dominating the cross-correlations in Equations (2.15) and (2.17). For any one earthquake, we select one seismometer from the backbone array and normalise all recordings of that event to the absolute maximum amplitude of the event recorded

on the chosen backbone seismometer. Following this processing step, all earthquake recordings are of a similar amplitude, regardless of their original measured magnitude, and no single event will hold a significantly greater weight in the summations over earthquake sources in Equations (2.15) and (2.17).

3.4.2 Constructing Γ and C

We first construct the point-spread function Γ as in Equation (2.15) for each $\mathbf{x}$ and $\mathbf{x_A}$ located along the backbone array. The earthquake signals recorded on $\mathbf{x}$ and $\mathbf{x_A}$ are cross-correlated. A summation is then performed over all earthquakes at locations $\mathbf{x}_{\mathbf{S}_i}$ to construct the point-spread function $\Gamma(\mathbf{x}, \mathbf{x_A})$. For N seismometers within the backbone array, we construct N point-spread functions with a different seismometer occupying the location of $\mathbf{x_A}$ each time. Transforming to the frequency domain, $\mathbf{\Gamma}$ is a NxN matrix for each frequency component.

Second, we construct the correlation function C as in Equation (2.17) between the target sensor $\mathbf{x_B}$ and each seismometer $\mathbf{x_A}$ (for $\mathbf{x} = \mathbf{x_A}$) within the backbone array. Earthquake signals recorded on $\mathbf{x_B}$ and $\mathbf{x_A}$ are cross-correlated. Summation over all earthquake recordings constructs the correlation function C that represents the response at $\mathbf{x_B}$ from a virtual source at the location of $\mathbf{x_A}$. This correlation function is not the true response recorded at $\mathbf{x_B}$ from an impulsive source at $\mathbf{x_A}$ as the earthquake sources are not regularly distributed around a closed boundary and we cannot assume a lossless medium. Transforming to the frequency domain, $\mathbf{C}$ is a 1xN row vector for each frequency component.

3.4.3 Singular value decomposition

Before evaluating Equation (2.22) we must invert the point-spread function $\mathbf{\Gamma}$. Unless the source-receiver geometry is such that the earthquake sources perfectly illuminate the backbone seismometers, $\mathbf{\Gamma}$ will not be full-rank and its inversion will be ill-posed. To stabilise the MDD solution, we perform singular value decomposition as in Equation (2.21).

We first study the singular values of $\mathbf{\Gamma}$ to determine the tolerance value of the inversion: this tolerance value is defined as a percentage of the global maximum singular value of the system over all frequencies and determines the number of singular values to be included in the inversion. Any singular values with an amplitude below the tolerance value are excluded from the inversion.

We calculate the pseudoinverse of the point-spread function using the *pinv* function in Matlab. This evaluates Equation (2.21) with *r* set to the tolerance value specified.

3.4.4 Green's function estimation

To estimate the true Green's function $G(\mathbf{x_B}, \mathbf{x_A})$, the inverted point-spread function $\mathbf{\Gamma^{-1}}$ is inserted into Equation (2.22). This is evaluated for each frequency to estimate the new Green's function as a common receiver gather. In the frequency domain, $\mathbf{G}$ is thus a 1xN row vector for each frequency component. This represents the response at $\mathbf{x_B}$ from an impulsive source at the location of $\mathbf{x_A}$, constructed from an irregular distribution of earthquake sources recorded on a regularly distributed receiver boundary, on which $\mathbf{x_A}$ is located.

Green's function estimation by MDD is presented in Chapter 7 and the results are compared with those constructed using noise interferometry. We experiment with the tolerance value and provide examples of the inversion of $\mathbf{\Gamma}$ performed with tolerance values of both 1% and 10%.

3.5 Summary and Look Ahead for Inter-Receiver Interferometry

The methodology described in Section 3.2 can be used to perform inter-receiver interferometry on any data set providing one has at least two receivers and a surrounding boundary of sources. Here we assume mutually uncorrelated noise sources and invoke ambient noise interferometry as in Equation (2.14), but in an exploration seismology setting the source boundary would typically consist of active seismic shots that are fired sequentially and recorded by the two receivers. Noise interferometry relies on pairs of receivers whose installation dates are coincident by at least six months and we assume that the estimated Green's functions constructed do not vary dramatically over time. We also note that the inter-receiver distance is important in constructing high quality estimates of the Green's functions. In Section 3.3 we proposed that, for the station geometries considered in this thesis, this distance should be kept short (up to $\sim$ 1500 km) where possible.

An alternative method for Green's function estimation was discussed is Section 3.4: earthquake data was processed and cross-correlated to construct inter-

receiver Green's function estimates by multidimensional deconvolution (MDD) as in Equation (2.22). MDD requires an array of regularly distributed receivers that is illuminated sufficiently by earthquake sources. The settings in which MDD can be performed are thus less pervasive than those which support ambient noise interferometry, but MDD requires far fewer data. MDD is more computationally intensive than noise interferometry as it involves matrix inversion as opposed to trace-by-trace correlation. When the earthquake sources do not sufficiently illuminate the backbone array, this inversion will be ill-posed. To stabilise it we provide a methodology for singular value decomposition.

The following section introduces a more specific methodology to apply source-receiver interferometry (SRI). We shall focus on the schematic geometry outlined in Figure 3.8A where a receiver at $\mathbf{r}$ and a source at $\mathbf{s}$ are surrounded by an inner boundary of receivers on S and an outer boundary of sources on S'. We thus invoke correlation-correlation SRI as in Equation (2.31), using noise interferometry as in Equation (2.14) to construct the SRI propagators. To comment on the terminology in the subsequent section, receivers $\mathbf{x}$ on boundary S will make up our "backbone seismometer array", receiver $\mathbf{r}$ will become our "target sensor", sources at locations such as $\mathbf{x}'$ on boundary S' will represent our mutually uncorrelated noise sources, and source $\mathbf{s}$ will be our earthquake source. Throughout Chapters 5 and 6 we also invoke correlation-convolution SRI pertaining to the geometry in Figure 3.8B. The practical methodology described herein for correlation-correlation SRI is also invoked for correlation-convolution SRI, but with processes of correlation in Equation (2.31) replaced by processes of convolution as in Equation (2.32).

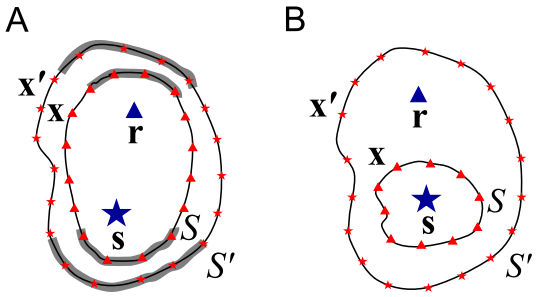

Figure 3.8: Possible schematic geometries for source-receiver interferometry (SRI) pertaining to (A) correlation-correlation SRI, and (B) correlation-convolution SRI. Stars are sources, triangles are receivers. Grey shaded regions in (A) represent the stationary phase regions for the source-receiver line between $\mathbf{s}$ and $\mathbf{r}$. For full derivations of the SRI integrals used in each example see Curtis and Halliday (2010).

3.6 Source-Receiver Interferometry (SRI)

To perform SRI for the geometry outlined in Figure 3.8A we consider three stages:

1. Construct estimated Green's functions between each target sensor at $\mathbf{r}$ and backbone seismometers at $\mathbf{x} \in S$ using noise interferometry as in Equation (2.14). These are the SRI propagators in Equation (2.31).

2. Cross-correlate these SRI propagators with seismograms from a real earthquake at $\mathbf{s}$ recorded on the same backbone seismometers, thus constructing the integrands for inter-source interferometry (in Equation (2.31)).

3. Integrate (sum) over all backbone seismometers to reconstruct earthquake seismograms on target sensors, thereby completing the inter-source interferometry step according to Equation (2.31).

The following sections shall describe these processes in more detail.

3.6.1 Station criteria

Whilst seismometer selection for inter-receiver interferometry requires coincident installation dates between stations in each pair, we need to consider more complex criteria to perform SRI. These station criteria were developed to adhere to stationary phase approximations similar to those introduced by Snieder (2004), where it is shown that complete boundaries of sources/receivers are not needed for interferometric integrals as long as the sources/receivers that do exist lie around regions of the boundary within which the interferometric integrands become approximately stationary. These stationary phase regions are shown schematically in Figure 3.8A for the two boundaries and thus for the two interferometric integrals, used in SRI.

The following criteria for SRI station selection have been tested and iteratively adjusted during this PhD until they reached a stable point that was found to work for most cases. We start by knowing the date, time and location of an earthquake, the seismograms of which we wish to construct using SRI. A search of the installation dates of all USArray stations determines the number of seismometers deployed when the event occurred. Of these seismometers, those that satisfy the following spatial criteria are selected for the backbone seismometer array (for a schematic illustration of these criteria see Figure 3.9):

- A great circle path (GCP) from the earthquake epicentre intersects the seismometer array approximately perpendicularly (at a local inter-section angle of between 70° and 110°).
- The same GCP intersects at least one target sensor at location **r** (a seismometer that did not record the event).
- Seismometers are operational at the time the event occurred and all have at least six months in common of ambient seismic noise recordings.
- The seismometer array consists of at least two parallel lines of seismometers.

A justification of these station criteria is provided in Section 3.7 after introducing all steps required to implement in practice the SRI theory in Chapter 2.

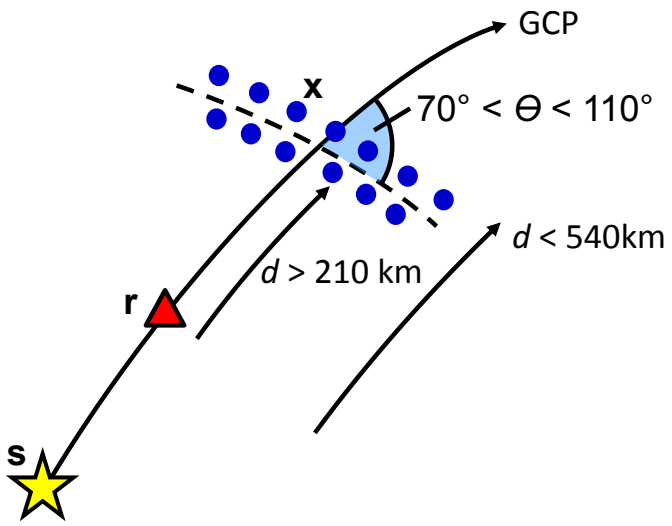

Figure 3.9: Schematic diagram illustrating the spatial criteria specified in Section 3.6.1 for a source **s** (star), target sensor **r** (triangle), backbone seismometers **x** (circles) and great circle path (GCP). When the target sensor is located close to the backbone seismometer array ($d < 540$ km), an additional criterion is specified such that the backbone seismometers should lie on average between approximately 210 km - 540 km from the target sensor.

3.6.2 Processing

For seismometers that satisfy the above criteria, instrument response files and up to two years of daily ambient noise records sampled at four samples per second

(sps) are downloaded from the IRIS database using the IRISWS request tool. These seismometers make up our backbone seismometer array. Earthquake signals recorded on these selected backbone seismometers are also downloaded. Each earthquake trace is cut from the origin time of the event and is 14,400 s in length.

All ambient noise data are then processed following the methodology outlined in Section 3.2.2. Steps 1 and 2 of this methodology are also performed for the earthquake data recorded at each backbone seismometer: the mean, trend and instrument response are removed and the records are filtered between 1 s - 100 s period.

3.6.3 Green's function estimation

For SRI we define a "station pair" as the pairing of a target sensor ($\mathbf{r}$) with a backbone array seismometer ($\mathbf{x}$). For each of these pairings we calculate the estimated Green's functions $G(\mathbf{x}, \mathbf{r})$ using noise interferometry as in Equation (2.14) and as described in Section 3.2.3. Quality control checks are performed on these SRI propagators at the stages indicated in Section 3.2.4. $G(\mathbf{x}, \mathbf{r})$ is thus an estimate of the response that would have been recorded on the backbone seismometer if an impulsive source had been fired at the location of the target sensor, using the target sensor as a "virtual source".

3.6.4 Inter-source interferometry

The second step of SRI is to perform inter-source interferometry between the earthquake source ($\mathbf{s}$) and the virtual source ($\mathbf{r}$) using backbone seismometers ($\mathbf{x}$) on boundary S. Here we invoke Equation (2.31) for a single source $\mathbf{s}$, rather than as a collection of sources $\mathbf{s}$ on fault plane F. Terms such as $G(\mathbf{x}, \mathbf{r})$ and $T(\mathbf{s})G(\mathbf{x}, \mathbf{s})$ thus represent the SRI propagators constructed between the target sensor-backbone seismometer receiver pairs and the recordings of the individual earthquake with source signature $T(\mathbf{s})$ on those same backbone seismometers, respectively. Equation (2.31) represents a cross-correlation between the SRI propagators and the real earthquake signals, but convolution is used as in Equation (2.32) if the acquisition geometry pertains to that shown in Figure 3.8B. Correlation-convolution SRI as shown in Figure 3.8B is applied and discussed further in Chapter 5.

Prior to cross-correlation, a bandpass filter is applied to the earthquake data with corner frequencies at 0.02 Hz and 0.1 Hz (10 s - 50 s period). This ensures that the earthquake data and the newly constructed SRI propagators sample the same frequency band. Cross-correlation of these waveforms as in Equation (2.31) constructs a set of

cross-correlation functions. These correlation functions are the values of the integrand in Equation (2.31) for each backbone seismometer at $\mathbf{x}$.

In the case where one has full, regularly spaced boundaries of sources and receivers one would now integrate over the receiver boundary S to turn the temporary virtual source at $\mathbf{r}$ into a "virtual sensor". In taking the acausal part of the reconstruction only $\big(T(\mathbf{s})^* G^*(\mathbf{r},\mathbf{s})\big)$ and time-reversing the result one would construct the earthquake response at the target sensor, $T(\mathbf{s})G(\mathbf{r},\mathbf{s})$, thus completing the inter-source interferometry step in Equation (2.31) for a single earthquake source at $\mathbf{s}$, rather than for a collection of sources on fault plane F. When receiver boundaries are incomplete however, which is often the case when using active seismometer arrays that may suffer from spatial irregularities and instrument malfunctions, we found it was necessary to perform an interpolated sum over the values of the integrands for each $\mathbf{x}$ in the inter-source interferometry step. The interpolation should be such that it improves the approximation of this summation to the integration in Equation (2.31) and we do this by embedding the backbone seismometer array within a rectangular patch of 2D spatial Voronoi cells such that seismometer coordinates become Voronoi cell centres. Assigning the integrand value at $\mathbf{x}$ to all points in the assigned Voronoi cell, the integrand can then be integrated over a continuous boundary.

3.6.5 Voronoi cells

Voronoi cells are used for 'gridding' irregularly spaced geophysical data and interpolating the data into the surrounding medium, in two or three (or higher) dimensions. For example, in seismic tomography one may know the velocity values at a set of points (nodes) in space. Using Voronoi cells one is able to obtain an estimate of the velocity structure of the medium between the nodes (in two or three dimensions) by interpolating the known velocity values between neighbouring nodes. Here we use Voronoi cells to reduce the effects of spatial irregularities within backbone seismometer arrays. This is to ensure that the values of the integrand of Equation (2.31) for each backbone seismometer $\mathbf{x}$ contribute appropriately to the final interferometric surface integral: where the backbone seismometer density is high, each seismometer should individually contribute less to the integration than when the backbone array seismometers are sparsely distributed. We now provide a step-by-step account of how we construct the Voronoi cells and determine the appropriate weighted contributions of the correlation functions to the integral in Equation (2.31).

Construct Voronoi cells

Backbone seismometer arrays are embedded within a rectangular patch of 2D spatial Voronoi cells, such that seismometer coordinates become Voronoi cell centres. A set of Voronoi cells are illustrated in Figure 3.10 - polygons shaded according to their size, normalised to the largest cell: for the given backbone seismometers within the array (circles), the minimum and maximum latitude ($\lambda_{min}, \lambda_{max}$) and longitude ($\phi_{min}, \phi_{max}$) values of the seismometers are determined. These values are used to define a rectangular patch that surrounds the array: $[\lambda_{min} - 0.4^{\circ} : \lambda_{max} + 0.4^{\circ}, \phi_{min} - 0.4^{\circ} : \phi_{max} + 0.4^{\circ}]$. For each 1° latitude-longitude square in the rectangular patch, the area is divided into a fine-scale grid of 161 x 161 points. All points within this grid are then used to construct the Voronoi cells (shaded polygons), such that each point is assigned to the Voronoi cell whose centre it is closest to. Original and adapted codes by Malcolm Sambridge and Erica Galetti are used for these computations, including Nearest Neighbour algorithms (Sambridge et al., 1995; Sambridge, 1999a,b) and computational geometry packages.

We are now able to visualise the spatial irregularity of our backbone arrays: Voronoi cells with large areas may highlight missing seismometers (e.g., cells 1, 2 and 3 in Figure 3.10), whilst regular rows of smaller Voronoi cells that are almost square-like in shape highlight a dense, regularly spaced band of seismometers (e.g., cells 4, 5 and 6 in Figure 3.10).

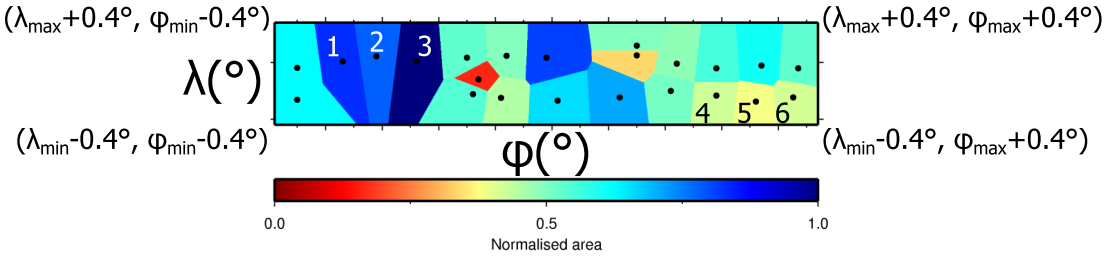

Figure 3.10: An illustration of backbone seismometers (circles) embedded within Voronoi cells (shaded polygons, colour normalised by the largest cell). A rectangular patch surrounding the backbone seismometers is defined by the minimum and maximum latitudes (λ°) and longitudes (ϕ°) of the backbone seismometers, $\pm$ 0.4°. Numbers highlight those Voronoi cells referenced in the text.

Assign the values of the integrand

For a backbone seismometer at $\mathbf{x}$ and a target sensor at $\mathbf{r}$ the value of the integrand of Equation (2.31) was constructed by cross-correlating the SRI propagators between $\mathbf{x}$ and $\mathbf{r}$ with the real earthquake seismograms recorded at $\mathbf{x}$. Each backbone seismometer location $\mathbf{x}$ has become a Voronoi cell centre, thus each point in a Voronoi cell is assigned the value of the integrand of Equation (2.31) from the seismometer $\mathbf{x}$ at its centre.

Define the weighting coefficients

A tapered cosine window is applied to the full rectangular patch in the x- and y-directions such that the first and last 25 % of the points in each direction are weighted by half-cosines normalised to lie in the interval [0,1] and the middle 50 % of the points are left unchanged. The value of the integrand assigned to each fine-scale grid point is therefore multiplied by a tapering coefficient within the range $0 - 1$ depending on the location of the point within the rectangular patch. Thus, the values of the integrand assigned to points towards the edges of the patch are multiplied by a coefficient tapering to 0, whilst the values of the integrand assigned to points within the centre of the defined boundary, closest to the stationary phase region of the array, are multiplied by a coefficient of 1. Tapering and weighting the values of the integrand in Equation (2.31) helps to account for two problems:

1. Edge effects. This is an effect imposed by our own initial selection of the surrounding rectangular patch: $[\lambda_{min} - 0.4^\circ : \lambda_{max} + 0.4^\circ, \phi_{min} - 0.4^\circ : \phi_{max} + 0.4^\circ]$. The value of $\pm 0.4^\circ$ was chosen as it approximated the average distance between USArray seismometers along lines of latitude and longitude ($\sim$70 km - $\sim$100 km). The boundary edges thereby define where we expect to find the next seismometer and thus the next Voronoi centre. By tapering the outermost points to 0 we reduce some of the error associated with this arbitrary boundary selection.

2. Seismometers that lie outside of the stationary phase region. The cosine tapers prevent the values of the integrand from backbone seismometers located closer to the boundary edges from dominating the SRI integral in Equation (2.31) over boundary S. Instead, contributions to this surface integral from points

within the stationary phase region are enhanced as the values of the integrands from backbone seismometers located towards the centre of the array provide the strongest contribution to the final SRI reconstructions.

Integrate

To complete the SRI process we evaluate the integral in Equation (2.31) by summing (integrating) over the regularly spaced grid of "interpolated" integrands. This becomes a summation over thousands to millions of points depending on the size of the defined rectangular patch, rather than a summation over just tens of seismometers which actually make up the backbone array. By Equation (2.31) selecting the acausal part of this final integration only and time-reversing the result thus approximates the earthquake response at the target sensor, $T(\mathbf{s})G(\mathbf{r},\mathbf{s})$. In the case where the target sensor was not deployed when the earthquake occurred, this is a new seismogram constructed retrospectively from only ambient noise recordings and recordings of the earthquake on a backbone seismometer array. The real earthquake response recorded on the target sensor is not required nor ever used to create the SRI reconstruction.

Importance of Voronoi cells in earthquake seismology

We find that embedding backbone seismometer arrays within a rectangular patch of 2D spatial Voronoi cells greatly improves the evaluation of SRI surface integrals in an earthquake seismology setting; this is further justified in Chapter 4 by a worked example that reconstructs earthquake seismograms by SRI with and without Voronoi interpolation. It is not uncommon for seismometers to be inactive for periods of time due to instrument error or instrument downtime during maintenance. With the exception of seismic arrays such as USArray, it is also common for seismometers to be distributed irregularly throughout a region, with greater concentrations of seismometers existing in tectonically active regions and far fewer seismometers existing in seismically quiescent zones. Voronoi cells allow us to compensate for these spatial irregularities by interpolating existing data into nearby surrounding regions where data is missing/not available. This is likely to be a useful methodology in other areas of seismology that require spatial integrations on receiver arrays, such as migration based imaging methods.

3.7 Justification of the Station Criteria for SRI

Finally we provide a justification of the 4 criteria outlined in Section 3.6.1 that determine the selection of stations for use in SRI. The station criteria were chosen following trial and error test on a selection of inter-station geometries. All geometries satisfied the source and receiver geometry for correlation-correlation SRI as shown schematically in Figure 3.8A, but the final criteria equally applies to the geometry in Figure 3.8B pertaining to correlation-convolution SRI. The final criteria are also represented schematically in Figure 3.9 for a backbone seismometer array located close ($<$ 540 km) to a target sensor.

3.7.1 Criteria 1-3

The first two conditions involving the orientation of the GCP allow us to approximate the integrals in Equation (2.25) with their approximations using only monopoles in Equations (2.27) and (2.28). This is because these approximations require that the waves from the earthquake traverse the receiver boundary approximately perpendicularly. Also, for the stationary phase approximation to become valid, the backbone array seismometers need to lie within the correct angular aperture of the GCP. In addition if the distance d between the target sensor and the backbone array is relatively small, the length of the array needed will be smaller than that needed if d is large. We neglect the stationary phase region of the source boundary S' as we are using uncorrelated noise sources and we assume the energy from them to be propagating from all azimuths.

Third, the deployment dates of the backbone array seismometers and target sensors must coincide by at least six months. Cross-correlation of the time-averaged recordings of ambient seismic noise over this period allows us to construct approximate estimates of the inter-receiver Green's functions between the target sensors and all backbone array seismometers.

3.7.2 Criterion 4

We now consider the distribution and number of backbone array seismometers that are needed to construct accurate SRI seismograms. The final spatial criteria decided upon, illustrated schematically in Figure 3.9, shows that when an array of potential backbone seismometers lies close to the target sensor (within 540 km), those seismometers

that make up the final backbone array should be located on average between 210 km and 540 km from the target sensor and combined they should comprise two approximately parallel lines of seismometers. For the distributions of USArray seismometers used herein, this corresponded to 12-14 seismometers. To obtain this final criteria we analysed different combinations of backbone seismometers and used these combinations to construct SRI seismograms of two earthquakes on up to seven target sensors. For example, we aimed to reconstruct the earthquake seismograms from a magnitude 5.5 event that occurred in Mexico and a magnitude 5.8 event that occurred in Guerrero, Mexico. The earthquake locations, the target sensors and the backbone array seismometers used for these studies are shown in Figure 3.11. To fully understand the effects of different seismometer combinations and distributions on the results of SRI, we do not interpolate the integrands of Equation (2.31) to points within Voronoi cells. Instead a simple integration (summation) is performed over the individual values of the integrands. We expect Voronoi interpolation of the integrands to improve the results of SRI on most occasions.

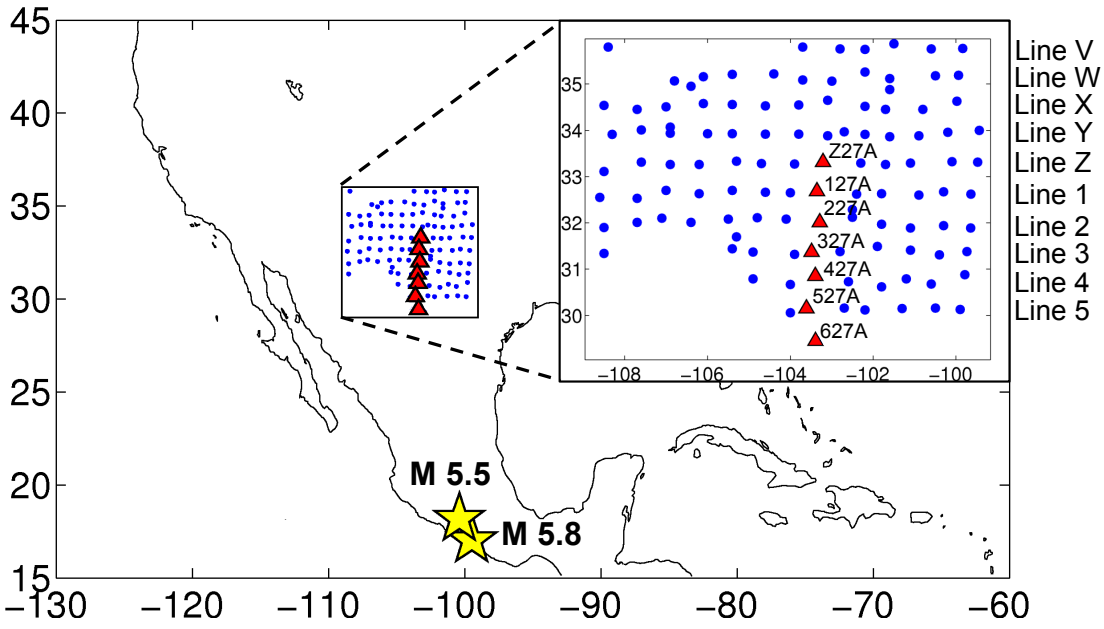

Figure 3.11: Source and receiver geometries for two earthquakes (stars) located in Mexico. Correlation-correlation SRI as in Equation (2.31) and Figure 3.8A is performed to construct seismograms of the events on the seven target sensors (triangles) using combinations of lines of seismometers from within the backbone array (circles).

Test 1

First we consider the M 5.5 earthquake and construct SRI seismograms at each of the seven target sensors using correlation-correlation SRI and *all* of the seismometers within the backbone array that pertain to the geometry for correlation-type interferometry: at target sensor 627A we use all backbone array seismometers shown, whilst at target sensor Z27A we only use those seismometers along lines V, W, X and Y. Thus, to correctly apply correlation-correlation SRI as in Figure 3.8A we use only those backbone seismometers that lie to the North of each target sensor. Applying SRI for each target sensor and its corresponding set of backbone array seismometers constructs the SRI seismograms shown in Figure 3.12. Here they are compared with the real recordings of the event on the same target sensors and we observe that the match is poor, with the SRI reconstructions exhibiting non-physical arrivals prior to the main surface wave arrivals. The surface waves are poorly constructed on all target sensors, with the exception of target sensor 127A where the SRI seismogram is constructed fairly well. Here we attribute this success to the orientation of the GCP that intersects both the location of 127A and the backbone array seismometers that are located north of the target sensor. This GCP is shown in Figure 3.13A and it approximately intersects the centre of the backbone array, with almost equal numbers of the array seismometers being distributed on either side of the GCP. The stationary phase region of the receiver boundary S is thus approximated more successfully. By comparison, the distribution of backbone array seismometers around the GCP that intersects target sensor 627A and its backbone array is biased, with more array seismometers being located to the East of the GCP than to the West. This irregular distribution of array seismometers can be seen in Figure 3.13B. Such spatial irregularities within the backbone array thus appear to introduce non-physical arrivals into the SRI reconstructions as all stationary phase points of the receiver boundary S are not occupied and the integral over S is not evaluated correctly. Similar observations have been made by Halliday and Curtis (2008, 2009) for incomplete source boundaries.

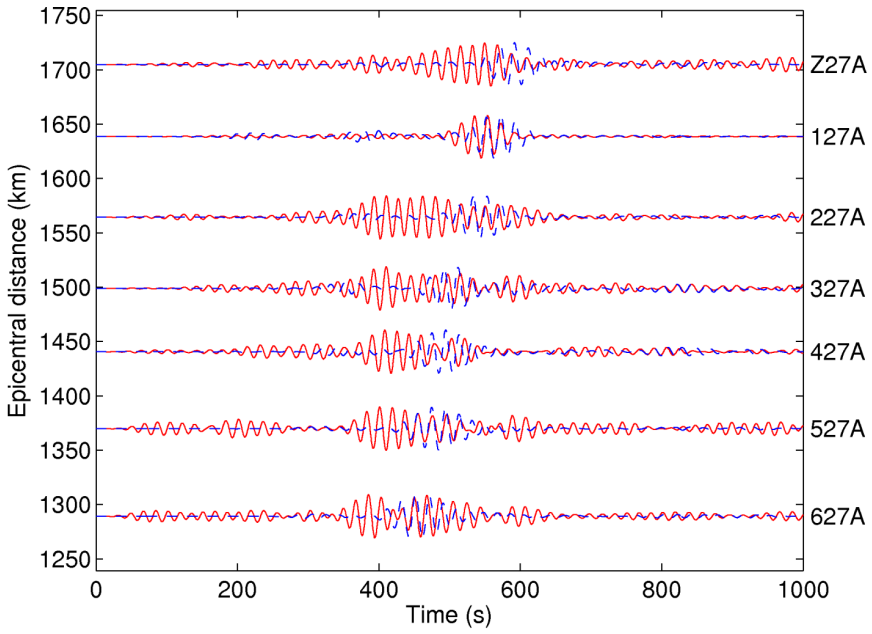

Figure 3.12: Reconstructions of the M 5.5 Mexico earthquake using correlation-correlation SRI (solid/red lines) compared with the real recordings of the event (dashed/blue traces) at target sensors Z27A-627A. All backbone array seismometers shown in Figure 3.11 that pertain to the geometry for correlation-type interferometry are used to construct the SRI seismograms at each target sensor, such that all array seismometers that lie to the North of each target sensor are used in the SRI reconstruction at that sensor.

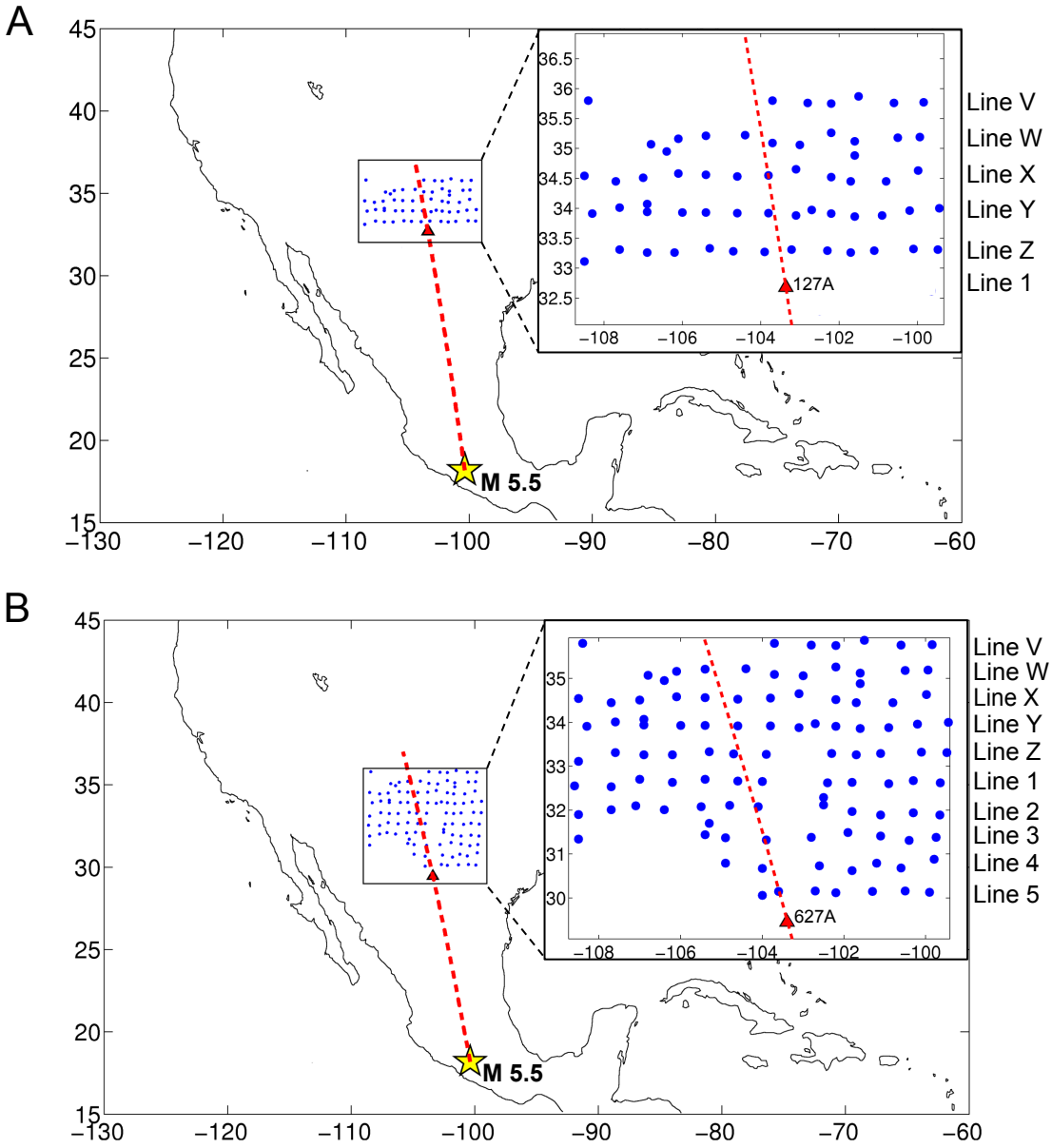

Figure 3.13: The source and receiver geometries for the M 5.5 Mexico earthquake (star) constructed at (A) target sensor 127A and (B) target sensor 627A (triangles) using the backbone array seismometers shown (circles). The SRI seismograms constructed at 127A and 627A using these corresponding geometries are shown in Figure 3.12 (second trace from top (127A) and bottom trace (627A)). The great circle paths (GCP) from the earthquake epicentre that intersect the target sensors and the backbone arrays approximately perpendicularly are shown (dashed lines).

Test 2

Next we consider using three lines of seismometers from within the backbone array to construct the SRI seismograms of the M 5.5 earthquake on all target sensors. We use the same three lines of seismometers for each reconstruction and correlation-correlation SRI. We use those seismometers along lines W, X and Y as they lie to the North of all target sensor locations and adhere to correlation-type interferometry. The SRI seismograms are compared with the real recordings of the event in Figure 3.14. Again, we observe that SRI does not successfully construct the true earthquake seismograms at the target sensors. Non-physical arrivals are present before the main surface waves, the arrival times of which are again poorly constrained. Comparing Figure 3.14 with Figure 3.12 we observe very little change in the reconstruction at 127A, which is still constructed well compared to the other SRI seismograms.

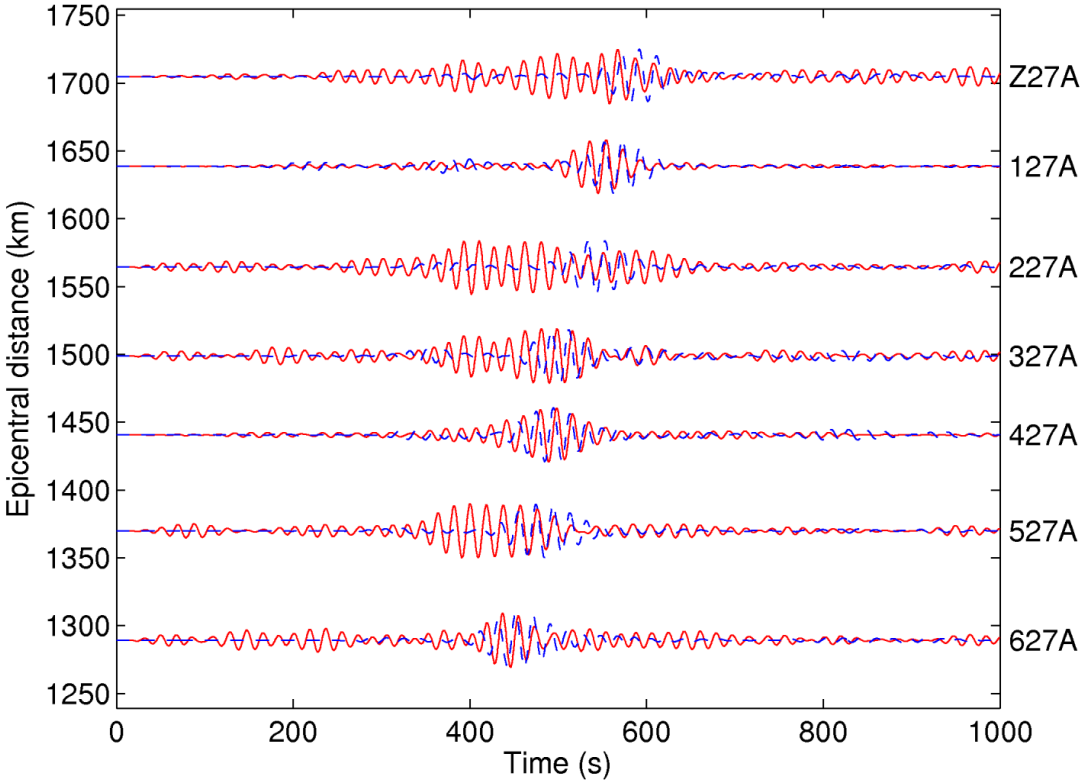

Figure 3.14: As in Figure 3.12 but SRI seismograms are constructed using only those backbone array seismometers located along lines W, X and Y.

Test 3

The SRI reconstruction at target sensor 127A was a close match to the real earthquake signals recorded on that same sensor when using seismometers along lines W, X and Y in Test 2. However, the SRI seismograms constructed at Z27A and 227A (the two target sensors located directly to the North and South of 127A, respectively) were far from perfect using those same three lines of seismometers. It was thus apparent that the backbone seismometers selected for any one SRI reconstruction at a target sensor should be unique for that target sensor, and the distance (and hence aperture) of the backbone array from the target sensor was important. In an attempt to improve the SRI reconstruction at target sensor 127A even further, just two lines of backbone array seismometers were chosen in this next test.

These backbone seismometers were located along lines W and X. The seismometers along line Y were not used as the result of the previous test at target sensor Z27A appears to show that if seismometers are located too close to the target sensors, non-physical arrivals are introduced. Thus, for each SRI reconstruction we will use lines of seismometers that lie approximately between 210 km and 540 km from the target sensors (the approximate distance between target sensor 127A and seismometers located along lines W and X). Due to the regular spacing of seismometers within the USArray network, this distance range covers seismometers located within two approximately East-West lines, and the seismometers selected for a target sensor are always located two lines from that target sensor (a distance of $\sim$ 200 km). Thus, to construct the SRI seismogram at target sensor Z27A we used the seismometers along the two northernmost lines of the array along lines V and W (two lines of seismometers (lines X and Y) are located between the backbone seismometers selected and target sensor Z27A); at target sensor 127A we used the seismometers along lines W and X; and so on until the SRI seismogram constructed at target sensor 627A used backbone array seismometers located along lines 2 and 3. Backbone seismometers along lines 4 and 5 are unused. Again, see Figure 3.11 for the locations of all backbone array seismometers, the lines they occupy and the target sensors.

A comparison of real and SRI seismograms constructed at each of the seven target sensors using these 2-line combinations of backbone seismometers is shown in Figure 3.15 and the two lines of seismometers used for each reconstruction is detailed in the figure. We observe a good match between the two traces recorded/constructed at

each target sensor. Many of the non-physical arrivals present in Figures 3.12 and 3.14 have been suppressed in this example, and the main surface wave arrivals constructed using SRI are in phase with the real recordings. The SRI seismograms are still far from perfect reconstructions of the real earthquake records at some of the target sensors. We consider one possible explanation for these misfits to be due to spatial irregularities within the two lines of array seismometers used for the reconstructions. For example, the main surface waves at sensors Z27A and 627A are not as well constrained as at other target sensors, and we observe large gaps in the two lines of seismometers used for these reconstructions, i.e., there are seismometers missing along Line V for the reconstruction at Z27A and along Line 3 for the reconstruction at 627A. The effects of such spatial irregularities within the backbone array are discussed in more detail in Chapters 4 to 6, but we note that the interpolations of the integrands of Equation (2.31) to points within Voronoi cells go some way to reducing these effects in the real data applications.

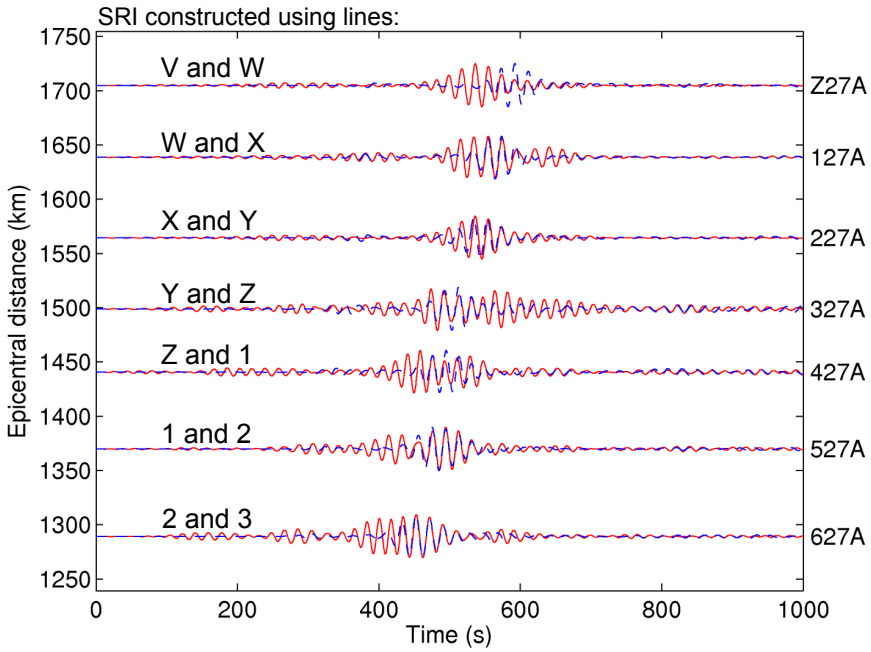

Figure 3.15: As in Figure 3.12 but SRI seismograms are constructed using seismometers along 2-line combinations of the backbone array shown in Figure 3.11. At target sensor Z27A we use those seismometers along lines V and W; at target sensor 127A we use those seismometers along lines W and X; and so on, until at target sensor 627A we use those seismometers along lines 2 and 3. These 2-line combinations of seismometers define our final spatial criteria described in Section 3.6.1, such that backbone array seismometers located between approximately 210 km and 540 km from a target sensor are used to construct the SRI seismogram at that sensor's location.

Test 4

In one final comparison of real and SRI seismograms of the M 5.5 earthquake, we consider just those backbone seismometers located along Line 2 (which is a complete line of seismometers with few spatial irregularities) and use them to construct the SRI seismogram at target sensor 527A. This SRI construction is compared with the real recording in Figure 3.16A and we observe that the main surface wave is in phase with the real recording. However, there are additional large amplitude arrivals prior to this main arrival at ∼150 s and ∼300 s. In Figure 3.16B we show the SRI seismogram constructed at target sensor 527A using the two lines of backbone array seismometers that satisfy the final spatial criteria (seismometers along lines 1 and 2). This reiterates that using a 2-line combination of backbone seismometers constructs the most reliable SRI seismograms.

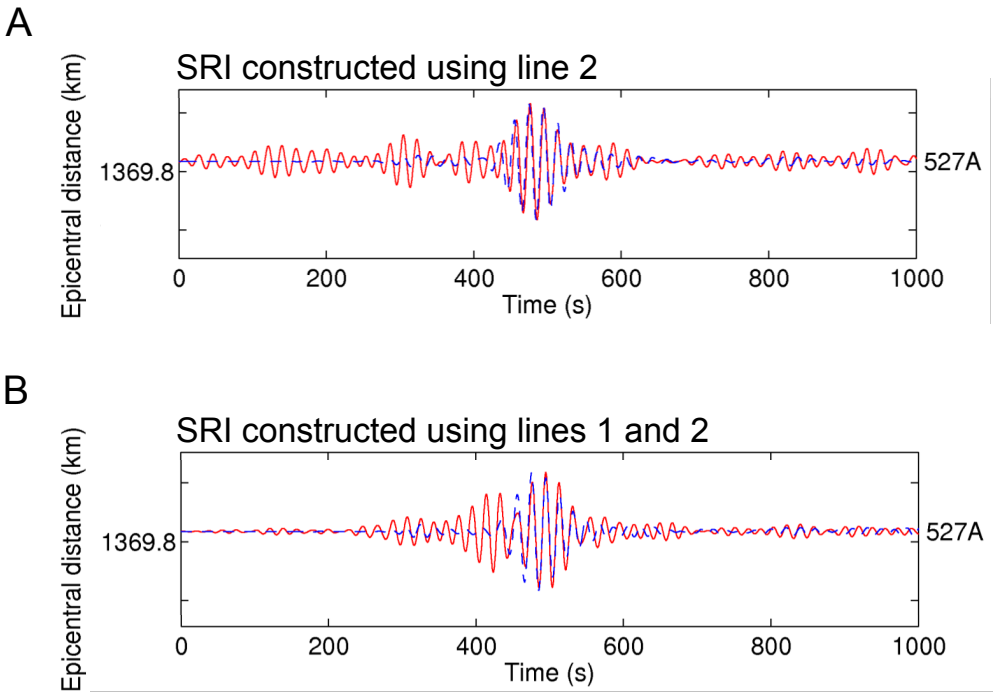

Figure 3.16: As in Figure 3.12 for target sensor 527A only. (A) SRI seismogram constructed using only those seismometers in Figure 3.11 that lie along Line 2. (B) SRI seismogram constructed using the two lines of seismometers along lines 1 and 2 of the backbone array that satisfy the final spatial criteria described in Section 3.6.1.

Test 5

Finally, we provide one similar test using the M 5.8 Guerrero earthquake. We construct the SRI seismogram at target sensor 627A using three lines of backbone array seismometers, and compare this construction to the SRI seismogram constructed by satisfying the final spatial criteria determined from the previous studies. These SRI seismograms are shown in Figure 3.17A and B, respectively, and are compared with the real recording of the M 5.8 earthquake at sensor 627A. Again, we observe that using 2-line combinations of backbone seismometers constructs a good SRI seismogram (Figure 3.17B). The surface wave is clearly constructed and there are few non-physical arrivals prior to this main event. When using an additional line of seismometers to construct the SRI seismogram however (Figure 3.17A), we observe a much poorer reconstruction as the main surface wave arrival time cannot be accurately estimated without the real recording for guidance.

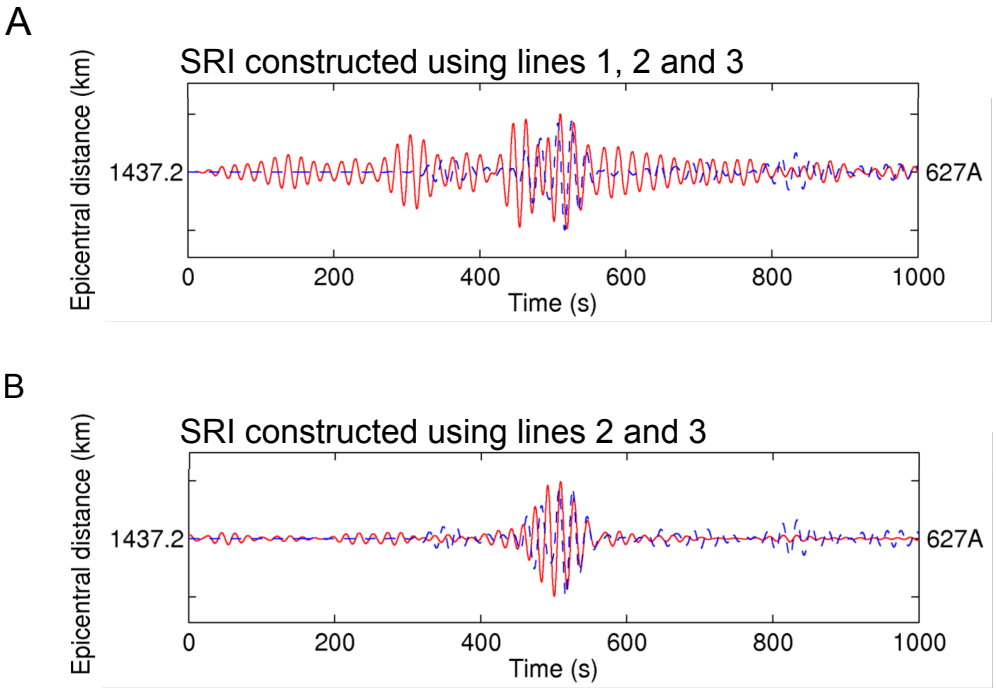

Figure 3.17: Reconstructions of the M 5.8 Guerrero earthquake using correlation-correlation SRI (solid/red lines) compared with the real recording of the event (dashed/blue traces) at target sensor 627A. (A) SRI seismogram constructed using the backbone array seismometers in Figure 3.11 that lie along lines 1, 2 and 3. (B) SRI seismogram constructed using the two lines of seismometers along lines 2 and 3 of the backbone array that satisfy the final spatial criteria described in Section 3.6.1.

3.7.3 Summary

We have shown that if the final spatial criteria outlined in Section 3.6.1 are used to select backbone array seismometers for SRI, accurate SRI seismograms can be constructed on target sensors located 'close' to the backbone array (within 540 km for the station geometries considered here). Throughout this thesis we thus adhere to these criteria when selecting backbone array seismometers for SRI at this small length scale. When the target sensors are located at larger distances from the backbone arrays the criteria are relaxed. We still use two lines of seismometers to construct the SRI seismograms, but the inter-station distances are not restricted. We do note however that the quality of inter-receiver Green's functions decreases when constructed over large inter-station distances. This was described earlier in Section 3.3 and should thus be considered when selecting backbone array seismometers that are located more than 1200 km from the target sensor at which one would like to construct a new SRI seismogram.

3.8 Chapter Summary

To summarise, this Chapter provides a comprehensive review of the methodologies developed and fine-tuned throughout this PhD. They are applied to real noise and earthquake datasets in Chapters 4 to 7.

Section 3.2 details a methodology to accurately perform inter-receiver interferometry using ambient seismic noise data. We start with station selection and data download before discussing the filtering of the data and temporal and spectral normalisation. Estimated Green's functions are constructed through processes of cross-correlation and stack summation. Quality control checks are described and applied to cross-correlated data pre- and post-stack. In Section 3.3 we provide a brief discussion on the quality of the estimated Green's functions constructed over varying inter-station distances using this method, focussing on signal-to-noise ratios and root-mean-square values of estimated signal windows.

In Section 3.4 we introduce an alternative method to Green's function estimation by cross-correlation or convolution: multidimensional deconvolution (MDD). This method uses cross-correlations of real earthquake data as opposed to ambient noise, thus reducing the amount of data required, and deconvolves a particular point-spread function. It is however more computationally intensive as it involves matrix inversion

by singular value decomposition. A practical application of MDD is presented in Chapter 7.

Finally, Section 3.6 details a methodology to most accurately perform source-receiver interferometry (SRI) using ambient seismic noise data and real earthquake seismograms. We start by defining a more complex set of criteria to be used for station selection, which is reviewed in Section 3.7. The methodology for noise interferometry developed in Section 3.2 is then incorporated to construct the estimated Green's functions (the SRI propagators) between "target" sensors and seismometers from within a backbone array. Here we focussed on methods of cross-correlation to perform inter-source interferometry but convolution can also be used. This will be discussed and applied in detail in Chapter 5. We find SRI surface integrals are improved by evaluating the integrals over 2D spatial Voronoi cells containing fine-scale grids of points. The construction of Voronoi cells and their importance and relevance in earthquake seismology studies are discussed in Section 3.6.5, and their use in SRI are detailed in Chapters 4 to 6.

These methodologies have been tried and tested using seismometers from the dense and reliable Transportable and Reference arrays within the USArray seismic network, although theoretically they can be applied to any earthquake seismology dataset. Steps in the methodologies can be reduced significantly when using exploration seismology data: replacing ambient noise data with active transient sources eliminates the need to temporally and spectrally normalise the data. Quality control checks could still be performed but SNR cut-off values would need to be modified from the values presented herein. Since receiver arrays are often regularly spaced in exploration experiments, Voronoi cells are not required to improve the SRI surface integral over the receiver boundary. Instead, we show in Section 4.4.1 that direct summation over all receiver positions within a backbone array accurately constructs the response from an active seismic shot at new target receiver locations.

Bibliography

Baptie, B. (2010), Lava dome collapse detected using passive seismic interferometry, Geophysical Research Letters, 37, doi:{10.1029/2010GL042489}.

Bensen, G. D., M. H. Ritzwoller, M. P. Barmin, A. L. Levshin, F. Lin, M. P. Moschetti, N. M. Shapiro, and Y. Yang (2007), Processing seismic ambient noise data to obtain reliable broad-band surface wave dispersion measurements, Geophysical Journal International, 169(3), 1239–1260, doi:{10.1111/j.1365-246X.2007.03374.x}.

Bensen, G. D., M. H. Ritzwoller, and N. M. Shapiro (2008), Broadband ambient noise surface wave tomography across the United States, Journal of Geophysical Research - Solid Earth, 113(B5), doi:{10.1029/2007JB005248}.

Curtis, A., and D. Halliday (2010), Source-receiver wave field interferometry, Physical Review E, 81(4, 2), doi:{10.1103/PhysRevE.81.046601}.

Derode, A., E. Larose, M. Tanter, J. de Rosny, A. Tourin, M. Campillo, and M. Fink (2003), Recovering the Green's function from field-field correlations in an open scattering medium (L), Journal of the Acoustical Society of America, 113(6), 2973–2976, doi:{10.1121/1.1570436}.

Halliday, D., and A. Curtis (2008), Seismic interferometry, surface waves and source distribution, Geophysical Journal International, 175(3), 1067–1087, doi:{10.1111/j.1365-246X.2008.03918.x}.

Halliday, D., and A. Curtis (2009), Seismic interferometry of scattered surface waves in attenuative media, Geophysical Journal International, 178(1), 419–446, doi:{10.1111/j.1365-246X.2009.04153.x}.

Lin, F., M. H. Ritzwoller, J. Townend, S. Bannister, and M. K. Savage (2007), Ambient noise Rayleigh wave tomography of new Zealand, Geophysical Journal International, 170(2), 649–666, doi:{10.1111/j.1365-246X.2007.03414.x}.

Nicolson, H., A. Curtis, B. Baptie, and E. Galetti (2012), Seismic interferometry and ambient noise tomography in the British Isles, Proceedings of the Geologists Association, 123(1), 74–86, doi:{10.1016/j.pgeola.2011.04.002}.

Nicolson, H., A. Curtis, and B. Baptie (2014), Rayleigh wave tomography of the British Isles from ambient seismic noise, Geophysical Journal International, 198(2), 637–655, doi:{10.1093/gji/ggu071}.

Sambridge, M. (1999a), Geophysical inversion with a neighbourhood algorithm - I. Searching a parameter space, Geophysical Journal International, 138(2), 479–494, doi:{10.1046/j.1365-246X.1999.00876.x}.

Sambridge, M. (1999b), Geophysical inversion with a neighbourhood algorithm - II. Appraising the ensemble, Geophysical Journal International, 138(3), 727–746, doi:{10.1046/j.1365-246x.1999.00900.x}.

Sambridge, M., J. Braun, and H. McQueen (1995), Geophysical Parametrization and Interpolation of Irregular Data Using Natural Neighbors, Geophysical Journal International, 122(3), 837–857, doi:{10.1111/j.1365-246X.1995.tb06841.x}.

Shapiro, N. M., and M. Campillo (2004), Emergence of broadband Rayleigh waves from correlations of the ambient seismic noise, Geophysical Research Letters, 31(7), doi:{10.1029/2004GL019491}.

Shapiro, N. M., M. Campillo, L. Stehly, and M. H. Ritzwoller (2005), High-resolution surface-wave tomography from ambient seismic noise, Science, 307(5715), 1615–1618, doi:{10.1126/science.1108339}.

Shapiro, N. M., M. H. Ritzwoller, and G. D. Bensen (2006), Source location of the 26 sec microseism from cross-correlations of ambient seismic noise, Geophysical Research Letters, 33(18), doi:{10.1029/2006GL027010}.

Snieder, R. (2004), Extracting the Green's function from the correlation of coda waves: A derivation based on stationary phase, Physical Review E, 69(4, 2), doi:{10.1103/PhysRevE.69.046610}.

Stehly, L., M. Campillo, and N. M. Shapiro (2007), Traveltime measurements from noise correlation: stability and detection of instrumental time-shifts, Geophysical Journal International, 171(1), 223–230, doi:{10.1111/j.1365-246X.2007.03492.x}.

CHAPTER 4

Source-Receiver Interferometry Using A Joint Correlation-Correlation Approach[1]

4.1 Outline

If energy emitted by a seismic source such as an earthquake is recorded on a suitable backbone array of seismometers, source-receiver interferometry (SRI) is a method that allows those recordings to be redatumed (projected) to the location of another target seismometer, thus providing an estimate of the seismogram that would have been recorded at that location. Since the other seismometer may not have been deployed at the time the source occurred, this renders possible the concept of "retrospective seismology" whereby the installation of a sensor at one period of time allows the construction of virtual seismograms as though that sensor had been active before or after the period of its installation. Here we show that such virtual seismograms can be constructed on target sensors in both industrial seismic and earthquake seismology settings, using both active seismic sources and ambient seismic noise to construct projection operators. In each case we compare seismograms constructed at target sensors by SRI to those actually recorded on the same sensors. First we test the method using active seismic shots recorded on a linear backbone array of 24 receivers located up to 62 m from six target sensors. Then we use earthquake data and

[1]Combined with Chapter 5, this chapter has been submitted to the Journal of Geophysical Research. Co-authors: Andrew Curtis - *University of Edinburgh*; Erica Galetti - *University of Edinburgh*; Giovanni Meles - *University of Edinburgh*; Brian Baptie - *British Geological Survey*. Section 4.4.1 was wholly undertaken by Erica Galetti.

ambient seismic noise recorded on an irregular backbone array of seismometers located between approximately 210 km and 540 km from seven target sensors. Finally we use ambient seismic noise and earthquake data recorded on a backbone seismometer array located up to 1920 km from three target sensors in the western US. We show that spatial integrations required by interferometric theory can be calculated over our irregular seismometer arrays by embedding these arrays within 2D spatial Voronoi cells to improve spatial interpolation. We also reconstruct virtual seismograms at sensors that were previously active but were subsequently removed before the earthquake events occurred; thus we create truly novel virtual seismograms at those sensors, retrospectively.

4.2 Introduction

Traditional seismology uses the propagation of elastic waves from large earthquakes or explosions to infer earthquake or Earth properties and structure. This encouraged the deployment of seismometer networks worldwide, particularly in regions of high seismicity. However, earthquake seismogram data are only sensitive to Earth properties on paths of energy propagation between earthquakes and seismometers. Recent developments in the field of seismic or wavefield interferometry (sometimes referred to as Green's function estimation) create new data types that are sensitive to a variety of different spatial volumes using the same seismometer networks and seismic source distributions (for reviews see Curtis et al. (2006); Wapenaar et al. (2010a,b); Galetti and Curtis (2012)). These seismic interferometry methods were introduced theoretically in Chapter 2 and their practical methodologies were described in detail in Chapter 3. Here we investigate the method of source-receiver interferometry (SRI), on a range of spatial and (novelly) temporal scales.

SRI can be derived either directly from representation theorems (Curtis and Halliday, 2010; Halliday and Curtis, 2010), or by combining the theories of inter-receiver and inter-source interferometry (Curtis, 2009; Curtis et al., 2012). The result is that a Green's function between a source and a receiver can be constructed from data recorded from a set of other sources on an array of other receivers (herein referred to as a backbone array). As described in Chapter 1 this has led to the development of methods which use SRI for some form of spatial redatuming of recorded data. Earlier we also introduced SRI as a method for *temporally* redatuming seismic data (Curtis et al., 2012).

In this chapter we expand on the work of Curtis et al. (2012) by reconstructing active source signals using SRI, in three seismic experiments spanning three different length scales. Each length scale is determined by the distance between a new, "target" sensor and a backbone array of receivers that recorded the source energy. Here we focus only on correlation-correlation SRI. An application of correlation-convolution SRI is presented in Chapter 5.

4.3 Method

Consider the geometry for correlation-correlation SRI in Figure 4.1:

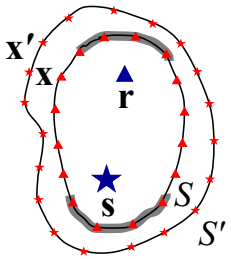

Figure 4.1: One possible geometry for correlation-correlation SRI. Stars are sources, triangles are receivers. The grey shaded regions highlight schematically the stationary phase regions on the receiver boundary S which contribute constructively to energy in SRI integrals; only one or other stationary phase region need be used provided back-scattered energy is weak across the boundary, but we discuss the case where both regions are occupied and the extra information this provides in Section 4.6. For full derivations of the SRI integral pertaining to this geometry see Curtis and Halliday (2010).

A source $\mathbf{s}$ and receiver $\mathbf{r}$ are surrounded by a boundary of receivers $\mathbf{x}$ on S and a boundary of sources $\mathbf{x}'$ on S'. The aim of correlation-correlation SRI is to estimate the response from the source at $\mathbf{s}$ on the receiver at $\mathbf{r}$ without ever recording that response directly. In overview, this may be achieved by a 2-step process (Curtis et al., 2012): 1) An Inter-receiver interferometry step constructs estimates of the Green's functions $G(\mathbf{x}, \mathbf{r})$ between the backbone array seismometers (at locations $\mathbf{x}$) and the target sensor (at $\mathbf{r}$). These Green's functions are called the *propagators* in SRI and are constructed as in Equation (2.28). 2) These propagators are used to project the recordings of the energy source $G(\mathbf{x}, \mathbf{s})$ on the backbone array to the location of the target sensor: this is achieved by performing inter-source interferometry between the real source and the target sensor (now a virtual source) as in Equation (2.27). Combining the theories of

inter-receiver and inter-source interferometry in this way is one possible derivation of correlation-correlation SRI, as introduced in Section 2.4.

The specifics of the method differ between the small length scale, engineering seismology example and the larger length scale, earthquake seismology examples due to the available data. We shall discuss each in turn in Sections 4.4.1 and 4.5, respectively, referring to the theoretical equations in Chapter 2 and the methodologies in Chapter 3 where necessary.

4.4 Application at Exploration Seismology Scale

4.4.1 Example 1 at a short scale

We applied correlation-correlation SRI to construct the seismogram between an active source and a number of receivers in a small exploration or engineering scale seismic experiment performed in the field adjacent Schlumberger Gould Research (Duguid et al., 2011). The acquisition geometry is shown in Figure 4.2: active seismic sources consisting of an accelerated weight drop, were placed at intervals of 4 m along the running-track shaped boundary S'. This boundary encloses a grid of receivers, some of which we use as target sensors, and a receiver line S which acted as the backbone array in this case. Active shots were also recorded at all receiver positions from a source at location $\mathbf{s}$. Our goal is to construct seismograms from source $\mathbf{s}$ on target receivers $\mathbf{r}_i$ using correlation-correlation SRI, and compare these to the real recordings.

We constructed the seismograms between source $\mathbf{s}$ and receivers $\mathbf{r}_i$ by applying correlation-correlation SRI using Equations (2.27) and (2.28), and without using the direct recordings of the source on $\mathbf{r}_i$. Thus we simulate the case where the source at $\mathbf{s}$ was fired before or after the period during which the receivers at $\mathbf{r}_i$ were installed, and hence where the source was only recorded on the backbone receiver boundary S. This was achieved by first using seismic energy propagating from sources on boundary S' to estimate the Green's function propagators between $\mathbf{r}_i$ and S, thus turning receivers $\mathbf{r}_i$ into virtual sources recorded by receivers on S using inter-receiver interferometry as in Equation (2.28). We then redatum the signals from the backbone array S to the target sensors $\mathbf{r}_i$, turning the virtual sources at $\mathbf{r}_i$ into virtual receivers using inter-source interferometry as in Equation (2.27).

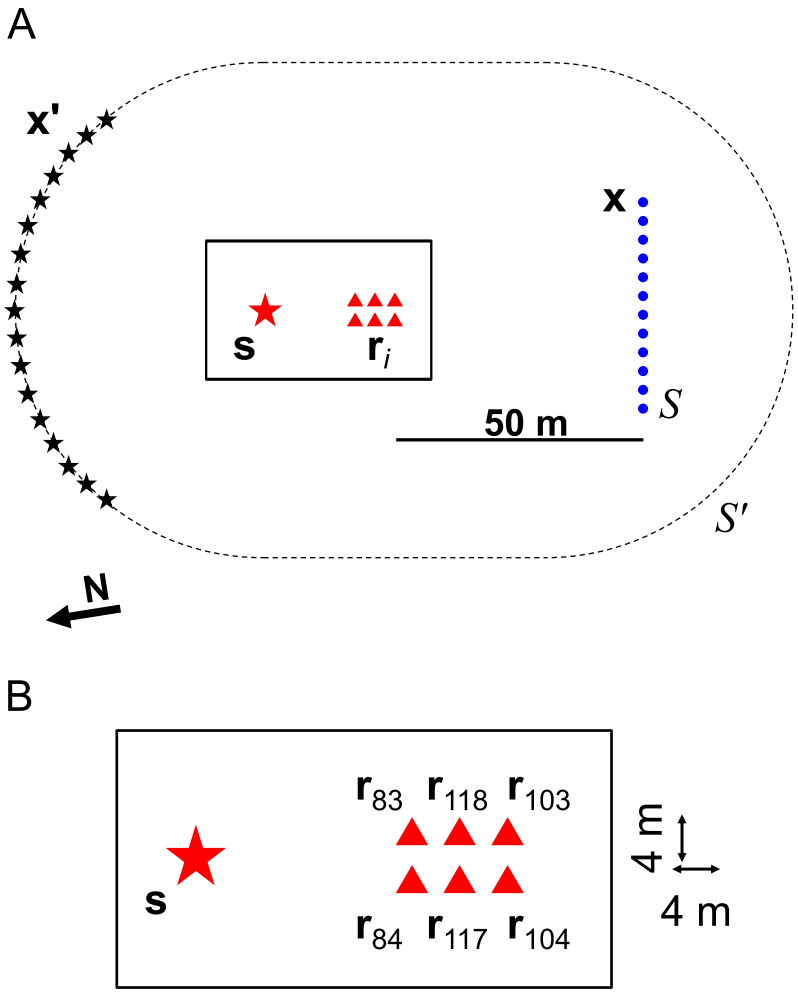

Figure 4.2: Geometry for the small-scale seismic experiment. (A) Active sources are located along the dashed boundary S' (small stars) and at position $\mathbf{s}$ (large star). Receivers are located along line S (circles - every second receiver is shown here for clarity) and at points $\mathbf{r}_i$ (triangles) close to the source at $\mathbf{s}$. Only those boundary sources located around the stationary-phase region of S' are used (small stars). (B) Magnified view of the target receivers marked by triangles and the active source: results for these receivers are shown in Figure 4.3.

The active-source data were acquired at 250 Hz in a field adjacent to Schlumberger Gould Research (SGR) in July 2010. As different types of geophones were deployed during acquisition (with responses centred at 4.5 Hz, 10 Hz and 14 Hz in the target sensors, and at only 4.5 Hz at receiver line S), transfer functions from 4.5 Hz to 10 Hz, and from 14 Hz to 10 Hz were estimated from the recorded data and applied to the 4.5 Hz and 14 Hz data before any subsequent processing (Duguid et al., 2011). In order to ensure coherency in the frequency content across all receivers, the data from boundary S' was filtered between 8 Hz and 22 Hz before the inter-receiver step. In accordance with the stationary-phase principles of Snieder (2004), only a subset of boundary sources providing a constructive contribution to the inter-receiver Green's functions was used (see Figure 4.2). Before the inter-source step, a second filter (15.5 Hz - 20 Hz) was applied to the signals recorded by the backbone array, and to those recorded from the active source $\mathbf{s}$ at the receivers $\mathbf{r}_i$, as this was the only frequency band with significant energy that overlapped between all signals.

The results of SRI for the six receivers $\mathbf{r}_i$ are shown in Figure 4.3. The dominant arrival is the emerging surface wave (ground roll) which can be seen to move out from the source for increasingly distant receivers. The match is not perfect, and this is likely partly because the equations for correlational interferometry assume an elastic (non-attenuating) medium which is an approximation. Also, similar weight drop sources were used at locations $\mathbf{x}'$ and $\mathbf{s}$: thus in the first step of interferometry both Green's functions on the right of Equation (2.28) are in fact convolved with the source time function and the result on the left will therefore be multiplied by the source power spectrum. This extra factor is then multiplied into the SRI result in Equation (2.27), but will not be present in the real recording. Of course, since we have both the real recordings and the SRI seismograms at receivers $\mathbf{r}_i$ in this case, in principle we could divide one by the other to obtain the source power spectrum. We do not produce this here as first it assumes a non-attenuative medium, and second we focus on testing the case where we do not have any direct recordings at $\mathbf{r}_i$.

Nevertheless, in all cases the match between the real and SRI traces is reasonably good, showing the reliability of the method in a controlled experiment when an ideal geometry of sources and receivers is available. In the next sections, we apply the principles of SRI and retrospective seismology to less controlled scenarios in earthquake seismology, showing the potential of this method when the distribution of sources and receivers is far from perfect.

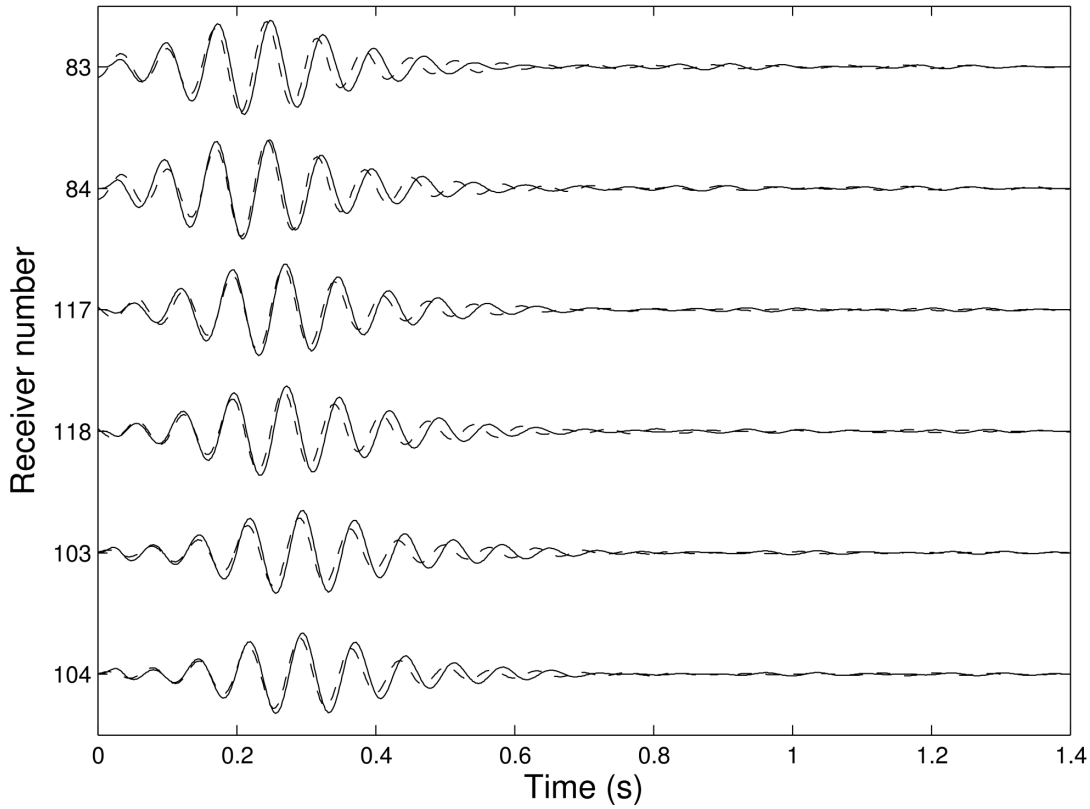

Figure 4.3: Comparison of surface wave (ground roll) seismograms constructed using correlation-correlation SRI (solid traces) with the real recordings (dashed traces) at the target sensors $\mathbf{r}_i$ shown in Figure 4.2B. All seismograms are bandpassed in the frequency range 15.5 Hz - 20 Hz, chosen because that contained all dominant amplitudes that were common to all recordings at $\mathbf{x}$ and $\mathbf{r}_i$ in Figure 4.2.

4.5 Applications in Earthquake Seismology

We now apply correlation-correlation SRI in two earthquake seismology settings using ambient wavefield fluctuations recorded on a backbone array of seismometers $\mathbf{x}$ and on target sensors $\mathbf{r}$, as described by Equations (2.14) and (2.31). We construct the seismograms from two earthquakes retrospectively, on two target sensors (seismometers) that were deployed and then removed before the earthquakes occurred, and thus which did not record the events. To test the robustness of the method, we also reconstruct the event seismograms on up to seven other target sensors that *were* operational at the time the earthquakes occurred, and compare the reconstructed seismograms with those actually recorded. The quality of the match between the real

and SRI seismograms constructed at any one target sensor is quantified by calculating the correlation coefficient across the lengths of the traces.

4.5.1 Data selection, processing and methodology

Here we use the exact methodologies as described in Chapter 3. Earthquakes, backbone seismometers and target sensors were chosen to obey the station criteria outlined in Section 3.6.1. Earthquake data and noise data were then downloaded and processed according to Sections 3.2.1 and 3.2.2.

First we use noise interferometry as in Equation (2.14) to construct the inter-receiver Green's functions $G(\mathbf{x}, \mathbf{r})$. These are our SRI propagators and are constructed in practice as described in Section 3.2. Second we perform inter-source interferometry as described mathematically by Equation (2.31) and practically in Section 3.6.4. We evaluate the integral in Equation (2.31) by interpolating the values of the integrands for each $\mathbf{x}$ into 2D spatial Voronoi cells and integrating (summing) over all values as described in Section 3.6.5. This completes the correlation-correlation SRI process and we construct an estimate of the earthquake seismogram $R(\mathbf{r}, \mathbf{s})$ at the location of the target sensor $\mathbf{r}$ (as Equation (2.30) but for a single source $\mathbf{s}$, not a collection of sources on fault plane F).

4.5.2 Example 2 at an intermediate scale

We first reconstruct the seismograms from a magnitude 5.8 earthquake on eight target sensors using a backbone array comprising 93 seismometers that satisfied the spatial sampling criteria outlined in Section 3.6.1, and correlation-correlation SRI (Equations (2.14) and (2.31), Figure 4.1). The backbone array and the eight target sensors at which seismograms are constructed are shown in Figure 4.4. Earthquake signals are reconstructed at each of the eight sensors using combinations of seismometers on two lines located on average between approximately 210 km and 540 km from the sensors: the caption to Figure 4.4 states which lines were used for which target sensor. On average 22 seismometers are used for each reconstruction. Figure 4.4 shows the locations of the array seismometers within 2D spatial Voronoi cells. The number of seismometers available for each reconstruction varies depending on the deployment history of the seismometers and the outcome of the quality control checks. Each remaining backbone seismometer becomes a Voronoi cell centre, and 2-line combinations of Voronoi cells are used to interpolate across grids of square cells,

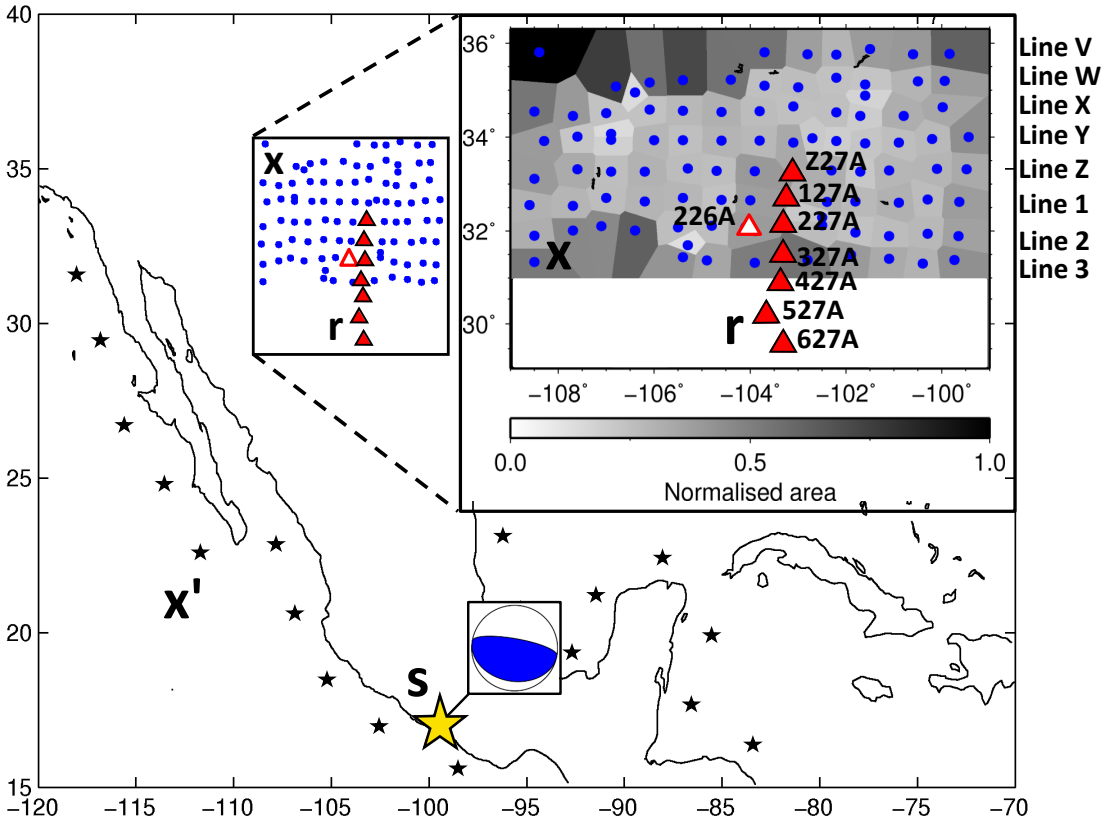

Figure 4.4: Source and receiver geometries used to reconstruct the virtual seismograms of the 27/04/2009 M 5.8 Mexico earthquake (large star with source mechanism) using correlation-correlation SRI (Figure 4.1). Ambient noise fluctuations from source locations such as $\mathbf{x}'$ (small stars in oceans) are recorded on the backbone seismometer array $\mathbf{x}$ (circles) and at the eight target sensors $\mathbf{r}$ (filled and unfilled triangles) located within New Mexico. The backbone array consists of eight approximately parallel lines of seismometers from Line V in the north of the array, to Line 3 in the south (the letters derive from station notation employed by the USArray Transportable Array and were described in Section 3.3). 2-line combinations of the backbone array seismometers are used to reconstruct the earthquake seismograms at each target sensor by interpolating interferometric integrals across the Voronoi cells shown in the figure (polygons - shaded according to their area). To reconstruct the virtual earthquake seismogram at sensor Z27A, only those seismometers along lines V and W comprise the backbone array; to reconstruct the virtual earthquake seismogram at sensor 127A, only seismometers along lines W and X comprise the backbone array; and so on, until the virtual earthquake seismogram at sensor 627A is reconstructed using an array comprised of seismometers from lines 2 and 3 only. This station selection was described and justified in Section 3.7.

the grid having dimensions between 1.5° - 1.8° in latitude and 7.7° - 9.9° in longitude. See Section 3.6.5 for a description of Voronoi cells and their use herein.

The final SRI seismograms are then compared with the real recordings of the event at seven of the target locations. The real seismograms and the SRI reconstructions are band-passed with corner frequencies at 0.04 Hz and 0.06 Hz to sample the frequency band where both the earthquake and noise spectra overlap with significant energy. SRI results and real earthquake recordings at all target sensors are plotted as a function of epicentral distance in Figure 4.5. The quality of the match between the real and SRI seismograms is quantified by the correlation coefficient as listed on the right, above each trace. The moveout of the main surface wave arrival with distance is clearly visible. Also, almost all of the main arrivals estimated using SRI are almost exactly in phase with the actual recorded seismograms at the same sensor (where the latter exists) and correlation coefficients reach values up to 0.92. Sensor 226A (unfilled triangle in Figure 4.4), was active prior to the earthquake but was removed from its site before the earthquake occurred. The seismogram at 226A is thus a new virtual seismogram of the earthquake constructed at a seismometer location selected retrospectively. This also demonstrates that even after a sensor has been removed, seismograms can still be obtained at their previous locations provided that the backbone array remains intact (Curtis et al., 2012).

4.5.3 Example 3 at the largest scale

Finally we created a large scale example designed to challenge the method. Correlational interferometry contains an underlying assumption of elasticity (i.e. no attenuation), and as propagation distance increases this assumption becomes increasingly questionable. We also wanted to test the method when using target sensors that lie relatively close to the earthquake source compared to the locations of the backbone array seismometers. We reconstructed earthquake seismograms at target sensors WDC, BMN, DUG and P21A using seismometers along lines 24A and 25A of the USArray Transportable Array network (Figure 4.6) and correlation-correlation SRI (Equations (2.14) and (2.31), Figure 4.1). A total of 54, 55, 56 and 51 array seismometers were used as the backbone seismometers to construct the virtual earthquake seismogram at target sensors WDC, BMN, DUG and P21A, respectively. These array seismometers were embedded within 2D spatial Voronoi cells spanning 18.9° in latitude and 3.2° in longitude (inset, Figure 4.6) that are used for interpolation as described in Section 3.6.5. This area is divided into a fine-scale grid of square cells,

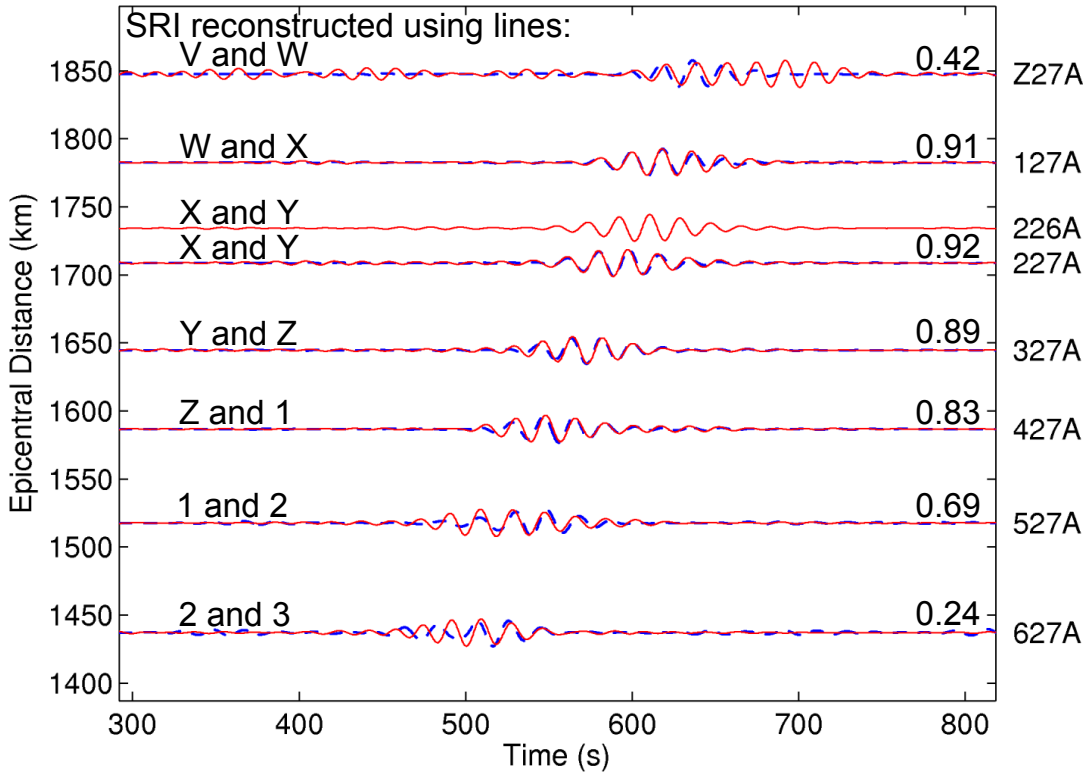

Figure 4.5: Seismograms of the M 5.8 Mexico earthquake constructed using correlation-correlation SRI (solid/red traces) compared with the real recordings (dashed/blue traces) at target sensors Z27A to 627A and at 226A. At 226A there is no real recording of the event. The quality of the match between the real and SRI seismograms is quantified by the correlation coefficient, listed on the right above each trace. SRI seismograms are constructed by integrating over 2-line combinations of seismometers within the Voronoi cells shown in Figure 4.4, as described in the caption of that figure.

each of which assumes an interpolated value from the Voronoi interpolation. A 2D tapered cosine window is applied to the grid in the x- and y-directions. All weighted values were then summed to construct the final SRI seismograms at the four target sensors.

These reconstructed seismograms are shown in Figure 4.7. SRI results are plotted against epicentral distance and overlain by the real earthquake recordings at these locations (where the latter exists). As for the previous example, a bandpass filter with corner frequencies at 0.04 Hz to 0.06 Hz has been applied to both the SRI and real recordings. The main surface wave arrivals are reconstructed but there are differences in the phase of these arrivals compared to the recorded data. Artefacts are present both before and after the main surface wave arrivals at sensors BMN and DUG, but we note

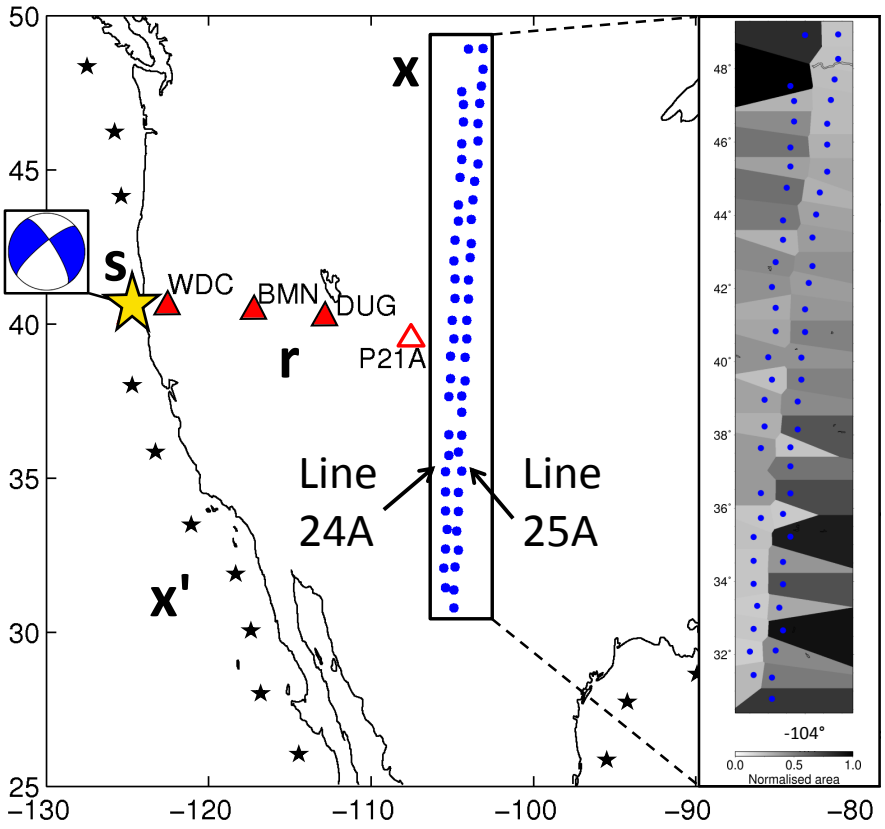

Figure 4.6: Source and receiver geometries used to reconstruct the virtual seismograms of the 10/01/2010 M 6.5 earthquake that occurred off the coast of California using correlation-correlation SRI (Figure 4.1). Key as in Figure 4.4. The backbone array consists of two adjacent lines of seismometers with Line 24A in the west and Line 25A in the east. Combinations of the 57 seismometers within the array are used to construct virtual earthquake seismograms at target sensors WDC, BMN, DUG and P21A by interpolating interferometric integrands across the Voronoi cells shown in the inset (shaded polygons).

that the best reconstruction is at target sensor WDC, which is located over 1900 km from the backbone array and within 200 km of the earthquake epicentre. The quality of the match between the real and SRI seismograms is quantified by the correlation coefficient and we observe a maximum value of 0.64 for the reconstruction at WDC.

Target sensor P21A (unfilled triangle in Figure 4.6) was previously active but was removed from its site before the earthquake occurred. This seismogram is thus constructed at a truly retrospective location - a location chosen from previous seismometer locations after the event occurred. The result is shown at the top of Figure 4.7 and constitutes a new seismogram for that receiver, from an earthquake that occurred after the receiver had been removed. The main surface wave appears to

be constructed but large amplitude non-physical arrivals are also constructed at earlier travel times (at $\sim$ 50 s and $\sim$ 400 s), thus making the reconstruction unreliable.

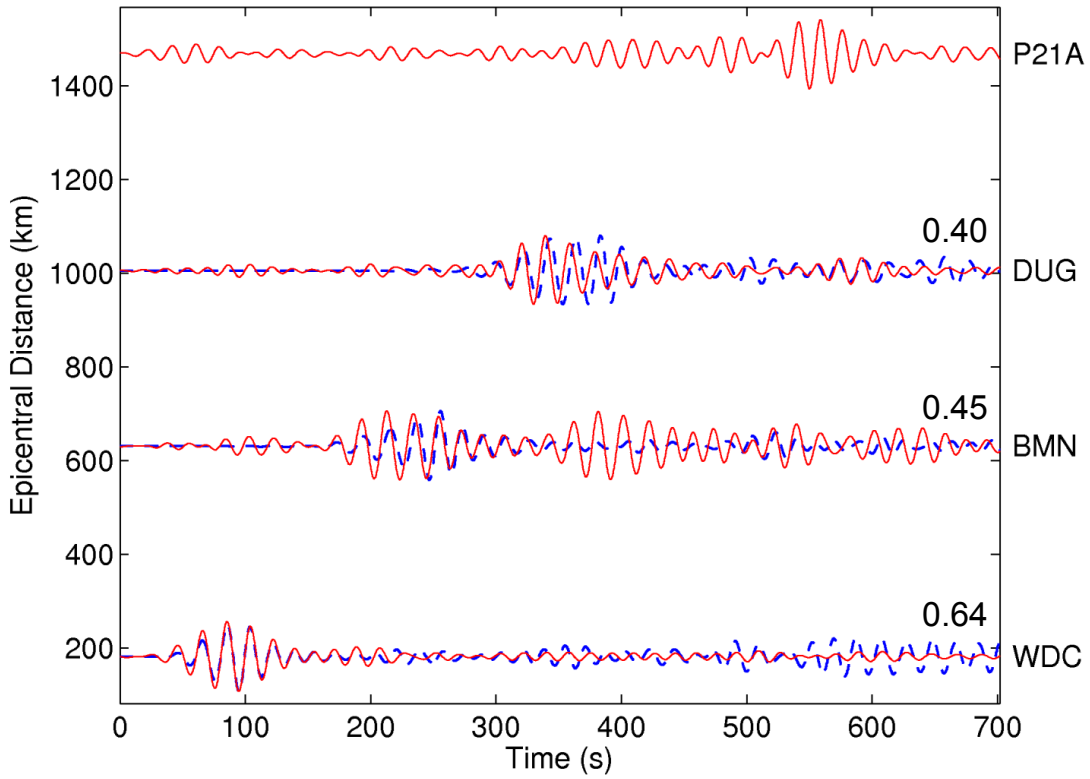

Figure 4.7: Seismograms of the M 6.5 earthquake that occurred off the coast of California constructed using correlation-correlation SRI (solid/red traces) compared with the real recordings (dashed/blue traces) at target sensors WDC, BMN, DUG and P21A. At P21A there is no real recording of the event. Key as in Figure 4.5. The geometry for this application of correlation-correlation SRI is shown in Figure 4.6

.

4.6 Discussion

By using three separate example applications we are able to assess the ability of correlation-correlation SRI to reconstruct seismograms on target seismometers across different spatial scales. In most cases considered here, SRI reconstructions are fairly good for the main surface wave arrivals and some of the reconstructions match recorded seismograms some way into the coda (as found at one length scale by Curtis et al. (2012)).

At an engineering seismology scale (Section 4.4.1) the seismograms constructed by correlation-correlation SRI were very good but even under such controlled conditions they did not perfectly reconstruct the real recordings of the active source. These imperfections were likely caused by a combination of the power spectrum of the weight-drop source being multiplied into the SRI seismograms, and a breakdown of the assumption in correlational interferometry that the medium is non-attenuating.

When SRI seismograms were constructed on target sensors located between 210 km - 540 km from a backbone array of seismometers, correlation-correlation SRI constructed surface wave arrivals that were a close match to the real recordings of the earthquake on those same sensors. A few artefacts (non-physical arrivals) exist in the SRI reconstructions which we attribute to errors in correlation-type interferometry when the medium is attenuative and when source (or receiver) apertures are limited (see below for further discussion).

Correlation-correlation SRI was then used to construct SRI seismograms on target sensors located up to 1922 km from a backbone array of seismometers. At these largest length scales we observe a poorer quality in the match between the real recordings and their corresponding SRI seismograms as the highest correlation coefficient is just 0.60. We conclude that as the distance between the backbone array and the target sensors increases, we can no longer assume that the medium is non-attenuating and this deviation from the theory introduces errors into the results of correlation interferometry in the form of non-physical arrivals. The SRI propagators constructed as in Equation (2.14) are thus less reliable, so we are less successful at projecting earthquake energy recorded on the backbone array to the locations of the most distant target sensors.

The inter-receiver Green's function estimates (the SRI propagators) are clearly key, and were constructed using Equation (2.14). To get the one-sided Green's function $G(\mathbf{x}, \mathbf{r})$ for Equation (2.31), the Green's function constructed at negative time in G_H was time-reversed and added to the Green's function constructed at positive time. This would not be necessary if one side of the estimated Green's function was predominantly noise; instead one could simply take the side within which the signal is constructed. Here we did not notice any particular consistent increase or decrease in the quality (signal-to-noise ratio) of the estimated Green's function when using a stacked summation of both sides of the Green's function, so we decided to continue with that approach to be consistent with our previous studies.

Since attenuation may be an issue over longer inter-receiver distances, another approach to estimate these propagators might be to use deconvolutional interferometry in place of correlational interferometry (Snieder and Safak, 2006). Multidimensional deconvolution (MDD) (Wapenaar et al., 2008) has been shown to compensate for various deficiencies in correlational interferometry, so there may be merit in future testing of deconvolutional SRI. We begin to explore this theory in a preliminary study in Chapter 7: SRI propagators are constructed using MDD (Equation (2.18)) and compared with those of traditional correlational noise interferometry (Equation (2.14)).

To compensate for spatial irregularities within the backbone arrays, and to thus evaluate the inter-source interferometric integrals in Equation (2.31) more precisely, the backbone seismometer arrays used in Sections 4.5.2 and 4.5.3 were embedded within 2D spatial Voronoi cells. Figure 4.8 shows the SRI seismograms of the M 5.8 Mexico earthquake studied in Section 4.5.2 constructed *without* Voronoi interpolation of the integrands of Equation (2.31). Instead, the integral in Equation (2.31) was approximated by performing a simple summation of the integrand over all backbone seismometer locations. Comparing Figure 4.8 with Figure 4.5 we observe that the matches between the real recordings and the SRI seismograms are of a much poorer quality when the integration is performed without Voronoi interpolation and include large amplitude artefacts prior to the main surface waves. Since we use Voronoi interpolation to approximate the second step of SRI above, and since that step is simply the reciprocal of inter-receiver interferometry, it is likely that more generally Voronoi interpolation would increase the accuracy of most applications of interferometry where boundary source or receiver locations are known.

When reconstructing SRI seismograms at the intermediate length scale (Section 4.5.2), only a small subset of the array seismometers were actually used in any one reconstruction, despite over 90 seismometers fitting the criteria outlined in Section 3.6.1, and in both earthquake seismology examples (Sections 4.5.2 and 4.5.3) only two lines of seismometers were used to create the SRI reconstructions. In Section 3.7 we found that a thicker band of seismometers did not improve the SRI results. This contradicts what might be expected given the results of Draganov et al. (2004), Halliday and Curtis (2008) and Kimman and Trampert (2010) whose work suggests that thicker boundaries should provide better results if the boundary is not in the very far field. For a target sensor located within or close to the backbone array, the final geometrical criteria that we found to work best are described in Section 3.6.1 and illustrated schematically in Figure 3.9.

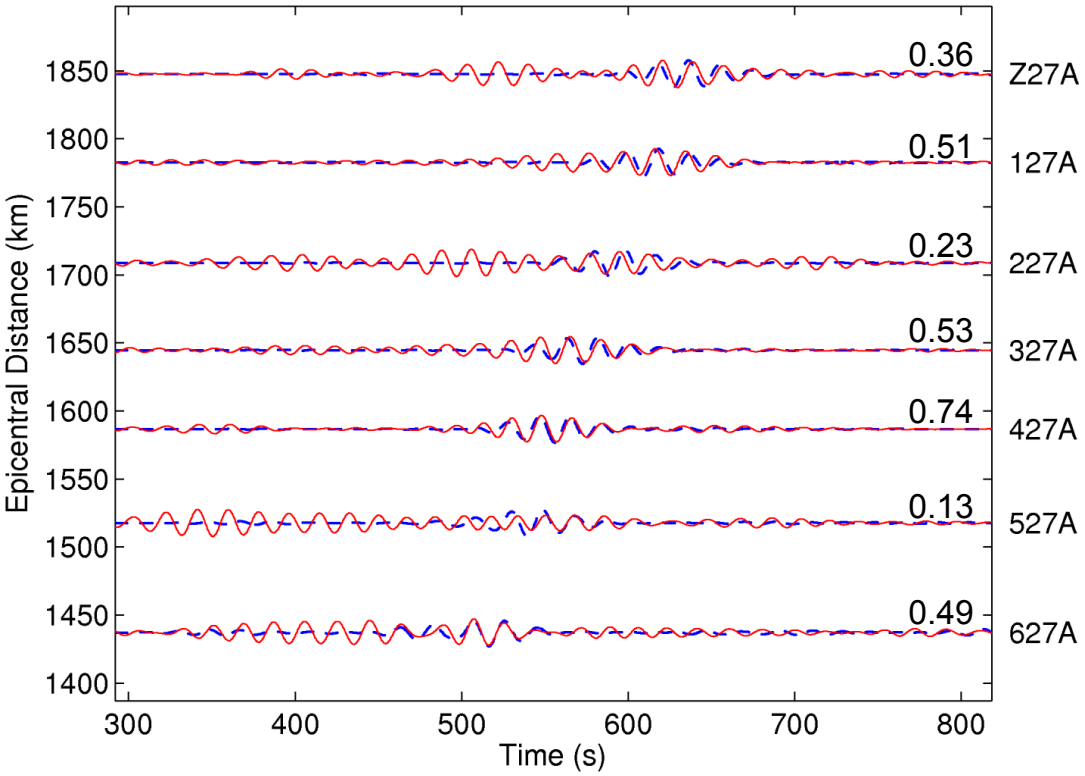

Figure 4.8: Seismograms of the M 5.8 earthquake in Mexico constructed using correlation-correlation SRI (solid/red traces) compared with the real recordings of the event (dashed/blue traces) at target sensors Z27A-627A. The SRI integral in Equation (2.31) is evaluated by performing a direct summation (integration) over all backbone seismometer locations rather than as an interpolated sum over Voronoi cells. The match between the real and SRI seismograms is quantified by the correlation coefficient as listed on the right of the figure above each trace.

We observed that even a slight deviation from these criteria can result in significantly poorer SRI reconstructions. For example, consider the final criterion in Section 3.6.1, that the backbone array should comprise two approximately parallel lines of regularly spaced seismometers. This condition aims to fulfil the requirement that the backbone array seismometers occupy the stationary phase points of the receiver boundary in Equation (2.31). In the backbone array shown in Figure 4.4 we observe that lines V and 3 are the most spatially irregular, comprising far fewer seismometers than the other lines. Seismometers along lines V and 3 were used to reconstruct the SRI seismograms at target sensors Z27A and 627A, respectively, and in Figure 4.5 we notice that the SRI seismograms constructed at these target sensors exhibit the lowest correlation coefficients. We thus conclude that these poorer reconstructions are partly a consequence of spatial irregularities within the two parallel lines of backbone

array seismometers. This breaks the condition that receivers are to be located around the stationary phase points of the receiver boundary, and consequentially introduces non-physical arrivals into the interferometric reconstructions. Nevertheless, Voronoi interpolation does contribute to resolve the issue of spatial irregularity as data are effectively interpolated into areas of the receiver boundary where seismometers are missing. It may be that in future a more accurate (higher order) method of interpolation within and across Voronoi cells may further diminish such issues.

The large scale source and receiver geometries outlined in Section 4.5.3 were chosen specifically to challenge the method. Nevertheless, when using correlation-correlation SRI we were able to reconstruct surface wave arrivals at target sensor WDC located between 1400 km - 1920 km from the backbone array seismometers, to almost the same degree of accuracy as reconstructions made at the much smaller target-to-backbone seismometer distances in Section 4.5.2. A comparison of the real recordings with the correlation-correlation SRI seismograms in Figure 4.7 shows that all surface wave arrivals follow the same moveout curve, but small artefacts are introduced in the phase as inter-station distance between the target sensors and the backbone array increases.

The reconstruction at WDC is unique in this aspect: the first surface wave arrival is constructed well, but the SRI propagators are required to operate over large distances, in this case to within 200 km of the earthquake epicentre. Over short epicentral distances seismic waves encounter fewer subsurface heterogeneities, reducing the amount of scattering. As the epicentral distance increases, scattering and attenuation of the earthquake energy becomes more prominent. This creates more complex wavefields that have longer codas after the direct surface wave arrivals which may have amplitudes more comparable to that arrival. This may explain why the reconstructions close to a source appears to be of high quality.

The projection operators are selected to have a high signal-to-noise ratio (SNR) and hence (by our definition of SNR) are usually dominated by a main surface wave arrival. During the second correlational step of SRI, the phase effects of the waves propagating from the target sensor to the backbone array are undone; that is, the phase of the propagators is subtracted from the phase of the backbone recordings. This has the effect of (computationally) refocussing the recorded energy onto the target location, but dominantly this focusses the main surface wave arrival since that energy dominates the projection Green's functions. Since the recording closest to the epicentre is also most dominated by this main arrival, that virtual seismogram is most successfully

reconstructed by SRI.

Since target sensor WDC is located less than 200 km from the earthquake epicentre, it approaches the proximity of the location of rapid response local temporary seismometer arrays that are often deployed around large earthquake epicentres after the event has occurred, in order to continuously monitor the area for subsequent aftershocks. If such temporary seismometers are deployed for six months and ambient noise data is collected, this example shows that correlation-correlation SRI might then be applied to construct local virtual seismograms of the earthquake retrospectively, even when the event occurs far away from the permanent backbone array. Alternatively, one can construct virtual SRI seismograms of an earthquake immediately after the event has occurred using seismometers that used to be deployed close to where the earthquake has occurred, but which have since been removed. All one requires is a backbone array of seismometers whose deployment spans both the time at which the earthquake occurred and the time during which the target sensors were previously deployed.

Thus we see the benefit of seismometer arrays with deployment strategies similar to the USArray Transportable Array which routinely deploys approximately regularly spaced seismometers for up to two years before they are moved to a set of new locations. During their deployment, recordings of ambient seismic noise can be made on all seismometers and cross-correlated to construct all possible inter-receiver Green's functions. This creates an archive of the propagators needed for SRI which can subsequently be inserted into Equation (2.31) when an earthquake occurs. Virtual earthquake seismograms can then be reconstructed on any seismometer deployed before, during or after the event, provided that a suitably dense geometry of other seismometers recorded the earthquake. We note though that the ideal array deployment strategy for SRI would be for a dense backbone array to remain permanently in place while other roving sensors occupy temporary recording locations, as outlined in Curtis et al. (2012), which unfortunately was not the design of the deployment strategy used for USArray.

At the intermediate length scale we identify spurious events in the correlation-correlation SRI seismograms that appear prior to the first surface wave arrivals. These can be seen in the reconstruction at target sensor Z27A in Figure 4.5 between approximately 350 s and 450 s. These spurious arrivals are associated with non-physical arrivals that should cancel but do not when the medium is strongly scattering or when the surrounding source (or receiver) boundary is incomplete. Such non-

physical arrivals are constructed by cross-correlating direct and scattered wavefields and in the stationary phase approach of Halliday and Curtis (2009) are represented by terms $T2$ and $T3$ in the notation of that paper. In lossless media, these non-physical arrivals are cancelled out by a fourth term that contributes to the interferometric estimation (term $T4$) that represents the cross-correlation of scattered wavefields recorded at two receiver locations (Halliday and Curtis, 2009). The arrivals in $T4$ are purely non-physical and are equal but opposite in sign to the non-physical arrivals in terms $T2$ and $T3$. Thus, under ideal conditions all non-physical arrivals mutually cancel. However, when the medium is strongly attenuating energy is lost during the propagation of the wavefields from the boundary sources (in this case noise sources) to the receiver locations. This introduces amplitude imbalances into the non-physical arrivals such that the amplitudes of the non-physical arrivals in terms $T2$ and $T3$ are no longer equal to the amplitudes of the non-physical arrivals in term $T4$. Thus, in the presence of attenuation, non-physical arrivals do not cancel and artefacts are introduced into the interferometric estimation.

Furthermore, Halliday and Curtis (2009) find that non-physical arrivals are also enhanced when the source aperture is limited i.e. when sources are not present at all required stationary phase points. The same argument can also be made for a limited receiver aperture in inter-source interferometry, i.e., when spatial irregularities in the backbone array result in unoccupied stationary phase points on the receiver boundary. Since correlation refers to processes of complex conjugation (time-reversal), and wavefields can not theoretically be time-reversed in an attenuative medium without the re-injection of all of the lost (attenuated) energy, Halliday and Curtis (2009) propose the method of convolution over correlation when attenuation is strong. When following a convolution approach, the non-physical arrivals in terms $T2$ and $T3$ cancel to zero and term $T4$ provides a zero contribution (Halliday and Curtis, 2009). Thus, the mutually cancelling terms do not exist and no artefacts are introduced into the interferometric result due to amplitude imbalances. Similarly, limited apertures do not introduce non-physical arrivals when using a convolution approach. In Chapter 5 we will thus explore using methods of convolution within the inter-source interferometry step of SRI; we expect to reduce the non-physical arrivals associated with correlation-type interferometry and thus construct more robust SRI seismograms.

Finally, we comment on the results of Curtis et al. (2012) in which the SRI reconstructions were used to determine independent information about the source phase. In order to obtain this information correctly one would require the source-

receiver geometry outlined in Figure 4.1 in which backbone seismometers occupy *both* stationary phase regions of the boundary S surrounding the earthquake source at $\mathbf{s}$ and the target sensor at $\mathbf{r}$ (see the grey shaded regions in Figure 4.1 for a schematic representation of these stationary phase regions). Using both stationary phase regions of the receiver boundary, one would correctly construct both the causal ($C = T^*G$, where $T = |T|e^{it}$ and $G = |G|e^{ig}$, and t and g are the phases of T and G, respectively) and acausal ($A = T^*G^*$) sides of $T^*G_H(\mathbf{r}, \mathbf{s})$ in Equation (2.31). Curtis et al. (2012) then theoretically show that by calculating the ratio C/A, independent information about the phase of the source time function t can be determined. Unfortunately in the current study we did not have backbone array seismometers in both stationary phase regions, hence we could not test this method here.

4.7 Conclusion

We demonstrate the reconstruction of virtual seismograms of waves from seismic sources on sensors that were not necessarily deployed when the source occurred. We do this using correlation-correlation source-receiver interferometry (SRI): cross-correlations of seismic energy recorded over one period of time are used as propagators to redatum the source signals currently recorded at one set of locations onto new sensor locations, at any time after the source has occurred, using processes of correlation. The source signals need never be physically recorded at the new sensor locations.

This is possible on a variety of length scales and in a variety of settings. A small length scale, engineering seismology example uses correlation-correlation SRI to yield reconstructions of an active seismic shot on six sensors located up to 62 m from a regular line of receivers. An intermediate length scale example in an earthquake seismology setting uses correlation-correlation SRI to reconstruct virtual seismograms of a M 5.8 earthquake on eight target sensors located approximately between 210 km and 540 km from a backbone array of seismometers. A comparison between the SRI seismograms and the real recordings of the earthquake on seven of the target sensors shows that the main surface waves are constructed accurately, but non-physical arrivals are present in some of the reconstructions. Here we attribute these artefacts to limited aperture in the backbone array of seismometers which introduces errors into the results of correlational interferometry. Such errors are associated with terms in equations that should (but may not) mutually cancel when using correlation-correlation SRI. Finally, a large length scale example within an earthquake seismology setting was designed to

challenge the methodology: this shows that correlation-correlation SRI can be used to reconstruct the surface wave arrivals from a M 6.5 earthquake on four target sensors located between 660 km and 1920 km from a backbone array, and between 200 km and 1500 km from the source. Even on this largest length scale we are able to reconstruct the main surface wave arrivals but artefacts associated with the SRI propagators (and thus errors induced by correlational interferometry) are present as the inter-station distance increases.

On the two larger length scales, the quality of the match between the real earthquake seismograms and those constructed by correlation-correlation SRI is quantified by the correlation coefficient, which is as high as 0.92 on one occasion. We also construct two completely new virtual seismograms. These are predicted recordings of the earthquakes on two sensors that were not deployed when the events occurred. When plotted alongside the seismograms reconstructed on the target sensors at which we have real recordings, we see that all reconstructions follow the same moveout curves. The new "virtual" seismograms are thus robust and show that correlation-correlation SRI can be used to construct surface wave estimates of past earthquakes.

These multi-length scale applications of SRI in both exploration and earthquake seismology settings pave the way for a new type of seismology: "retrospective seismology" where truly novel seismograms can be constructed at new, desired locations - locations determined after the energy from the source has dissipated and where, with hindsight, one would have liked to have had sensors installed.

Bibliography

Curtis, A. (2009), Source-receiver seismic interferometry, chap. 733, pp. 3655–3659, Society of Exploration Geophysicists, doi:{10.1190/1.3255626}.

Curtis, A., and D. Halliday (2010), Source-receiver wave field interferometry, Physical Review E, 81(4, 2), doi:{10.1103/PhysRevE.81.046601}.

Curtis, A., P. G. Gerstoft, H. Sato, R. Snieder, and K. Wapenaar (2006), Seismic interferometry; turning noise into signal, Leading Edge (Tulsa, OK), 25(9), 1082–1092, doi:{10.1190/1.2349814}, n/a.

Curtis, A., Y. Behr, E. Entwistle, E. Galetti, J. Townend, and S. Bannister (2012), The benefit of hindsight in observational science: Retrospective seismological observations, Earth and Planetary Science Letters, 345, doi:{DI10.1016/j.epsl.2012.06.008}.

Draganov, D., K. Wapenaar, and J. Thorbecke (2004), Passive imaging in the presence of white noise sources, The Leading Edge, 9, 889–892.

Duguid, C., D. Halliday, and A. Curtis (2011), Source-receiver interferometry for seismic wavefield construction and ground-roll removal, The Leading Edge, 30(8), 838–843, doi:{10.1190/1.3626489}.

Galetti, E., and A. Curtis (2012), Generalised receiver functions and seismic interferometry, Tectonophysics, 532, 1–26, doi:{10.1016/j.tecto.2011.12.004}.

Halliday, D., and A. Curtis (2008), Seismic interferometry, surface waves and source distribution, Geophysical Journal International, 175(3), 1067–1087, doi:{10.1111/j.1365-246X.2008.03918.x}.

Halliday, D., and A. Curtis (2009), Seismic interferometry of scattered surface waves in attenuative media, Geophysical Journal International, 178(1), 419–446, doi:{10.1111/j.1365-246X.2009.04153.x}.

Halliday, D., and A. Curtis (2010), An interferometric theory of source-receiver scattering and imaging, Geophysics, 75(6), SA95–SA103, doi:{10.1190/1.3486453}.

Kimman, W. P., and J. Trampert (2010), Approximations in seismic interferometry and their effects on surface waves, Geophysical Journal International, 182(1), 461–476, doi:{10.1111/j.1365-246X.2010.04632.x}.

Snieder, R. (2004), Extracting the Green's function from the correlation of coda waves: A derivation based on stationary phase, Physical Review E, 69(4, 2), doi:{10.1103/PhysRevE.69.046610}.

Snieder, R., and E. Safak (2006), Extracting the building response using seismic interferometry: Theory and application to the Millikan Library in Pasadena, California, Bulletin of the Seismological Society of America, 96(2), 586–598, doi:{10.1785/0120050109}.

Wapenaar, K., E. Slob, and R. Snieder (2008), Seismic and electromagnetic controlled-source interferometry in dissipative media, Geophysical Prospecting, 56, 419–434, doi:{10.1190/1.2976118}.

Wapenaar, K., D. Draganov, R. Snieder, X. Campman, and A. Verdel (2010a), Tutorial on seismic interferometry: Part 1-Basic principles and applications, Geophysics, 75(5), A195–A209, doi:{10.1190/1.3457445}.

Wapenaar, K., E. Slob, R. Snieder, and A. Curtis (2010b), Tutorial on seismic interferometry: Part 2-Underlying theory and new advances, Geophysics, 75(5), A211–A227, doi:{10.1190/1.3463440}.

CHAPTER 5

Source-Receiver Interferometry Using A Joint Correlation-Convolution Approach[1]

5.1 Outline

Seismic interferometry is a technique that focuses on processes of correlation, convolution or deconvolution to estimate the Green's function between two receivers (seismometers), two sources, or a source and a receiver. Source-receiver interferometry (SRI) is one such interferometric technique that combines these processes to estimate new seismic responses at locations that were once previously occupied by receivers. In Chapter 4 we showed that this was possible using two correlation-type interferometric integrals. This introduced the theory behind correlation-correlation SRI and three practical examples of the method were presented in industrial seismic and earthquake seismology settings: weight-drop source and earthquake source seismograms were reconstructed on target sensors after all the energy from the sources had dissipated.

Herein we introduce correlation-convolution SRI, invoking one correlation-type and one convolution-type interferometric integral, and provide practical examples using the same earthquake data presented in Chapter 4: on the smallest length scale we construct SRI seismograms of the M 5.8 Mexico earthquake on four target sensors located approximately 220 km - 470 km from a backbone array of seismometers aligned East-West in New Mexico. These SRI seismograms were also constructed

[1]Combined with Chapter 4, this Chapter has been submitted to the Journal of Geophysical Research. Co-authors: Andrew Curtis - *University of Edinburgh*; Erica Galetti - *University of Edinburgh*; Giovanni Meles - *University of Edinburgh*; Brian Baptie - *British Geological Survey*

using correlation-correlation SRI in Chapter 4, thus a direct comparison can be made between the results of the two methods. On a larger length scale we then reconstruct seismograms of the M 6.5 earthquake that occurred off the coast of California. In this case, correlation-convolution SRI allows the source-to-receiver geometry to be extended to four target sensors located almost 4000 km from the earthquake epicentre and up to 2420 km from a backbone array of seismometers aligned North-South in the centre of the United States. Over this largest length scale we thus test the successes and limitations of the underlying SRI theories and methodologies.

5.2 Introduction

In Chapters 2 to 4 we have focussed primarily on correlation-correlation SRI, derived from two correlation-type reciprocity theorems (Curtis and Halliday, 2010), and defined for practical use in earthquake seismology by Equations (2.14) and (2.31). We demonstrated that the method is capable of reconstructing active source or earthquake source seismograms on target sensors that were not necessarily deployed when the events occurred. SRI thus spatially and (novelly) temporally redatums (projects) seismic data to new locations. This was of particular significance in earthquake seismology as "virtual" earthquake seismograms were constructed at new, more desirable seismometer locations, chosen with the benefit of hindsight of the earthquake location or magnitude estimates.

However, we noticed that the results of correlation-correlation SRI were often contaminated by non-physical arrivals. We attributed these spurious events to two potential causes: 1) a breakdown in the underlying assumption of correlation-type interferometry that the medium is elastic (non-attenuating), and 2) spatial irregularities within the backbone seismometer arrays that leave stationary phase points of the receiver boundary unoccupied, thus causing the integral in Equation (2.31) to be invoked incorrectly (Snieder, 2004; Halliday and Curtis, 2009). Halliday and Curtis (2009) propose that these problems can be addressed by invoking convolution over correlation. This follows from the theory that: a) convolution can be performed in attenuative media as complex conjugation (time-reversal) is not required, and b) terms in equations for correlation-type interferometry that should cancel but do not in the presence of attenuation do not exist in the equations for convolution-type interferometry. These "non-cancelling" terms were discussed in more detail in Section 4.6 and are fully introduced and evaluated by Halliday and Curtis (2009).

The next obvious advance for SRI is thus to invoke convolution in place of correlation. Here we do this for one of the interferometric integrals only, thus invoking correlation-convolution SRI to provide two practical applications of the method. Note that convolution-convolution SRI is a third type of SRI that invokes two convolution interferometric integrals. Unfortunately we do not evaluate this method within this current thesis due to time constraints.

Consider the geometry for correlation-convolution SRI in Figure 5.1 where a boundary of sources $\mathbf{x}'$ on S' surrounds a receiver at $\mathbf{r}$ and an individual source at $\mathbf{s}$, which is further surrounded by a boundary of receivers $\mathbf{x}$ on S. The full, exact equation for this joint correlation-convolution approach to SRI is derived by Curtis and Halliday (2010), but its practical application is defined by Equations (2.14) and (2.32) in Chapter 2. Comparing Equation (2.32) with the equivalent equation for correlation-correlation SRI (Equation (2.31)), one observes that the only difference is in the term $R(\mathbf{x}, \mathbf{s})$, which undergoes complex conjugation (and hence cross-correlation) in Equation (2.31).

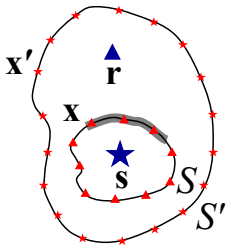

Figure 5.1: One possible geometry for correlation-convolution SRI. Stars are sources, triangles are receivers. The grey shaded region highlights schematically one of the stationary phase regions along the source-receiver line between $\mathbf{s}$ and $\mathbf{r}$. For full derivations of the SRI integral pertaining to this geometry see Curtis and Halliday (2010).

To perform correlation-convolution SRI in a real earthquake seismology setting we follow the 2-step methodology described in Chapter 3: 1) An Inter-receiver interferometry step constructs estimates of the Green's functions $G(\mathbf{x}, \mathbf{r})$ between the backbone array seismometers (at locations $\mathbf{x}$) and the target sensor (at $\mathbf{r}$). These Green's functions are called the *propagators* in SRI. They are constructed as in Equation (2.14), which is described practically in Section 3.2. 2) These propagators are used to project the recordings of the energy source $R(\mathbf{x}, \mathbf{s})$ on the backbone array to the location of the target sensor: this is achieved by performing inter-source interferometry between the real source and the target sensor (now a virtual

source) as in Equation (2.32) and as described practically in Section 3.6.4, substituting Equation (2.32) in place of Equation (2.31) where necessary.

In an attempt to evaluate the integral in Equation (2.32) more precisely, the values of the integrand for each backbone seismometer $\mathbf{x}$ are interpolated into points within surrounding Voronoi cells. The Voronoi cells are constructed as in Section 3.6.5 and the integral in Equation (2.32) then becomes a summation over a fine scale grid of interpolated values, which more accurately represents a continuous boundary. This constructs an estimate of the response from the earthquake source at $\mathbf{s}$ on the target sensor at $\mathbf{r}$, without ever recording $\mathbf{s}$ on $\mathbf{r}$ directly.

5.3 Application

We invoke Equations (2.14) and (2.32) in two real, earthquake seismology settings to reconstruct the seismic responses from two earthquakes on a set of target sensors. We first consider a small length scale example in which four target sensors are located approximately 220 km - 470 km from a backbone seismometer array consisting of 25 seismometers aligned East-West in New Mexico. Here we reconstruct the virtual seismograms of a magnitude 5.8 earthquake that occurred in Mexico on 27th April 2009 on target sensors Z27A, 127A, 227A and 226A. The acquisition geometry for this event can be seen in Figure 5.2. Target sensor 226A was not deployed at the time of the event. The SRI reconstruction at 226A will thus be a new, novel seismogram. SRI seismograms of this event were also reconstructed at the exact same four target sensors using correlation-correlation SRI in Section 4.5.2. This allows a direct comparison to be made between the results of the two SRI methods.

We then consider a larger length scale example in which four target sensors are located up to 2420 km from a backbone array consisting of 139 seismometers aligned North-South in the centre of the United States. Here we reconstruct the virtual seismograms from a magnitude 6.5 earthquake that occurred off the coast of California on 10th January 2010 on target sensors R29A, R30A and R31A, located between 235 km and 1200 km from the backbone array seismometers, and on target sensor GOGA located between 1930 km and 2420 km from the backbone array. The acquisition geometry for this event can be seen in Figure 5.3A. This earthquake and backbone array geometry was used in part in Section 4.5.3 to construct correlation-correlation SRI seismograms on four target sensors located to the West of the backbone array. Here we use correlation-convolution SRI to extend this source to receiver geometry to

target sensors located to the east of the backbone array. This allows the successes and limitations of the SRI methodologies to be determined.

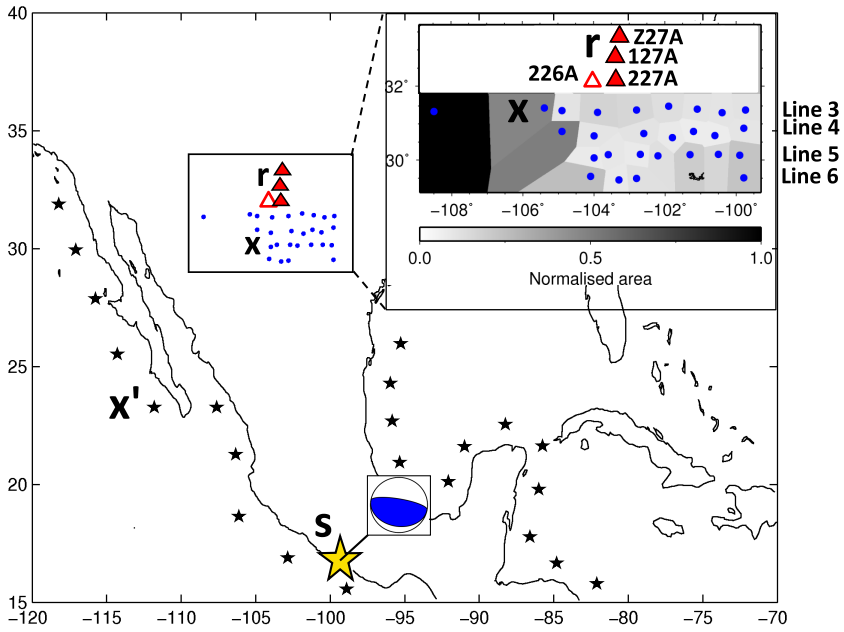

Figure 5.2: Source and receiver geometries required by correlation-convolution SRI (Equations (2.14) and (2.32) and Figure 5.1) to construct virtual seismograms of the 27/04/2009 M 5.8 earthquake in Mexico (large star). Ambient noise fluctuations from source locations such as $\mathbf{x}'$ (small stars in oceans) are recorded on the East-West aligned backbone seismometer array $\mathbf{x}$ (circles) and on the four target sensors $\mathbf{r}$ (filled and unfilled triangles) located within New Mexico. The backbone array consists of four approximately parallel lines of seismometers from Line 6 in the south, to Line 3 in the north. Line notation arises from the naming convention of the USArray Transportable Array as described in Section 3.3. Inset: Backbone array seismometers are embedded within 2D Voronoi cells (shaded polygons normalised to the largest cell). 2-line combinations of the 25 seismometers within the backbone array are used to reconstruct virtual earthquake seismograms at target sensors Z27A, 127A, 227A and 226A using SRI. Seismometers along lines 3 and 4 are used to construct the SRI seismogram at target sensor Z27A; seismometers along lines 4 and 5 are used to construct the SRI seismogram at target sensor 127A, and seismometers along lines 5 and 6 are used to construct the SRI seismograms at target sensors 227A and 226A.

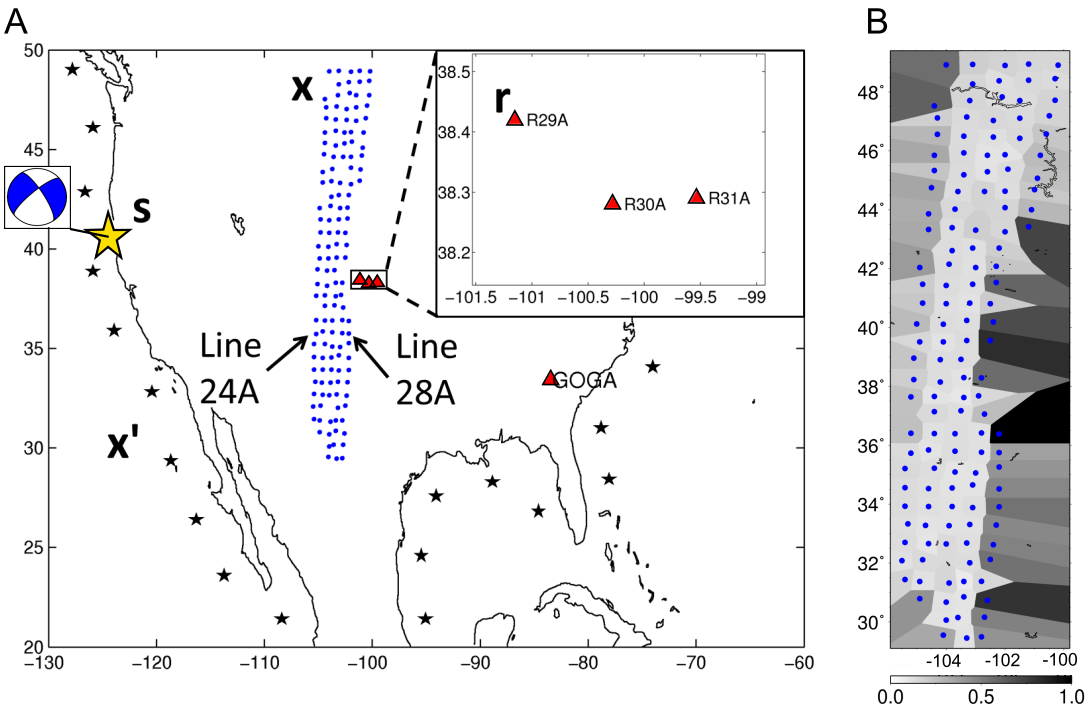

Figure 5.3: Source and receiver geometries required by correlation-convolution SRI (Equations (2.14) and (2.32) and Figure 5.1) to construct virtual seismograms of the 10/01/2010 M 6.5 earthquake off the coast of California. Key as in Figure 5.2. The North-South aligned backbone array in the centre of the United States consists of five adjacent lines of seismometers from Line 24A in the west, to Line 28A in the east. 2-line combinations of the 139 seismometers within the backbone array are used to reconstruct virtual earthquake seismograms at target sensors R29A, R30A, R31A and GOGA by interpolating inteferometric integrands across the Voronoi cells shown in (B) (shaded polygons). Seismometers along lines 24A and 25A are used to construct the SRI seismogram at target sensor GOGA; seismometers along lines 25A and 26A are used to construct the SRI seismogram at target sensor R29A; seismometers along lines 26A and 27A are used to construct the SRI seismogram at target sensor R30A, and seismometers along lines 27A and 28A are used to construct the SRI seismogram at target sensor R31A.

5.4 Results

On the smallest length scale, correlation-convolution SRI is used to reconstruct the seismograms of the M 5.8 earthquake on target sensors Z27A, 127A, 227A and 226A. These SRI seismograms are shown in Figure 5.4 and compared with the real recordings of the earthquake on those same sensors, where the latter exist. We observe almost perfect reconstructions as the phases of the main surface wave arrivals are a close match to the phases of the real recordings and some of the later arrivals are also matched well. Correlation coefficients quantify the match between the real and SRI seismograms and we see values of up to 0.84 for the seismograms recorded/constructed on target sensor 227A. The surface wave constructed at the location of target sensor 226A appears to follow the same moveout curve as the other SRI/real seismograms. Thus, we assume that the virtual, retrospective seismogram constructed at this location is a true representation of the seismogram that would have been recorded at that location, had sensor 226A been deployed when the earthquake occurred.

Figure 5.5 shows the SRI reconstructions of the M 6.5 earthquake on target sensors R29A, R30A and R31A located up to 1200 km from the backbone array and at the most distant target sensor, GOGA, located up to 2420 km from the backbone array and almost 4000 km from the earthquake epicentre. All reconstructions are compared with the real recordings of the event at those locations. We observe a few similarities between the SRI seismograms and the real recordings as most arrivals are in phase. At target sensors R29A-R31A the correlation coefficients are of intermediate values (up to 0.69) but the arrival times of the surface waves are poorly constructed: the main surface wave arrivals constructed using SRI are offset by almost 100 s compared to the real surface wave arrivals. At the largest length scale at target sensor GOGA there are artefacts in the SRI reconstruction prior to the main surface wave arrival between 600 s and $\sim$ 900 s. The surface wave constructed at the location of target sensor GOGA is not as accurately constrained as those surface waves constructed at the locations of target sensors R29A, R30A and R31A. This is represented in the very low correlation coefficient of 0.08.

5.5 Discussion

Here we have shown the success with which correlation-convolution SRI has reconstructed earthquake seismograms on target sensors sampling two different spatial

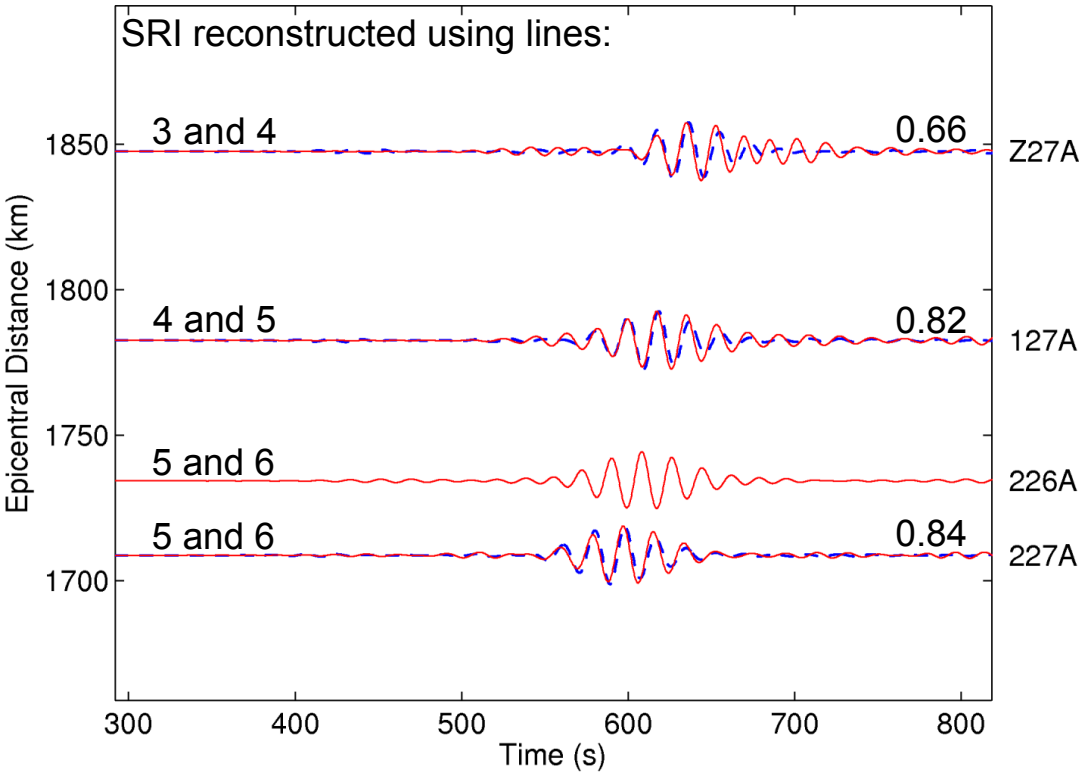

Figure 5.4: Seismograms of the M 5.8 Mexico earthquake constructed using correlation-convolution SRI (solid/red traces) compared with the real recordings (dashed/blue traces) at target sensors Z27A, 127A, 227A and 226A. At 226A there is no real recording of the event. The quality of the match between the real and SRI seismograms is quantified by the correlation coefficient, listed on the right above each trace. SRI seismograms are constructed by integrating over 2-line combinations of seismometers within the Voronoi cells shown in Figure 5.2 (inset) as described in the caption of that figure.

scales. This is the first time correlation-convolution SRI has been used in such a setting and in most cases the method appears to construct good surface wave estimates that are in phase with the real earthquake seismograms recorded on those same sensors.

On the smallest length scale SRI seismograms were reconstructed on target sensors located between 220 km and 470 km from a backbone array of seismometers (Figure 5.4). The main surface wave arrivals are a close match with the real recordings of the earthquake on those same sensors, as correlation coefficients reach values up to 0.84. In Figure 5.6 we compare the results of correlation-correlation SRI as constructed previously in Section 4.5.2 (blue/dashed traces), with the results of correlation-convolution SRI as constructed herein (solid/red traces). We observe that processes of convolution within the inter-source interferometry step in Equation (2.32)

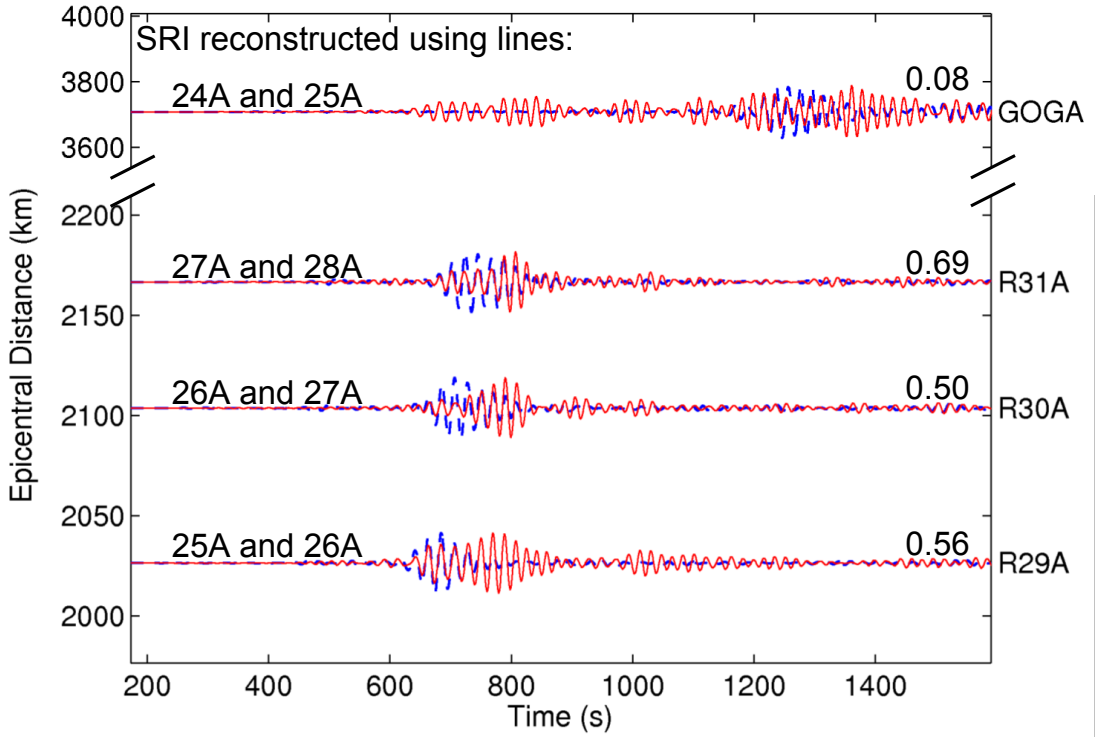

Figure 5.5: As Figure 5.4 for seismograms of the M 6.5 earthquake that occurred off the coast of California, constructed/recorded at target sensors R29A, R30A, R31A and GOGA. The geometry for this application of correlation-convolution SRI is shown in Figure 5.3.

act to stabilise the reconstructions, removing spurious events associated with amplitude errors in the second-order cancelling terms that appear when using a correlation approach and do not cancel out completely in the final correlation gather. Such non-physical arrivals are accentuated by limited aperture and strong attenuation in the background medium (Halliday and Curtis, 2009). These spurious signals can be seen in Figure 5.6 (dashed/blue traces), prior to the first surface wave arrivals between 0 s - 450 s and are described for electromagnetic wavefields in lossy media by Slob et al. (2007) and for scattered surface waves in attenuating media by Halliday and Curtis (2009).

In Figure 5.2 we observe that the East-West aligned backbone array is spatially irregular. This is emphasised by the Voronoi cell distributions which are more irregular in shape when compensating for missing seismometers. Despite this limited receiver aperture in the backbone array, correlation-convolution SRI is still able to construct robust SRI seismograms. This follows from the theory that non-physical arrivals in the cross-terms associated with scattered surface waves cancel to zero in convolution-

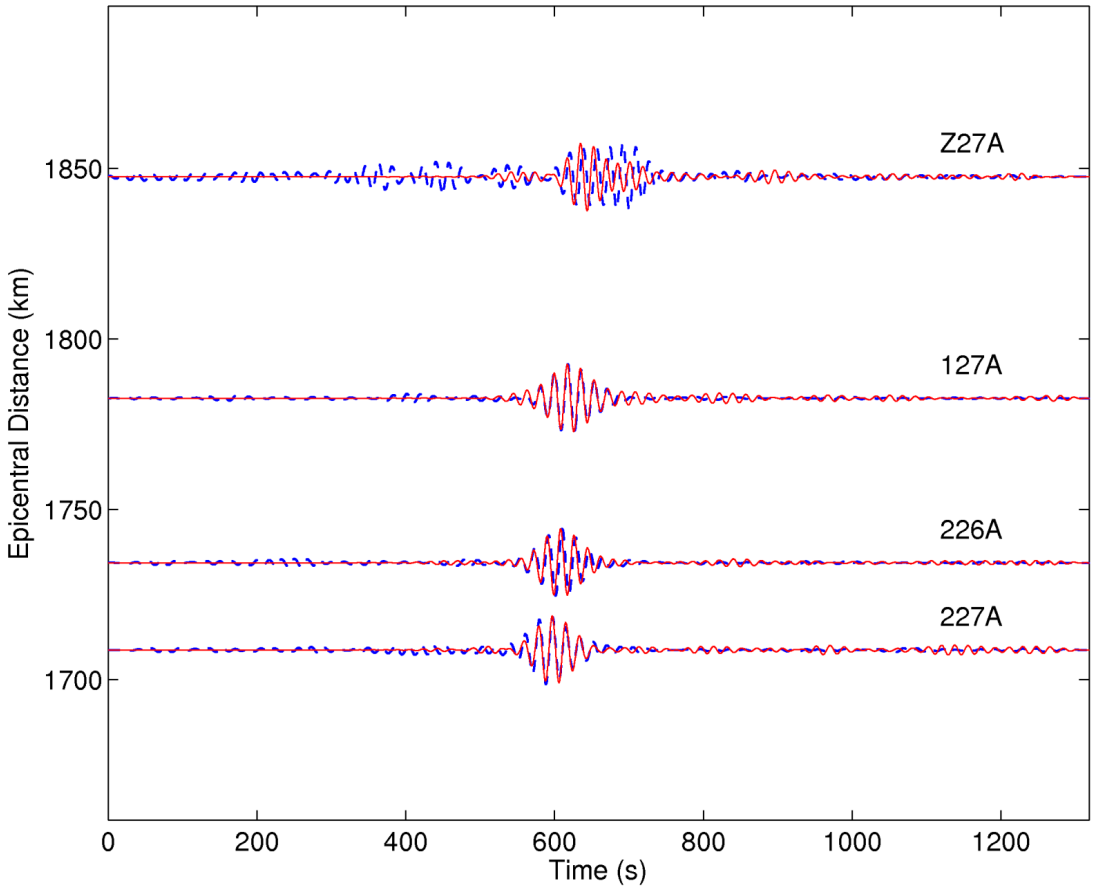

Figure 5.6: Seismograms of the M 5.8 Mexico earthquake constructed using correlation-correlation SRI (dashed/blue traces) compared with those constructed using correlation-convolution SRI (solid/red traces) at target sensors Z27A, 127A, 227A and 226A.

type interferometry (Halliday and Curtis, 2009). Correlation-correlation SRI however is affected by limited aperture and this is evident through the non-physical arrivals present in the reconstruction at target sensor Z27A between approximately 350 s and 450 s in Figure 5.6 (dashed/blue trace). Note that in Section 4.6 we attributed these non-physical arrivals to the spatial irregularity of the backbone array used to perform correlation-correlation SRI. Comparing both correlation-correlation and correlation-convolution SRI data thus allows one to discriminate between physical and non-physical arrivals in the SRI reconstructions.

At the largest length scale we used correlation-convolution SRI to significantly extend the source-to-receiver geometry. SRI seismograms were constructed on target sensors located almost 4000 km from the earthquake epicentre and up to 2420 km from the backbone array of seismometers. We note that although convolutional

interferometry does not have an implicit assumption of zero attenuation, herein noise-based correlational interferometry is still used to construct the SRI propagators $G(\mathbf{x}, \mathbf{r})$, hence this correlation-convolution approach to SRI still has an implicit elastic assumption, which is questionable at these large propagation distances. The results of correlation-convolution SRI were questionable at these distances as surface wave arrivals were out of phase with the real recordings and large non-physical arrivals dominated the SRI reconstruction at the largest length scale at target sensor GOGA.

Correlation-based noise interferometry as in Equation (2.14) derives the propagators necessary for interferometry i.e. estimates of the Green's functions $G(\mathbf{x}, \mathbf{r})$ which are used to project the earthquake seismograms recorded on backbone seismometers $\mathbf{x}$ to a new location - that of the target sensor $\mathbf{r}$. The larger length scale example shows that SRI performs less effectively when these propagators are required to redatum seismic responses over larger distances. Target sensor GOGA is located almost 4000 km from the earthquake epicentre and up to 2420 km from the backbone array. The SRI seismogram constructed at this location contains spurious arrivals that do not appear in the SRI seismograms constructed at R29A, R30A and R31A, or in the SRI seismograms constructed on the smallest length scale at sensors Z27A, 127A, 227A and 226A.

Here we attribute these artefacts to correlation-induced non-physical arrivals that are most prominent when the distances over which the SRI propagators operate are large. We begin by considering the three wavefield components that contribute to the SRI reconstructions: 1) the estimated Green's functions constructed between each backbone array seismometer and the target sensor that act as the interferometric propagators ($G(\mathbf{x}, \mathbf{r})$ constructed via correlation as in Equation (2.14)), 2) the real earthquake signals recorded on the backbone array seismometers ($R(\mathbf{x}, \mathbf{s})$ as in Equation (2.32)) that are back-projected to the new target sensor location via the projection operators, and 3) the convolution functions constructed at each backbone array seismometer that are weighted and stacked (summed) to construct the final SRI seismogram at the new target sensor location (the integrand of Equation (2.32) for each backbone seismometer at $\mathbf{x}$). These three components are deconstructed and shown in Figures 5.7 and 5.8A-C for the SRI seismograms constructed at target sensors GOGA and R29A, respectively.

On the largest length scale, the estimated Green's functions constructed between GOGA and each backbone seismometer (Figure 5.7A) contain prominent non-physical arrivals prior to the main surface wave arrivals that are outlined by the thick black

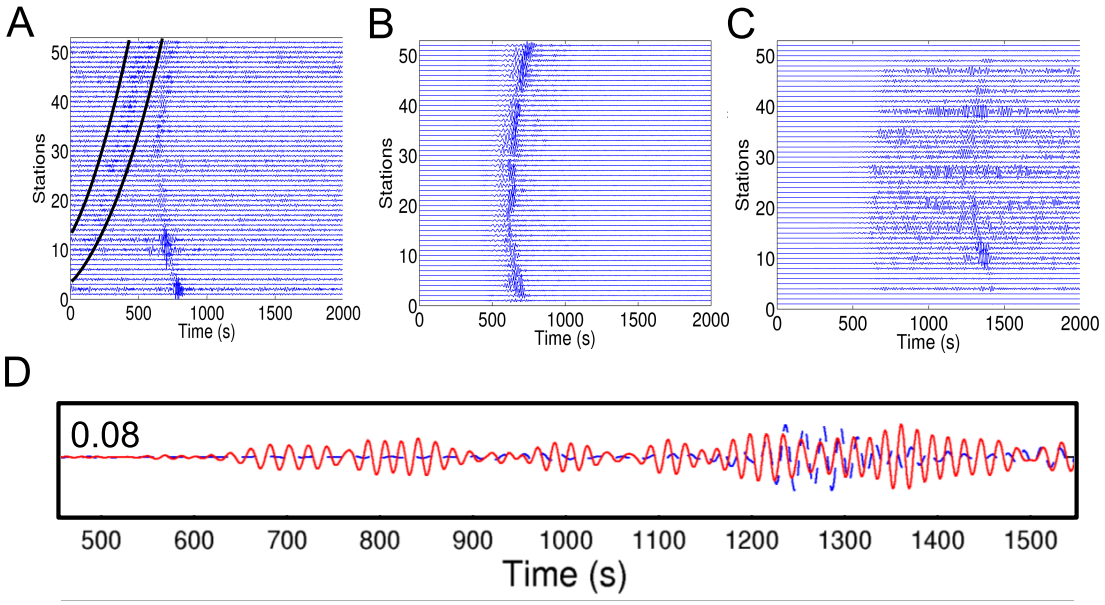

Figure 5.7: The three components (A-C) of the SRI reconstruction (D): (A) The estimated Green's functions $G(\mathbf{x}, \mathbf{r})$ constructed as in Equation (2.14) between target sensor GOGA and 52 of the seismometers located along lines 24A and 25A of the backbone seismometer array. The thick black lines highlight the prominent non-physical arrivals that occur prior to the main surface waves. (B) The recordings of the M 6.5 earthquake at each of the 52 backbone seismometers ($R(\mathbf{x}, \mathbf{s})$). (C) The convolution functions constructed by convolving the traces in (A) with the traces in (B), thus constructing the integrand of Equation (2.32) for all backbone seismometers at $\mathbf{x}$. (D) Integration (summation) over all traces in (C) as in Equation (2.32) constructs the SRI seismogram $TG(\mathbf{r}, \mathbf{s})$ (solid/red trace) and is compared here to the real recording of the earthquake at GOGA (dashed/blue trace). The match between the real and SRI seismograms is quantified by the correlation coefficient and is shown here in (D) above the traces on the left of the figure.

lines in Figure 5.7A. The recordings of the M 6.5 earthquake that occurred off the coast of California are constructed well on all backbone seismometers (Figure 5.7B). The individual convolution functions constructed on each backbone seismometer however are less well constructed (Figure 5.7C) and integration (summation) over all of these traces constructs the SRI seismogram at target sensor GOGA. This seismogram is compared with the real recording of the earthquake at that same sensor in Figure 5.7D and a very low correlation coefficient of 0.08 is calculated. We see that the artefacts in the convolution functions prior to the main surface wave arrivals between approximately 500 s and 1000 s have interfered constructively in the final SRI reconstruction to produce the early, non-physical arrivals at $\sim$ 800 s in Figure 5.7D. We conclude that when the distance between the backbone array seismometers and the target sensors is large (in this case up to 2420 km), we can no longer assume the medium is non-attenuating. This breakdown in the underlying assumption of elasticity for correlation-type interferometry thus introduces non-physical arrivals into the projection operators constructed via processes of correlation (Equation (2.14)) These spurious arrivals have large amplitudes and can be seen prior to the main surface waves in Figure 5.7A (outlined by the thick black lines). Furthermore, these non-physical arrivals are transferred into the convolution functions through processes of convolution with the recorded data (in Equation (2.32)). Constructive interference of all arrivals in the final integration (summation) thus constructs spurious arrivals in the final SRI seismogram. Replacing correlation with convolution in the inter-source interferometry step (e.g. applying Equation (2.32) over Equation (2.31)) does not therefore diminish the non-physical arrivals when the distance over which the SRI propagators are constructed is large.

On the other hand, the shorter distance between the backbone seismometers and sensor R29A (between 200 km and 1200 km) allows one to construct robust estimated Green's functions that contain fewer non-physical arrivals (Figure 5.8A). These SRI propagators are thus able to successfully project the real earthquake energy (Figure 5.8B) to the location of sensor R29A, without introducing too many non-physical arrivals into the convolution functions (Figure 5.8C) and hence into the SRI seismogram (Figure 5.8D). We see that the convolution functions have interfered constructively in Figure 5.8D to recreate an SRI seismogram that is a close match to the real recording of the earthquake (a correlation coefficient of 0.56).

Finally, we consider the three wavefield components of the SRI seismograms constructed over the smallest length scale. These are shown in Figure 5.9 for the

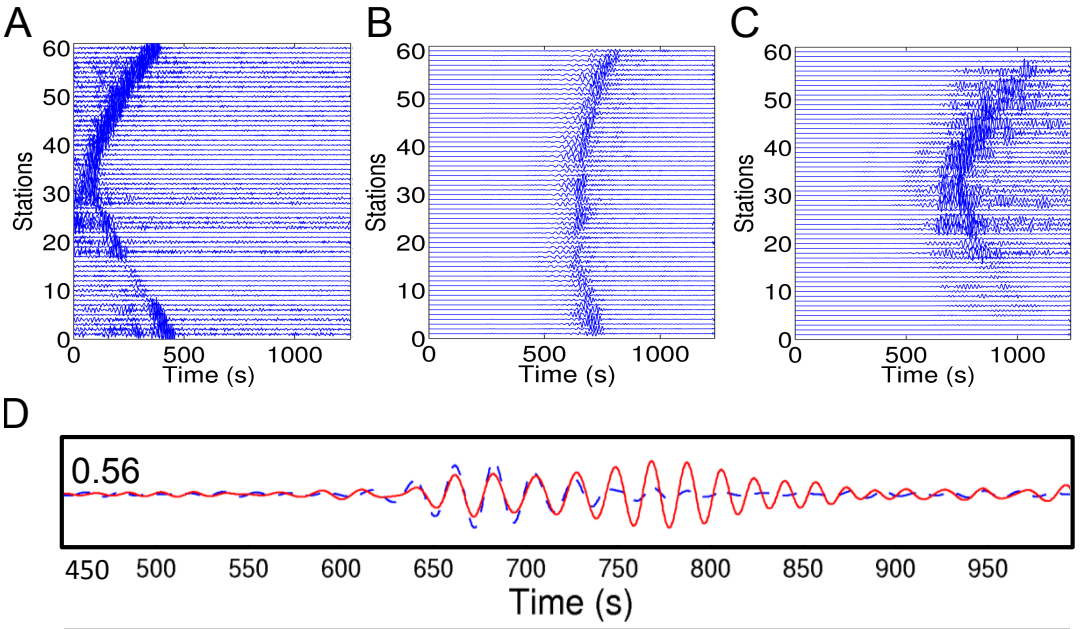

Figure 5.8: The three components of the SRI reconstruction as in Figure 5.7 but for target sensor R29A, which is located less than 1200 km from 60 of the seismometers located along lines 25A and 26A of the North-South aligned backbone array.

SRI reconstruction at target sensor 227A. A comparison of this SRI seismogram with the real recording of the M 5.8 earthquake is shown in Figure 5.9D. In Figure 5.9A we observe that the estimated Green's functions are constructed well - clear surface wave arrivals are constructed between target sensor 227A and each of the 10 backbone array seismometers that are located just 210 km - 435 km from the target sensor. At this small length scale, correlation-induced non-physical arrivals do not obscure the main surface wave estimates. Convolving these SRI propagators with the real earthquake seismograms recorded on the backbone seismometers (shown here in Figure 5.9B) constructs the convolution functions and we again observe clear surface wave reconstructions with very few non-physical arrivals appearing before the main arrivals (Figure 5.9C). Integrating over the 10 backbone seismometers projects the real earthquake recordings to the location of target sensor 227A and it is this constructive interference of the convolution functions that constructs a near perfect retrospective seismogram of the earthquake, as shown here in Figure 5.9D with a correlation coefficient of 0.84. We thus conclude that SRI is most successful at smaller length scales (inter-station distances up to $\sim$ 1200 km) as correlation-type interferometry introduces fewer (or smaller amplitude) non-physical arrivals into the SRI propagators

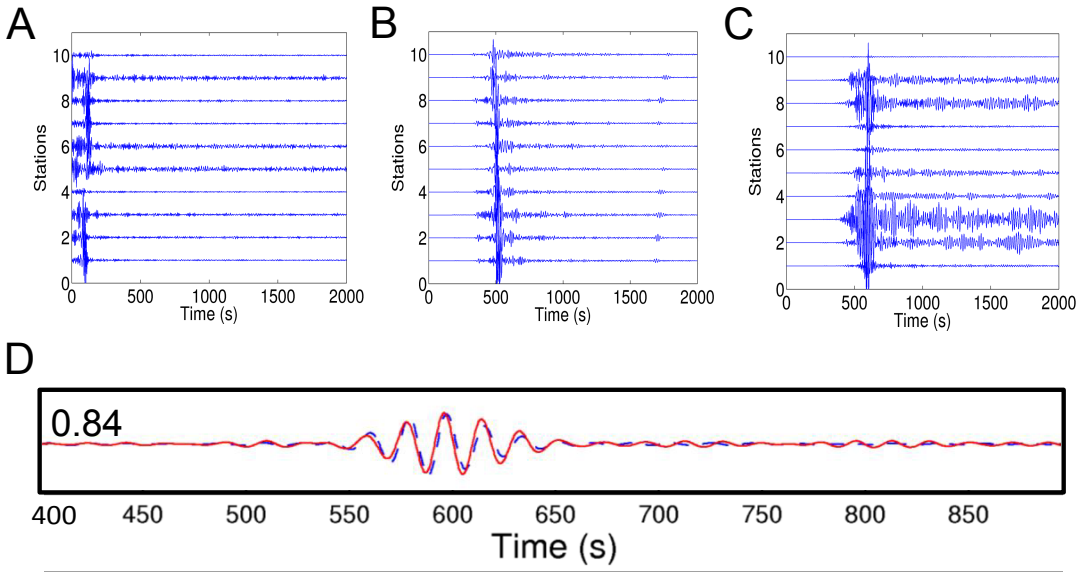

Figure 5.9: The three components of the SRI reconstruction as in Figure 5.7 but for target sensor 227A, which is located less than 435 km from 10 of the seismometers located along lines 5 and 6 of the East-West aligned backbone array.

at these length scales and thus a clearer, more accurate SRI seismogram is constructed.

Deconstructing the SRI seismograms into the three individual wavefield components allows a qualitative set of criteria to be defined for constructing accurate correlation-convolution SRI seismograms. First, it is important for the noise interferometric Green's functions (constructed using processes of correlation) to exhibit clear surface wave arrivals and few artefacts, as these estimated Green's functions are the SRI propagators that project the earthquake energy to the locations of the target sensors. Second, the surface wave arrivals propagating from the earthquake source need to be recorded clearly on the backbone seismometer array. This is important as it is this energy that is redatumed (projected) to the locations of the target sensors via processes of convolution. Third, the surface wave estimates present in the convolution functions (constructed by convolving the SRI propagators with the real earthquake recordings) need to interfere constructively when stacked (summed) over all backbone seismometers. Any artefacts that exist in the SRI propagators are transferred to the convolution functions and are thus incorporated into the final SRI reconstruction in this final stack summation.

In Chapter 6 we shall perform both correlation-correlation and correlation-convolution SRI to reconstruct 87 earthquakes on up to eight target sensors. We will perform a quantitative analysis on the signal-to-noise ratios of each of the three

wavefield components of the SRI seismograms and this will allow us to quantify the successes and limitations of the SRI methodologies when performed over different spatial and magnitude scales.

Furthermore, in Chapter 7 we shall provide an alternative approach to Green's function estimation. We shall use the method of multidimensional deconvolution (MDD) in place of correlation-based noise interferometry in an attempt to improve the quality of the SRI propagators when constructed over large propagation distances ($>$ 500 km).

5.6 Conclusion

We have used correlation-convolution source-receiver interferometry (SRI) to reconstruct earthquake seismograms on eight target sensors located at small and large length scales from backbone arrays of seismometers on which the earthquake energy was originally recorded.

At the smallest length scale we reconstruct a M 5.8 earthquake on four target sensors located approximately 220 km - 470 km from a backbone seismometer array consisting of 25 seismometers aligned East-West in New Mexico. At this length scale we find that correlation-convolution SRI successfully constructs near perfect earthquake seismograms retrospectively and allows one to discriminate between physical and non-physical arrivals that contaminate the SRI seismograms constructed using correlation-correlation SRI.

At the larger length scale we reconstruct a M 6.5 earthquake on three target sensors located approximately 235 km - 1200 km from a backbone seismometer array consisting of 139 seismometers aligned North-South in the centre of the United States. At this length scale we find that the SRI seismograms do not accurately approximate the surface wave arrival times of the real recordings of the earthquake at those locations. Finally, at the largest length scale we reconstruct the same M 6.5 earthquake on a target sensor located up to 2420 km from the same North-South aligned backbone seismometer array, and almost 4000 km from the earthquake epicentre. Again, the SRI surface wave estimates are not accurately constructed as there is a poor match between the real and SRI seismograms recorded/constructed on this sensor. Furthermore, the SRI seismogram is obscured by large amplitude artefacts at earlier travel times. We attribute these artefacts to errors in the SRI propagators constructed via noise interferometry and processes of correlation.

At this largest length scale, the SRI propagators are constructed over distances up to 2420 km and we are unable to make the assumption for correlation-type interferometry that the medium is non-attenuating. This breakdown in one of the underlying assumptions of correlation-type interferometry introduces non-physical arrivals into the SRI propagators. We thus find that correlation-convolution SRI as discussed herein is most successful when the SRI propagators are required to operate over distances up to $\sim$ 500 km. Over these distances fewer correlation-induced non-physical arrivals are present in the SRI propagators and processes of convolution act to eliminate any non-physical arrivals that would be associated with an irregular distribution of backbone seismometers.

To conclude, correlation-convolution SRI is capable of extending the source-to-receiver geometry considerably, but this is not without its limitations. Over larger length scales the constructed noise interferometric Green's functions are less robust, which in turn constructs unreliable correlation-convolution SRI seismograms. In Chapter 7 we will introduce an alternative method to noise interferometry in an attempt to improve the Green's function estimates over these largest length scales. Here we propose that correlation-convolution SRI is best invoked over shorter length scales (up to $\sim$ 500 km) as the effects of attenuative media on the SRI reconstructions are likely to be weaker, i.e., non-physical arrivals will have lower amplitudes which will thus obscure the SRI seismograms less.

Bibliography

Curtis, A., and D. Halliday (2010), Source-receiver wave field interferometry, Physical Review E, 81(4, 2), doi:{10.1103/PhysRevE.81.046601}.

Halliday, D., and A. Curtis (2009), Seismic interferometry of scattered surface waves in attenuative media, Geophysical Journal International, 178(1), 419–446, doi: {10.1111/j.1365-246X.2009.04153.x}.

Slob, E., D. Draganov, and K. Wapenaar (2007), Interferometric electromagnetic Green's functions representations using propagation invariants, Geophysical Journal International, 169(1), 60–80, doi:{10.1111/j.1365-246X.2006.03296.x}.

Snieder, R. (2004), Extracting the Green's function from the correlation of coda waves: A derivation based on stationary phase, Physical Review E, 69(4, 2), doi: {10.1103/PhysRevE.69.046610}.

CHAPTER 6

A Quantitative Analysis of Source-Receiver Interferometry Invoking Multiple Spatial and Magnitude Scales

6.1 Outline

In Chapters 4 and 5 we introduced correlation-correlation source-receiver interferometry (SRI) and correlation-convolution SRI as methods to both spatially and temporally redatum (project) earthquake data to new measurement locations, allowing the construction of new earthquake seismograms retrospectively. Here we expand on the results presented in Chapters 4 and 5 in order to assess the successes and limitations of SRI.

We perform correlation-correlation SRI and correlation-convolution SRI to construct SRI seismograms of 87 earthquakes. These earthquakes sample multiple magnitude scales, from M 2.4 to M 7.8, and are located up to 11,000 km from two backbone seismometer arrays. We use the same two backbone arrays introduced in Chapters 4 and 5, and thus invoke two length scales over which we perform SRI. On the smallest length scale we construct SRI seismograms of 32 earthquakes on target sensors located up to 540 km from a backbone array aligned East-West in New Mexico. On the larger length scale we first construct the SRI seismograms of 36 earthquakes on eight target sensors located up to 2420 km from a second backbone array aligned North-South in the centre of the United States. These 36 earthquakes predominantly originate in regions west of the backbone array. We then construct the

SRI seismograms of the remaining 19 earthquakes over these same large length scales. These 19 earthquakes originate in regions east of the backbone array. Separating the earthquakes in this way allows us to determine the effect of wave propagation directivity on the SRI reconstructions.

On all occasions we analyse the signal-to-noise ratios (SNRs) of the three components of the SRI seismograms: the estimated Green's functions (SRI propagators), the event signals recorded on the backbone array, and the correlation/convolution functions. These analyses allow us to quantify the success with which each component is constructed and to determine the quality of data that is required to perform SRI successfully.

6.2 Introduction

In Chapters 4 and 5 we demonstrated the success with which earthquake seismograms could be constructed over two different length scales using correlation-correlation source-receiver interferometry (SRI) and correlation-convolution SRI. These studies provided robust preliminary examples for both SRI methods, particularly correlation-convolution SRI which has never before been performed in an earthquake seismology setting. At the smaller length scale, the ability of correlation-convolution SRI to remove non-physical arrivals from the results of correlation-correlation SRI was a novel finding that significantly improved the accuracy of SRI seismograms constructed in attenuative media. At the largest length scale, correlation-convolution SRI was used to extend the source-to-receiver geometry to target sensors located up to 2420 km from a backbone array of seismometers (an array required by interferometric theory) and almost 4000 km from the earthquake epicentre. SRI seismograms were compared with real recordings of the earthquake on the same target sensors, and the results of SRI were unreliable: the quality of the match between the real and SRI seismograms was quantified by the correlation coefficient, which was low at 0.08 on one occasion.

To further our understanding of SRI as a method for reconstructing earthquake seismograms retrospectively, we thus automate and apply the SRI methodologies introduced theoretically in Chapter 2 and practically in Chapter 3 to construct the seismograms of 87 earthquakes at new seismometer locations. We use the same receiver geometries presented in Chapters 4 and 5 such that SRI seismograms are constructed on up to eight "target" sensors that are located at varying distances from a backbone array of seismometers - one such array is aligned East-West in New

Mexico and the second is aligned North-South in the centre of the United States. All seismometers are a part of the USArray seismic network.

The 87 earthquakes have been chosen to utilise both backbone seismometer arrays: we use the East-West aligned array and correlation-correlation SRI to construct SRI seismograms of 32 earthquakes on eight target sensors located between approximately 210 km and 540 km from the array seismometers. We then apply correlation-convolution SRI and use the same East-West aligned backbone array to construct SRI seismograms on four of those same target sensors, thus providing further comparisons between correlation-correlation and correlation-convolution SRI. Second, we use the North-South aligned array to construct SRI seismograms of 36 earthquakes on eight target sensors located up to 2420 km from the array seismometers. Here we use both correlation-correlation SRI and correlation-convolution SRI to extend the inter-receiver geometry to these larger length scales. These 36 events originated in regions west of the backbone array. In Section 6.5.1 we then use the North-South aligned array again to construct SRI seismograms of an additional 19 earthquakes on the same eight target sensors located up to 2420 km from the array seismometers. These 19 events originated in regions east of the backbone array and were chosen to test the effect of wave propagation directivity on the SRI reconstructions.

All 87 earthquakes sample a range of magnitude scales from magnitude 2.4 to magnitude 7.8. Furthermore, all earthquakes are located at varying epicentral distances from the backbone seismometer arrays. We separate these events into three classes of earthquake to test the successes and limitations of the SRI methods on reconstructing the seismograms from earthquakes of variable magnitude and location. The first class consists of earthquakes of a small magnitude (up to M 4.0) that occurred locally to the backbone seismometer arrays (within 2500 km); the second includes earthquakes with magnitudes greater than M 4.0 that again occurred locally to the backbone seismometer arrays, and the third includes earthquakes with magnitudes greater than M 5.0 that occurred at teleseismic distances from the backbone seismometer arrays (up to 11,000 km).

Herein we will present a selection of key examples from the group of 87 earthquakes, but all events have been analysed and have thus formed the basis of our conclusions. All 87 earthquakes are listed in Appendix A.

6.3 Method

Consider the geometries shown in Figure 6.1A and Figure 6.1B pertaining to correlation-correlation SRI and correlation-convolution SRI, respectively. The aim of SRI is to estimate the response from the earthquake source at $\mathbf{s}$ on the target sensor at $\mathbf{r}$ without ever recording that response directly. To invoke either correlation-correlation or correlation-convolution SRI we follow the 2-step methodology described in Chapter 3, in which inter-receiver interferometry and inter-source interferometry are combined to perform either SRI method.

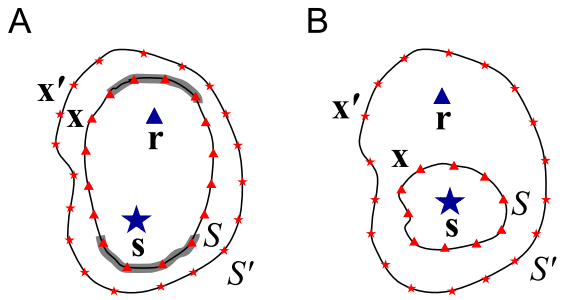

Figure 6.1: Two possible geometries for source-receiver interferometry (SRI) pertaining to (A) correlation-correlation SRI and (B) correlation-convolution SRI. Stars are sources, triangles are receivers. The grey shaded regions in (A) highlight schematically the stationary phase regions on the receiver boundary S which contribute constructively to energy in SRI integrals. Only one or other stationary phase regions need be used provided back-scattered energy is weak across the boundary. For full derivations of the SRI integrals used in each example see Curtis and Halliday (2010).

Step 1: Inter-receiver interferometry

In step 1, we construct the inter-receiver Green's functions $G(\mathbf{x}, \mathbf{r})$ as in Equation (2.28): responses from sources such as $\mathbf{x}'$ on boundary S' are recorded on the target sensor at $\mathbf{r}$ and on seismometers $\mathbf{x}$ on boundary S and cross-correlated. Integration over all source positions estimates the Green's function between $\mathbf{x}$ and $\mathbf{r}$ that represents the response that would have been recorded on the seismometer at location $\mathbf{x}$ if an impulsive source had been fired from the location of $\mathbf{r}$, thus turning the target sensor at $\mathbf{r}$ into a "virtual" source. In practical earthquake seismology settings we simplify this process and construct the estimated Green's functions using ambient noise interferometry as described theoretically in Equation (2.14). We thus replace

the individual sources at locations $\mathbf{x}'$ with mutually uncorrelated noise sources, and the integration over boundary S' becomes a summation over time-averaged cross-correlations of ambient noise. A methodology for Green's estimation by noise interferometry is described in Section 3.2.

Step 2: Inter-source interferometry

In step 2 we perform inter-source interferometry between the target sensor at $\mathbf{r}$ (now a virtual source) and the real earthquake source at $\mathbf{s}$. This process differs between correlation-correlation SRI and correlation-convolution SRI. Thus, consider first the geometry in Figure 6.1A for correlation-correlation SRI: recordings of the earthquake source on all seismometers at locations $\mathbf{x}$ ($R(\mathbf{x},\mathbf{s})$ in Equation (2.30) for a single source at $\mathbf{s}$) are cross-correlated with the newly constructed Green's function estimates ($G(\mathbf{x},\mathbf{r})$) as in Equation (2.31). Integration (summation) over the receiver boundary S completes the inter-source interferometry step and constructs an approximation to the response $T^*G_H(\mathbf{r},\mathbf{s})$, where $T(\mathbf{s})$ is the source signature of the earthquake at $\mathbf{s}$. Note, $T(\mathbf{s})^*G(\mathbf{r},\mathbf{s})$ is not the true response of the earthquake source $\mathbf{s}$ on target sensor $\mathbf{r}$ as G is convolved with the time-reverse of T, rather than with T itself. Thus, when performing correlation-correlation SRI we take only the time-negative part of the integral ($T^*G^*(\mathbf{r},\mathbf{s})$) as, after time-reversal (complex conjugation) we estimate the desired $TG(\mathbf{r},\mathbf{s})$ ($= R(\mathbf{r},\mathbf{s})$). This full derivation for correlation-correlation SRI is provided in Section 2.4.

Next consider the geometry in Figure 6.1B for correlation-convolution SRI. Here, the recordings of the earthquake source $R(\mathbf{x},\mathbf{s})$ on all seismometers at locations $\mathbf{x}$ are *convolved* with the newly constructed Green's function estimates $G(\mathbf{x},\mathbf{r})$. Integration (summation) over the receiver boundary S completes the inter-source interferometry step and constructs the desired one-sided estimate of $R(\mathbf{r},\mathbf{s})$ in Equation (2.30) (for a single source at $\mathbf{s}$) directly, without the need for time-reversal (complex conjugation) of the wavefields. This whole process is defined by Equation (2.32) in Section 2.4.

The full methodologies describing the practical aspects of these processes are provided in Section 3.6. Note that as in Chapters 4 and 5, the final integration (summation) in step 2 described above is performed as an interpolation of the integrands of Equations (2.31) and (2.32) over 2D spatial Voronoi cells. This is described in detail in Section 3.6.5

6.4 Results

Herein we attempt to reconstruct the seismograms of 68 earthquakes on up to eight target sensors using both correlation-correlation SRI and correlation-convolution SRI. SRI seismograms are compared with the real recordings of the events on those same sensors, where the latter exist. The quality of the match between the real and SRI seismograms is quantified by the correlation coefficient which is calculated along the length of each trace. For simplicity, we display these correlation coefficients as an average over the seven target sensors but individual values are presented in the example figures.

6.4.1 SRI reconstructions using the East-West aligned array

First we construct SRI seismograms on eight target sensors from a run of 32 earthquakes recorded on the East-West aligned backbone seismometer array (see Figure 6.2 for a map of all earthquake locations and Figure 6.3 for the array geometry). Combinations of two lines of seismometers from within the backbone array were used to construct the SRI seismograms at the target sensors. These array seismometers obey the spatial criteria defined in Section 3.6.1 and are located between approximately 210 km and 540 km from the target sensors. Of the 32 events, five were of magnitude 3.8 or 3.9 and were located up to 2500 km south of the backbone seismometers, 10 had magnitudes greater than magnitude 4 and were located up to 2400 km south of the backbone seismometers, and the remaining 17 events were of magnitude 5.6 or greater and occurred more than 1900 km south of the backbone seismometers, predominantly originating within the East Pacific Rise. Correlation-correlation SRI was used to construct the SRI seismograms on all target sensors. Correlation-convolution SRI was then used to test the quality and robustness of the SRI seismograms constructed on four of those same target sensors (Z27A, 127A, 227A and 226A). Target sensor 226A (unfilled triangle in Figure 6.3) was removed from its site in February 2009 and thus did not actively record the majority of the 32 earthquakes that occurred between January 2009 and December 2010. The SRI seismograms constructed at this location thus represent new earthquake seismograms constructed retrospectively. Note however that for earthquakes that occurred in January and early February 2009 there are real recordings of those events on target sensor 226A. In those cases we do not construct any "virtual" seismograms but use all SRI seismograms to test the success of the SRI methods at reconstructing earthquake seismograms retrospectively.

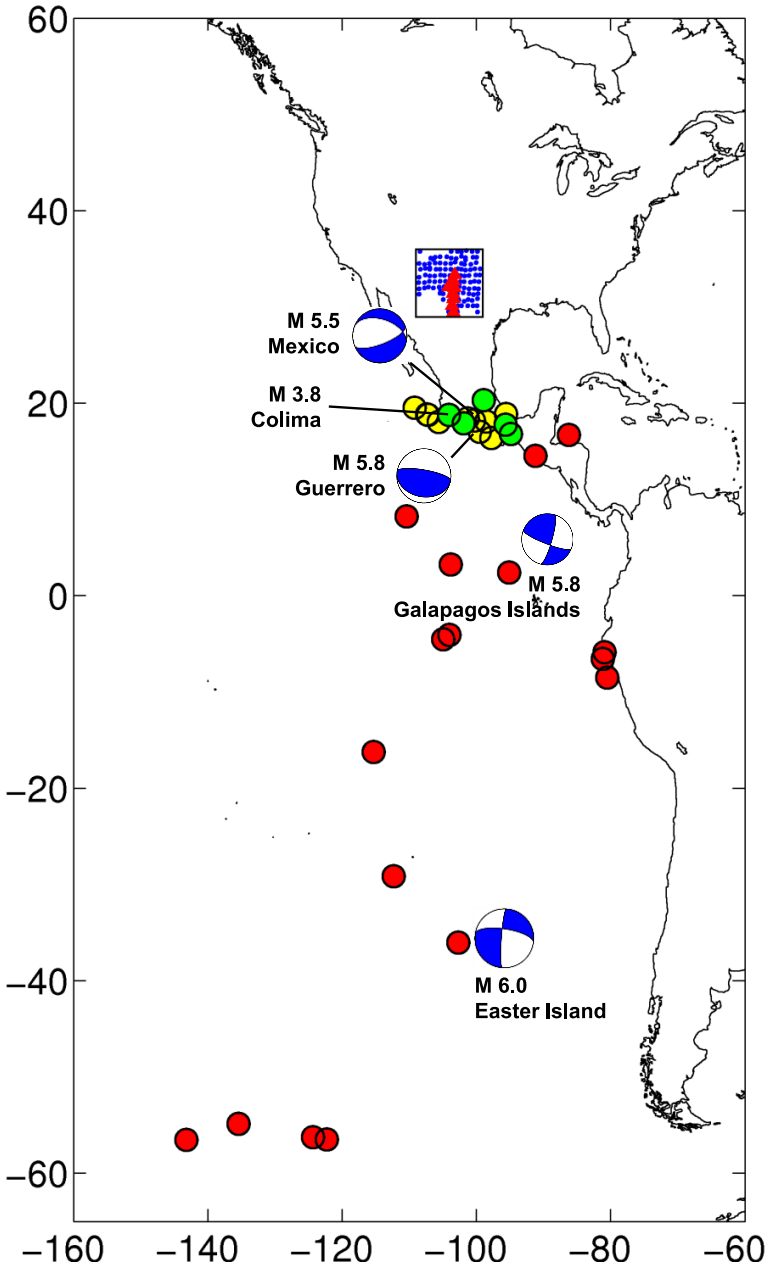

Figure 6.2: Map of all 32 earthquakes (red, yellow and green circles), the seismograms of which are reconstructed using SRI and the East-West aligned array located in New Mexico (blue dots in the square box - see the inset of Figure 6.3 for a detailed map of this seismometer array). Green circles = Earthquakes with M 3.8 or M 3.9, Yellow circles = Earthquakes with M $>$ 4.0, Red circles = Earthquakes with M $>$ 5.5. Earthquake magnitude and source mechanism information highlights those events discussed in the text.

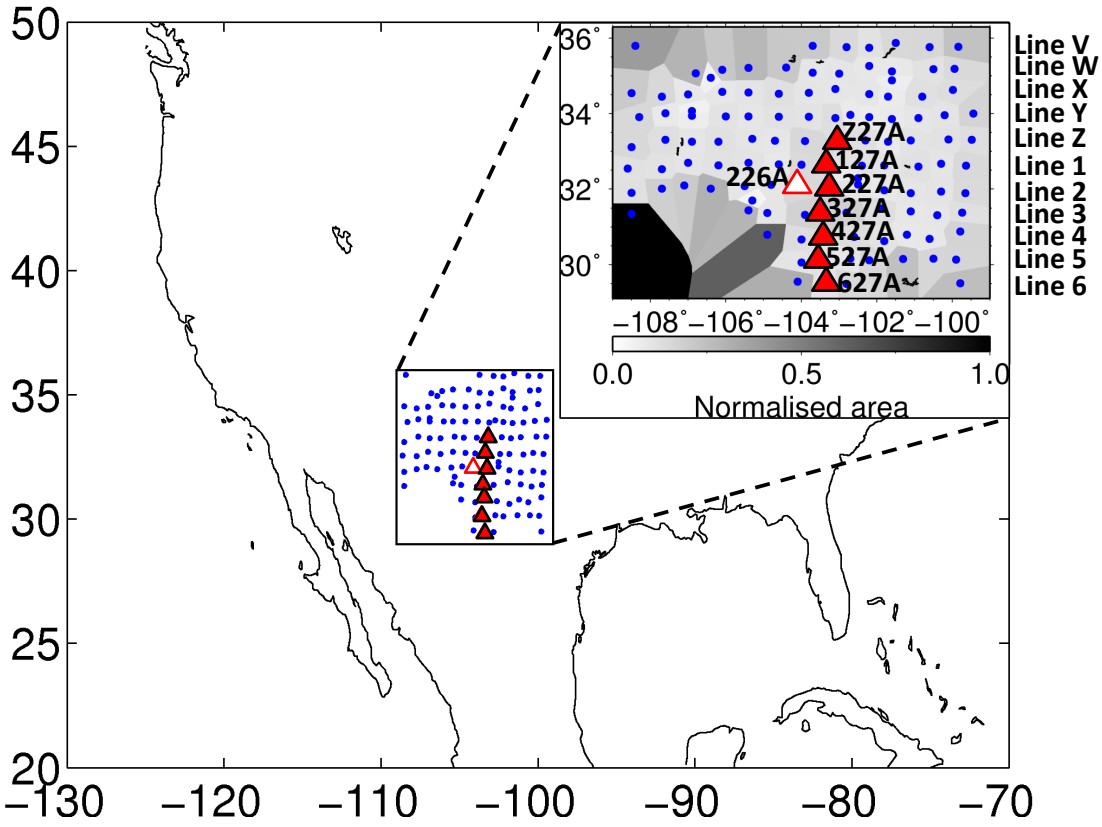

Figure 6.3: Backbone array of seismometers (circles) aligned East-West in New Mexico and the eight target sensors (filled and unfilled triangles) at which earthquake seismograms are constructed using SRI. The backbone array consists of parallel lines of seismometers from the USArray Transportable Array (TA) from Line V in the north to Line 6 in the south (the letters derive from station notation employed by the USArray TA network). 2-line combinations of the backbone array seismometers are used to construct earthquake seismograms at each target sensor by interpolating interferometric integrands (from Equations (2.31) and (2.32)) across Voronoi cells (polygons - shaded according to their area).

The five earthquakes with magnitudes 3.8 or 3.9 (green circles in Figure 6.2) were reconstructed poorly using correlation-correlation SRI (correlation coefficients less than 0.1). These events are listed in Table 6.1. There are no real recordings of the M 3.9 Hidalgo earthquake on the target sensors, thus an average correlation coefficient can not be calculated. Figure 6.4A shows the correlation-correlation SRI seismograms of the M 3.8 earthquake that occurred off the coast of Colima, Mexico, compared with the real recordings of the event on the target sensors, where the latter exist. The same event was reconstructed at sensors Z27A, 127A, 227A and 226A using correlation-convolution SRI and a comparison of these SRI seismograms with the real

recordings is shown in Figure 6.4B. Here we see much greater stability (fewer spurious arrivals) in the SRI seismograms and clear surface wave arrivals can be identified. Using correlation-convolution SRI, the average correlation coefficient across the target sensors increases to a value of 0.4. We conclude that the spurious events between $\sim$ 350 s - 450 s, prior to the main surface wave arrivals in Figure 6.4A (top four traces) are associated with errors in correlation-type interferometry and may be caused by a number of factors including: a lack of receivers at depth, attenuation in the background medium and limited aperture in the receiver boundary (Halliday and Curtis, 2009).

Table 6.1: Earthquakes with magnitudes $<$ M 4.0. SRI seismograms of each event are constructed using the East-West aligned backbone seismometer array. The quality of the SRI seismograms is quantified by the correlation coefficient, taken as an average over all target sensors on which there is a real recording of the event for comparison. Average correlation coefficients are calculated for SRI seismograms constructed using both correlation-correlation SRI and correlation-convolution SRI ('Correlation' and 'Convolution', respectively).

Magnitude	Location	Average Correlation Coefficient	
		Correlation	Convolution
3.8	Offshore Colima, Mexico	0.08	0.40
3.8	Oaxaca, Mexico	0.03	0.10
3.8	Offshore Guerrero, Mexico	0.10	0.05
3.9	Veracruz, Mexico	-0.07	0.12
3.9	Hidalgo, Mexico		

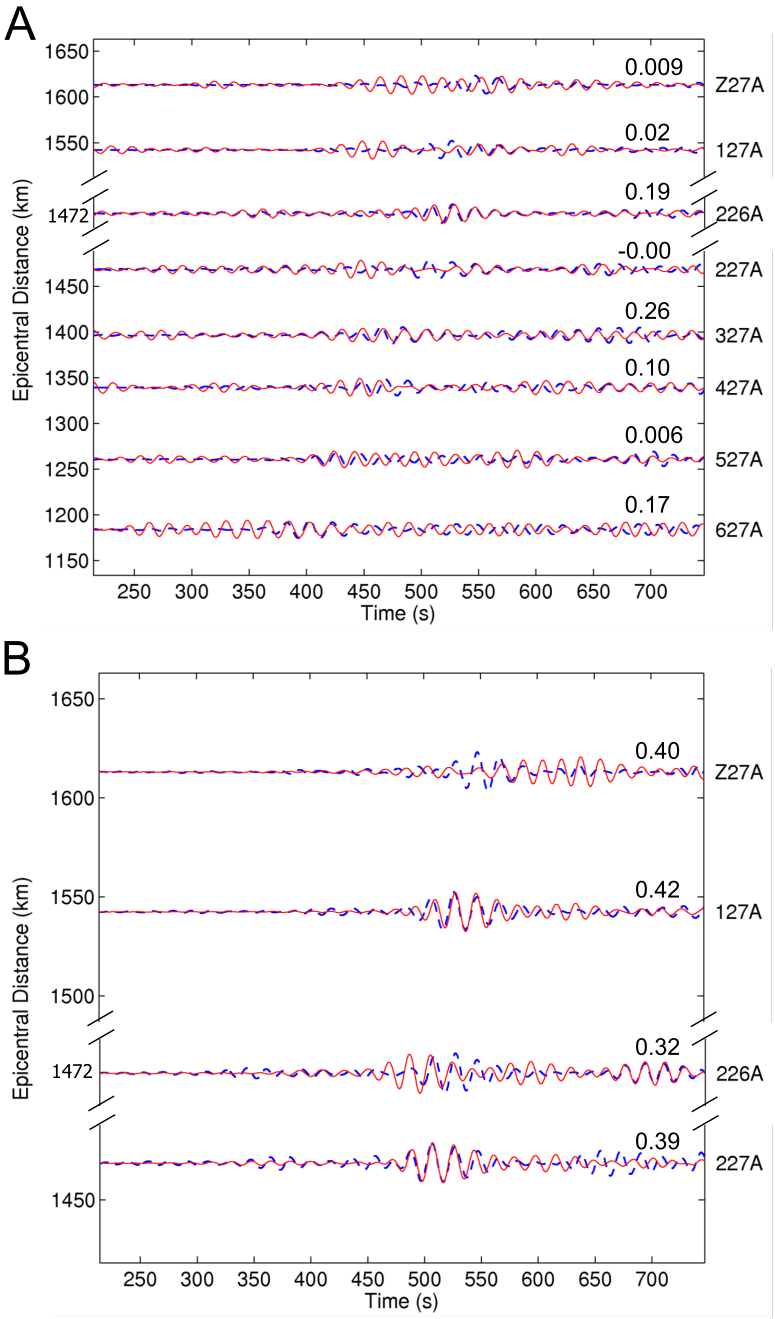

Figure 6.4: SRI seismograms of the M 3.8 earthquake that occurred off the coast of Colima, Mexico. (A) SRI seismograms constructed using correlation-correlation SRI (solid/red traces) and compared with the real recordings of the event (dashed/blue traces) on target sensors Z27A-627A, and sensor 226A, which *was* active at the time the event occurred. The match between the real and SRI seismograms is quantified by the correlation coefficients as listed on the right above each trace. (B) As (A) for SRI seismograms constructed using correlation-convolution SRI on target sensors Z27A, 127A, 227A and 226A.

Next we constructed SRI seismograms of 10 earthquakes of magnitude 4 and greater that occurred within 2400 km of the East-West aligned backbone seismometer array (yellow circles in Figure 6.2). The quality of the SRI seismograms is summarised in Table 6.2.

Table 6.2: Same as Table 6.1 but for SRI seismograms of earthquakes with magnitudes greater than M 4.0.

Magnitude	Location	Average Correlation Coefficient	
		Correlation	Convolution
4.0	Guerrero, Mexico	0.23	0.20
5.5	Mexico	0.58	0.48
5.6	Puebla, Mexico	0.42	-0.01
5.6	Off the coast of Jalisco, Mexico	0.31	-0.11
5.6	Revilla Gigedo Islands region	0.51	0.40
5.7	Offshore Veracruz, Mexico	0.71	0.72
5.8	Guerrero, Mexico	0.70	0.77
6.2	Off the coast of Jalisco, Mexico		
6.3	Oaxaca, Mexico		
6.4	Off the coast of Jalisco, Mexico	0.59	0.38

The negative correlation coefficients are a consequence of some SRI seismograms being out of phase with the real recordings of those events. Events of magnitude 5.5 and greater are constructed well using correlation-correlation SRI: the SRI seismograms are in phase with the real recordings of the events and clear surface wave arrivals can be traced across all target sensors. Furthermore, average correlation coefficients are greater than 0.3 for seven of the nine earthquakes. Figure 6.5 shows the SRI seismograms of the M 5.5 Mexico earthquake reconstructed on the target sensors using (A) correlation-correlation SRI and (B) correlation-convolution SRI. Correlation-correlation SRI does a better job at reconstructing the main surface waves compared to correlation-convolution SRI. However, the spurious signals at $\sim$ 300 s in the SRI seismograms constructed using correlation-correlation SRI (top four traces in Figure 6.5A) are removed by applying convolution within the inter-source interferometry step (see Figure 6.5B). Since target sensor 226A did not record the earthquake the SRI seismogram constructed at this location is a new seismogram. We observe that the surface wave arrival follows the same moveout curve as the surface waves constructed/recorded on the other target sensors. We thus assume that the phase

of this virtual seismogram has been constructed to the same degree of accuracy as those seismograms constructed on the other sensors, on which real recordings provide a reliable comparison.

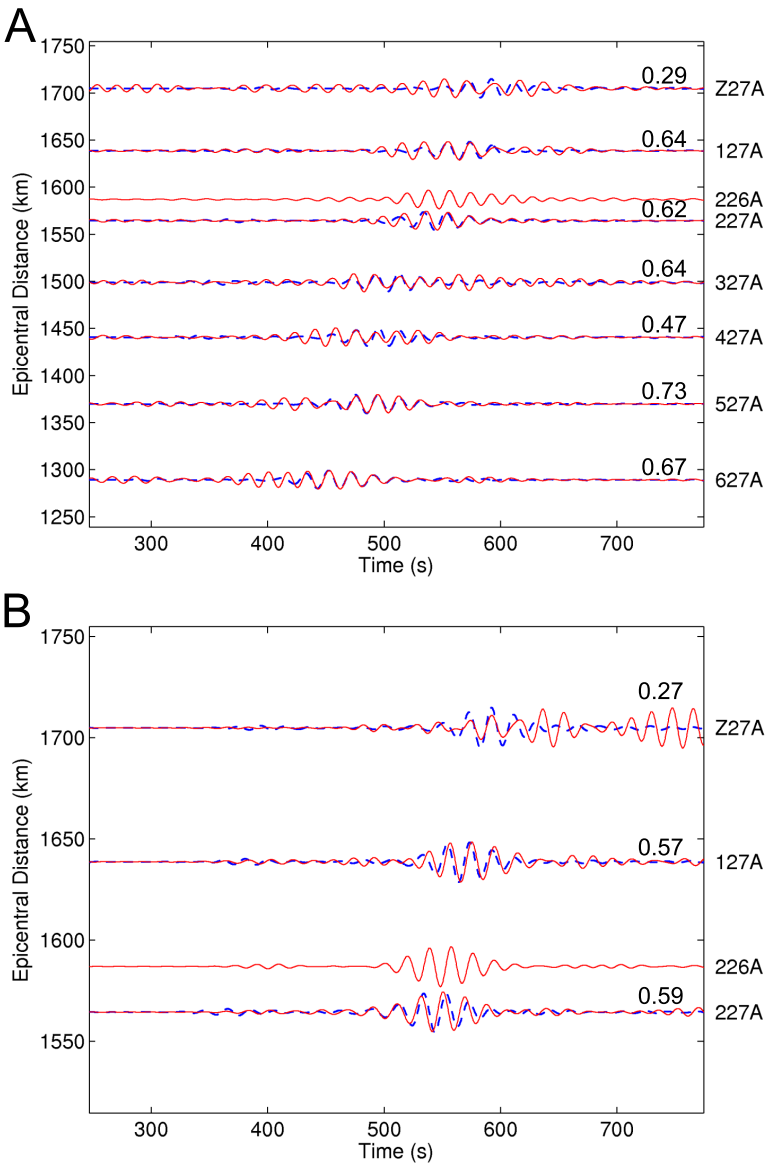

Figure 6.5: Same as Figure 6.4 but for the M 5.5 earthquake that occurred in Mexico. Target sensor 226A was *not* deployed when the event occurred.

Now we construct SRI seismograms of 17 earthquakes of magnitude 5.6 and greater that occurred at teleseismic distances from the East-West aligned backbone array (red circles in Figure 6.2). All earthquakes were located more than 1900 km from the backbone array and nine were located at epicentral distances $>$ 5000 km. The quality of these SRI seismograms is summarised in Table 6.3.

Table 6.3: Sane as Table 6.1 but for SRI seismograms of earthquakes with magnitudes greater than M 5.5.

Magnitude	Location	Average Correlation Coefficient	
		Correlation	Convolution
5.6	East Central Pacific Ocean	0.48	-0.01
5.6	Central East Pacific Rise	0.42	0.45
5.7	Pacific-Antarctic Ridge	0.31	0.47
5.7	Central East Pacific Rise	0.50	0.70
5.8	Galapagos Islands	0.68	0.35
6.0	Pacific-Antarctic Ridge		
6.0	Southern East Pacific Rise	0.40	0.19
6.0	Southeast of East Island	0.56	0.66
6.0	Galapagos Triple Junction	0.66	0.58
6.1	Southern East Pacific Rise	0.38	0.07
6.2	Easter Island region	0.42	0.18
6.3	Southern East Pacific Rise		
6.3	Guatemala	0.38	0.30
7.3	Offshore Honduras	0.62	0.38
5.7	Off the coast of northern Peru		
6.0	Off the coast of northern Peru	0.14	0.10
6.1	Off the coast of northern Peru	0.08	0.09

All 17 events are constructed well using correlation-correlation SRI (correlation coefficients $>$ 0.3), with the exception of the three earthquakes that occurred off the coast of northern Peru. These events were chosen as their epicentres diverged from the traditional great-circle path used to identify potential earthquakes and thus did not follow the spatial criteria in Section 3.6.1 exactly. These events tested the effect of the direction of wave propagation, from an earthquake epicentre to the backbone array, on the SRI reconstructions. Figure 6.6 shows the SRI reconstructions of the M 5.8 earthquake that occurred in the Galapagos Islands with epicentre (2.43,-95.12), using (A) correlation-correlation SRI and (B) correlation-convolution SRI. In Figure 6.6A

we see that the phase of the arrivals are constructed almost perfectly and the moveout of the surface waves can be traced clearly across the line of target sensors. Sensor 226A did not record the event and the seismogram constructed here is thus a truly novel seismogram. In Figure 6.6B however we see that correlation-convolution SRI poorly constructs the surface wave arrivals at target sensors Z27A and 127A as the correlation coefficients are low at -0.01 and 0.27, respectively.

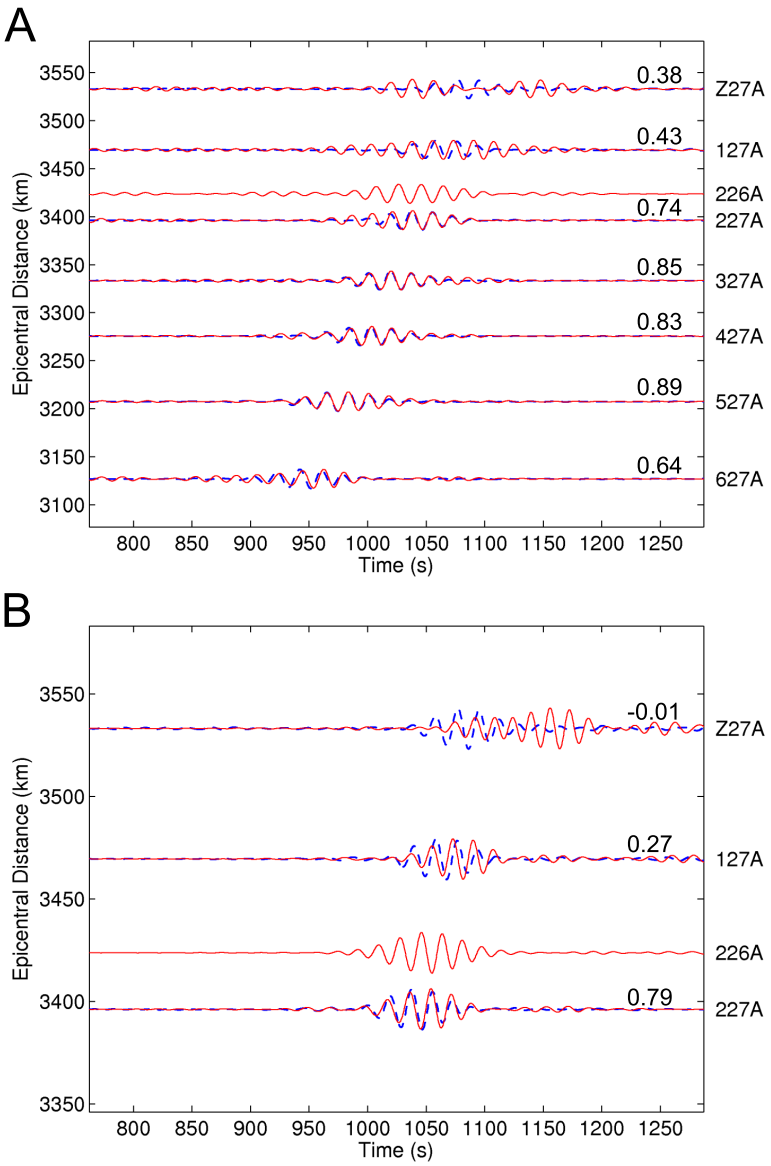

Figure 6.6: Same as Figure 6.4 but for the M 5.8 earthquake that occurred in the Galapagos Islands.

Finally, we look at one result from an earthquake located up to 8000 km from the backbone array. Figure 6.7 shows the correlation-correlation SRI (A) and correlation-convolution SRI (B) seismograms of the M 6.0 earthquake that occurred to the southeast of Easter Island. The SRI seismograms compare well with the real recordings of the event using both methods. In Figure 6.7B we note the success of correlation-convolution SRI in removing the non-physicals arrivals in the SRI seismogram constructed at target sensor Z27A using correlation-correlation SRI, thus increasing the correlation coefficient from 0.19 to 0.61. An SRI seismogram has been constructed at sensor 226A using both methods. In Figure 6.7B we observe that this virtual SRI seismogram may not be constructed to the same quality as the other reconstructions as the main surface wave arrival does not appear to follow the same moveout curve as the other data.

To summarise, at this smallest length scale in which the target sensors are located between approximately 210 km and 540 km from the backbone array of seismometers we observe that both SRI methods are able to successfully reconstruct earthquake seismograms on target sensors if those earthquakes are of magnitude 5.5 or greater and originate in regions southwest of the backbone seismometer array. These regions lie along a great-circle path that intersects the backbone array and target sensors approximately perpendicularly, thus obeying the criteria in Section 3.6.1. SRI was also successful at reconstructing earthquake seismograms of events that occurred up to 8000 km from the backbone array, but was less successful at reconstructing earthquake seismograms of events with low magnitudes. Comparing correlation-correlation SRI with correlation-convolution SRI has allowed physical and non-physical arrivals to be discriminated.

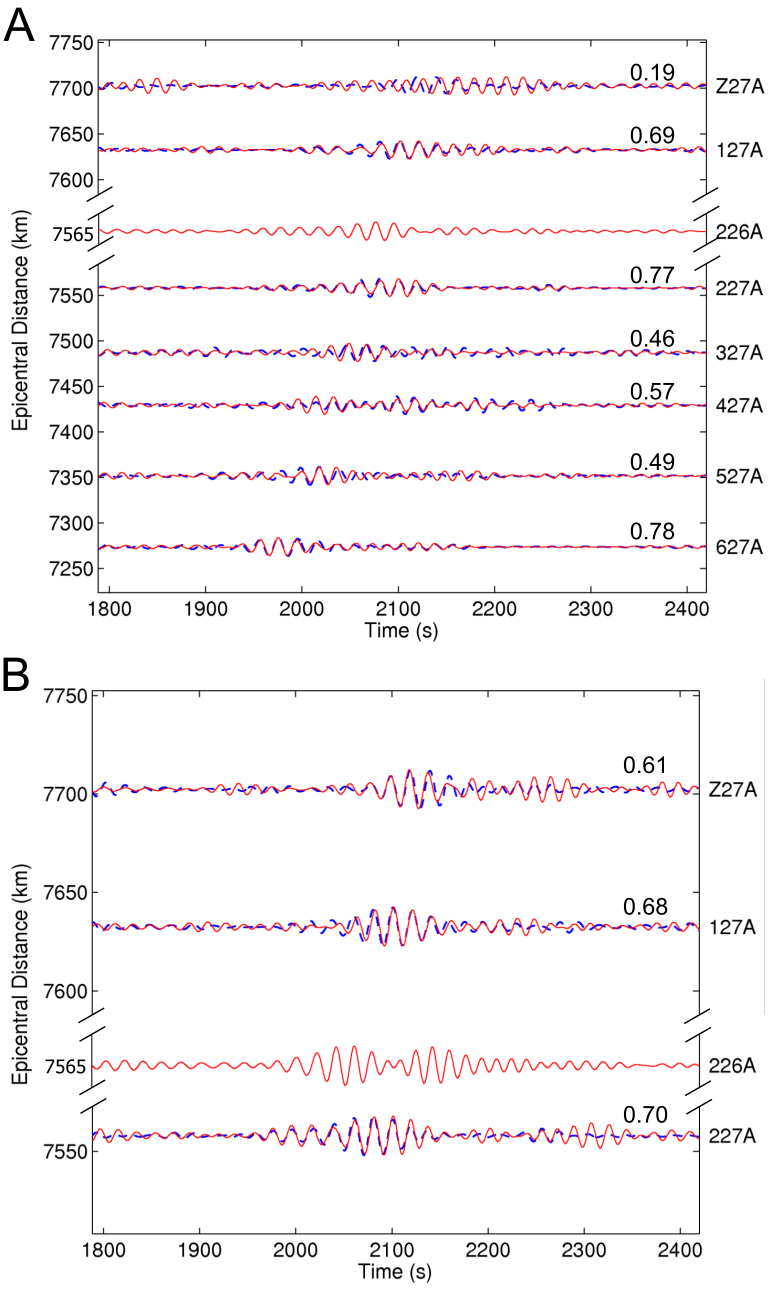

Figure 6.7: Same as Figure 6.4 but for the M 6.0 earthquake that occurred to the southeast of Easter Island.

6.4.2 SRI reconstructions using the North-South aligned array

Next we extend the receiver geometries and apply both correlation-correlation SRI and correlation-convolution SRI to construct SRI seismograms on eight target sensors from a run of 36 earthquakes recorded on the North-South aligned backbone array of seismometers (see Figure 6.8 for a map of all earthquake locations and Figure 6.9A for the array geometry). 2-line combinations of seismometers from the backbone array were most successful at constructing the SRI seismograms at the eight target sensors: at target sensors WDC, BMN, DUG and GOGA we used seismometers along lines 24A and 25A of the backbone array. This defined the larger length scales as target sensor WDC was located over 1900 km to the west of the backbone array seismometers chosen for SRI, whilst target sensor GOGA was located up to 2420 km to the east of those same array seismometers. At target sensors P21A, R29A, R30A and R31A we used 2-line combinations of backbone seismometers located along lines 24A-28A of the North-South aligned array and between 200 km and 1200 km from the target sensors. These target sensor-backbone seismometer distances are more comparable to the smaller length scales introduced in Section 6.4.1. The 2-line combinations of backbone seismometers thus obey the spatial criteria defined in Section 3.6.1, but with inter-receiver distances extending up to 1200 km for backbone seismometers located in the northernmost and southernmost sections of the array. Target sensor P21A (unfilled triangle in Figure 6.9A) was removed from its site in November 2009 and did not actively record some of the 36 earthquakes. The SRI seismograms constructed at this location thus represent new earthquake seismograms constructed retrospectively. Those earthquakes that occurred prior to November 2009 *were* recorded on sensor P21A; they instead provide a test of the method rather than novel seismograms.

Of the 36 events, 12 had magnitudes between M 2.4 and M 3.8 and were located within 2200 km of the backbone seismometer array; 16 events had magnitudes greater than M 4.0 and occurred up to 2400 km from the backbone seismometer array, predominantly off the coast of California; eight events occurred at distances greater than 6000 km from all backbone seismometers and had magnitudes greater than M 6.0. Either correlation-correlation or correlation-convolution SRI was used to construct the SRI seismograms of these events on the eight target sensors: the majority of these events were located to the west of the array, thus correlation-correlation SRI was used to construct the SRI seismograms at sensors WDC, BMN, DUG and P21A, whilst correlation-convolution SRI was used to construct the SRI seismograms for the same event at sensors R29A, R30A, R31A and GOGA.

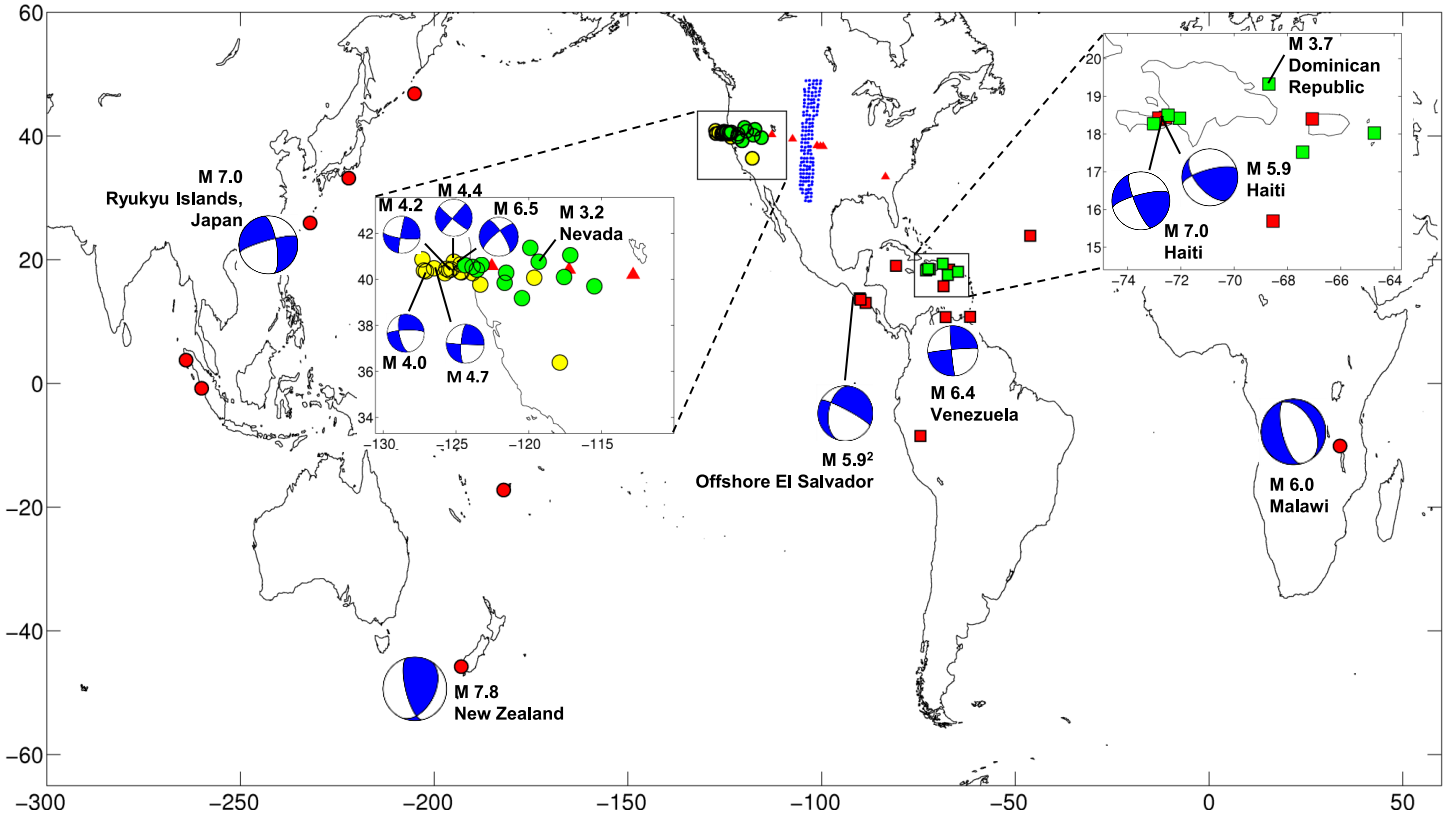

Figure 6.8: Map of all 55 earthquakes (red, yellow and green circles), the seismograms of which are reconstructed using SRI and the North-South aligned array located in the central United States (small dots - see Figure 6.9A and Figure 6.9B for a detailed map of this seismometer array). Green circles = Earthquakes with M 2.0 - M 4.0, Yellow circles = Earthquakes with M $>$ 4.0, Red circles = Earthquakes with M $>$ 5.5. The green and red squares represent the earthquakes discussed in Section 6.5. These events follow the same magnitude-colour code as the earthquakes represented by circles. Earthquake magnitude and source mechanism information highlights those events discussed in the text.

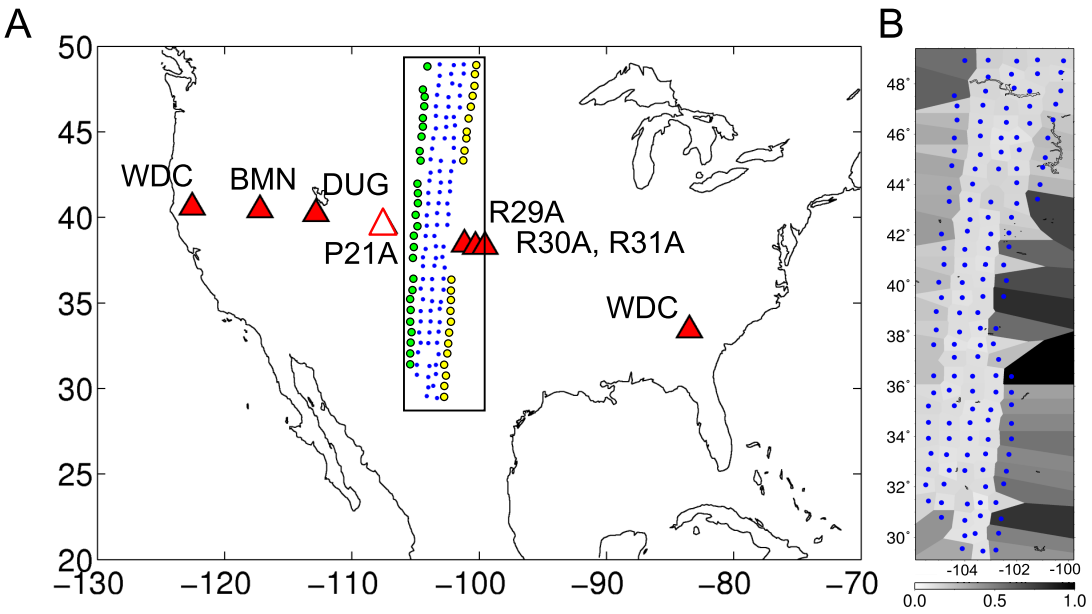

Figure 6.9: Same as Figure 6.3 but for the backbone seismometer array aligned North-South in the centre of the US. The backbone array consists of five vertical lines of seismometers from the USArray TA network, from Line 24A (green circles) in the west to Line 28A (yellow circles) in the east. (B) The Voronoi cells within which the backbone seismometers are embedded and the values of the interferometric integrands are interpolated.

We find that for earthquakes of the smallest magnitude the quality of both their real signals recorded on the target sensors and their corresponding SRI reconstructions are very poor, as the surface wave arrivals are unidentifiable on all seismograms. For the locations of these 12 small magnitude earthquakes see Figure 6.8 and the cluster of green circles in the northwestern United States. The quality of the SRI seismograms as an average over all target sensors is detailed in Table 6.4. SRI is most successful at reconstructing the seismograms from four of the five Nevada earthquakes which display average correlation coefficients > 0.15. Figure 6.10 shows the SRI reconstructions of the M 3.2 Nevada event that occurred within 2000 km of the backbone seismometer array. We observe a good match between the real and SRI seismograms recorded/constructed on target sensors R29A, R30A and R31A, which are located close to the backbone array seismometers (within 1200 km) (correlation coefficients of 0.62, 0.41 and 0.52, respectively). As the distance between the target sensors and the backbone seismometers increases, the SRI seismograms are of a poorer quality, with individual correlation coefficients low at -0.08. This can be seen in Figure 6.10 for the seismograms constructed on target sensors BMN and

WDC. We conclude that, when reconstructing earthquakes with magnitudes below M 4.0, the inter-receiver Green's functions (the SRI propagators) constructed using noise interferometry as in Equation (2.14) are only able to successfully project the earthquake energy recorded on the backbone array to the locations of the target sensors when the backbone array is within 2000 km of the earthquake source and when the target sensors are located at distances up to 1200 km from the backbone seismometers. For length scales outwith these specifications we find that the majority of the SRI reconstructions are out of phase with the real recordings, where they exist, and for a given event there are no common features that are traceable across the seismograms constructed on each of the target sensors. This is further justified through the average correlation coefficients which are very low for earthquakes that originated at large distances from the array and with low magnitudes (e.g. the M 2.6 earthquake that occurred off the coast of California, the SRI seismograms of which were constructed with an average correlation coefficient of 0.09).

Table 6.4: Earthquakes with magnitudes between M 2.0 and M 4.0. SRI seismograms of each event are constructed using the North-South aligned backbone seismometer array. The quality of the SRI seismograms is quantified by the correlation coefficient, taken as an average over all target sensors on which there is a real recording of the event for comparison.

Magnitude	Location	Average Correlation Coefficient
2.4	Northern California	0.14
2.6	Off the coast of California	0.09
2.8	Northern California	0.21
2.8	Northern California	0.03
3.0	Northern California	0.06
3.7	Northern California	0.03
3.8	Northern California	0.16
2.8	Nevada	0.16
3.0	Nevada	0.04
3.2	Nevada	0.27
3.4	Nevada	0.21
3.8	Nevada	0.19

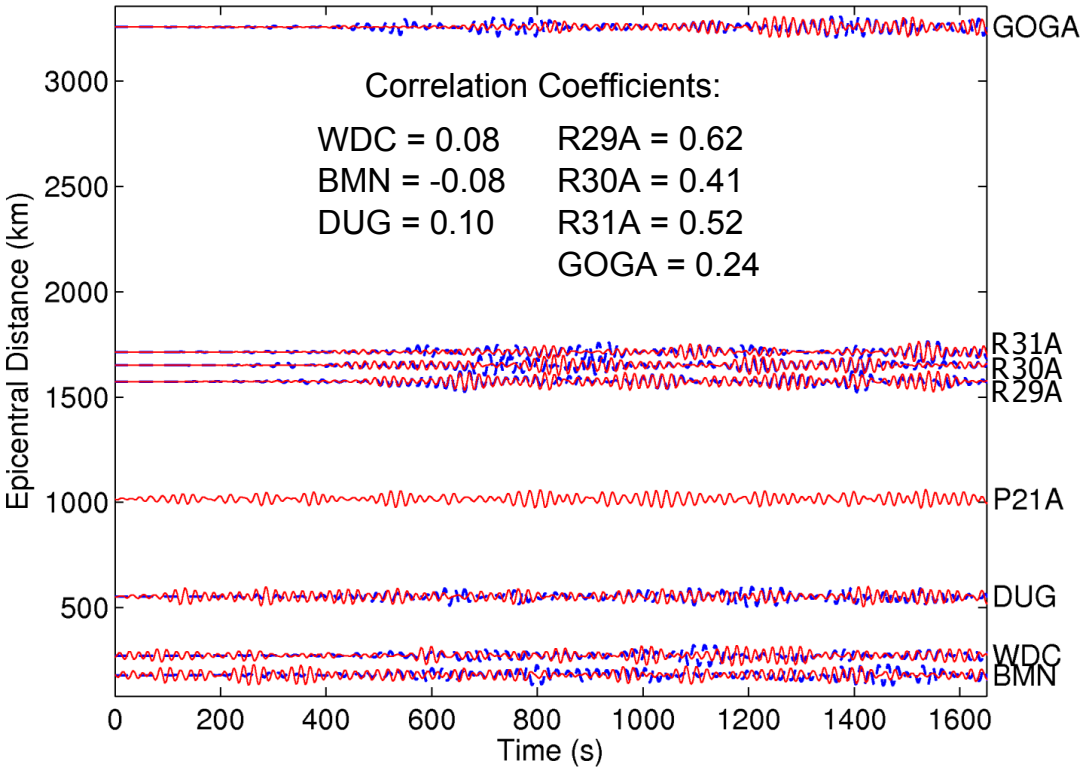

Figure 6.10: SRI seismograms of the M 3.2 Nevada earthquake (solid/red traces) compared with the real recordings of the event (dashed/blue traces) on target sensors WDC, BMN, DUG, P21A, R29A, R30A, R31A and GOGA. Correlation-correlation SRI was used to construct the seismograms at target sensors WDC, BMN, DUG and P21A, whilst correlation-convolution SRI was used to construct the seismograms at sensors R29A, R30A, R31A and GOGA. Target sensor P21A was not deployed when the event occurred. The match between the real and SRI seismograms is quantified by the correlation coefficient as listed in the centre of the figure for each target sensor.

The quality of the SRI seismograms of 16 events of magnitude 4 and greater (yellow circles in Figure 6.8) are summarised in Table 6.5. We notice a discernible difference in the quality of the SRI seismograms with earthquake magnitude, e.g., the SRI seismograms of earthquakes with magnitudes below M 4.4 are of a poor quality as the average correlation coefficients are low (< 0.3) (see Figure 6.11 for the SRI seismograms of the M 4.0 earthquake that occurred off the coast of California).

Table 6.5: Same as Table 6.4 but for SRI seismograms of earthquakes with magnitudes $>$ M 4.0.

Magnitude	Location	Average Correlation Coefficient
4.0	Off the coast of California	0.09
4.0	Northern California	0.10
4.1	Off the coast of California	0.2
4.1	Northern California	0.26
4.2	Nevada	0.05
4.2	Off the coast of California	0.13
4.2	Off the coast of California	0.10
4.2	Off the coast of California	-0.02
4.4	Off the coast of California	0.34
4.5	Off the coast of California	0.16
4.5	Off the coast of California	0.24
4.5	Off the coast of California	0.34
4.7	Off the coast of California	0.37
5.0	Off the coast of California	0.24
5.1	Central California	0.23
6.5	Off the coast of California	0.47

However, the SRI seismograms of events of M 4.4 and greater are better constructed. This is further emphasised when one considers earthquakes of similar epicentre but different magnitude: seismograms of the M 4.2 earthquake that occurred off the coast of California with epicentre (40.46,-125.66) were reconstructed poorly on the eight sensors using SRI and the average correlation coefficient was low at 0.13 (see Figure 6.12). Meanwhile, the seismograms from two other earthquakes that occurred with similar epicentres at (40.77,-125.15) and (40.49,-126.51) but with magnitudes of 4.4 and 4.7, respectively, were reconstructed well using the SRI methods and average correlation coefficients reached 0.34 and 0.37, respectively. These reconstructions are shown in Figures 6.13 and 6.14 and we observe that the surface waves are reconstructed well on target sensors R29A, R30A and R31A as there is a good match between the phase of the SRI seismograms and the phase of the real signals (correlation coefficients up to 0.75). It is with this same confidence that we reconstruct the SRI seismogram on sensor P21A that did not actively record the event. We see that for both the M 4.4 and the M 4.7 earthquakes, the surface wave arrivals constructed on sensor P21A follow the same moveout as the surface waves recorded/constructed on the neighbouring target

sensors. These surface waves are not reproducible at the largest length scales however and one can see far less coherency between the real and SRI seismograms recorded and constructed on target sensors GOGA and WDC. At these largest length scales, the individual correlation coefficients are low (between -0.26 and 0.17) indicating that the SRI seismograms are out of phase with the real recordings of the events. Thus, the SRI seismograms of earthquakes with magnitudes $>$ M 4.4 are best constructed on target sensors located closer to the backbone array (sensors R29A, R30A and R31A which are located less than 1200 km from the array).

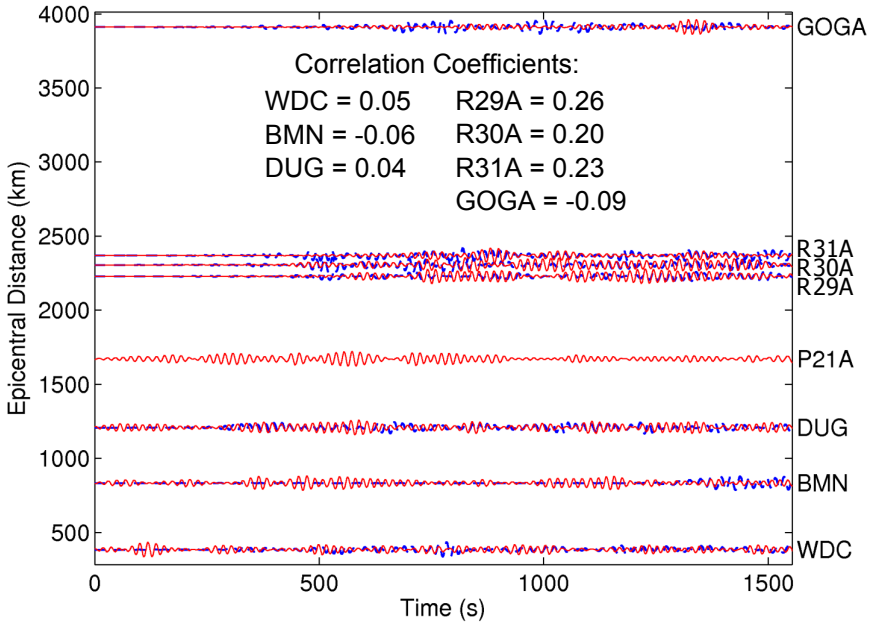

Figure 6.11: Same as Figure 6.10 but for the M 4.0 earthquake that occurred off the coast of California.

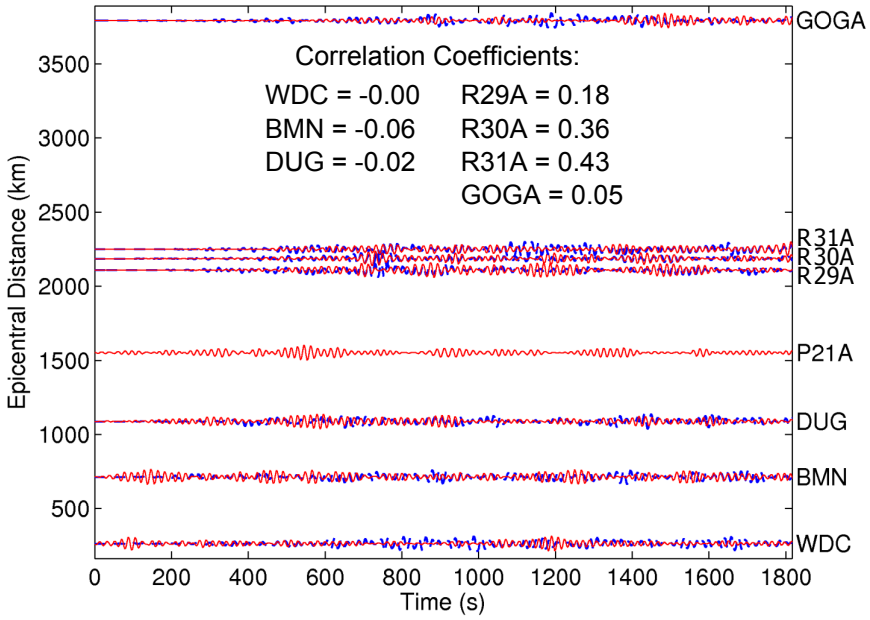

Figure 6.12: Same as Figure 6.10 but for the M 4.2 earthquake that occurred off the coast of California.

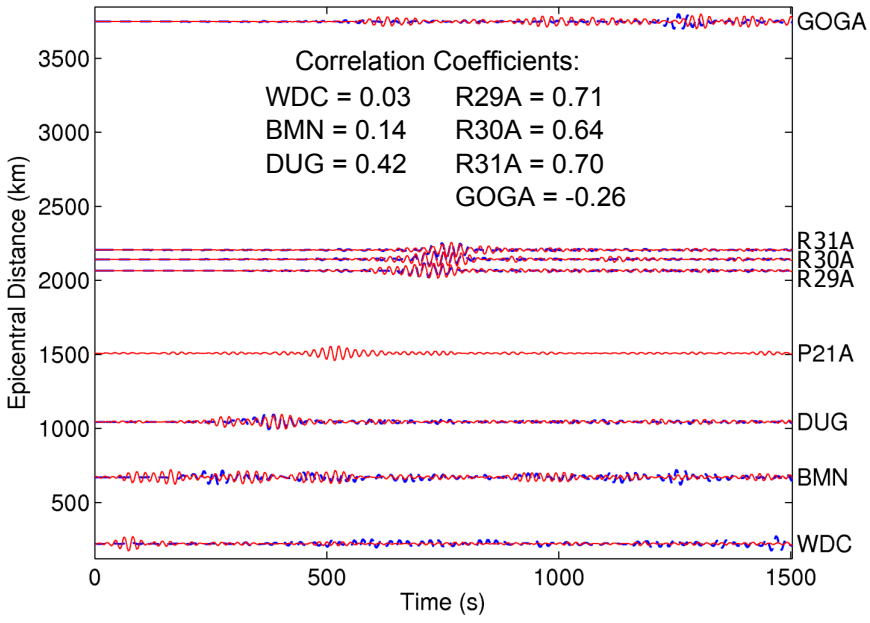

Figure 6.13: Same as Figure 6.10 but for the M 4.4 earthquake that occurred off the coast of California.

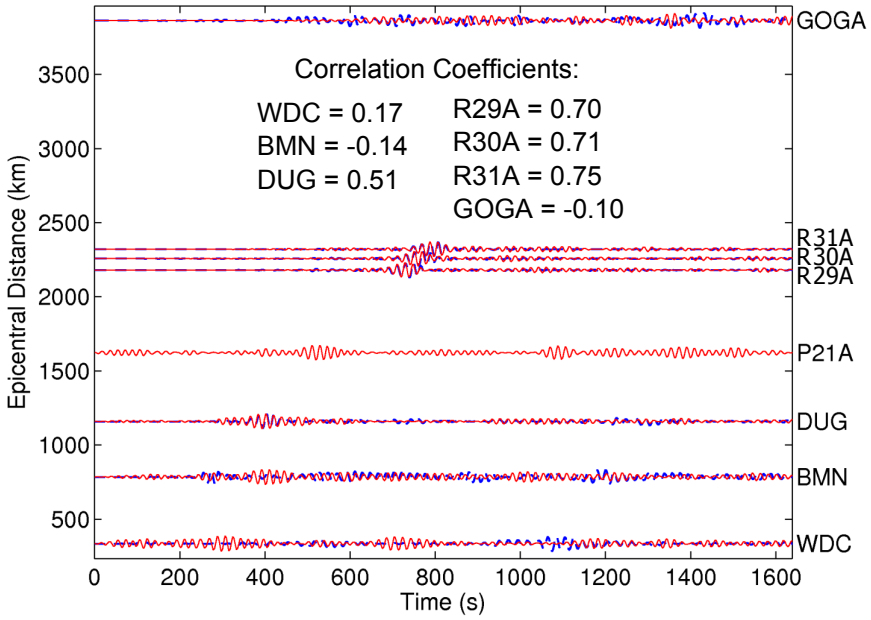

Figure 6.14: Same as Figure 6.10 but for the M 4.7 earthquake that occurred off the coast of California.

Finally, we construct the SRI seismograms of eight earthquakes of magnitude 6 and greater that occurred at teleseismic distances from the North-South aligned backbone array (red circles in Figure 6.8). A summary of the quality of these reconstructions is shown in Table 6.6. If we consider the first seven events, the average correlation coefficients are typically ~ 0.32. This value is higher than the majority of average correlation coefficients calculated previously for the SRI reconstructions of lower magnitude earthquakes. Earthquakes of large magnitude are thus more successfully reconstructed using SRI.

We now take a closer look at the SRI seismograms of the M 7.0 event that occurred in the Ryukyu Islands, Japan, (Figure 6.15) and the M 7.8 event that occurred off the west coast of the South Island, New Zealand (Figure 6.16). For the M 7.0 Ryukyu event we observe the greatest coherency between the real recordings and the SRI seismograms constructed on target sensors R29A, R30A and R31A, as correlation coefficients are high (up to 0.75) and surface wave arrivals can be identified. Furthermore, the surface waves can be traced back to the SRI seismogram at sensor P21A, and almost to the largest length scale at target sensor GOGA. Similar results can be seen for the SRI seismograms of the M 7.8 New Zealand earthquake: the greatest matches between the real and SRI seismograms are observed on target sensors R29A, R30A and R31A as the correlation coefficients have values of 0.62, 0.53 and

0.44, respectively. Although the correlation coefficients of these reconstructions are large, the surface waves are still difficult to identify on the seismograms above the background noise level. This implies that the earthquake surface wave energy was poorly recorded on the backbone array, and thus little energy was projected to the locations of the target sensors by the SRI propagators. Alternatively, source time functions for large earthquakes are often much longer and more convoluted than smaller earthquakes. Hence, surface wave energy may not arrive as a nice "pulse".

Table 6.6: Same as Table 6.4 but for SRI seismograms of earthquakes with magnitudes $>$ M 6.0.

Magnitude	Location	Average Correlation Coefficient
7.0	Ryukyu Islands, Japan	0.30
7.1	South coast of Honshu, Japan	0.33
7.2	Northern Sumatra, Indonesia	0.27
7.3	Fiji	0.35
7.4	East of the Kuril Islands	0.27
7.6	Southern Sumatra, Indonesia	0.31
7.8	Off the west coast of the South Island, NZ	0.42
6.0	Malawi	0.62

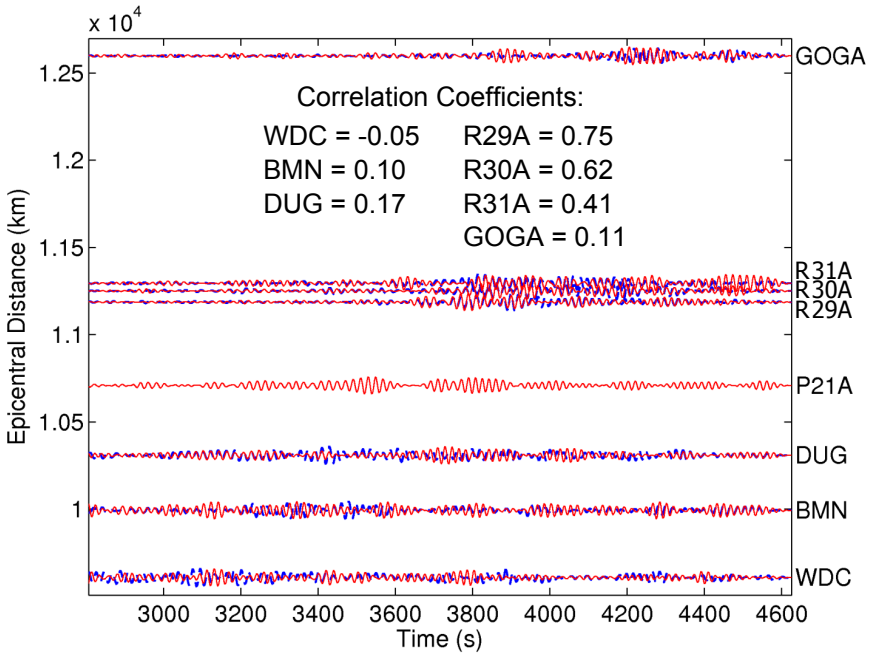

Figure 6.15: Same as Figure 6.10 but for the M 7.0 earthquake that occurred in the Ryukyu Islands, Japan.

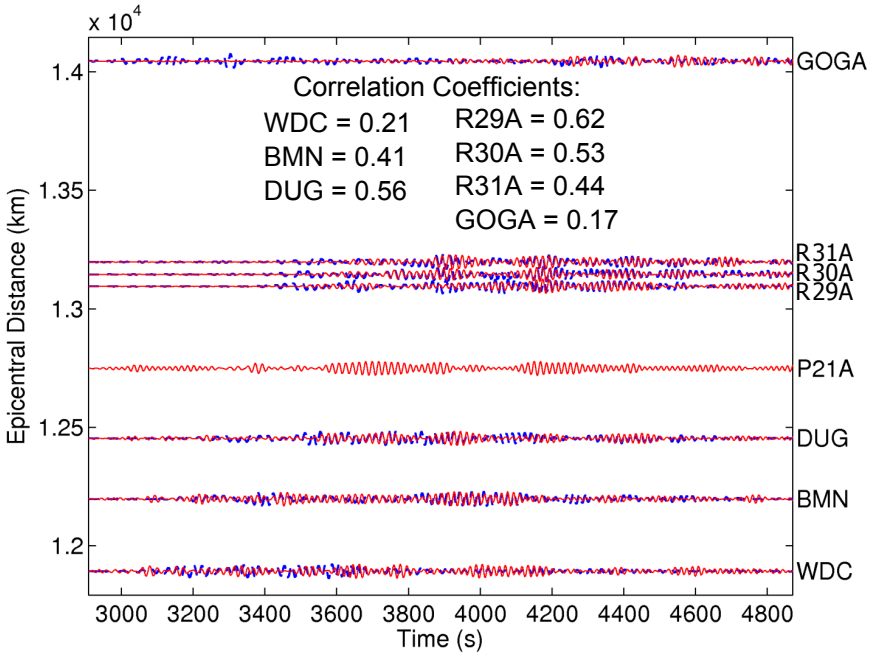

Figure 6.16: Same as Figure 6.10 but for the M 7.8 earthquake that occurred off the west coast of South Island, New Zealand.

All events herein have originated to the west of the backbone array seismometers and the earthquake energy has thus propagated across the United States from West to East. Next we consider one final event: the M 6.0 Malawi earthquake whose seismic energy propagated towards the North-South aligned array from the east. To construct the SRI seismograms of this event at target sensors WDC, BMN, DUG and P21A we thus use correlation-convolution SRI as now the geometry pertains to that shown in Figure 6.1B: the backbone array of seismometers now lies between the earthquake epicentre and the target sensors. Meanwhile, correlation-correlation SRI is used to construct the SRI seismograms on target sensors R29A, R30A, R31A and GOGA as the source-receiver geometries now pertain to that shown in Figure 6.1A; the backbone array is now approximately situated around the stationary phase region of a receiver boundary S that should ideally (and theoretically) completely surround the target sensors and the earthquake epicentre.

The SRI seismograms of the M 6.0 Malawi earthquake are constructed on the target sensors and compared with the real recordings of the event in Figure 6.17. Clear surface wave arrivals are identifiable in the SRI seismograms constructed on all target sensors and all arrivals are almost exactly in phase with the real recordings of the event on those same sensors, where they exist. With the exception of the reconstruction at target sensor GOGA, correlation coefficients are exceptionally large (> 0.68). Furthermore, the largest correlation coefficient is calculated for the SRI reconstruction at target sensor WDC, which is located almost 16,000 km from the earthquake epicentre and over 1900 km from the backbone array of seismometers. Similarly, sensors BMN and P21A are located over 14,900 km from the earthquake epicentre and up to 1540 km and 1080 km from the backbone seismometer array, respectively. These two sensors did not record the event but the surface waves in the SRI seismograms follow the same moveout curve as the available data. We thus place the same confidence in these new, novel seismograms as the SRI seismograms constructed at the other target sensors on which there are real recordings for comparison.

To summarise, at all earthquake magnitude scales the SRI seismograms are best constructed on target sensors R29A, R30A and R31A which lie within 1200 km of the backbone array seismometers. Of the 36 earthquakes studied herein, the seismograms of the M 6.5 earthquake that occurred off the coast of California (as discussed in great detail in Chapters 4 and 5) and of the M 6.0 Malawi earthquake are the only ones to be reconstructed with any reasonable accuracy on target sensors located at the largest length scales.

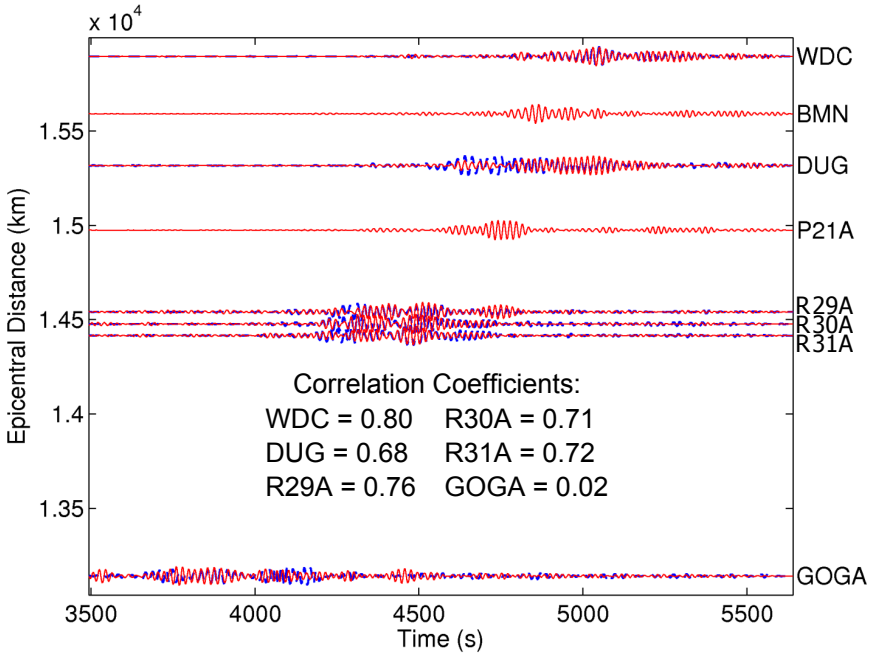

Figure 6.17: SRI seismograms of the M 6.0 earthquake that occurred in Malawi (solid/red traces) compared with the real recordings of the event (dashed/blue traces) on target sensors WDC, DUG, R29A, R30A, R31A and GOGA. Here, correlation-correlation SRI was used to construct the seismograms at target sensors R29A, R30A, R31A and GOGA, whilst correlation-convolution SRI was used to construct the seismograms at sensors WDC, BMN, DUG and P21A. Target sensors BMN and P21A were not deployed when the event occurred.

6.5 Discussion

We have constructed the SRI seismograms of 68 earthquakes (see Figures 6.2 and 6.8 for maps of all earthquake locations) on target sensors using two backbone arrays of seismometers: one orientated East-West in New Mexico (Figure 6.3) and the second orientated North-South in the centre of the United States (Figure 6.9A). On both occasions earthquake seismograms were reconstructed on up to seven target sensors and compared to real earthquake signals recorded on those same sensors. We also constructed the SRI seismograms on two additional target sensors that were deployed and subsequently removed before most of the events occurred. The SRI constructions at these two additional locations are thus truly novel seismograms and demonstrate that even after a sensor has been removed, seismograms can still be obtained at those locations previously occupied provided that the backbone array remains intact (Curtis et al., 2012).

We have tested the SRI method over two length scales: on a small length scale where the backbone array seismometers are located between 210 km and 540 km from the target sensors, and on a larger length scale where the backbone seismometers are located up to 2420 km from the target sensors. We find that the SRI methods are most successful when operating over the smallest length scales as SRI seismograms are constructed with high correlation coefficients (typically > 0.40) when compared with the real earthquake seismograms, and surface wave arrivals are traceable across all target sensors. As the distance between the backbone seismometers and the target sensors increases, SRI seismograms are still constructed well on target sensors located up to 1200 km from the backbone array seismometers (correlation coefficients are often > 0.50 for seismograms constructed on target sensors R29A, R30A and R31A, for example), but the SRI method is far less effective at the largest length scales. With the exception of the M 6.0 Malawi earthquake and the M 6.5 earthquake that occurred off the coast of California, the SRI seismograms of very few events are constructed well at target sensors WDC and GOGA using SRI.

Below we discuss why there are such differences in the quality of the SRI seismograms when constructed over different inter-station distances, but we begin by discussing the differences in the SRI seismograms constructed for earthquakes that originated to the west of the North-South aligned backbone array, compared to those seismograms constructed for earthquakes that originated to the east.

6.5.1 West vs. East: The geological effects of the US

Of the 36 earthquakes reconstructed using the North-South aligned backbone seismometer array, all but one event originated to the west of the array such that the energy from these events propagated towards the backbone array from West to East. The exception was the M 6.0 Malawi event whose seismic energy propagated across the United States from East to West. We observed that when the energy propagated from this latter direction, the SRI seismograms were of much higher quality and were reconstructed well on all target sensors. The main surface wave arrivals could be clearly identified and there was a striking similarity between the phase of the SRI reconstructions and the phase of the real recordings, even at one of the larger length scales at target sensor WDC. This was replicated in the high correlation coefficients which reached a value of 0.80 for the SRI seismogram constructed at target sensor WDC. We explain the difference in the quality of the SRI reconstructions for

earthquakes originating west of the North-South aligned array to those originating to the east to be a result of the underlying geology.

The seismic energy from earthquakes that originate off the coast of California, towards the Cascadia subduction zone, propagates towards the North-South aligned backbone array from West to East, thus sampling the structurally complex western United States Cordillera first. This province extends from the Pacific Coast to the Rocky Mountains and portions of it have undergone severe tectonic activity from early in the Cenozoic era to the present day (Baqer and Mitchell, 1998). East of the Rocky Mountains and extending to the Atlantic Ocean is the second major province of the United States and, in contrast to the western province, it is one that is relatively stable, both structurally and tectonically. A map outlining the main geomorphological units that comprise these two major provinces is shown in Figure 6.18 and a geological map of the United States is shown in Figure 6.19.

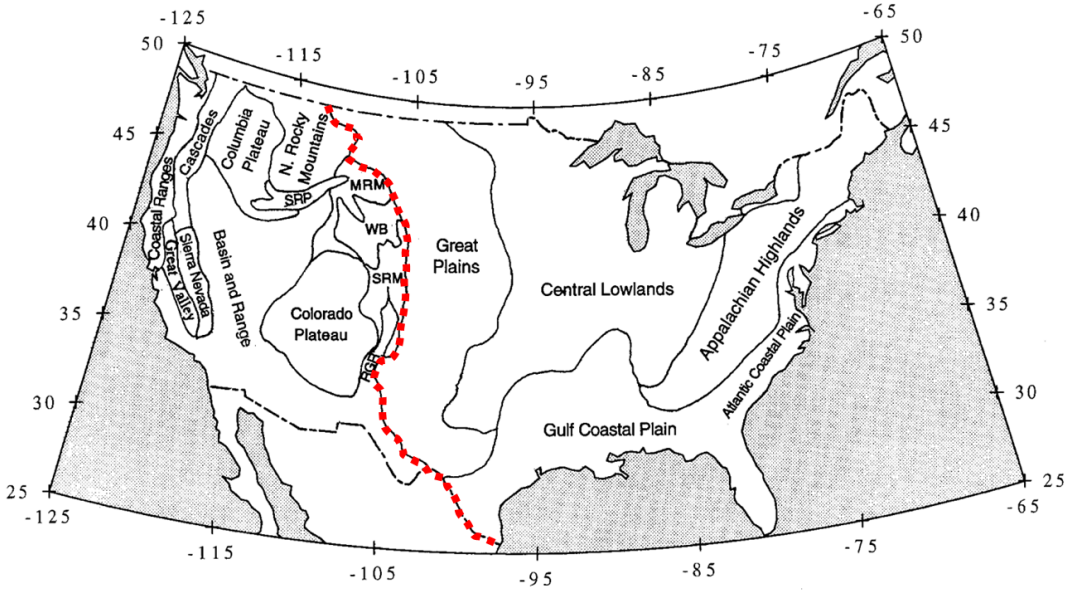

Figure 6.18: The main geomorphological units comprising the two major provinces in the United States, separated here by the dashed (red) line (adapted from Baqer and Mitchell (1998) where SRP = Snake River Plain, MRM = Middle Rocky Mountains, WB = Wyoming Basin, SRM = South Rocky Mountains, and RGR = Rio Grande Rift).

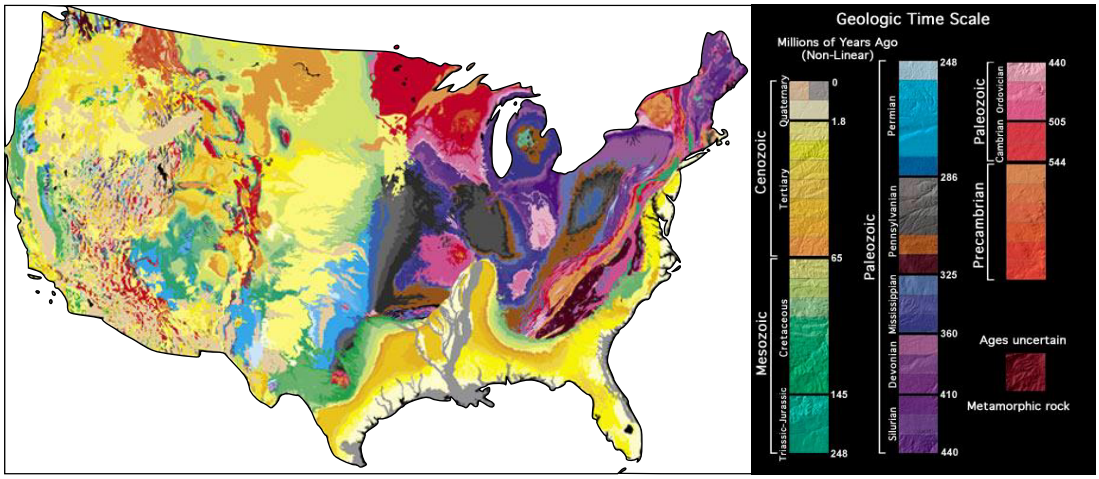

Figure 6.19: The geology of the United States of America colour coded according to the Geologic Time Scale (right). The map is taken from `http://tapestry.usgs.gov/two/color.html`. We observe the highly heterogeneous region of the western United States that compliments the features present in the western geologic province highlighted to the left of the dashed line in Figure 6.18. Similarly, the eastern United States consists of larger, more homogeneous geologic structures that compliment the more structurally stable nature of the eastern province (to the right of the dashed line in Figure 6.18).

Many studies have discussed the physical differences between the tectonically active western US and the stable cratonic eastern US. For example, Dalton and Ekström (2006) undertook a global study of surface wave attenuation and observed a clear distinction between the highly attenuative western US and the less attenuative eastern US (Figure 6.20A), with differences assumed to be thermal in origin. Furthermore, Lin et al. (2012) used USArray data to study broadband surface wave amplification across the US. This new observable allowed the authors to better constrain properties such as elastic velocities, density and anelastic attenuation within the crust and upper mantle. Focusing on the attenuation results, Lin et al. (2012) detected clear differences in the Rayleigh wave attenuation structure of the western US compared to the eastern provinces. These attenuation maps are shown in Figure 6.20 for (B) 30 s and (C) 60 s Rayleigh waves. A much higher attenuation is observed in the western US compared to the eastern US. For the 30 s Rayleigh wave, the observed attenuation structure was found to agree well with known geological features characterised by higher temperatures, such that hotter crust and upper mantle in the west, e.g., beneath the Snake River Plain/Yellowstone hotspot track (see Figures 6.18 and 6.19), was characterised by a higher attenuation/lower Q (Lin et al., 2012).

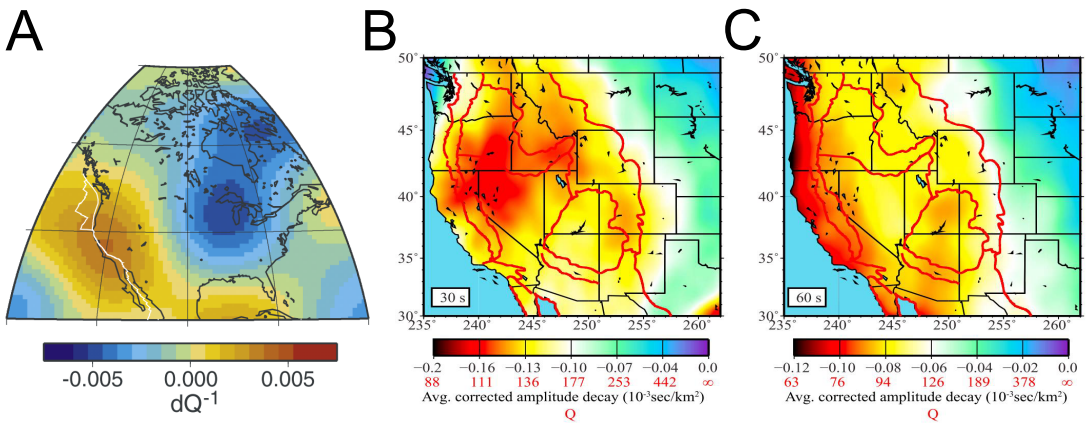

Figure 6.20: Attenuation maps of the United States for (A) 150 s Rayleigh waves (Dalton and Ekström, 2006)), (B) 30 s Rayleigh waves (Lin et al., 2012), and (C) 60 s Rayleigh waves (Lin et al., 2012). In (B) and (C) approximate Q values are given in red below the scale bar.

To further understand these differences in the geologic structure of the United States on the results of SRI, we shall now consider a second group of earthquakes that originated to the east of the North-South aligned backbone array (green and red squares in Figure 6.8). The SRI seismograms of a M 7.0 earthquake that occurred in Haiti and a M 6.4 earthquake that occurred off the coast of Venezuela are shown in Figures 6.21 and 6.22, respectively. On both occasions the SRI seismograms are constructed well as surface wave arrivals can be traced across all target sensors and the phase of the SRI reconstructions are comparable to the phase of the real signals recorded on those same sensors. Correlation coefficients are high for all SRI seismograms, reaching a maximum value of 0.94 for the reconstruction of the M 7.0 Haiti earthquake constructed at R29A. Furthermore, the correlation coefficients of the SRI seismograms constructed at target sensor WDC are also large, reaching a value of 0.64 for the reconstruction of the M 6.4 event that occurred off the coast of Venezuela. Target sensor P21A did not record either of the events. However, we observe that the SRI surface wave arrivals constructed on P21A follow the same moveout as the surface waves constructed on the other seven target sensors. We thus conclude that when earthquake signals propagate through the stable, less attenuating eastern US first, the quality of the SRI reconstructions are improved compared to when the earthquake signals sample the highly attenuating western US first.

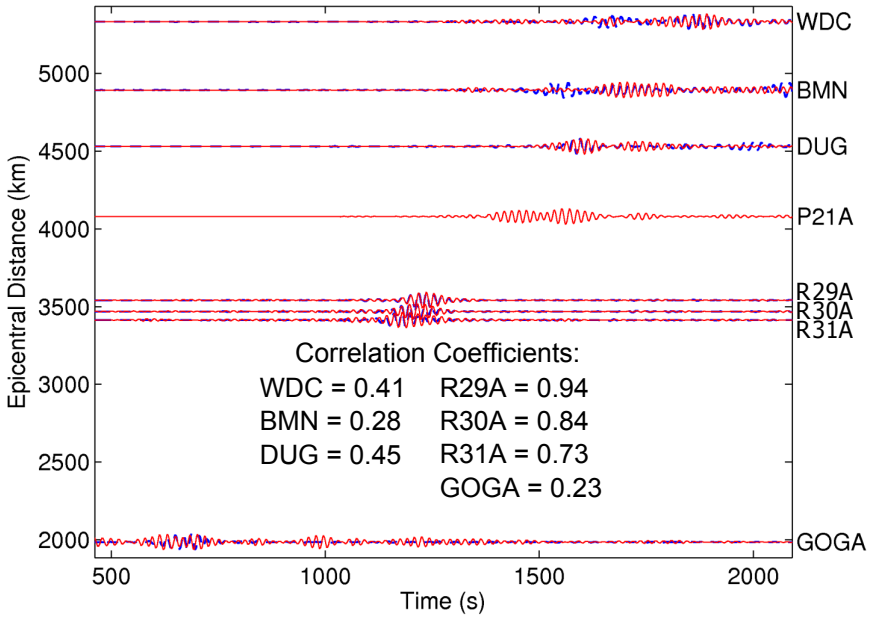

Figure 6.21: Same as Figure 6.17 but for the M 7.0 earthquake that occurred in Haiti.

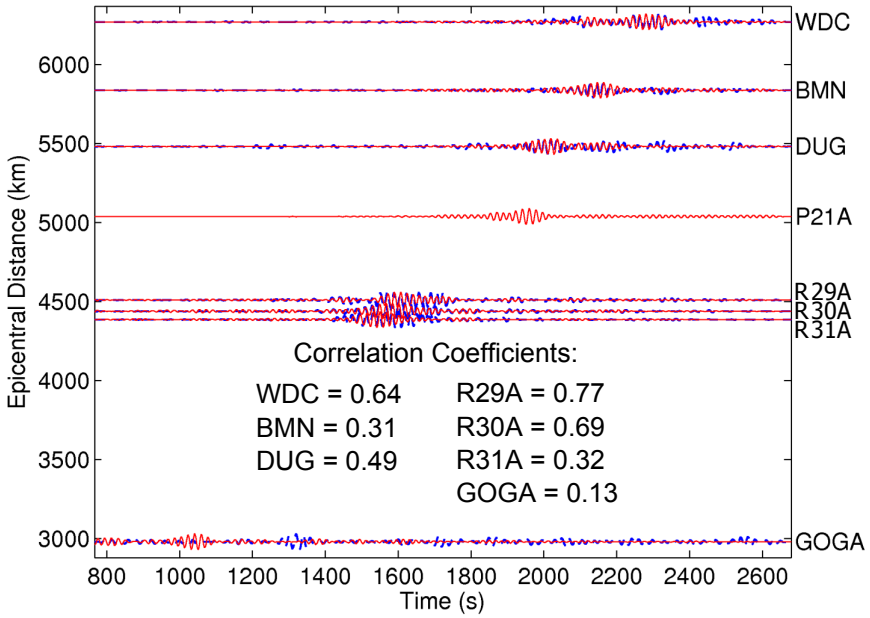

Figure 6.22: Same as Figure 6.17 but for the M 6.4 earthquake that occurred off the coast of Venezuela.

If we break down the steps involved in constructing the SRI seismograms, we can begin to understand the effects of the differences in Rayleigh wave attenuation across the United States on the SRI reconstructions. Figures 6.23 and 6.24 show the three components of the seismograms of the M 7.0 Japan earthquake and the M 7.0 Haiti earthquake, respectively, reconstructed on target sensor WDC using SRI.

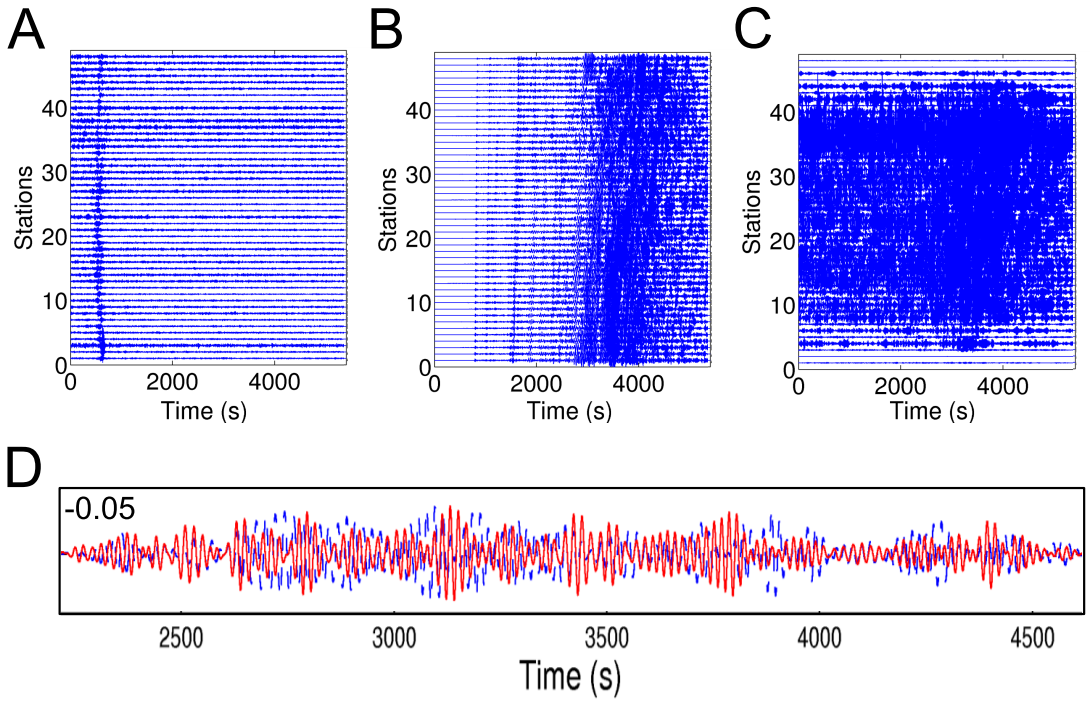

Figure 6.23: The three components of SRI: (A) the estimated Green's functions $G(\mathbf{x}, \mathbf{r})$ constructed between target sensor WDC and the seismometers along lines 24A and 25A of the North-South aligned backbone seismometer array, (B) the real recordings of the M 7.0 Japan earthquake on those same backbone seismometers $R(\mathbf{x}, \mathbf{s})$, and (C) the correlation functions constructed for each backbone seismometer by cross-correlating the traces in (A) with those in (B) (Equation (2.31)). (D) Interpolating the traces in (C) to points within 2D tapered Voronoi cells and integrating (summing) over all points constructs the SRI seismogram $R(\mathbf{r}, \mathbf{s})$ (solid/red trace), compared here to the real recording of the event (dashed/blue trace) at target sensor WDC. The quality of the match between the real recording and the SRI seismogram is quantified by the correlation coefficient, given here above the traces in (D).

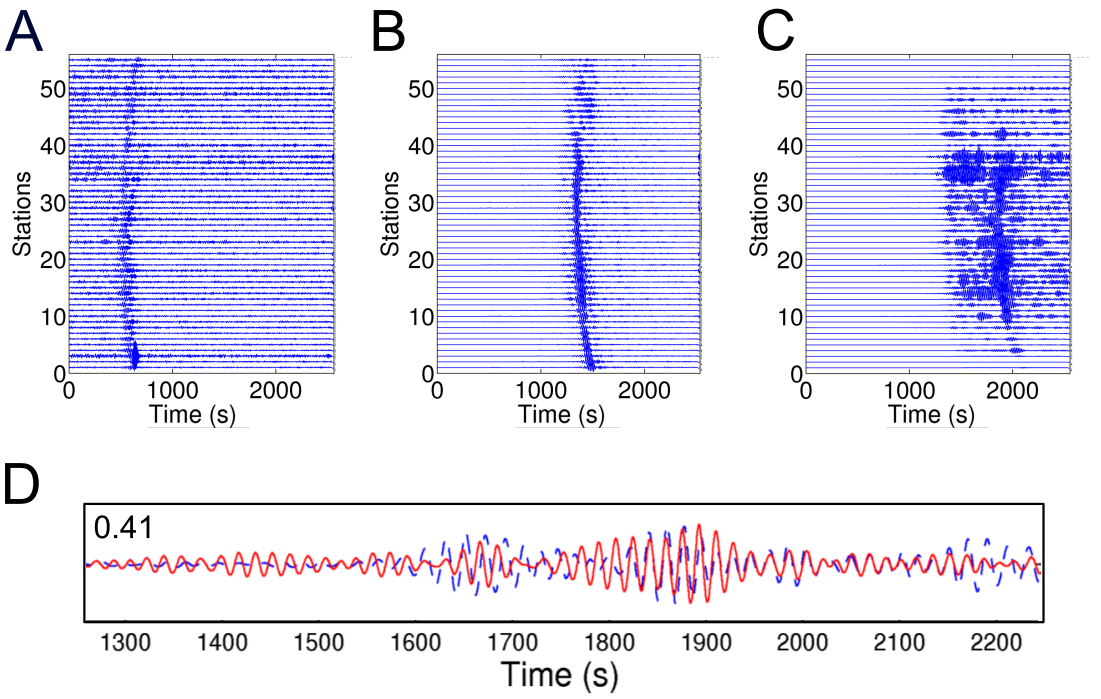

Figure 6.24: Same as Figure 6.23 but for the M 7.0 Haiti earthquake. The same estimated Green's functions are displayed in (A) as in Figure 6.23A. Here, convolution (Equation (2.32)) is used to construct the convolution functions in (C).

The estimated Green's functions in Figure 6.23A and Figure 6.24A are constructed using noise interferometry as in Equation (2.14) for each station pair between target sensor WDC and seismometers along lines 24A and 25A of the North-South aligned backbone seismometer array. Figure 6.23B and Figure 6.24B show the real signals from the Japan and Haiti earthquakes, respectively, recorded on each of these backbone seismometers. The integrand in Equation (2.31) is evaluated by cross-correlating each trace in Figure 6.23A with its corresponding trace in Figure 6.23B to construct the correlation functions between each station pair, shown here in Figure 6.23C. Interpolating these correlation functions to points within 2D Voronoi cells surrounding the backbone array seismometers and integrating (summing) over all such points as in Equation (2.31) constructs the SRI seismogram of the M 7.0 Japan earthquake at target sensor WDC. This reconstruction is plotted in Figure 6.23D (solid/red trace) and compared with the real recording of the event at WDC (dashed/blue trace). The surface wave arrival can not be clearly identified, although some of the arrivals are in phase. The poor quality of the SRI seismogram is not surprising given the little clarity, i.e., no clear surface wave arrivals, in the correlation functions in Figure 6.23C. Thus consider how these correlation functions are constructed: the real earthquake

signals propagate through the highly attenuating western US and are recorded on the backbone seismometers. The surface waves are thus strongly attenuated and multiple scattering is likely to have occurred. The estimated Green's functions then act to project these real recordings back to target sensor WDC located close to the Pacific coast through processes of correlation. Since the scattering nature of the western US is also represented in the estimated Green's functions, the real recordings of the earthquake are thus subjected to the attenuative medium of the western US for a second time as they are projected back through the Rocky Mountain provinces, the Basin and Range, the Cascades, the Sierra Nevada and the Coastal Ranges via the estimated Green's functions. This constructs the correlation functions between target sensor WDC and all backbone seismometers and we observe that the high amplitude signals at the expected surface wave arrival times ($\sim$ 3000 s) are masked by much noisier, multiply scattered arrivals.

By comparison, consider the M 7.0 Haiti earthquake whose seismic energy propagated towards the North-South aligned backbone array from the east, sampling the stable Gulf Coastal Plain, the Central Lowlands and the Great Plains. From Figure 6.24B we immediately see that the earthquake signals recorded on the backbone seismometer array exhibit much greater clarity than those recordings of the Japan earthquake, as the surface wave arrivals are well defined at $\sim$ 1500 s. The traces in Figure 6.24C are constructed by convolving each trace in Figure 6.24A with its corresponding trace in Figure 6.24B, as in Equation (2.32). Interpolating these convolution functions to points within 2D Voronoi cells surrounding the backbone array seismometers and integrating over all such points as in Equation (2.32) constructs the SRI seismogram of the M 7.0 Haiti earthquake at target sensor WDC. This reconstruction is plotted in Figure 6.24D (solid/red trace) and compared with the real recording of the event at WDC (dashed/blue trace). We observe that the high amplitude arrivals in Figure 6.24C interfere constructively during the integration to reproduce the large amplitude arrivals between 1500 s - 2000 s, which are in phase with the real arrivals recorded at sensor WDC. In this example, the real earthquake recordings never directly sampled the highly attenuating western US. These recordings were only projected through the western province to the location of sensor WDC through processes of convolution with the estimated Green's functions. Prior to this, the earthquake energy had only propagated across the less attenuating Gulf Coastal Plain, the Central Lowlands and the Great Plains, and will have experienced less scattering compared to signals propagating through the western US. This reduced scattering

thus introduced fewer high amplitude surface wave arrivals into the earthquake signals recorded on the backbone seismometers, which thus resulted in more stable convolution functions. By comparing Figure 6.24C with Figure 6.23C we also directly notice the greater stability (i.e. fewer spurious arrivals) in the SRI reconstructions that comes with performing convolution over correlation, as discussed by Halliday and Curtis (2009) for scattered surface waves in attenuative media and by Slob et al. (2007) for electromagnetic waves in lossy media.

Table 6.7: Same as Table 6.4 but for SRI seismograms of earthquakes with magnitudes $>$ M 5.0. All events originated in regions such that the energy from them propagated across the backbone array from East to West.

Magnitude	Location	Average Correlation Coefficient
3.1	Puerto Rico	0.15
3.2	Haiti	0.14
3.5	Virgin Islands	0.06
3.6	Haiti	0.17
3.7	Dominican Republic	-0.08
4.0	Haiti	0.04
5.0	Trinidad and Tobago	0.11
5.4	Dominican Republic	0.15
5.7	El Salvador	0.17
5.8	Puerto Rico	0.37
$5.9^{(1)}$	Offshore El Salvador	0.12
$5.9^{(2)}$	Offshore El Salvador	0.26
5.9	Central Peru	0.16
5.9	Cayman Islands	0.45
5.9	Haiti	0.54
6.0	Northern Mid-Atlantic Ridge	0.39
6.0	Haiti	0.53
6.4	Offshore Carabobo, Venezuela	0.52
7.0	Haiti	0.55

Table 6.7 above summarises the quality of the SRI seismograms of 19 additional earthquakes of magnitude 3 and greater that occurred predominantly in the Caribbean, such that the energy from them propagated across the North-South aligned array from East to West. The seismograms of earthquakes of the smallest magnitude (up to M 4.0) are still reconstructed poorly using SRI as all correlation coefficients are low (< 0.20).

It is unlikely that such low magnitude events would be recorded on the North-South aligned array with enough energy to be successfully projected to the locations of the target sensors by the SRI propagators. We observe that the seismograms of earthquakes with magnitudes greater than M 5.0 and epicentres within the nothernmost Caribbean (Haiti, Cayman Islands, Puerto Rico), are constructed well on all target sensors using SRI. An example was shown earlier in Figure 6.21 for the M 7.0 Haiti earthquake. Events that occur west of the Caribbean are less well constructed. An example is shown here in Figure 6.25 for the M $5.9^{(2)}$ event that occurred off the coast of El Salvador.

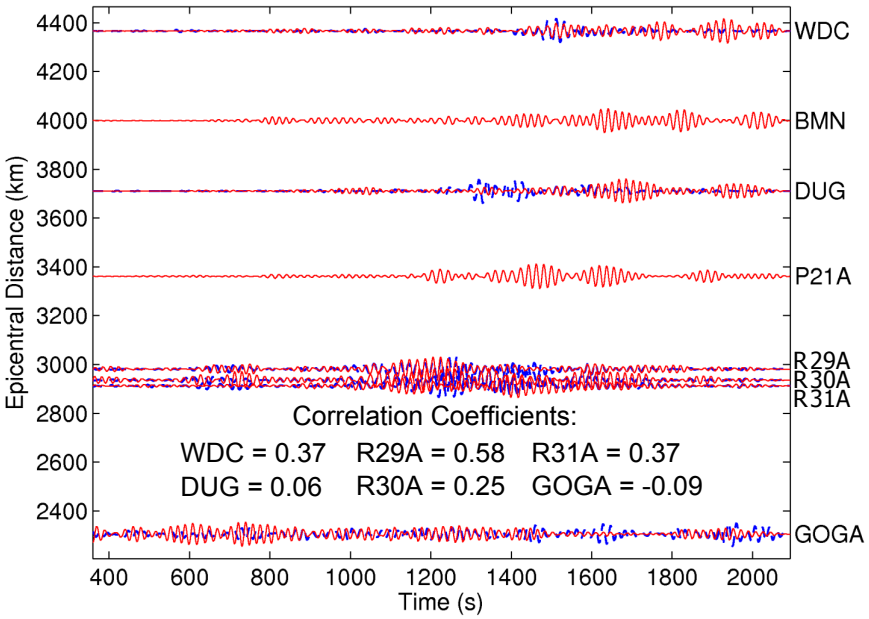

Figure 6.25: Same as Figure 6.17 but for the M $5.9^{(2)}$ earthquake that occurred off the coast of El Salvador. Target sensors P21A and BMN did not actively record the event.

In Figure 6.25, the SRI seismograms are constructed reasonably well on target sensors R29A, R30A and R31A (correlation coefficients of 0.58, 0.25 and 0.37, respectively) but the method is less successful at the largest length scales (correlation coefficient of -0.09 at target sensor GOGA). We conclude that events that originated in the western Caribbean are located in regions too far west of the great-circle path that best intersects the North-South aligned backbone array approximately perpendicularly. As a result, the backbone seismometers would not be distributed around regions of the boundary S in which the integrand in Equation (2.31) (or Equation (2.32)) becomes

approximately stationary, and the stationary phase approximation of Snieder (2004) would thus be invoked incorrectly. Halliday and Curtis (2009) previously showed that leaving stationary phase points of a source boundary unoccupied contributes to errors in correlation-type interferometry in the form of non-physical arrivals. We thus extend this theory to unoccupied stationary phase points on a receiver boundary and emphasise the importance of the location of the backbone seismometer array in relation to the target sensor and the earthquake epicentre. As described by the spatial criteria in Section 3.6.1, the backbone array should be located approximately perpendicularly to a great-circle path that extends from the earthquake epicentre and intersects the target sensor at which we wish to construct a new earthquake seismogram.

6.5.2 Quantitative Analysis: SNR analyses of the components of SRI

Let us now compare the success of the SRI method when performed at the two different length scales. In Section 6.4.1 SRI was performed over short inter-station distances, such that the distance between the target sensors and seismometers from within the East-West aligned backbone array was within the range 210 km - 540 km. In Section 6.4.2 SRI was then performed over much larger length scales as target sensors were located up to 2420 km from the North-South aligned array of backbone seismometers. At the shortest length scale the majority of earthquake seismograms were reconstructed well on all target sensors, whilst at the largest distances i.e. at target sensors WDC and GOGA, we observed a severe decline in the quality of the SRI seismograms. To understand the effect of this inter-station distance on the SRI reconstructions, we again deconstruct the SRI seismograms into their three components (i.e., 1) the estimated Green's functions, 2) the recordings of the earthquakes, and 3) the correlation/convolution functions) as described earlier in Section 5.5 and above in Section 6.5.1, but this time we perform a quantitative analysis on the signal-to-noise ratios (SNRs) of the individual components of each SRI seismogram. Furthermore, we calculate one standard deviation of the average SNR values and represent these values as percentages of the average SNR values. This allows us to determine the variation in the SNR values across the data.

Throughout, we consider only those station pairs between a target sensor and the backbone array seismometers that are used to construct the final SRI seismograms at that target sensor. Thus, the backbone seismometers are always located along 2-line combinations of the East-West or North-South aligned backbone arrays. Regardless of

the SRI component being studied, we start by defining a 'signal window'. This is a time window within which we expect the first surface wave to arrive and is defined using an average group velocity of 3.25 km/s and the appropriate inter-station or epicentral distance. A 500 s 'noise window' is then defined such that it trails the signal window temporally.

All subsequent tables refer to 'Target Sensors' at which SRI seismograms have been constructed; 'n Seismometers' that are used in each reconstruction and are located along two approximately parallel lines of the backbone arrays ('Array Seismometers'); the average signal-to-noise ratio (SNR) taken over n seismometers; one standard deviation of the average SNR ('1σ') and the standard deviation represented as a percentage of the average SNR value.

Estimated Green's functions

First consider the estimated Green's functions constructed between each target sensor-backbone seismometer receiver pair using noise interferometry as in Equation (2.14). A brief analysis of these estimated Green's functions was provided in Section 3.3 but we now expand on the results. The average SNR values of the estimated Green's functions and 1σ are listed in Table 6.8. Here we also calculate the average root-mean-square (RMS) values of the signal windows of the estimated Green's functions and these values are also listed in Table 6.8. All estimated Green's functions are normalised (divided) by their absolute maximum amplitude, thus the maximum possible RMS value is 1.00.

We observe distinct differences in the average RMS and SNR values as the distances between the target sensors and the backbone array seismometers increase. For example, consider the estimated Green's functions constructed between the target sensors and seismometers within the North-South aligned backbone array (top table in Table 6.8). At the largest length scales at target sensors WDC, BMN and GOGA, the RMS values are low (0.28 - 0.31) and the average SNR values are poor ($<$ 7.00). At shorter inter-station distances however (between the backbone array and target sensors DUG, P21A, R29A, R30A and R31A), the average RMS values are much higher (between 0.68 and 0.77), and the average SNR values have more than doubled (between 15.0 and 29.0). Thus, estimated Green's functions display clear surface waves that are discernible from the noise when constructed over short (up to 1200 km) inter-station distances. We do note however that over these shorter inter-station distances the standard deviations of the average SNR values are large. This variation

in the SNR values of the individual estimated Green's functions will cause some inter-station paths to dominate the SRI reconstructions, i.e. earthquake energy will be projected over some inter-station paths better than others. These dominant station pairs typically exist between the target sensors and those backbone seismometers located within the centre of the array. These array seismometers approximate the stationary phase region of the receiver boundary and we assume that the stack summation of all correlation/convolution functions in the final inter-source interferometry step (Equation (2.31) or Equation (2.32)) provides the sufficient averaging over the whole backbone array. Thus, these variations in the SNR values of the individual estimated Green's functions should not greatly effect the SRI seismogram constructed at a single target sensor, but should allow the stationary phase approximation (Snieder, 2004) to be invoked more accurately.

Furthermore, consider the other two sections of Table 6.8 which highlight the RMS and SNR values of the estimated Green's functions constructed between target sensors and seismometers within the East-West aligned backbone array. Here we show two different sets of results for the two different approaches to SRI as the backbone array seismometers used for each SRI reconstruction changes depending on the SRI method used. The distances between all station pairs is approximately between 210 km - 540 km and at this shorter inter-station distance we construct excellent estimated Green's functions: the average RMS values are high (> 0.8) and the average SNR values are also large (up to 42.0). One standard deviation of the average SNR values is typically less than 50 % of the average SNR values. Thus, over these shorter length scales there is less variation in the quality of the individual estimated Green's functions constructed between a target sensor and the n seismometers along the backbone array, compared to those estimated Green's functions constructed at larger length scales. We thus place high confidence in these estimated Green's functions as the inter-receiver surface waves are clearly constructed over the background noise level, i.e., the SNR values are high.

Table 6.8: The average root-mean-square (RMS) values and signal-to-noise ratios (SNRs) of all estimated Green's functions constructed between target sensors ('Target Sensors') and n seismometers located along 2-line combinations of a backbone array ('Array Seismometers'). See Figures 6.3 and 6.9 for a map of all station locations. One standard deviation (σ) is calculated for the average SNR and displayed as a percentage of the average SNR.

North-South Aligned Array						
Target Sensors	Array Seismometers	n Seismometers	Average RMS	Average SNR	1σ	σ as % of ave. SNR
WDC	24A-25A	55	0.28	6.94	2.94	42.33
BMN	24A-25A	56	0.28	6.92	3.30	47.68
DUG	24A-25A	57	0.68	15.43	5.59	36.25
P21A	24A-25A	51	0.88	25.27	16.16	63.92
R29A	25A-26A	60	0.77	28.91	18.89	65.35
R30A	26A-27A	55	0.70	26.19	19.78	75.52
R31A	27A-28A	53	0.70	23.76	16.51	69.48
GOGA	24A-25A	52	0.31	6.19	4.08	65.86
East-West Aligned Array - For Correlation-Correlation SRI						
Target Sensors	Array Seismometers	n Seismometers	Average RMS	Average SNR	1σ	σ as % of ave. SNR
Z27A	V-W	17	1.00	39.95	16.76	41.96
127A	W-X	22	0.93	40.68	17.77	43.69
227A	X-Y	26	1.00	41.98	13.83	32.95
327A	Y-Z	26	0.94	31.56	15.65	49.59
427A	Z-1	23	0.84	31.60	16.96	53.67
527A	1-2	23	0.96	39.28	16.96	43.17
627A	2-3	21	0.96	36.06	13.51	37.45
226A	X-Y	17	1.00	29.47	11.88	40.30
East-West Aligned Array - For Correlation-Convolution SRI						
Target Sensors	Array Seismometers	n Seismometers	Average RMS	Average SNR	1σ	σ as % of ave. SNR
Z27A	3-4	16	0.91	33.61	19.82	58.97
127A	4-5	13	0.83	25.34	13.29	52.46
227A	5-6	11	0.84	32.75	22.64	69.15
226A	5-6	6	1.00	32.65	10.31	31.57

Earthquake recordings

Second, we calculate the average SNR values of the individual earthquake signals recorded on the backbone array seismometers. Table 6.9 shows the average SNR values of the signals of three earthquakes recorded on seismometers within the North-South aligned backbone array.

First, we observe that for each earthquake there is little variation in the standard deviation between the four sets of array seismometers used. For example, 68% (1σ) of the SNR values of the individual signals of the M 3.7 Dominican Republic earthquake recorded on all backbone array seismometers lie within 12-19% of the average SNR values given. The largest variation between the four 2-line combinations of array seismometers is seen for the M 5.9 Haiti earthquake. Here, there is a 16.5% difference between the values of σ as a percentage of the average SNR. Finally, the largest dispersion from the average SNR is seen for the recordings of the M 5.9 Haiti earthquake on the 53 backbone seismometers that are used to construct the SRI seismogram at target sensor R31A. Here, 1σ is $\sim 65\%$ of the average SNR value. Thus, we see the most scatter in the SNR values of this event recorded on the backbone array seismometers, but we still observe that between the different 2-line combinations of seismometers the standard deviations are very similar (between $\sim$ 3.5 and 4.5).

From this, we conclude that the earthquake signals recorded on the backbone array seismometers are not the largest contributing factor to the differences in the SRI seismograms constructed on different target sensors and thus over different length scales. If the earthquake recordings were responsible for these differences, we would expect there to be large differences in the average signal-to-noise ratios of event recordings made on varying lines of seismometers within the array. Instead we observe that the standard deviations of the signal-to-noise ratios as percentages of the average signal-to-noise ratios do not vary much over the whole backbone array.

However, we do obtain other important information from this study. A comparison of the average SNR values calculated for each of the three events represented in Table 6.9 shows that there are large variations in the average SNR values calculated. These average values vary from $\sim$ 3 (for recordings of the M 3.7 Dominican Republic earthquake) to a maximum value of $\sim$ 23 (for recordings of the M 6.5 earthquake that occurred off the coast of California). When the average SNR is $\sim$ 3 there is very little coherent earthquake energy recorded on the backbone array seismometers. This may be because the earthquake was of a low magnitude, the earthquake was too far away from the backbone array or because a lot of the surface

Table 6.9: Average signal-to-noise ratios (SNRs) of earthquake signals recorded on n backbone array seismometers from within the North-South aligned backbone seismometer array. Backbone seismometers are located along the 2-line combinations of the USArray network specified by 'Array Seismometers'. The n backbone seismometers are used to construct the SRI seismograms at the target sensors listed. One standard deviation (σ) of the average SNR and the standard deviation as a percentage of the average SNR is given.

M 3.7 Dominican Republic Earthquake					
Target Sensor	Array Seismometers	n Seismometers	Average SNR	1σ	σ as % of ave. SNR
WDC	24A-25A	49	3.21	0.39	12.18
BMN	24A-25A	50	3.21	0.39	12.05
DUG	24A-25A	51	3.21	0.38	11.94
P21A	24A-25A	45	3.23	0.38	11.85
R29A	25A-26A	56	3.19	0.38	11.84
R30A	26A-27A	47	3.23	0.45	14.00
R31A	27A-28A	46	3.26	0.63	19.35
GOGA	24A-25A	46	3.23	0.39	11.94
M 5.9 Haiti Earthquake					
Target Sensor	Array Seismometers	n Seismometers	Average SNR	1σ	σ as % of ave. SNR
WDC	24A-25A	50	7.35	3.50	47.62
BMN	24A-25A	51	7.30	3.48	47.59
DUG	24A-25A	52	7.25	3.46	47.68
P21A	24A-25A	46	6.79	3.34	49.25
R29A	25A-26A	59	7.08	3.82	53.94
R30A	26A-27A	55	7.59	3.95	52.08
R31A	27A-28A	53	6.90	4.46	64.61
GOGA	24A-25A	47	7.03	3.55	50.47
M 6.5 Earthquake off the Coast of California					
Target Sensor	Array Seismometers	n Seismometers	Average SNR	1σ	σ as % of ave. SNR
WDC	24A-25A	55	22.45	8.71	38.80
BMN	24A-25A	56	22.39	8.64	38.61
DUG	24A-25A	57	22.54	8.64	38.34
P21A	24A-25A	51	22.25	8.70	39.11
R29A	25A-26A	60	22.60	8.68	38.41
R30A	26A-27A	55	21.85	8.39	38.40
R31A	27A-28A	53	21.65	7.43	34.30
GOGA	24A-25A	52	22.73	8.36	36.79

wave energy had been attenuated. If this is the case, one would not perform SRI to construct new seismograms as there would be little surface wave energy for the estimated Green's functions (the SRI propagators $G(\mathbf{x}, \mathbf{r})$) to project to the locations of the new target sensors. An example of this is the M 3.7 Dominican Republic earthquake, the SRI seismograms of which are poorly constructed on the target sensors (correlation coefficients < 0.1).

For larger signal-to-noise ratios (i.e. SNR > 10), recorded surface waves are discernible above the background noise level and, on most occasions, SRI propagators are able to successfully project those recordings to the locations of the target sensors. This is the case for the M 6.5 earthquake that occurred off the coast of California. This event was studied in detail in Chapters 4 and 5 and, with the exception of the SRI seismogram constructed at target sensor GOGA, SRI seismograms were comparable with the real recordings of the event on the target sensors (correlation coefficients up to 0.69).

Finally, we observe that when the average SNR values of earthquake recordings are of intermediate values, i.e., between 4 and ~ 10, the results of SRI are more unpredictable: some earthquake seismograms are constructed well using SRI, e.g., the seismograms of the M 6.4 earthquake that occurred off the coast of Venezuela whose event recordings have an average SNR value of 4.07 and the correlation coefficients of the SRI seismograms average 0.5. However, some earthquake seismograms are not constructed as successfully using SRI, but their corresponding event recordings on the backbone seismometers have higher average SNR values. This is the case for the M 4.5 earthquake that occurred of the coast of California and whose event recordings have an average SNR value of 5.99 but the average correlation coefficient of the SRI seismograms is just 0.3.

We note that when the SNR values of the event recordings are of these intermediate values, SRI is most successful at constructing SRI seismograms on target sensors located closer to the backbone seismometer array, i.e., at target sensors R29A, R30A and R31A. We previously showed that over these shorter distances, the estimated Green's functions are constructed well as RMS values are high at ~ 0.7 (see Table 6.8). These estimated Green's functions are thus more successful at projecting earthquake energy to the new sensor locations than estimated Green's functions that have low SNR values. This is the case for the M 5.9 Haiti earthquake - SRI seismograms of the event are constructed exceptionally well on target sensors R29A, R30A and R31A (correlation coefficients up to 0.93), but less successfully on the largest length scales at

target sensors WDC and BMN (correlation coefficients of 0.19 and 0.38, respectively).

Similar trends can be seen for the 32 earthquakes recorded on the East-West aligned backbone seismometer array. Three example events are shown in Table 6.10 for low, intermediate and high SNR values of event signals recorded on the backbone array seismometers. Here, the highest SNR values are for the M 5.8 Guerrero event and the values are almost twice as high as any of the SNR values of the events recorded on the North-South aligned array. This could be due to the different crustal environments through which the earthquake energy propagates. Earthquake energy propagating towards the East-West array from the south arrives at the backbone array seismometers after propagating mainly through oceanic crust, whilst energy arriving on the North-South aligned backbone array largely propagates through continental crust. Thus, due to the azimuths from which we chose our earthquakes to originate, the earthquake energy arriving on the East-West aligned backbone array is typically less attenuated and the surface waves are of higher amplitude (and thus have higher signal-to-noise ratios). The SRI seismograms of the M 5.8 Guerrero earthquake were successfully constructed on all target sensors and comparisons with the real recordings of the event on the same target sensors show correlation coefficients averaging 0.7 and on some occasions reaching values greater than 0.9 (this event was studied in greater detail in Chapters 4 and 5).

The signals from the M 3.8 Colima earthquake are the most poorly recorded as all average SNR values are < 3. Furthermore, the SRI seismograms of this event were poorly constructed on the target sensors and this is represented in the low correlation coefficients that average 0.08.

Finally, the signals from the M 5.8 Galapagos Islands earthquake were recorded well on the East-West aligned array seismometers as average SNR values are of intermediate values, up to ~ 24. The SRI seismograms of this earthquake are constructed well on all target sensors and correlation coefficients average 0.68, reaching a maximum value of 0.89 on one occasion.

Table 6.10: Same as Table 6.9 but for earthquake signals recorded on n backbone array seismometers from within the East-West aligned backbone seismometer array.

M 3.8 Colima, Mexico, Earthquake					
Target Sensor	Array Seismometers	n Seismometers	Average SNR	1σ	σ as % of ave. SNR
Z27A	V-W	12	2.98	0.40	13.47
127A	W-X	18	2.89	0.45	15.59
227A	X-Y	21	2.79	0.50	17.87
327A	Y-Z	20	2.61	0.52	19.90
427A	X-1	18	2.54	0.50	19.52
527A	1-2	17	2.59	0.41	15.86
627A	2-3	14	2.49	0.41	16.36
226A	X-Y	17	2.77	0.51	18.46
M 5.8 Galapagos Islands Earthquake					
Target Sensor	Array Seismometers	n Seismometers	Average SNR	1σ	σ as % of ave. SNR
Z27A	V-W	12	18.54	9.41	50.79
127A	W-X	19	20.40	10.33	50.66
227A	X-Y	23	21.26	10.45	49.18
327A	Y-Z	23	21.92	11.37	51.86
427A	X-1	22	23.28	14.55	62.50
527A	1-2	23	21.69	13.37	61.64
627A	2-3	21	19.28	8.83	45.81
226A	X-Y	17	23.15	11.45	49.43
M 5.8 Guerrero, Mexico, Earthquake					
Target Sensor	Array Seismometers	n Seismometers	Average SNR	1σ	σ as % of ave. SNR
Z27A	V-W	17	41.77	21.09	50.49
127A	W-X	22	48.09	23.31	48.48
227A	X-Y	26	46.62	22.08	47.37
327A	Y-Z	26	44.49	23.29	52.35
427A	X-1	23	43.53	24.80	56.96
527A	1-2	23	39.50	20.86	52.81
627A	2-3	21	36.79	21.10	57.36
226A	X-Y	17	57.01	21.00	36.84

To conclude, it is important to first study the quality of the earthquake energy recorded on the backbone array seismometers as it indicates how successful the SRI method will be at reconstructing the earthquake seismograms. We found that over the largest inter-station distances (between seismometers within the North-South aligned array and target sensors WDC, BMN and GOGA), SRI should only be performed if the earthquake signals recorded on the backbone array seismometers have SNR values $>$ 10. At shorter inter-station distances (up to 1200 km), SRI is more successful and we have shown that, on occasion, even poorly recorded earthquake energy (SNR $\sim$ 5) can be projected to the locations of the target sensors. Here, we rely on estimated Green's functions that have high signal-to-noise ratios (> 20).

The average SNR values of the earthquake energy recorded on the East-West aligned backbone array are typically higher than any of the average SNR values of the earthquake energy recorded on the North-South aligned array. We expect this is a consequence of the azimuths from which the earthquakes originate and thus propagate towards the array seismometers.

Finally, it is a combination of the event recordings and the estimated Green's functions (the SRI propagators) that determines the success of SRI over different spatial scales. Even earthquake energy recorded on backbone array seismometers with exceptionally high SNR values will not be projected effectively if the SRI propagators are poorly constructed (i.e. have low SNR values).

For a summary of the average SNR values of the signals of all 87 earthquakes recorded and used throughout this study see Appendix B. For simplicity, average SNR values have been calculated over whole backbone arrays as opposed to the 2-line combinations as shown above. There is thus one average SNR value for each earthquake. We decided that this was a reasonable way to display the data as, for most earthquakes considered herein, the average distance between lines of seismometers within the backbone arrays is small compared to the distance over which the earthquake energy propagates.

Correlation/Convolution Functions

In this last section we analyse the average signal-to-noise ratios of the correlation/convolution functions. For target sensors that pertain to the geometry for correlation-correlation SRI (Figure 6.1A), the correlation functions are constructed between that target sensor and n backbone array seismometers by cross-correlating the estimated Green's functions for each receiver pair with the earthquake signals recorded on the backbone seismometers. Integrating over all correlation functions as in Equation (2.31) constructs the SRI seismogram at that target sensor. For target sensors that pertain to the geometry for correlation-convolution SRI (Figure 6.1B), the *convolution* functions are constructed by replacing correlation in Equation (2.31) with convolution, as in Equation (2.32).

Table 6.11 lists three earthquakes that were recorded on the North-South aligned backbone array. The SRI seismograms of these events were then constructed at the locations of the eight target sensors. The average SNR values of the correlation/convolution functions used to construct these SRI seismograms are shown. From here onwards we shall refer in a broad sense to "correlation functions" for simplicity, but note that for some target sensors these functions are actually constructed using processes of convolution as in Equation (2.32).

We first observe that the correlation functions used to reconstruct seismograms of the M 3.7 Dominican Republic earthquake (the smallest earthquake listed) have low average SNR values ($\sim$ 3). Thus, little surface wave energy has been reconstructed in the correlation functions, which in turn has constructed poor SRI seismograms (average correlation coefficient of -0.08).

The average SNR values of the correlation functions used to reconstruct the seismograms of the M 5.9 Haiti earthquake vary across the eight target sensors. We obtain higher SNR values for the correlation functions constructed between the backbone array seismometers and those target sensors located closer to the array - sensors R29A, R30A and R31A. This is expected as the estimated Green's functions constructed over these shorter distances had the highest SNR values. We also observe that the SRI seismograms of this event constructed at target sensors R29A, R30A and R31A have the highest correlation coefficients (0.93, 0.84 and 0.66, respectively) when compared with the real earthquake signals recorded on those same sensors. As the distance between the array seismometers and the target sensors increases, the correlation functions have lower SNR values (i.e., at target sensors WDC, BMN and GOGA the average SNR values of the correlation functions are as low as 3). Again,

Table 6.11: Average signal-to-noise ratios (SNRs) of the correlation functions constructed between the target sensors and n seismometers located along the 2-line combinations of the North-South aligned backbone seismometer array ('Array Seismometers'). One standard deviation (σ) of the average SNR and the standard deviation as a percentage of the average SNR is given.

M 3.7 Dominican Republic Earthquake					
Target Sensor	Array Seismometers	n Seismometers	Average SNR	1σ	σ as % of ave. SNR
WDC	24A-25A	49	2.77	0.56	20.16
BMN	24A-25A	50	2.71	0.46	17.05
DUG	24A-25A	51	2.94	0.58	19.63
P21A	24A-25A	45	3.11	0.64	20.63
R29A	25A-26A	56	3.29	0.59	17.84
R30A	26A-27A	47	3.04	0.61	20.16
R31A	27A-28A	46	3.16	0.46	14.71
GOGA	24A-25A	46	3.34	0.59	17.66
M 5.9 Haiti Earthquake					
Target Sensor	Array Seismometers	n Seismometers	Average SNR	1σ	σ as % of ave. SNR
WDC	24A-25A	50	3.14	1.20	38.15
BMN	24A-25A	51	2.97	1.24	41.59
DUG	24A-25A	52	3.64	2.37	65.14
P21A	24A-25A	46	4.18	3.07	73.37
R29A	25A-26A	59	7.80	3.18	40.77
R30A	26A-27A	55	8.35	3.44	41.19
R31A	27A-28A	53	7.15	3.00	41.92
GOGA	24A-25A	47	3.79	1.55	40.92
M 6.5 Earthquake off the coast of California					
Target Sensor	Array Seismometers	n Seismometers	Average SNR	1σ	σ as % of ave. SNR
WDC	24A-25A	55	5.29	2.43	45.95
BMN	24A-25A	56	6.51	3.67	56.40
DUG	24A-25A	57	12.16	5.49	45.11
P21A	24A-25A	51	18.68	7.71	41.28
R29A	25A-26A	60	6.60	5.70	86.37
R30A	26A-27A	55	6.92	5.31	76.79
R31A	27A-28A	53	5.55	5.38	97.05
GOGA	24A-25A	52	3.65	1.52	41.59

this is likely due to the low SNR values of the estimated Green's functions constructed over these large distances.

The average SNR values of the correlation functions used to construct the M 6.5 earthquake that occurred off the coast of California are the most difficult to interpret. The average SNR values at target sensors R29A, R30A and R31A are between 5.30 and 5.70 which is surprisingly low when one considers that the correlation coefficients of the SRI seismograms constructed at these sensors are of intermediate-to-high values (0.56, 0.50 and 0.69, respectively). The values of 1σ go some way to justifying these anomalously low average SNR values: 1σ is as large as 97 % of the average SNR value at target sensor R31A, and is greater than 75 % of the average SNR values at target sensors R29A and R30A. There is thus a large variation in the SNR values of the individual correlation functions constructed across the array of backbone seismometers. A closer look at the individual correlation functions constructed between target sensor R29A and seismometers located along lines 25A and 26A of the North-South aligned backbone array shows that 22 seismometers dominate the SRI reconstruction. The correlation functions constructed between these 22 seismometers and target sensor R29A have SNR values > 6.6 (the average SNR value) and reach a maximum value of 23, whilst the correlation functions of the remaining 38 seismometers along lines 25A and 26A have SNR values less than the average SNR value. The 22 seismometers whose correlation functions have SNR values above the average value are located around the region of the backbone array that intersects the great-circle path connecting the earthquake epicentre and target sensor R29A. The same variation in the SNR values of the correlation functions exists for the correlation functions constructed between target sensors R30A and R31A and their corresponding lines of backbone array seismometers. The great-circle paths that connect the earthquake epicentre and the target sensors, and intersect the backbone array seismometers, are shown in Figure 6.26. The backbone array seismometers whose corresponding correlation functions have SNR values larger than the average SNR value are also highlighted.

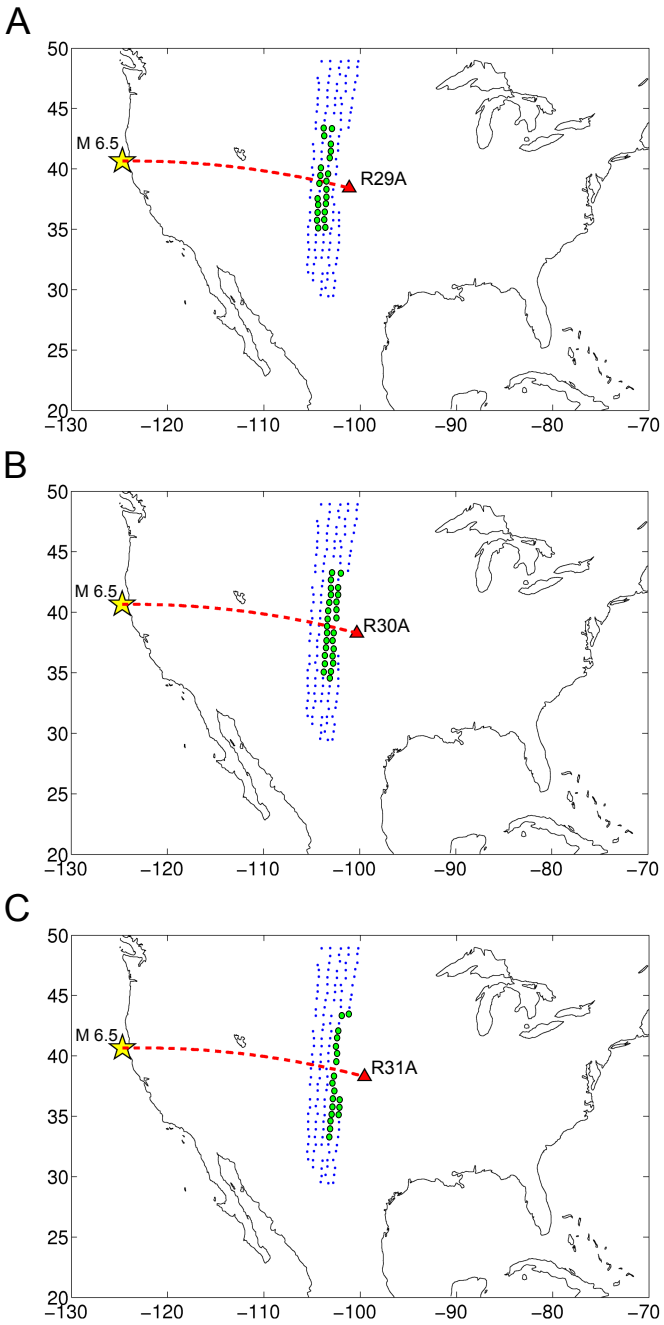

Figure 6.26: Source and receiver geometries for the M 6.5 earthquake that occurred off the coast of California (star), the North-South aligned backbone seismometer array (circles) and target sensors: A) R29A, B) R30A and C) R31A (triangles). The great-circle path (GCP) between the earthquake epicentre and each of the target sensors is plotted (dashed line). Green circles: backbone seismometers on which the convolution functions (the integrand of Equation (2.32) for each backbone seismometer at $\mathbf{x}$) have SNR values greater than the average SNR value taken across the whole array.

We conclude that the locations of these seismometers best approximate the locations of the stationary phase points of the receiver boundary, and thus interfere constructively in the final inter-source interferometric integral. The correlation functions constructed on these backbone seismometers thus contribute the most to the final SRI seismograms and are responsible for the high correlation coefficients of the SRI seismograms constructed at target sensors R29A, R30A and R31A. Similar trends can be seen in the correlation functions constructed between all other target sensor-backbone seismometer receiver pairs but the variation in the individual SNR values from the average is considerably less (1σ is between $\sim 40\%$ and $\sim 56\%$).

Finally, a summary of the SNR values of the correlation functions constructed between target sensors and backbone seismometers within the East-West aligned array is provided in Table 6.12. Three example earthquakes are listed. First consider the M 3.8 Colima earthquake. The average SNR values of the correlation functions are low (< 3). Thus, the final integration (summation) over all correlation functions constructs poor SRI seismograms (an average correlation coefficient of 0.08).

Seismograms of the M 5.8 Galapagos Islands earthquake and the M 5.8 Guerrero earthquake were constructed well on the target sensors using correlation-correlation SRI (average correlation coefficients of 0.68 and 0.70, respectively). The average SNR values of their correlation functions are also high, between 25 and 50. We note here however that 1σ is large (up to 65%), indicating a considerable variation in the SNR values of the individual correlation functions. Again, we take a closer look at the SNR values of the individual correlation functions and we observe that a selection of backbone seismometers dominate in the final integration, as was the case for earthquakes constructed using the North-South aligned backbone array.

When reconstructing the seismograms of the M 5.8 Guerrero earthquake, these dominant seismometers are located in regions close to where the great-circle path (GCP) propagating from the earthquake epicentre to the target sensors intersects the backbone array of seismometers. However, when reconstructing the M 5.8 Galapagos Islands earthquake, we observe that the SNR values are largest for the correlation functions constructed between the target sensors and seismometers located in the westernmost sections of the array (i.e. seismometers whose station name ends in the sequence '20A', '21A' or '22A'). These individual SNR values are often twice, or even three times the value of the average SNR listed in Table 6.12. For example, the average SNR value of the correlation functions constructed between target sensor 227A and seismometers located along lines X and Y of the backbone array is 33.51.

Table 6.12: Same as Table 6.11 but for the correlation functions constructed between the target sensors and n seismometers along the 2-line combinations of the East-West aligned backbone seismometer array.

M 3.8 Colima Earthquake					
Target Sensor	Array Seismometers	n Seismometers	Average SNR	1σ	σ as % of ave. SNR
Z27A	V-W	12	2.79	0.61	21.70
127A	W-X	18	2.64	0.57	21.65
227A	X-Y	21	2.66	0.41	15.42
327A	Y-Z	20	2.58	0.33	12.84
427A	Z-1	18	2.38	0.49	20.81
527A	1-2	17	2.48	0.51	20.61
627A	2-3	14	2.58	0.61	23.63
226A	X-Y	17	2.71	0.59	21.82
M 5.8 Galapagos Islands Earthquake					
Target Sensor	Array Seismometers	n Seismometers	Average SNR	1σ	σ as % of ave. SNR
Z27A	V-W	12	26.84	14.06	52.39
127A	W-X	19	36.06	21.50	59.64
227A	X-Y	23	33.51	20.62	61.54
327A	Y-Z	23	35.95	17.51	48.70
427A	Z-1	22	36.05	16.42	45.54
527A	1-2	23	37.76	16.15	42.76
627A	2-3	21	33.84	10.09	29.81
226A	X-Y	17	43.09	20.65	47.92
M 5.8 Guerrero Earthquake					
Target Sensor	Array Seismometers	n Seismometers	Average SNR	1σ	σ as % of ave. SNR
Z27A	V-W	17	30.48	15.40	50.55
127A	W-X	22	36.14	18.63	51.55
227A	X-Y	26	34.75	15.98	46.00
327A	Y-Z	26	34.09	20.39	59.80
427A	Z-1	23	34.53	22.41	64.90
527A	1-2	23	32.77	16.77	51.18
627A	2-3	21	29.98	16.41	54.75
226A	X-Y	17	48.84	20.37	41.71

The SNR values of the individual correlation functions constructed between target sensor 227A and backbone seismometers X21A, Y21A and Y22A however, are 91.80, 87.82 and 52.14, respectively, thus varying considerably from the average SNR value. A further look at the SNR values of the *event signals* recorded on the backbone array however indicates that the M 5.8 Galapagos Islands earthquake is better recorded on seismometers located on the western side of the array compared to seismometers located on the eastern side. This bias in energy propagation is likely due to local site effects around the individual seismometers within the backbone array. We note however that since the average inter-station distance between all USArray seismometers is short (typically $\sim$ 70 km), the M 5.8 Guerrero earthquake and the M 5.8 Galapagos Islands earthquake are still recorded adequately on all backbone array seismometers. Thus, the correlation functions are also constructed adequately and integration (summation) over all correlation functions constructs good SRI seismograms (correlation coefficients up to 0.92), regardless of this bias in energy propagation.

Summary

To summarise, a study of the three components that comprise the SRI seismograms is important when the distance between the target sensors and the backbone array seismometers is large ($>$ 1200 km). To obtain robust SRI seismograms of past earthquakes in this case, we require:

1. Estimated Green's functions constructed between a target sensor and all backbone array seismometers with SNR values $>$ 15. These are the SRI propagators and a high SNR value ensures that they are able to project the earthquake energy to the location of the target sensor.

2. Earthquake signals recorded on the backbone seismometers with intermediate-to-high SNR values ($>$ 4 but preferably $>$ 10). These SNR values of the event recordings are not definitive. We found that it is the combination of the event recordings with the estimated Green's functions through processes of correlation/convolution that is important. Thus, if the SNR values of the event recordings are low but the SNR values of the estimated Green's function are high, accurate SRI seismograms may still be constructed.

3. Correlation/convolution functions constructed with high SNR values. Again, definitive SNR values cannot be given as they are specific to each event, however

we note that correlation/convolution functions constructed for seismometers $\mathbf{x}$ that lie around the stationary phase regions of the receiver boundary have SNR values considerably higher than the average SNR value calculated over the whole array of seismometers. Hence,

4. Backbone seismometers should occupy the stationary phase points of the receiver boundary (the backbone array) where possible. The correlation/convolution functions constructed for seismometers located around these stationary phase regions provide the largest contribution to the final inter-source interferometric integral (over S in Equations (2.31) and (2.32)). Thus, if the SNR values of these correlation/convolution functions are high, accurate SRI seismograms can be constructed.

When the distance between the target sensors and the backbone array seismometers is much shorter (up to $\sim$ 540 km), SRI is typically more successful at reconstructing earthquake seismograms than at the larger length scales. The estimated Green's functions constructed over these distances have high SNR values ($>$ 25). Providing the earthquake energy recorded on the backbone array has an SNR value $>$ 3, correlation/convolution functions will be constructed well (SNR values typically $>$ 30) and integrations over the receiver boundaries in Equations (2.31) and (2.32) will have the potential to create accurate and robust SRI seismograms.

6.6 Conclusion

We have used two different inter-receiver (length) scales and multiple earthquake magnitude scales to demonstrate the capabilities and limitations of source-receiver interferometry (SRI) in constructing robust earthquake seismograms. We reconstructed the seismograms from a total of 87 earthquakes using both correlation-correlation SRI and correlation-convolution SRI. The results from all 87 earthquakes formed the basis of these conclusions.

On the smallest length scale, the seismograms of 32 earthquakes were constructed on eight target sensors located up to 540 km from an array of backbone seismometers aligned East-West in the New Mexico. Seismograms from earthquakes of M 5.5 and greater were reconstructed well over this small length scale as the phase of SRI seismograms matched the phase of real seismograms recorded on those same sensors, correlation coefficients were high (typically $>$ 0.40) and surface wave arrivals could be

traced across all target sensors. Applying correlation-convolution SRI improved some of the SRI seismograms by removing spurious events associated with correlation-type interferometry. These events typically occurred prior to the main surface wave arrivals in the results of correlation-correlation SRI. We thus used correlation-convolution SRI as a method to help discriminate between these physical and non-physical arrivals.

On the larger length scale, we first constructed the seismograms of 36 earthquakes on eight target sensors located up to 2420 km from an array of backbone seismometers aligned North-South in the centre of the United States. All but one of these earthquakes originated from regions west of the backbone array of seismometers. The exception was a M 6.0 earthquake that occurred in Malawi. SRI seismograms of earthquakes of M 4.4 and greater were constructed well on target sensors R29A, R30A and R31A, which were located 200 - 1200 km from the backbone array seismometers. For earthquakes with smaller magnitudes (M 2.8 - M 3.2) we found there were some similarities in the phase of the real and SRI seismograms constructed on these three target sensors, but these similarities were only reproducible for earthquakes that originated within 2000 km of the backbone array. At the largest length scale sampled in this study, SRI was rarely able to reconstruct earthquake seismograms on sensors WDC and GOGA, which were located up to 2420 km from the backbone array seismometers.

However, we found that SRI *was* successful at constructing the seismograms from the M 6.0 Malawi earthquake on these largest length scales (correlation coefficient of 0.8 for the SRI construction at target sensor WDC). Thus, we considered 19 additional earthquakes whose earthquake energy propagated towards the North-South aligned array from the east. Particularly robust SRI seismograms were constructed of events that originated within the northern Caribbean. From this azimuth, earthquake energy propagates through the stable eastern province of the United States before arriving at the backbone array, sampling the less attenuating regions of the Gulf Coastal Plain, the Central Lowlands and the Great Plains. Alternatively, when the earthquakes originate west of the backbone array, off the coast of California and further afield, e.g., in Japan and New Zealand, the earthquake energy is required to propagate across the western United States Cordillera before arriving at the backbone array. The structurally complex nature of this western province acts to strongly attenuate the seismic energy that propagates through it. Consequentially we found that SRI was less successful at reconstructing earthquake seismograms at the largest length scale within this tectonically active zone.

To further understand the effects of the different length scales on the SRI

reconstructions, we analysed the signal-to-noise ratios (SNRs) of the three components that comprise an SRI seismogram: 1) the estimated Green's functions, 2) the event recordings, and 3) the correlation/convolution functions. This allowed the limitations of the method to be determined. SRI performed effectively when using estimated Green's functions (SRI propagators) with SNR values > 15 to project earthquake signals that had been recorded on backbone array seismometers with SNR values > 4. These values are not definitive: providing the SRI propagators have high SNR values, we have shown that they can project poorly recorded earthquake energy (SNR ~ 3) to target sensors located < 1200 km from the backbone array seismometers. The correlation/convolution functions are constructed between all 'target sensor-backbone seismometer' receiver pairs and have been shown to exhibit varied SNR values depending on the positions of the backbone seismometers within the array. We rely on the correlation/convolution functions constructed on backbone seismometers located around approximate stationary phase regions of the receiver boundary to have the largest SNR values as they provide the largest contribution to the final SRI seismogram.

These SNR constraints thus provide additional criteria that should be added to the SRI methodologies developed throughout this PhD and discussed in Chapter 3. These new criteria should be invoked at each relevant stage in the data processing as extra quality control analyses, thus determining whether the available data should be used to perform SRI, or whether the method is likely to construct unreliable earthquake seismograms if those data are used.

Bibliography

Baqer, S., and B. Mitchell (1998), Regional variation of Lg coda Q in the continental United States and its relation to crustal structure and evolution, Pure and Applied Geophysics, 153(2-4), 613–638, doi:{10.1007/s000240050210}.

Curtis, A., and D. Halliday (2010), Source-receiver wave field interferometry, Physical Review E, 81(4, 2), doi:{10.1103/PhysRevE.81.046601}.

Curtis, A., Y. Behr, E. Entwistle, E. Galetti, J. Townend, and S. Bannister (2012), The benefit of hindsight in observational science: Retrospective seismological observations, Earth and Planetary Science Letters, 345, doi:{DI10.1016/j.epsl.2012.06.008}.

Dalton, C., and G. Ekström (2006), Global models of surface wave attenuation, Journal of Geophysical Research: Solid Earth, 111(B5), n/a–n/a, doi:10.1029/2005JB003997.

Halliday, D., and A. Curtis (2009), Seismic interferometry of scattered surface waves in attenuative media, Geophysical Journal International, 178(1), 419–446, doi:{10.1111/j.1365-246X.2009.04153.x}.

Lin, F.-C., V. Tsai, and M. H. Ritzwoller (2012), The local amplification of surface waves: A new observable to constrain elastic velocities, density, and anelastic attenuation, Journal of Geophysical Research: Solid Earth, 117, doi:{10.1029/2012JB009208}.

Slob, E., D. Draganov, and K. Wapenaar (2007), Interferometric electromagnetic Green's functions representations using propagation invariants, Geophysical Journal International, 169(1), 60–80, doi:{10.1111/j.1365-246X.2006.03296.x}.

Snieder, R. (2004), Extracting the Green's function from the correlation of coda waves: A derivation based on stationary phase, Physical Review E, 69(4, 2), doi:{10.1103/PhysRevE.69.046610}.

CHAPTER 7

Green's Function Estimation by Multidimensional Deconvolution (MDD)

7.1 Outline

Here we construct inter-receiver Green's functions using multidimensional deconvolution (MDD). This is an alternative method to correlation which often does not construct the accurate Green's function G, but an estimate of G with a spatially-blurred source. This estimate of G is termed the correlation function C and the blurring of the true Green's function source is quantified by the interferometric point-spread function Γ. To obtain the true Green's function, the correlation function is deconvolved by the point-spread function. This inversion is performed and stabilised using singular value decomposition: a tolerance value is defined and singular values with an amplitude less than the tolerance value are excluded from the inversion. Both the correlation function and the point-spread function are constructed using processes of cross-correlation and, unlike other work that has used MDD for Green's function estimation, we cross-correlate real earthquake data recorded on seismometers from the USArray seismic network rather than using ambient noise. We separate these seismometers into two groups: one group consists of up to 12 seismometers that comprise our backbone seismometer array, the second group consists of four seismometers that become our target sensors. The Green's function estimates are then constructed between each target sensor-backbone seismometer pair. We compare the estimated Green's functions constructed using MDD with those same Green's

functions constructed using ambient noise interferometry as described in Section 3.2. The MDD method is often successful at constructing Green's function estimates that are comparable with those constructed using noise interferometry, despite using far fewer data. However, the success of the MDD method and the quality of the MDD results are limited by the location of the backbone seismometers with respect to the earthquake epicentres. Herein we have insufficient earthquake sources to provide full illumination of the backbone array of seismometers. This has significantly effected the outcome of MDD in this study, but the method is one which could be very effective in a real earthquake seismology setting if better source and receiver geometries were utilised.

7.2 Introduction

Chapters 4 to 6 have focussed on methods of correlational interferometry to estimate the Green's functions between pairs of receivers using ambient noise. These Green's function estimates were then used as the propagators to perform source-receiver interferometry (SRI), thereby constructing earthquake seismograms retrospectively. However, noise interferometry as in Equation (2.14) requires an implicit assumption that the medium is non attenuating, and that sources surround the volume of interest evenly (Wapenaar and Fokkema, 2006). The former follows from the processes of correlation, and thus time-reversal, that govern Equation (2.14) and are invalid in attenuative media, the latter follows from Green's theorem. Furthermore, in Section 3.3 we showed that the quality of the estimated Green's functions constructed using noise interferometry decreased as the distance between the receiver pair increased. These poorly constructed Green's function estimates then impeded the results of SRI in Chapters 4 to 6 over large length scales.

Here we provide an alternative approach to Green's function estimation in an attempt to improve the Green's function estimates constructed over large distances by noise interferometry. The improved, robust Green's functions can then be used as the propagators in SRI to construct earthquake seismograms more accurately, retrospectively.

We first introduce the method of multidimensional deconvolution (MDD) for Green's function estimation, which refers to the deconvolution of wavefields recorded on many receivers. The method expands on seismic interferometry by 1D deconvolution, which was first used by Snieder and Safak (2006) to extract the

building response of the Robert A. Millikan Library in Pasadena, California, using the deconvolution of waves recorded at different locations within the building. The deconvolved waves were then used to determine the shear velocity and the attenuation of the building. Similarly, Mehta et al. (2007) used the deconvolution of earthquake signals recorded on the Treasure Island Array, California, to obtain the upwards and downwards waves that propagate along the array. These waves were then used to estimate the P- and S-wave velocities of the near-surface. Extensive reviews of the theory and application of interferometry by deconvolution are provided by Vasconcelos and Snieder (2008a,b).

The natural transition to 2D or 3D wavefield deconvolution in seismic interferometry was introduced by Wapenaar et al. (2008a). The authors used multidimensional deconvolution for controlled-source seismic and electromagnetic data, which was later used by van der Neut et al. (2011) to redatum controlled seismic free-surface sources to downhole receiver arrays, and by van Dalen et al. (2014) to improve the virtual-source surface wave responses estimated by cross-correlation. The theory was extended to passive seismic data by Wapenaar et al. (2008b). The authors explain how MDD can be performed without knowledge of the source positions and the medium parameters, and, unlike correlation-type interferometry, it does not rely on the regularity of the source positions. Furthermore, MDD accounts for different types of sources, variations in the power spectra, non-uniform radiation characteristics and spatially extended sources (Wapenaar et al., 2008b). MDD has since been developed for both transient and noise sources (Wapenaar and van der Neut, 2010; van der Neut et al., 2010; Wapenaar et al., 2011a) and such derivations have been used in numerical examples to construct improved surface wave estimates (Wapenaar et al., 2011b).

Here we use MDD to estimate the Green's functions between pairs of seismometers from within the USArray seismic network. We follow the methods of Wapenaar and van der Neut (2010) where the correlation function C (Equation (2.17)) is proportional to the true Green's function with a blurred source. The blurring of the Green's function is quantified by the point-spread function Γ (Equation (2.15)).

This study is unique in that it utilises real earthquake data to construct the interferometric components C and Γ in Equations (2.15) and (2.17), respectively. In Equation (2.18) we show that this correlation function is proportional to the true, sought Green's function G, with its source smeared in space and time by the point-spread function. To "de-blur" the Green's function obtained by the correlation method and to obtain a true estimate of G, C is deconvolved for Γ as in Equation (2.22). For full

derivations of the theory behind MDD see Section 2.2.3, and for a detailed description of the practical methodology see Section 3.4.

7.3 Data and Methodology

Data

Here we consider 15 earthquakes that occurred between January 2009 and April 2010 with magnitudes between M 2.4 and M 6.5. All events were located west of the North-South aligned backbone array, in Nevada, Northern California or off the coast of California. These events are listed in Table 7.1 and shown in Figure 7.1 (yellow and red stars).

Table 7.1: A list of earthquakes used to perform MDD. The final four earthquakes are recorded on the backbone array seismometers with an amplitude greater than the background noise level. These events are used in a separate study to assess the quality of the earthquake data required to perform MDD.

Magnitude	Location	Origin date
2.4	Northern California	15.04.2010
2.6	Off the coast of California	15.01.2010
2.8	Northern California	11.03.2010
2.8	Nevada	06.12.2009
3.2	Nevada	12.02.2010
4.0	Off the coast of California	29.05.2009
4.0	Northern California	22.12.2009
4.1	Northern California	04.01.2010
4.2	Off the coast of California	04.11.2009
4.5	Off the coast of California	06.03.2010
4.7	Off the coast of California	02.10.2009
Surface wave signal greater than the noise		
4.5	Off the coast of California	15.04.2010
5.0	Off the coast of California	07.08.2009
5.1	Central California	01.10.2009
6.5	Off the coast of California	10.01.2010

Later, we consider only those events whose surface wave signals were recorded with an amplitude greater than the amplitude of the background noise level. The locations of these four earthquakes are highlighted by the red stars in Figure 7.1. Their details

are listed at the bottom of Table 7.1 and all four events have magnitudes greater than M 4.5. All lower magnitude events were not recorded clearly on the backbone seismometers as surface wave signals were not discernible from the noise. The effect of such low magnitude events on the MDD process is not yet fully understood, but loosely speaking, earthquake recordings that are predominantly noise may be more likely to impede the MDD process than improve the final Green's function estimate. The elimination of the noisy records in the final analysis below is an attempt to gain a better understanding of the quality of the earthquake data required to perform MDD. However, we do note that Wapenaar et al. (2011b) constructed accurate surface wave estimates by MDD in a numerical example using only modeled ambient seismic noise.

The earthquake signals are recorded on target sensors R29A, R30A, R31A and GOGA (triangles in Figure 7.1) and on seismometers from within the North-South aligned backbone seismometer array (circles in Figure 7.1). These backbone seismometers are located along 2-line combinations of seismometers from within the USArray TA network and were chosen as they obeyed the spatial criteria defined in Section 3.6.1 for source-receiver interferometry (SRI). Although SRI is not the purpose of this study, we kept the target sensor-backbone seismometer pairs the same so that a direct comparison could be made between MDD and the results of noise interferometry presented in Section 3.3 and used throughout Chapters 4 to 6. However, computational restrictions placed limits on the size of the matrices that could be constructed and the size of the inversion that could be executed, thus limiting the backbone array to just 11 or 12 of the central seismometers. The only deviation from the spatial criteria was for target sensor R31A. In Section 3.3 we constructed the Green's functions between R31A and all seismometers located along lines 27A and 28A of the USArray TA network. We note however that a large proportion of seismometers are missing from the central region of line 28A. Thus, at R31A we chose to change the 2-line combinations of the seismometers to include those seismometers along lines 26A and 27A. This created a denser array of backbone seismometers.

The earthquake signals recorded on the target sensors and backbone seismometers are downloaded and processed as detailed in Section 3.4. These signals are sampled and filtered at the same rate and frequency as the ambient noise data that were used to construct the estimated Green's functions via noise interferometry in Chapters 4 to 6.

We normalise the earthquake recordings to remove the effect of the varying earthquake magnitudes on the MDD process. For any one earthquake, we select one seismometer from the backbone array and normalise all recordings of that event

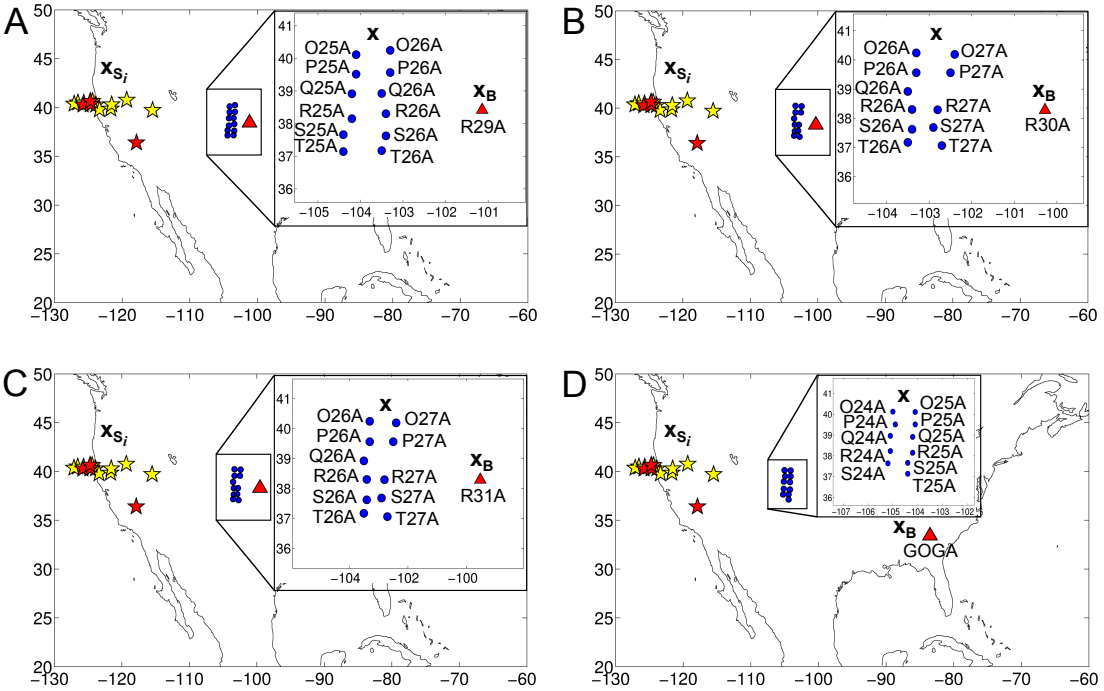

Figure 7.1: Source and receiver geometries used to perform MDD between a backbone array seismometer $\mathbf{x}$ (circles) and a target sensor at $\mathbf{x_B}$ (triangles) using 15 earthquakes (yellow and red stars) or four earthquakes (red stars only) originating from locations such as $\mathbf{x_{S_i}}$. Figures (A)-(D) show the different combinations of target sensors and backbone seismometers between which MDD is performed.

to the absolute maximum amplitude of the event recorded on the chosen backbone seismometer. Here, we choose seismometer R25A as it is located within the centre of the array and thus approximates the location of a stationary phase point on the receiver boundary (Snieder, 2004). R25A should thus be illuminated sufficiently by the earthquake sources. Following this normalisation, all event recordings are of a similar amplitude, regardless of their original recorded magnitudes, and no single event will hold a significantly greater weight in the summations over the earthquake sources in Equations (2.15) and (2.17). Although seismometer R25A is not always in the backbone array used for a target sensor, i.e., for target sensors R30A and R31A we use those backbone seismometers located along lines 26A and 27A (see Figure 7.1B and C), we kept this normalisation constant as all target sensors were located along similar great circle paths (GCP) that propagated from the earthquake epicentres and intersected the backbone array approximately perpendicularly. An illustration of this geometry is shown in Figure 7.2 for an arbitrary GCP (dashed line) that propagates from within the

cluster of earthquakes to the target sensors (triangles). We observe that seismometer R25A (circle) and all three target sensors lie close to this arbitrary GCP, thus allowing the stationary phase approximation to be invoked correctly (Snieder, 2004). If the target sensors were located a significant distance off this GCP, a new GCP would thus be defined and a new backbone seismometer (that lies close to this new GCP) would need to be chosen for the normalisation.

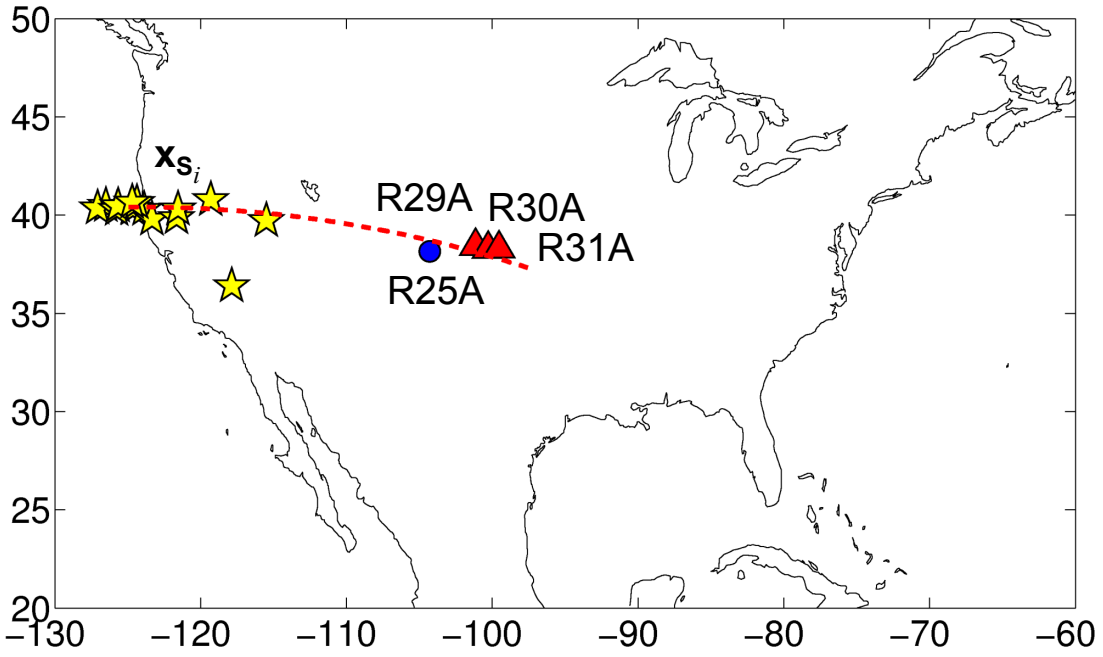

Figure 7.2: An illustration of an arbitrary great circle path (GCP) (dashed line) that propagates from within the cluster of earthquakes (stars) at locations $\mathbf{x}_{\mathbf{S}_i}$, towards seismometer R25A (circle) and target sensors R29A, R30A and R31A (triangles).

Method

Consider the geometry shown in Figure 7.1A for the 12 backbone seismometers at $\mathbf{x}$ and target sensor R29A at $\mathbf{x}_\mathbf{B}$. We first construct the point-spread function Γ as in Equation (2.15) for each $\mathbf{x}$ and for $\mathbf{x}_\mathbf{A}$ located along the backbone array. The earthquake signals are recorded on $\mathbf{x}$ and $\mathbf{x}_\mathbf{A}$ and cross-correlated. A summation is then performed over all 15 earthquakes at locations $\mathbf{x}_{\mathbf{S}_i}$ to construct the point-spread function $\Gamma(\mathbf{x}, \mathbf{x}_\mathbf{A})$. For the 12 seismometers within the backbone array, we construct 12 point-spread functions with a different seismometer occupying the location of $\mathbf{x}_\mathbf{A}$ each time. Transforming to the frequency domain, $\mathbf{\Gamma}$ is a 12x12 matrix for each frequency component.

Second, we construct the correlation function C as in Equation (2.17) between the target sensor $\mathbf{x_B}$ and each seismometer $\mathbf{x_A}$ (for $\mathbf{x} = \mathbf{x_A}$) within the backbone array. The earthquake signals are recorded on $\mathbf{x_B}$ and $\mathbf{x_A}$ and cross-correlated. Summation over all earthquake recordings constructs the correlation function C that represents the response at $\mathbf{x_B}$ from a virtual source at the location of $\mathbf{x_A}$. This correlation function is not the true response recorded at $\mathbf{x_B}$ from an impulsive source at $\mathbf{x_A}$ as the earthquake sources are not regularly distributed around a closed boundary and we cannot assume a lossless medium. C is instead blurred in space and time by the point-spread function. Transforming to the frequency domain, $\mathbf{C}$ is a 1x12 row vector for each frequency component.

The correlation function $C(\mathbf{x_B}, \mathbf{x_A})$ is proportional to the sought Green's function $G(\mathbf{x_B}, \mathbf{x})$ (for $\mathbf{x} = \mathbf{x_A}$) with its source smeared in space and time by the point-spread function $\Gamma(\mathbf{x}, \mathbf{x_A})$ (Equation (2.18)) (Wapenaar et al., 2011a). To find the true Green's function thus involves MDD as in Equation (2.22).

To perform MDD we invert the point-spread function $\mathbf{\Gamma}$ as in Equation (2.21). When using real data the inversion is likely to be ill-posed and we thus aim to stabilise it using singular value decomposition. The earthquake data is sampled at 4 sps, thus the Nyquist frequency is set to 2 Hz. Figure 7.3 shows a plot of the amplitudes of all 12 singular values for each frequency component. We will only consider up to ~ 0.49 Hz as the amplitudes of the singular values are significantly lower at higher frequencies.

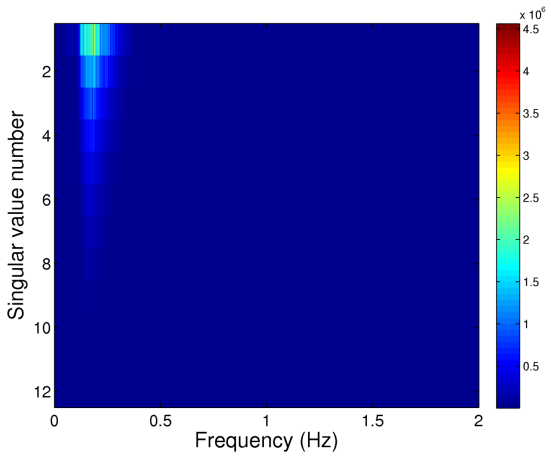

Figure 7.3: Singular values $\mathbf{\Delta}_r$ of the point-spread function $\mathbf{\Gamma}$ constructed between the 12 backbone seismometers in Figure 7.1A (circles). $\mathbf{\Gamma}$ is constructed using all 15 earthquakes shown in Figure 7.1A (yellow and red stars).

To perform the inversion via singular value decomposition we define a tolerance value below which the amplitudes of the singular values are set to zero. This tolerance value is a percentage of the global maximum singular value. Figure 7.4A shows the singular values of the 12x12 matrix $\mathbf{\Gamma}$ at each frequency (up to 0.49 Hz). The solid white line shows the contour of the tolerance value which is set to 10% of the global maximum singular value. This contour thus outlines the singular values that are included in the inversion for each frequency, i.e., between 0 Hz and 0.1 Hz only the first singular value is used, whilst at 0.15 Hz up to six singular values are included in the inversion. Figure 7.4B shows the amplitudes of the singular values at 0.19 Hz as indicated by the dotted white line in Figure 7.4A. We observe a severe decay in the amplitude between the first singular value and the second, shown by the large gradient of the first slope in Figure 7.4B. The decay is less severe and the slope is less steep between the second and sixth singular values. We then see a shallower slope again to the ninth singular value, but the final three singular values have amplitudes of almost zero, which is very low compared to the maximum amplitude. Our pseudoinverse problem is thus ill-posed and $\mathbf{\Gamma}$ is not a full rank matrix. Minato et al. (2011) show that one can improve the rank of the problem by increasing the illumination of the receiver array from the wavefield sources. Those authors do this by using both surface and subsurface sources and they see an increase in the number of singular values that can be used in the pseudoinverse calculation than is the case when just surface sources are used. Here we are restricted by the available earthquakes and propose that the rank of the point-spread function can only be increased by increasing the number of earthquake sources used in the summation in Equation (2.15), and by increasing the distribution of these sources so that they illuminate the backbone seismometer array more efficiently. This will be discussed more in Section 7.5.

We calculate the pseudoinverse of the point-spread function using the *pinv* function in Matlab and setting the tolerance value to between 1% and 10% of the global maximum singular value. We vary this tolerance value to see the effect of including and rejecting the smaller singular values in the inversion of $\mathbf{\Gamma}$. This effectively evaluates Equation (2.21) with r set to each tolerance value specified. The inverted point-spread function $\mathbf{\Gamma^{-1}}$ is then inserted into Equation (2.22), which is evaluated for each frequency to retrieve the 1x12 row vector $\mathbf{G}$. In the time domain, $G(\mathbf{x_B}, \mathbf{x_A})$ represents the response at $\mathbf{x_B}$ from an impulsive source at the location of $\mathbf{x_A}$, constructed from an irregular distribution of earthquake sources recorded on a regularly distributed receiver boundary, on which $\mathbf{x_A}$ is located. The target sensor at $\mathbf{x_B}$ must be located on the

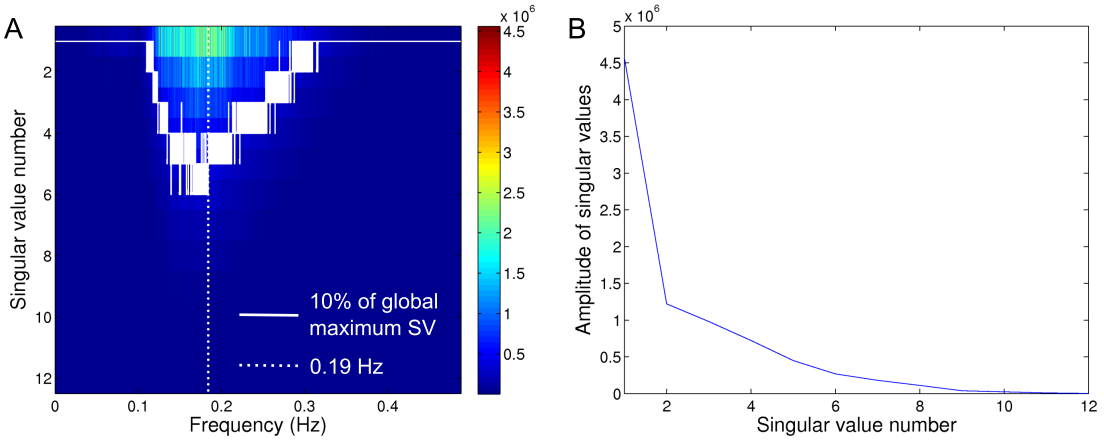

Figure 7.4: (A) Same as Figure 7.3 but up to $\sim$ 0.49 Hz. The solid white line shows the contour of the tolerance value, which is set to 10%: for each frequency, singular values with an amplitude less than 10% of the global maximum singular value, i.e., below the contour line, are excluded from the inversion. (B) Singular values of $\mathbf{\Gamma}$ at 0.19 Hz as indicated by the dotted line in (A).

opposite side of S to the earthquake sources at $\mathbf{x_{S_i}}$.

In the subsequent sections we will compare these estimates of G to the same sets of Green's functions constructed using noise interferometry as in Equation (2.14).

7.4 Results

First we focus on target sensor R29A and the 12 backbone seismometers shown in Figure 7.1A. All 15 earthquakes (yellow and red stars) are used to perform MDD. We aim to construct estimates of the Green's functions between R29A ($\mathbf{x_B}$) and each seismometer within the array ($\mathbf{x}$). The point-spread function is calculated for all 12 backbone seismometers to construct the 12x12 matrix $\mathbf{\Gamma}$, and the singular values are evaluated. Figure 7.4 shows the amplitudes of the 12 singular values up to 0.49 Hz and the tolerance value is set to 10% of the global maximum singular value, as discussed above. $G(\mathbf{x_B}, \mathbf{x})$ is shown in Figure 7.5 for backbone seismometers $\mathbf{x}$ at S25A, S26A, T25A and T26A. All four backbone seismometers are located in the south of the array. The results of MDD (solid/red trace) are compared with the results from noise interferometry (dashed/blue trace). We observe an excellent fit between the results of the two methods for all four estimates of G. In this case, MDD performs as well as ambient noise interferometry in constructing surface wave estimates of the sought Green's functions. The MDD results may contain more spurious arrivals than the noise

interferometry results (e.g., on panel C see the arrivals at $\sim$ 10 s and at $\sim$ 50 s), but the main surface wave arrival is comparable with that produced by noise interferometry.

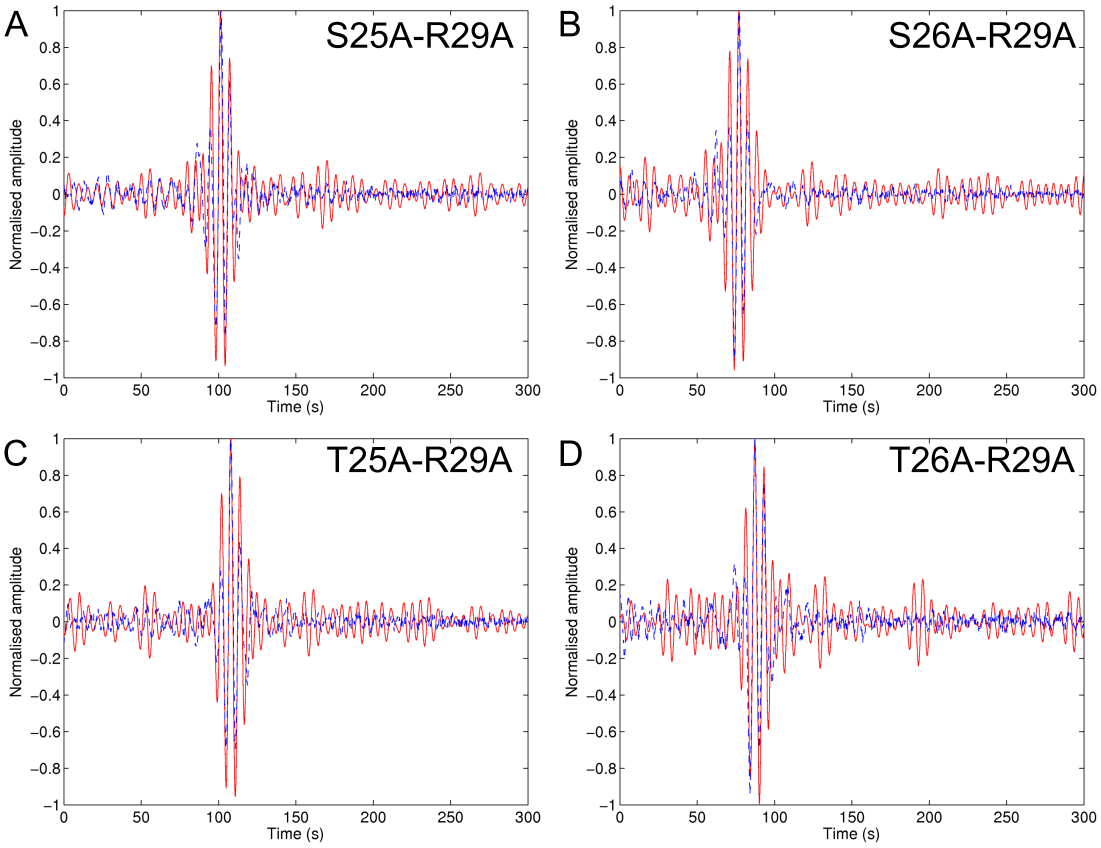

Figure 7.5: The estimates of $G(\mathbf{x_B}, \mathbf{x})$ between target sensor R29A ($\mathbf{x_B}$) and backbone seismometers ($\mathbf{x}$) located at (A) S25A, (B) S26A, (C) T25A, and (D) T26A. $G(\mathbf{x_B}, \mathbf{x})$ is constructed using MDD (solid/red traces) and compared with the results from ambient noise interferometry (dashed/blue traces). The components of MDD ($\mathbf{C}$ and $\mathbf{\Gamma}$) are constructed using the 15 earthquakes shown in Figure 7.1A (yellow and red stars). The inversion is performed using a tolerance value of 10% such that the singular values of $\mathbf{\Gamma}$ that lie below the solid white contour line in Figure 7.4A are set to zero.

Next we consider four seismometers located in the north of the backbone array. Figure 7.6 shows the estimates of G constructed between target sensor R29A and backbone seismometers P25A, P26A, Q25A and Q26A using MDD (solid/red traces) and noise interferometry (dashed/blue traces). Using the MDD method, the surface wave arrivals are difficult to identify as many large amplitude, spurious events obscure the first arrivals. However, the estimates of G from noise interferometry are also

poorly constructed on these backbone seismometers compared to the estimates of G that were constructed successfully on backbone seismometers S25A, S26A, T25A and T26A. We thus observe a strong bias in the results of both methods with respect to the backbone seismometer location. This is likely to be more pronounced in the results of MDD as the method requires a regular receiver boundary that is illuminated sufficiently by the earthquake sources. In noise interferometry however we presume that the noise sources are distributed homogeneously around the region of interest and thus that their energy illuminates a receiver boundary (that may be spatially irregular) isotropically.

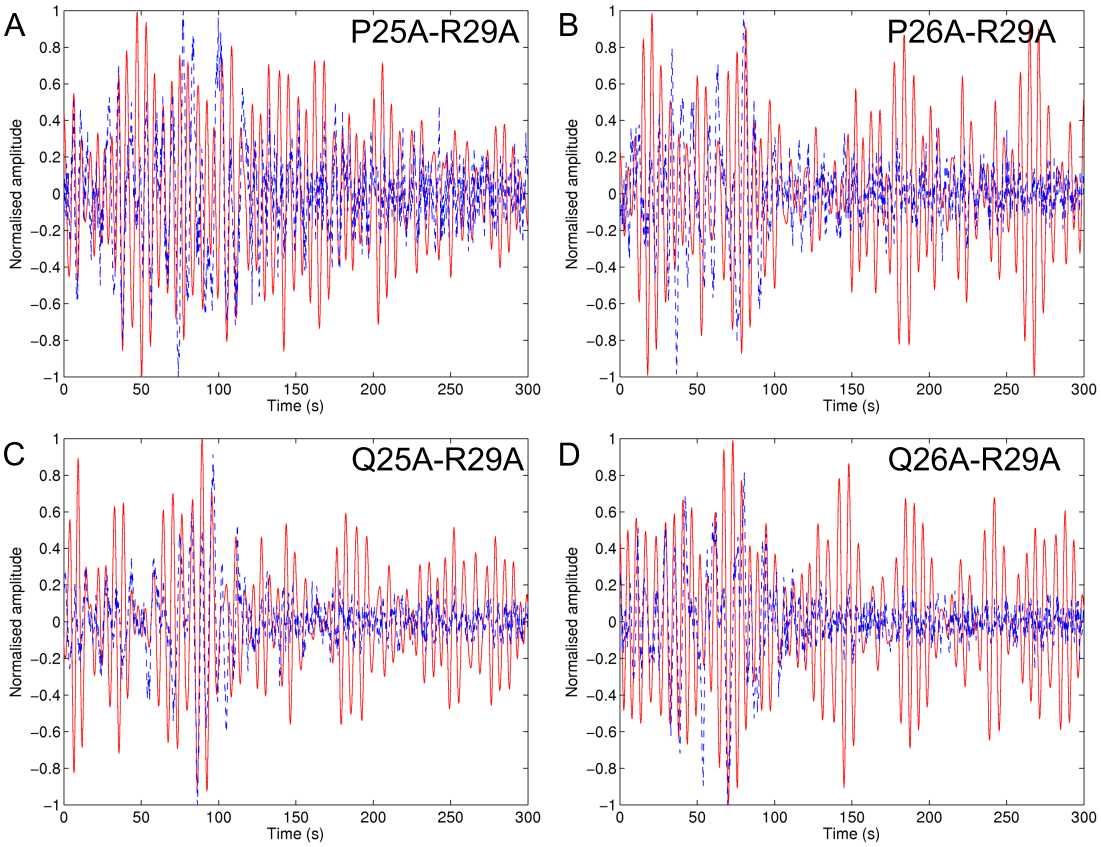

Figure 7.6: Same as Figure 7.5 but the Green's function estimates are constructed between R29A and backbone seismometers (A) P25A, (B) P26A, (C) Q25A, and (D) Q26A.

To test the effect of the pre-defined tolerance value on the MDD process, we lower the threshold to just 1% of the global maximum singular value. Thus, all singular values that have an amplitude less than 1% of the amplitude of the global maximum singular value are excluded from the inversion. The singular values whose amplitudes are

greater than 1% of the global maximum lie above the white contour line in Figure 7.7 and we observe that, for some frequencies (e.g., between $\sim$ 0.15 Hz and $\sim$ 0.22 Hz), 10 or 11 of the 12 singular values are used to calculate the pseudoinverse of $\mathbf{\Gamma}$.

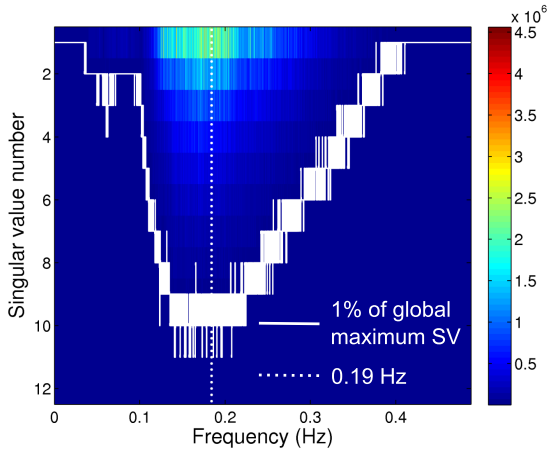

Figure 7.7: Same as Figure 7.4A but the white contour line is for a tolerance value of 1% of the global maximum singular value.

The estimates of G between target sensor R29A and backbone seismometers Q25A and S25A are shown in Figure 7.8 for MDD (solid/red traces) and ambient noise interferometry (dashed/blue traces). We again observe that the estimate of the Green's function between S25A and R29A is constructed well using MDD and the surface waves are comparable to those constructed using noise interferometry. Changing the tolerance value of the pseudoinverse calculation from 10% to 1% has thus had little effect on the final MDD construction of this Green's function estimate. The Green's function estimate between Q25A and R29A is less well constructed using MDD than that constructed between S25A and R29A. However, we observe that lowering the tolerance value to include singular values whose amplitude is greater than 1% of the global maximum singular value has improved the final Green's function estimate from that constructed using a tolerance value of 10% of the global maximum (Figure 7.6C). The surface waves constructed using MDD are now more comparable to the surface waves constructed using noise interferometry, but the results of both MDD and noise interferometry are 'noisy'. In this instance, including more singular values within the inversion at each frequency does however help to improve the Green's function estimate using MDD, and it does not deteriorate those Green's functions that were constructed well using the higher tolerance value of 10% (at seismometers S25A,

S26A, T25A and T26A).

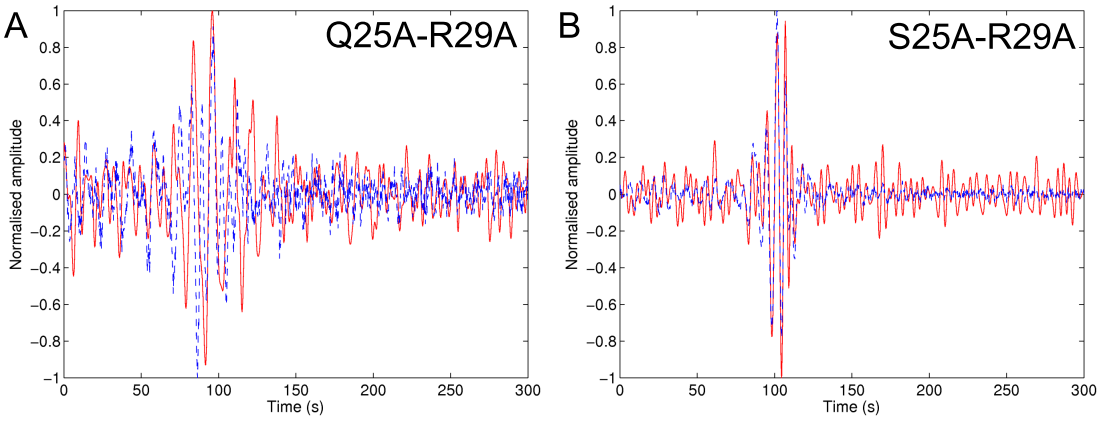

Figure 7.8: Same as Figure 7.5 but the Green's function estimates are constructed between target sensor R29A and backbone seismometers (A) Q25A, and (B) S25A. Furthermore, MDD is performed using a tolerance value of 1% such that the singular values of $\mathbf{\Gamma}$ that lie below the white contour line in Figure 7.7 are excluded from the inversion.

The final test determines the extent to which the quality of the earthquake data effects the MDD method. We consider just four earthquakes that occurred with magnitudes greater than M 4.5 and were recorded successfully on the backbone seismometers (i.e. the recorded surface wave arrivals were discernible above the background noise level). These four events are listed at the bottom of Table 7.1 and their epicentres are highlighted by the red stars in Figure 7.1. The signals from the four events are recorded on the backbone seismometers and the target sensors and cross-correlated to construct the point-spread functions $\Gamma(\mathbf{x}, \mathbf{x_A})$ (for each $\mathbf{x}$ and $\mathbf{x_A}$) and the correlation function $C(\mathbf{x_B}, \mathbf{x_A})$ as in Equations (2.15) and (2.17), respectively. The singular values of the point-spread function $\mathbf{\Gamma}$ are shown in Figure 7.9 for each frequency component up to 0.49 Hz. Comparing the decay of the singular values at 0.19 Hz in Figure 7.9B with the same plot in Figure 7.4B for $\mathbf{\Gamma}$ constructed using the recordings of all 15 earthquakes, we observe a much sharper decay in the amplitudes of the singular values when using just the four high magnitude events. In both figures there is a large decay between the first and second singular values and this decay is of the same order of magnitude regardless of the number of earthquakes used. However, when using just the four larger events, the singular values decay to zero by the 5^{th} singular value. Thus, more than half of the singular values are excluded from the inversion. We select a tolerance value of 1% such that all singular values whose amplitude is less than 1% of the global

maximum singular value are excluded from the inversion. This corresponds to all singular values below the solid white contour line in Figure 7.9A.

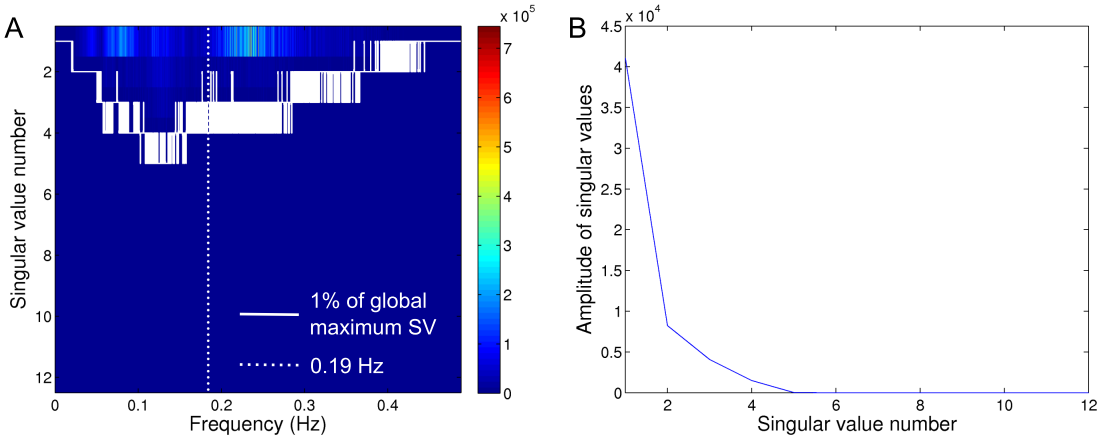

Figure 7.9: Same as Figure 7.4 but $\mathbf{\Gamma}$ is constructed using only those earthquakes whose surface wave arrivals were discernible above the background noise level The epicentres of the four earthquakes that fit this criteria are shown in Figure 7.1A (red stars). A tolerance value of 1% is chosen such that all singular values whose amplitude is less than 1% of the global maximum singular value are excluded from the inversion. These singular values lie below the solid white contour line and we observe that a maximum of five singular values are included in the inversion (e.g., for frequencies between $\sim$ 0.1 Hz and $\sim$ 0.15 Hz). (B) The decay of the singular values of $\mathbf{\Gamma}$ at 0.19 Hz as indicated by the dotted line in (A).

We perform MDD to construct estimates of $G(\mathbf{x_B}, \mathbf{x})$ (for $\mathbf{x} = \mathbf{x_A}$) between target sensor R29A and each of the 12 backbone seismometers shown in Figure 7.1A. Figure 7.10 shows the estimates of the Green's functions constructed between R29A and six of the 12 backbone seismometers using MDD (solid/red traces) and ambient noise interferometry (dashed/blue traces). Backbone seismometers O25A (A) and P26A (B) are located towards the north of the array. Here we observe that the estimated Green's functions are poorly constructed using both MDD and noise interferometry as the main surface wave arrival is masked by other large amplitude events (e.g., in Figure 7.10A between 0 s and 50 s). Seismometers Q25A (C) and R26A (D) are located approximately within the centre of the array and we observe that the surface wave estimates of the Green's functions are better constructed at these locations using both MDD and noise interferometry: both methods construct Green's function estimates that are in phase with one another and the surface wave arrival times are comparable at $\sim$ 80 s in Figure 7.10C and at $\sim$ 70 s in Figure 7.10D. Finally,

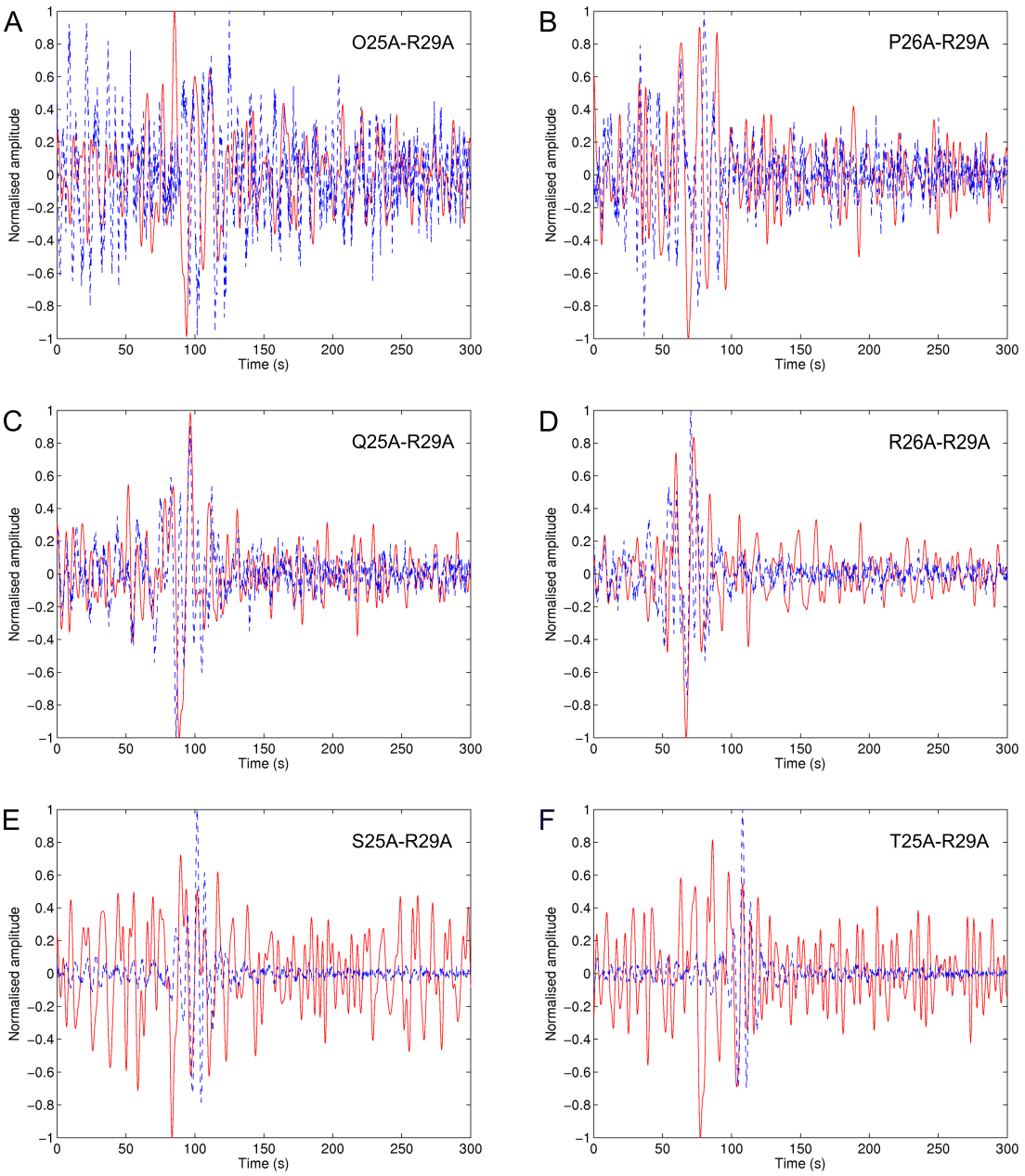

Figure 7.10: The estimates of $G(\mathbf{x_B}, \mathbf{x})$ between target sensor R29A ($\mathbf{x_B}$) and backbone seismometers ($\mathbf{x}$) located at (A) O25A, (B) P26A, (C) Q25A, (D) R26A, (E) S25A, and (F) T25A. $G(\mathbf{x_B}, \mathbf{x})$ is constructed using MDD (solid/red traces) and compared with the results from ambient noise interferometry (dashed/blue traces). The components of MDD ($\mathbf{C}$ and $\mathbf{\Gamma}$) are constructed using just four earthquakes (red stars in Figure 7.1). The inversion is performed using a tolerance value of 1% such that the singular values of $\mathbf{\Gamma}$ that lie below the white contour line in Figure 7.9A are set to zero.

seismometers S25A (E) and T25A (F) are located towards the south of the array. The Green's function estimates constructed using noise interferometry exhibit clear surface wave arrivals but these events are very poorly constructed using the MDD method. We thus conclude that when using only four earthquakes to construct the MDD matrices $\mathbf{C}$ and $\mathbf{\Gamma}$, the illumination of the receiver array is not sufficient to accurately invert $\mathbf{\Gamma}$ for MDD.

In this case, the MDD method performs best when the seismometers are located towards the centre of the receiver array. This is likely due to the cluster of three large magnitude earthquakes located off the coast of California which creates a bias in the illumination of the array. This bias is along the great circle path that propagates from the earthquake epicentres to the location of target sensor R29A. Those seismometers located along this great circle path are thus more strongly illuminated than seismometers located towards the edges of the array, further from the great circle path.

Finally, we present a selection of estimated Green's functions constructed between target sensors R30A, R31A and GOGA and combinations of backbone seismometers (see Figure 7.1B, C and D for the locations of all target sensors and their corresponding backbone arrays). The matrix components of MDD ($\mathbf{\Gamma}$ and $\mathbf{C}$) are constructed first using all 15 earthquakes, and second using just the four large magnitude events. Tolerance values of both 1% and 10% are used to perform the matrix inversions of $\mathbf{\Gamma}$ as in Equation (2.21). The results of MDD in all instances are compared with the results of noise interferometry.

R30A and R31A

Figure 7.11 shows the results of MDD (solid/red traces) constructed between target sensor R30A and backbone seismometers T27A and Q26A. The estimates of G are compared with the results from noise interferometry (dashed/blue traces). First we use all 15 earthquakes shown in Figure 7.1B (yellow and red stars) to construct the correlation function $\mathbf{C}$ and the point-spread function $\mathbf{\Gamma}$. $\mathbf{\Gamma}$ is then inverted as in Equation (2.21) using a tolerance value of 1% to exclude the smallest singular values from the inversion. The estimates of G obtained at backbone seismometers T27A and Q26A using these conditions are shown in Figure 7.11A and B, respectively. The Green's function estimate constructed between Q26A and R30A using MDD is comparable with that constructed using noise interferometry as the main surface wave

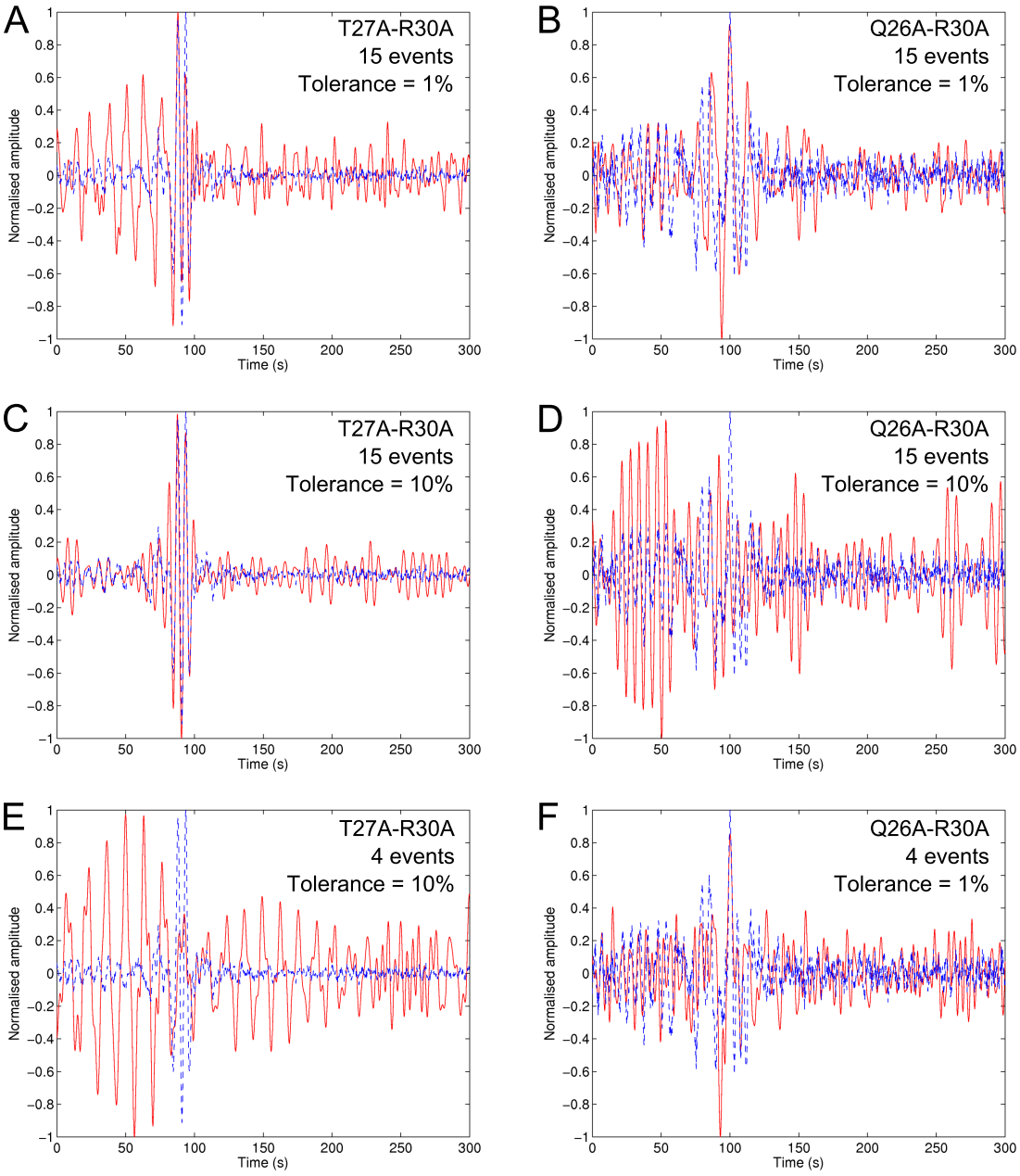

Figure 7.11: The estimates of $G(\mathbf{x_B}, \mathbf{x})$ between target sensor R30A ($\mathbf{x_B}$) and backbone seismometers ($\mathbf{x}$) located at (A,C,E) T27A, and (B,D,F) Q26A. $G(\mathbf{x_B}, \mathbf{x})$ is constructed using MDD (solid/red traces) and compared with the results from ambient noise interferometry (dashed/blue traces). (A,B) The matrix components of MDD ($\mathbf{C}$ and $\mathbf{\Gamma}$) are constructed using 15 earthquakes (yellow and red stars in Figure 7.1B) and the inversion is performed using a tolerance value of 1%. (C,D) Same as (A,B) but the inversion is performed using a tolerance value of 10%. (E,F) The MDD matrices are constructed using just four earthquakes (red stars in Figure 7.1B) and the inversion is performed using a tolerance value of (E) 10%, and (F) 1%.

arrivals are in phase. For the estimate of G constructed between T27A and R30A, large amplitude spurious arrivals obscure the first arriving surface waves (between 0 s and $\sim$ 75 s) when using the MDD method, and the match with the results of noise interferometry is thus poor.

Next we raise the tolerance value to 10% of the global maximum singular value thus excluding more singular values from the inversion. The results are significantly different. In Figure 7.11C we observe an almost perfect match between the main arrival of the estimated Green's function constructed between T27A and R30A using MDD, and that same Green's function constructed using noise interferometry. The large amplitude events that occurred up to $\sim$ 75 s in Figure 7.11A vanish from the reconstruction when fewer singular values are used in the inversion. In Figure 7.11D however, the Green's function constructed using MDD is poor in comparison to the results of noise interferometry and is also poor in comparison to the MDD result in B, which was constructed using a tolerance value of 1% in the inversion of $\mathbf{\Gamma}$. The difference in the quality of the Green's function estimate in C compared to that in D is likely due to the position of the backbone seismometer within the array and the illumination of the seismometers from the earthquake sources.

In one final comparison we construct the MDD matrices $\mathbf{C}$ and $\mathbf{\Gamma}$ using the signals from the four earthquakes that were recorded on the backbone seismometers with an amplitude greater than the background noise level (red stars in Figure 7.1B). The results of MDD for backbone seismometer T27A is shown in Figure 7.11E. We used a tolerance value of 10% in the inversion of $\mathbf{\Gamma}$ as this produced the best results when using all 15 earthquakes to construct the MDD matrices. In E we observe a very poor match between the results of MDD and the results of noise interferometry: the main surface wave arrival is not constructed at all using MDD, but large amplitude signals are constructed prior to the expected surface wave arrival time (between 0 s and $\sim$ 75 s) and afterwards from $\sim$ 125 s to the end of the plot. Excluding the 11 earthquakes of low amplitude does not improve the results of MDD in this instance. The results of MDD for backbone seismometer Q26A is shown in Figure 7.11F. Here we use a tolerance value of 1% in the inversion of $\mathbf{\Gamma}$ as this produced the best results when using all 15 earthquakes to construct the MDD matrices. This time we observe an improvement in the MDD result as the Green's function estimate constructed begins to strongly resemble the estimated Green's function constructed using noise interferometry. We thus again conclude that the position of the backbone seismometers with respect to the earthquakes used to construct the MDD matrices is important in constructing accurate

Green's function estimations through MDD.

Figure 7.12 provides the same analysis as described above, but for the estimates of the Green's functions constructed between target sensor R31A and backbone seismometers T27A and Q26A. We draw the same conclusions from these results as those stated above: when the illumination of the backbone seismometers from the earthquake sources is insufficient or biased, the success of MDD depends on the location of the backbone seismometers within the array, such that some estimates of $G(\mathbf{x_B}, \mathbf{x})$ are constructed better than others.

GOGA

Finally, consider target sensor GOGA which is located between 1935 km and 2050 km from the backbone seismometers (see Figure 7.1D for the locations of all seismometers and earthquakes). The results of MDD are shown in Figure 7.13 (solid/red traces) and compared with the results of noise interferometry (dashed/blue traces). Here we show the estimated Green's functions constructed between target sensor GOGA and just three of the 11 backbone seismometers: seismometers P25A, R24A and T25A. Immediately we observe that the estimated Green's functions constructed using noise interferometry are very poor as no clear surface waves can be identified above the background noise level. The aim for MDD is thus to improve these Green's function estimates.

A tolerance value of 10% of the global maximum singular value was used to perform the inversion of $\mathbf{\Gamma}$ and the results of MDD were poor. An example is shown in Figure 7.13A for the estimate of G constructed between P25A and GOGA which shows that no clear surface wave arrivals can be identified. From here onwards we will only consider those MDD results constructed from inverting $\mathbf{\Gamma}$ using a tolerance value of 1% of the global maximum singular value.

Figure 7.13C and Figure 7.13E show the results of MDD obtained from using 15 earthquakes to construct the MDD matrices. The surface wave arrivals are not constructed successfully and MDD has failed to improve the Green's function estimates from the results of noise interferometry. When we exclude the earthquakes that resemble noise and use only four earthquakes to construct $\mathbf{C}$ and $\mathbf{\Gamma}$, the results of MDD improve considerably. These constructions can be seen in Figure 7.13B, D and F between GOGA and backbone seismometers P25A, R24A and T25A, respectively, and surface waves appear to be constructed between 600 s and 650 s.

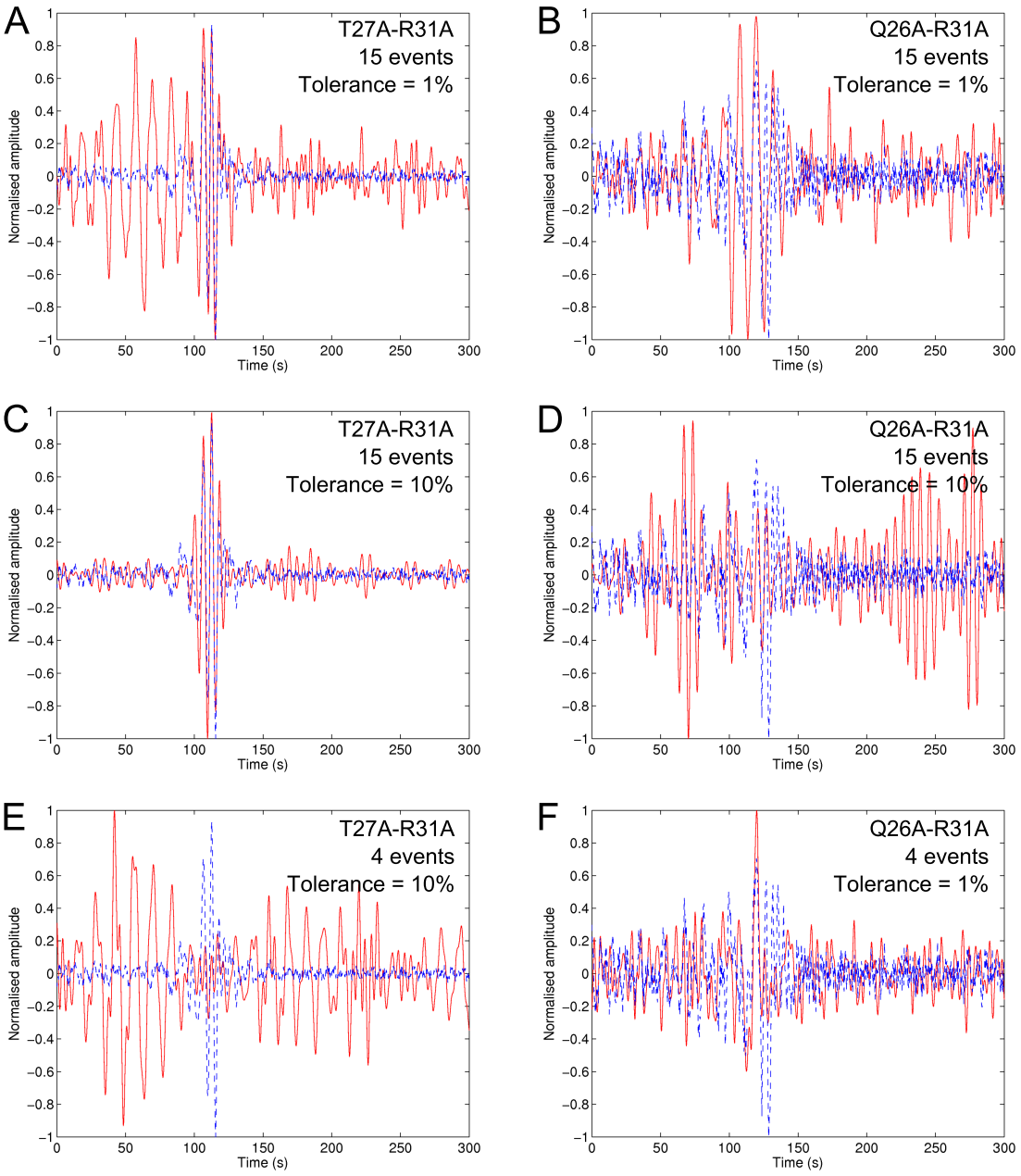

Figure 7.12: Same as Figure 7.11 but the estimated Green's functions are constructed between target sensor R31A and backbone seismometers T27A and Q26A. See Figure 7.1C for the locations of all seismometers.

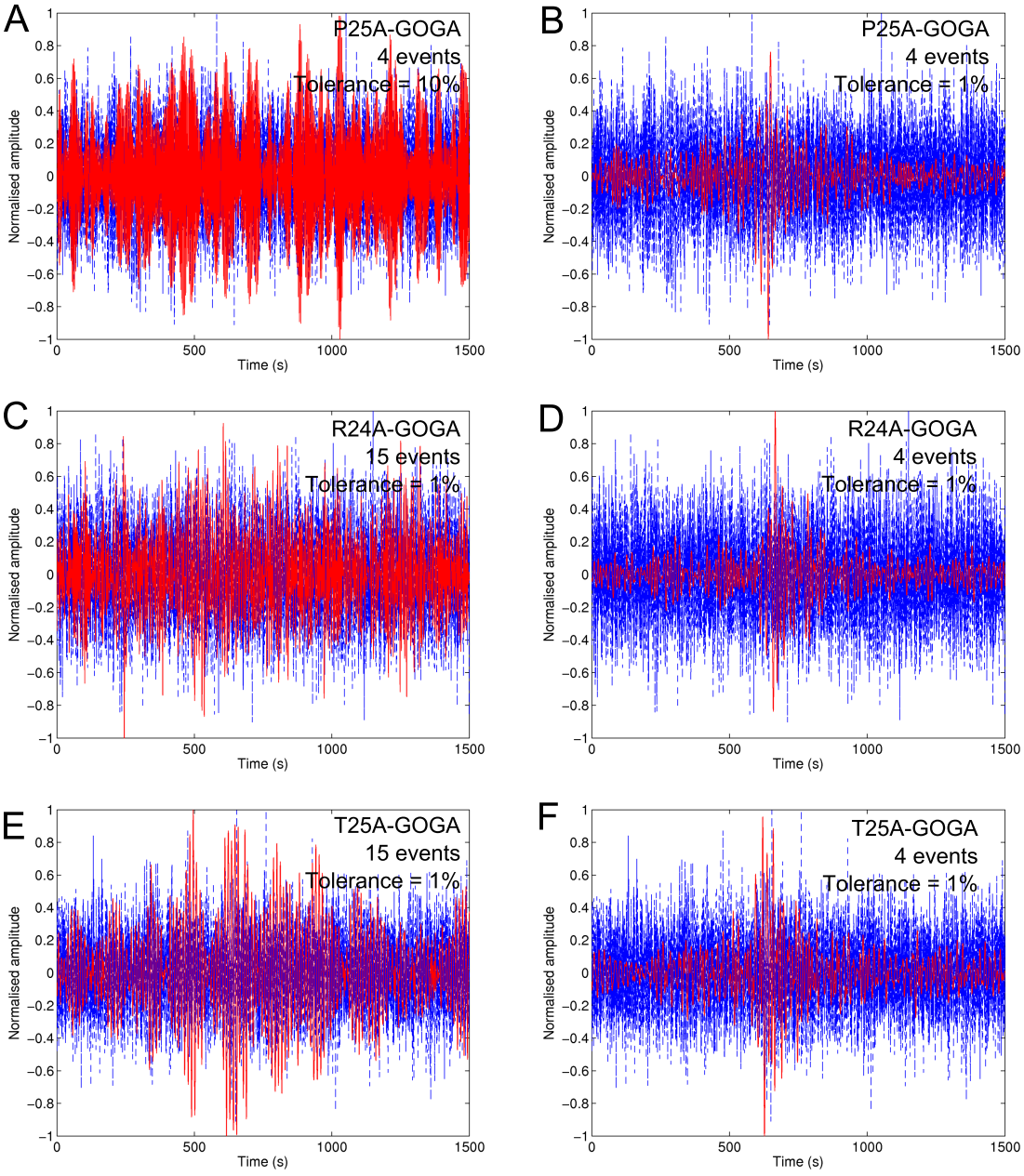

Figure 7.13: The estimates of $G(\mathbf{x_B}, \mathbf{x})$ between target sensor GOGA ($\mathbf{x_B}$) and backbone seismometers ($\mathbf{x}$) located at (A,B) P25A, (C,D) R24A, and (E,F) T25A. $G(\mathbf{x_B}, \mathbf{x})$ is constructed using MDD (solid/red traces) and compared with the results from ambient noise interferometry (dashed/blue traces). (A,B) The matrix components of MDD ($\mathbf{C}$ and $\mathbf{\Gamma}$) are constructed using just four earthquakes (red stars in Figure 7.1D) and the inversion is performed using a tolerance value of (A) 10%, and (B) 1%. (C,D) $\mathbf{C}$ and $\mathbf{\Gamma}$ are constructed using (C) 15 earthquakes (red stars in Figure 7.1D), and (D) four earthquakes (yellow and red stars in Figure 7.1D). The matrix inversion of $\mathbf{\Gamma}$ is performed using a tolerance value of 1% on both occasions. (E,F) Same as (C,D).

7.5 Discussion

We have used multidimensional deconvolution (MDD) as an alternative method to cross-correlational Green's function estimation. Unlike other work that uses MDD for such purposes (e.g. Wapenaar et al. (2008b); Wapenaar and van der Neut (2010); van der Neut et al. (2011); Wapenaar et al. (2011a,b); Minato et al. (2011); van Dalen et al. (2014)) we utilised real earthquake data recorded on real seismometer arrays located in the centre of the United States. This is the first time earthquake seismograms have been used to perform MDD. Wapenaar et al. (2011b) performed a similar analysis in an earthquake seismology setting but the authors synthesised (modeled) ambient seismic noise sources and modeled the surface wave responses from the sources using the PREM model. These modeled surface waves were then used to construct the point-spread function and the correlation function using time-averaging of the wavefields, as opposed to summation over the individual source locations as in Equations (2.15) and (2.17). Inversion of the point-spread function was then performed to estimate the Green's functions between pairs of USArray seismometers. The results of MDD were compared with the results of noise interferometry using the same modeled data, and with the results of the directly modeled surface waves between the receiver pairs. The MDD results were a significant improvement on the results of noise interferometry and were a close match with the modeled surface waves. By comparison, our results of MDD are less conclusive: the success of MDD is significantly limited by the source and receiver geometries and we propose that an insufficient illumination of the backbone seismometer array from the earthquake sources used here is the cause of the change in the quality of the MDD results between pairs of seismometers.

We noticed a discernible difference in the quality of the MDD results constructed on backbone seismometers located in the south of the array to those located in the north of the array. When using all 15 earthquakes shown in Figure 7.1 (yellow and red stars) to construct the point-spread function Γ and the correlation function C, MDD was most successful in reconstructing the Green's functions between the target sensors (R29A, R30A and R31A) and backbone seismometers S25A-S27A and T25A-T27A. A selection of results between these station pairs is shown in Figures 7.5, 7.11 and 7.12 and compared with the results of noise interferometry. The 15 earthquakes used to construct Γ and C cluster at $\sim 40^\circ$ latitude and this is creating a bias in the illumination of the backbone array. To provide full illumination of the whole of the backbone array and to thus properly discretise the integral along S in Equation (2.18),

we require a higher density of earthquake sources and for these sources to be more widely distributed along the whole length of the array.

We do note however that the geology of the western United States is highly heterogeneous as a consequence of severe tectonic activity throughout its history (e.g., Baqer and Mitchell (1998)). The strongly scattering nature of the medium between the earthquake epicentres and the backbone array may thus help to enhance the illumination of the array from the earthquake sources when the availability of earthquake data is limited, and may explain why some estimates of G are constructed better than others.

The effects of using low magnitude earthquakes to construct Γ and C

The 11 earthquakes represented by the yellow stars in Figure 7.1 are of low magnitude (M 2.4 - M 4.7) and their signals are recorded on the backbone seismometers with low amplitude: their surface wave arrivals have amplitudes similar to that of the background noise level. The effect of including such low amplitude signals in the summations in Equations (2.15) and (2.17) to construct Γ and C, respectively, was not known prior to this study. From the estimates of G presented in Figure 7.5 however, we show that these earthquake recordings that resemble background noise do not necessarily impede the MDD process. Above we discussed that to improve the estimates of G further, more earthquake sources and a greater distribution of earthquake sources are required. From this study we now understand that the strength/magnitude of these earthquake sources and the quality of the surface wave signals recorded on the seismometers are not the overriding considerations.

When using low magnitude earthquakes whose surface wave arrivals resemble background noise, the problem then becomes one similar to that presented by Wapenaar et al. (2011b), where ambient noise sources were synthesised and used to construct Γ and C. However, when one considers *real* ambient seismic noise, the directional separation of the noise wavefield is necessary. In Equations (2.15) and (2.17) we consider the full observed wavefield $u(\mathbf{x_B}, \mathbf{x_{S_i}})$ from the earthquake source at $\mathbf{x_{S_i}}$ and assume that the energy from the earthquake source propagates towards the backbone array and continues past the array without being scattered back into the medium between the sources and the array. When using ambient seismic noise however, individual source locations are unknown but we assume that they completely surround the backbone array and the target sensors. The observed wavefields must

thus be separated into their inward and outward propagating components, such that only the inwards-propagating part of the noise field at backbone seismometer $\mathbf{x_A}$ is cross-correlated with the full (or outward-propagating) noise field at target sensor $\mathbf{x_B}$ (Wapenaar et al., 2011a). Wapenaar et al. (2008b), van der Neut et al. (2010) and Wapenaar et al. (2011a) provide descriptions of the separation of wavefields for MDD with passive seismic sources but this is still to be performed and published on real field data. To perform MDD using real ambient noise sources was beyond the scope of this chapter but it is the next, most obvious advance into Green's function estimation by MDD in an earthquake seismology setting.

Furthermore, the strongly scattering nature of the western United States (as discussed above) may cause the scattering of the earthquake energy back into the medium between the sources and the backbone array. This would break our assumption that back-scattering is weak across the receiver boundary S. Directional separation of the wavefields may thus help to improve the results of MDD in this study.

The effects of normalising the earthquake data

As mentioned in Section 7.3, the signals from any one earthquake recorded on the backbone seismometers and the target sensors are normalised to the absolute maximum amplitude of that event recorded on backbone seismometer R25A. This seismometer was chosen as it lay in the centre of the backbone array and was located approximately within the stationary phase region of the receiver boundary S for the target sensors at R29A, R30A and R31A. Thus, a great circle path propagating from an earthquake epicentre that intersects both the centre of the backbone array and the target sensors should also intersect seismometer R25A. Following this normalisation process, all earthquake signals were of a similar amplitude, regardless of their original recorded magnitudes. This normalisation of the earthquake data may thus explain why the low magnitude events did not deteriorate the results of MDD. To test this hypothesis we now perform MDD using the un-normalised earthquake data to construct Γ and C. We expect the larger magnitude events to dominate the cross-correlations; the earthquake sources will thus illuminate the backbone array insufficiently and the matrix inversion of $\mathbf{\Gamma}$ will be a strongly ill-posed problem.

Figure 7.14 shows the singular values of $\mathbf{\Gamma}$ up to 0.49 Hz constructed using the un-normalised earthquake data. Tolerance values of 1% (Figure 7.14A) and 10% (B) are used to perform two separate inversions. Figure 7.14C shows a cross-section of the

singular values at 0.19 Hz. We observe a severe decay in the amplitude between the first singular value and the third. The slope of this decay becomes shallower up to the eighth singular value but then decays to zero for the last four singular values. From Figure 7.14A and Figure 7.14B we observe that only the first two singular values are used in the inversions as the amplitudes of all other singular values (below the white contour lines in the figures) are too low compared to the global maximum. These singular values are set to zero and excluded from the inversion. Our problem is thus strongly ill-posed and $\mathbf{\Gamma}$ is not a full-rank matrix.

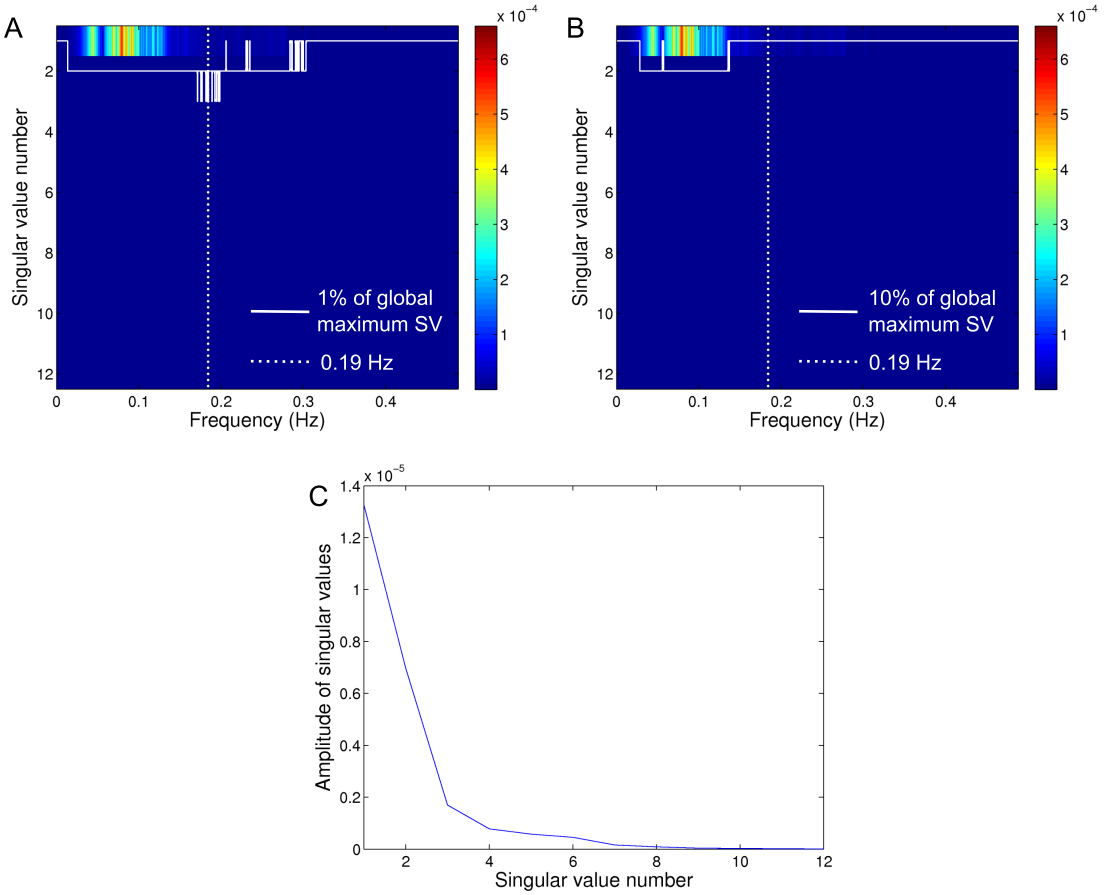

Figure 7.14: Same as Figure 7.4 but $\mathbf{\Gamma}$ is constructed using all 15 earthquakes shown in Figure 7.1A (yellow and red stars) but the recordings of these events on the backbone seismometers and target sensor R29A are not normalised. (A) Only those singular values greater than 1% of the global maximum singular value are included in the inversion of $\mathbf{\Gamma}$. This tolerance value for each frequency is outlined by the solid white contour line. (B) Same as (A) but for a tolerance value of 10%. (C) The singular values of $\mathbf{\Gamma}$ at 0.19 Hz as indicated by the dotted lines in (A) and (B).

Figure 7.15 shows a selection of results from MDD performed using the tolerance values of 1% (A,C) and 10% (B,D) as specified in Figure 7.14A and B, respectively. Estimated Green's functions are constructed between target sensor R29A and backbone seismometers Q25A (A,B) and T26A (C,D) using MDD (solid/red traces) and compared with the results of noise interferometry (dashed/blue traces). We first note that the estimated Green's function constructed at Q25A using a tolerance value of 1% (Figure 7.14A) is very similar to the estimate of G shown in Figure 7.10C, where only the four larger magnitude earthquakes were used to construct C and Γ. This supports our original hypothesis that the four larger magnitude events will dominate the cross-correlations when the earthquake data is not normalised. From Figure 7.15C and Figure 7.15D we observe that the estimates of G constructed at T26A using MDD do not match the estimates of G constructed using noise interferometry, regardless of the tolerance value specified for the inversion. Thus compare Figure 7.15D with Figure 7.5D, in which the same 15 earthquakes are used to construct C and Γ but the earthquake recordings have been normalised in the latter figure: dominant earthquakes deteriorate the results of MDD. Without normalisation, the four large amplitude events strongly bias the illumination of the receiver array and the 11 lower amplitude earthquakes add little energy to the system, thus lowering the singular values and the rank of $\mathbf{\Gamma}$.

We thus conclude that the normalisation of the earthquake data is important in ensuring sufficient illumination of the backbone array, especially if the earthquakes are of considerably different magnitudes. The 15 events used herein vary over four orders of magnitude, from M 2.4 to M 6.5. This corresponds to an increase in the energy E released by the earthquakes by a factor of $(10^4)^{3/2} = 10^6$, such that the M 6.5 event that occurred off the coast of California released 10^6 times more energy than the M 2.4 earthquake that occurred in Northern California.

Using MDD over large inter-station distances

Next we comment on the success of MDD in constructing the estimated Green's functions between target sensor GOGA and seismometers within the backbone array (see Figure 7.1D). Target sensor GOGA is located between 1935 km and 2050 km from the 15 backbone array seismometers. Figure 7.13 shows a selection of Green's functions constructed between GOGA and the backbone array using both MDD and noise interferometry. The results of noise interferometry are very poor in all figures

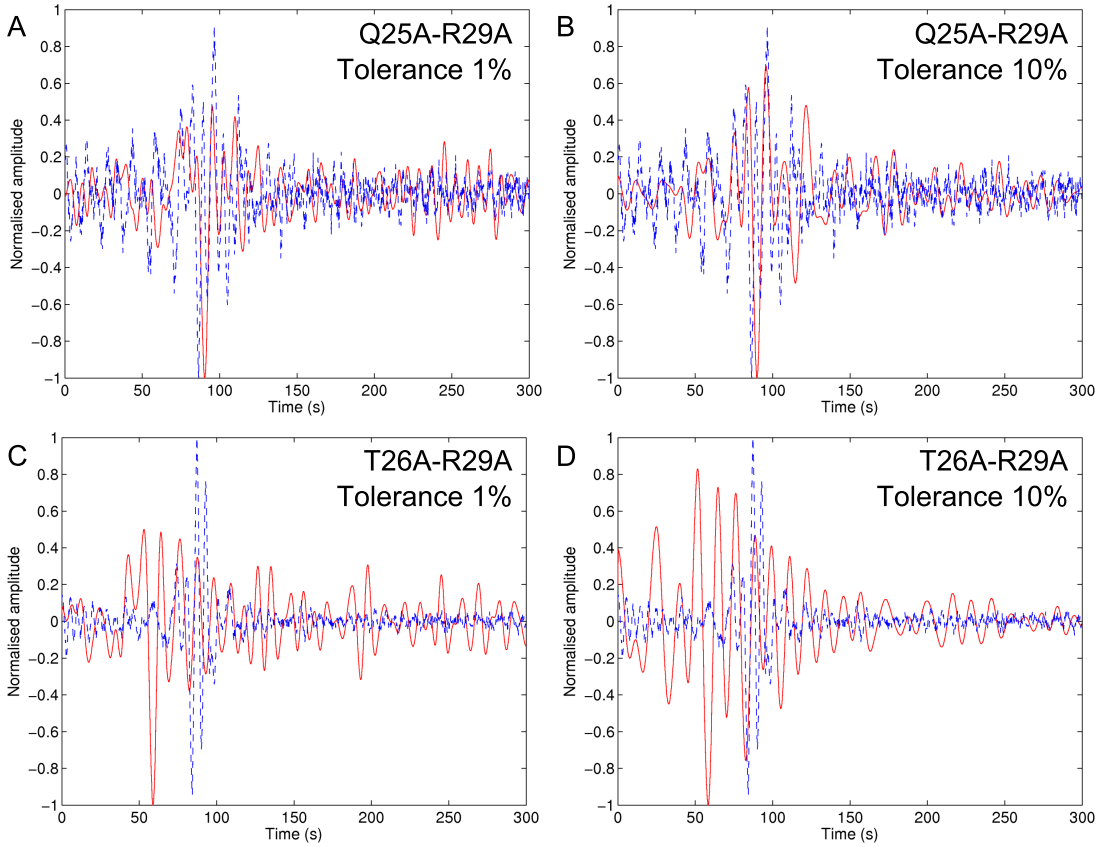

Figure 7.15: Same as Figure 7.5 but the estimated Green's functions are constructed between target sensor R29A and backbone seismometers (A,B) Q25A, and (C,D) T26A. The components of MDD ($\mathbf{C}$ and $\mathbf{\Gamma}$) are constructed using all 15 earthquakes shown in Figure 7.1A but the recordings of these events on the backbone seismometers and on target sensor R29A are not normalised. (A,C) A tolerance value of 1% is used in the inversion of $\mathbf{\Gamma}$ such that singular values below the white contour line in Figure 7.14A are set to zero and excluded from the inversion. (B,D) Same as (A,C) but for a tolerance value of 10% as indicated by the white contour line in Figure 7.14B.

as the surface wave arrivals cannot be identified. The poor quality of these estimated Green's functions was also documented in Chapter 3, which defined the average signal-to-noise ratio (SNR) of the estimated Green's functions constructed between GOGA and all 52 seismometers located along lines 24A and 25A of the backbone array to be 6.91, and the average root-mean-square (RMS) value of the expected first surface wave arrival was calculated to be 0.31 (out of a maximum possible value of 1.00). Over 340 days of ambient noise records were used in the constructions of the estimated Green's functions. Earlier we proposed that these estimated Green's functions were not poorly constructed due to insufficient data, but were a consequence of a breakdown in the underlying assumptions of correlation-type interferometry when operating over such large inter-station distances. Over these distances we cannot assume that the medium is elastic and non-attenuating. Our aim for MDD is thus to improve these estimates of G at the largest length scales as the MDD method holds in attenuative media.

We observe that when using just four out of the 15 earthquakes to construct Γ and C, and when performing the matrix inversion of $\mathbf{\Gamma}$ with a tolerance value of 1% of the global maximum singular value, we begin to construct signals that resemble surface waves between 600 s - 650 s (Figure 7.13B, D and F). Unfortunately we have no estimate of G between target sensor GOGA and the backbone seismometers with which to compare the results of MDD (in all previous comparisons we have used the result of noise interferometry as a comparable estimate of G). In Figure 7.16 we show the results of the noise interferometric Green's functions constructed between target sensor GOGA and all 52 seismometers located along lines 24A and 25A of the USArray TA network. The results have been bandpassed between 10 s and 50 s period which has enhanced the surface wave arrivals in the estimated Green's functions. The first surface wave arrivals and their moveout across the whole array can now be identified. Furthermore, quality control checks have been performed and any estimated Green's functions with SNR values ≤ 3 were removed from the study. For example, the estimated Green's function constructed between GOGA and Q25A is missing from this plot. The estimates of G are plotted according to the location of the backbone seismometer from North to South. The first trace at the top of Figure 7.16 is thus the estimated Green's function between GOGA and backbone seismometer A24A, and the last trace is the estimated Green's function between GOGA and 425A. The estimated Green's functions constructed between GOGA and backbone seismometers P25A, R24A and T25A are highlighted in red for comparison with the results of MDD in Figure 7.13. We observe that after filtering, the noise interferometric surface waves

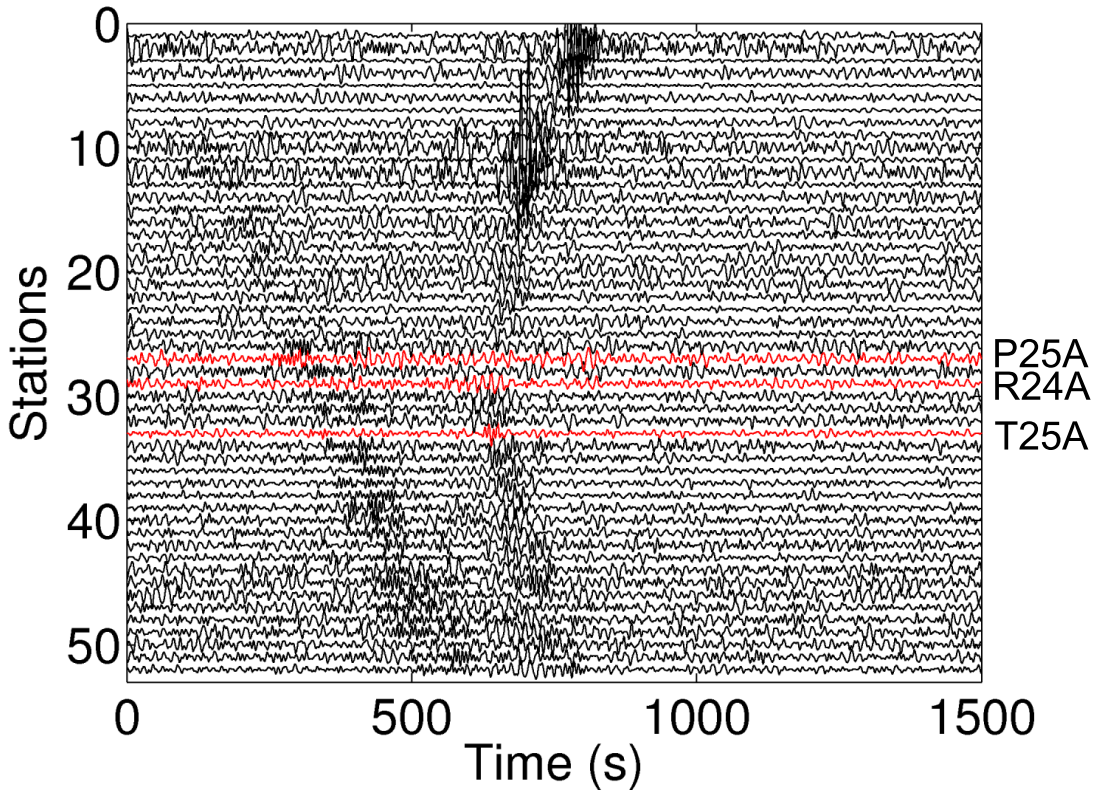

Figure 7.16: The estimated Green's functions G constructed using noise interferometry (Equation (2.14)) between target sensor GOGA and all seismometers along lines 24A and 25A of the USArray TA network. Seismograms have been bandpassed with corner frequencies at 0.02 Hz and 0.1 Hz (10 s - 50 s period). Estimates of G constructed at seismometers P25A, R24A and T25A are highlighted in red for comparison with the results of MDD in Figure 7.13.

are constructed between 600 s - 650 s at these three seismometers. These arrival times are comparable with those estimated using MDD. The frequency content of the constructed estimated Green's functions differs between the two methods, but this comparison allows us to place greater confidence in the results of MDD. If these results are correct, the MDD method has provided a significant improvement on the results of noise interferometry (for frequencies between 0.01 Hz and 1 Hz as demonstrated in Figure 7.13), despite only four earthquakes being used to construct Γ and C. This is in comparison to the 350+ days of ambient seismic noise that are used to construct the noise interferometric Green's functions between target sensor GOGA and backbone seismometers P25A, R24A and T25A.

Furthermore, we note here that for target sensor GOGA, a larger backbone array would be required to fully span the stationary phase region of the convolutional integral

on which MDD is based. Thus, to ensure the backbone seismometers are located within the correct angular aperture of the GCP for the stationary phase approximation to become valid at these larger inter-station distances, the receiver boundary S needs to be longer. Invoking a larger receiver array may thus help to improve the Green's function estimates constructed using MDD.

Earlier we discussed the strong geological heterogeneity in the western United States and proposed that the complex nature of the medium in this region would scatter the earthquake signals and enhance the illumination of the backbone array. This may be advantageous for the MDD method and the geometry shown in Figure 7.1. However, when the geometry is such that the target sensor is located to the west of the backbone array and the earthquake sources are located to the east, we are then required to construct the Green's functions within this highly attenuative region. In Section 3.3 we showed that noise interferometry constructed poor estimates of the Green's functions throughout this region: an average SNR value of 6.94 and an average RMS value of 0.28 was obtained for the Green's function estimates constructed between target sensor WDC (at location (40.58,-122.54)) and backbone seismometers located along lines 24A and 25A of the North-South aligned array (see Figure 3.4 for a map of all station locations). Correlation interferometry does not theoretically hold in an attenuative medium as time-reversal cannot be applied. We thus propose that MDD would be a more effective method than noise interferometry in constructing the Green's function estimates between WDC and the backbone array. Unfortunately this cannot be applied here as we do not have the suitable source-and-receiver geometry: earthquake sources need to be located on the opposite side of the backbone array to the target sensor.

Given the apparent success of MDD for target sensor GOGA, the next step is to insert the estimated Green's functions constructed using MDD into the methodology for source-receiver interferometry (SRI). This may improve the SRI seismograms constructed retrospectively, particularly over the larger length scales at target sensors GOGA and WDC.

Comparison of methods

The advantages and disadvantages of using MDD over noise interferometry to construct estimates of the Green's functions between pairs of seismometers are becoming clear. The MDD method has been shown to perform well over large inter-station distances: distances that are problematic in noise interferometry as the

underlying assumptions of correlation-type interferometry are violated. Furthermore, MDD only requires a small selection of earthquake sources to construct the point-spread function and the correlation function, whilst noise interferometry often requires the time-averaging of the recordings of at least six months of mutually uncorrelated noise sources (Lin et al., 2007) in order to obtain the diffusive wavefields necessary to construct an estimate of the Green's function.

We compare the two methods using the results shown in Figure 7.5 where both methods construct almost identical estimates of the Green's functions. MDD used the observations from just 15 earthquakes whilst noise interferometry used an average of 252 days of ambient seismic noise data recorded on the receiver pairs to construct the estimates of G. MDD thus requires far fewer data and can be performed at any time for any station pair, providing the signals from earthquakes are recorded on both seismometers within the pair. Within this setting (i.e., in land), noise interferometry however requires both seismometers within the station pair to be deployed for at least six months before an estimate of the Green's function between that station pair can be constructed.

However, to construct an estimate of the Green's function between a receiver pair by MDD, one of the receivers in the pair must be located on a spatially regular array of receivers on which the earthquake energy is recorded. Furthermore, the second receiver in the pair must be located on the opposite side of this receiver array to the locations of the earthquake sources. The source and receiver geometries in which MDD can be performed are thus far less pervasive than those required for noise interferometry, which can be performed between any receiver pair providing the noise sources can be assumed to be located homogeneously around the receivers.

Finally, we note that MDD is more computationally intensive in terms of processing than noise interferometry as MDD requires matrix inversion instead of trace-by-trace correlation. This has significantly restricted the spatial extent of this study as the backbone array was limited to just 12 seismometers due to memory limitations. Whilst this has been a successful preliminary study, we require a denser backbone array and more earthquake sources to obtain optimum results from MDD. This will increase the computational power required to solve this problem and we thus propose to move this study to the Terra-correlator: a computing facility for large data at the University of Edinburgh.

7.6 Conclusion

To conclude, we have used multidimensional deconvolution (MDD) to provide an alternative approach to estimating inter-receiver Green's functions in an earthquake seismology setting. The method involves inverting the point-spread function - a process that is often ill-posed when using real data. In this example we used singular value decomposition to stabilise the inversion, and defined two different tolerance values to test the sensitivity of the MDD results to the inversion. These tolerance values were defined as a percentage of the global maximum singular value of the system and determined the number of singular values to be included in the inversion. Any singular values with an amplitude below the tolerance value were set to zero and excluded from the inversion. We found that a tolerance value set to 1% of the global maximum singular value provided the best results on most occasions, but the results were dependent on the locations of the backbone seismometers within the array.

We compared the results of MDD with the results of noise interferometry, as introduced and used in Chapters 3 to 6. On some occasions the estimates of the Green's functions by MDD were a good match with those constructed using noise interferometry. Only 15 earthquakes were used in the constructions of the point-spread functions and the correlation functions for MDD, whilst 250+ days of ambient seismic noise were processed and cross-correlated to construct the noise interferometric results. The MDD method thus requires far fewer data than noise interferometry, but it is more computationally intensive as it requires matrix inversion whilst noise interferometry is a simple trace-by-trace process.

In a final test of the MDD method we attempted to construct the Green's functions between target sensor GOGA and backbone seismometers located 1935 km - 2050 km away. Noise interferometry had failed to construct accurate estimates of the Green's functions over these large inter-station distances due to a break down in one of the underlying assumptions of correlation-type interferometry in attenuative media. MDD performed well over these large distances as the constructed surface wave arrival times agreed with the results of noise interferometry, after the latter had been filtered and subjected to quality control analyses.

The 15 earthquake sources used herein did not sufficiently illuminate the backbone array. The success of the MDD method then became dependent on the location of the backbone seismometers within the array as the quality of the Green's function estimates varied with backbone seismometer position. To obtain the best

estimates of the Green's functions for all backbone seismometers by MDD, one requires a higher source density and a distribution of sources that extends over the whole length of the receiver array, so that all inter-receiver Green's functions are illuminated sufficiently.

There is huge scope for MDD in earthquake seismology. The results presented herein are preliminary and would be improved by larger backbone arrays and more earthquake data. Alternatively, the use of ambient seismic noise over earthquake data is another approach to the MDD method. This has been discussed theoretically but it requires the separation of wavefields into their inwards and outwards propagating components, which is beyond the practical scope of this chapter.

Bibliography

Baqer, S., and B. Mitchell (1998), Regional variation of Lg coda Q in the continental United States and its relation to crustal structure and evolution, Pure and Applied Geophysics, 153(2-4), 613–638, doi:{10.1007/s000240050210}.

Lin, F., M. H. Ritzwoller, J. Townend, S. Bannister, and M. K. Savage (2007), Ambient noise Rayleigh wave tomography of new Zealand, Geophysical Journal International, 170(2), 649–666, doi:{10.1111/j.1365-246X.2007.03414.x}.

Mehta, K., R. Snieder, and V. Graizer (2007), Extraction of near-surface properties for a lossy layered medium using the propagator matrix, Geophysical Journal International, 169(1), 271–280, doi:{10.1111/j.1365-246X.2006.03303.x}.

Minato, S., T. Matsuoka, T. Tsuji, D. Draganov, J. Hunziker, and K. Wapenaar (2011), Seismic interferometry using multidimensional deconvolution and crosscorrelation for crosswell seismic reflection data without borehole sources, Geophysics, 76(1), SA19–SA34, doi:{10.1190/1.3511357}.

Snieder, R. (2004), Extracting the Green's function from the correlation of coda waves: A derivation based on stationary phase, Physical Review E, 69(4, 2), doi:{10.1103/PhysRevE.69.046610}.

Snieder, R., and E. Safak (2006), Extracting the building response using seismic interferometry: Theory and application to the Millikan Library in Pasadena, California, Bulletin of the Seismological Society of America, 96(2), 586–598, doi:{10.1785/0120050109}.

van Dalen, K. N., K. Wapenaar, and D. F. Halliday (2014), Surface wave retrieval in layered media using seismic interferometry by multidimensional deconvolution, Geophysical Journal International, 196(1), 230–242, doi:{10.1093/gji/ggt389}.

van der Neut, J., E. Ruigrok, D. Draganov, and K. Wapenaar (2010), Retrieving the earth's reflection response by multi-dimensional deconvolution of ambient seismic noise, EAGE, Extended Abstracts, pp. P406–1–P406–4.

van der Neut, J., J. Thorbecke, K. Mehta, E. Slob, and K. Wapenaar (2011), Controlled-source interferometric redatuming by crosscorrelation and multidimensional deconvolution in elastic media, Geophysics, 76(4), SA63–SA76, doi:{10.1190/1.3580633}.

Vasconcelos, I., and R. Snieder (2008a), Interferometry by deconvolution: Part 1 - Theory for acoustic waves and numerical examples, Geophysics, 73(3), S115–S128, doi:{10.1190/1.2904554}.

Vasconcelos, I., and R. Snieder (2008b), Interferometry by deconvolution: Part 2 - Theory for elastic waves and application to drill-bit seismic imaging, Geophysics, 73(3), S129–S141, doi:{10.1190/1.2904985}.

Wapenaar, K., and J. Fokkema (2006), Green's function representations for seismic interferometry, Geophysics, 71, SI33–SI46, doi:{10.1190/1.2213955}.

Wapenaar, K., and J. van der Neut (2010), A representation for Green's function retrieval by multidimensional deconvolution, Journal of the Acoustical Society of America, 128(6), EL366–EL371, doi:{10.1121/1.3509797}.

Wapenaar, K., E. Slob, and R. Snieder (2008a), Seismic and electromagnetic controlled-source interferometry in dissipative media, Geophysical Prospecting, 56, 419–434, doi:{10.1190/1.2976118}.

Wapenaar, K., J. van der Neut, and E. Ruigrok (2008b), Passive seismic interferometry by multidimensional deconvolution, Geophysics, 73(6), A51–A56, doi:{10.1190/1.2976118}.

Wapenaar, K., J. van der Neut, E. Ruigrok, D. Draganov, J. Hunziker, E. Slob, J. Thorbecke, and R. Snieder (2011a), Seismic interferometry by crosscorrelation and by multidimensional deconvolution: a systematic comparison, Geophysical Journal International, 185(3), 1335–1364, doi:{10.1111/j.1365-246X.2011.05007.x}.

Wapenaar, K., E. Ruigrok, J. van der Neut, and D. Draganov (2011b), Improved surface-wave retrieval from ambient seismic noise by multi-dimensional deconvolution, Geophysical Research Letters, 38, doi:{10.1029/2010GL045523}.

CHAPTER 8

Conclusions and Further Work

Here we summarise the results presented in Chapters 3 to 7 and review their implications in future seismology studies.

We focus primarily on the application of source-receiver interferometry (SRI) in earthquake seismology, reviewing the practical methodologies and determining the success with which the methods are able to construct earthquake seismograms of past events retrospectively, on seismometers that were not necessarily deployed when the events occurred. All that is required is a backbone array of seismometers that: 1) recorded the earthquake energy, and 2) was deployed over the same period of time as the new seismometers on which we wish to construct the new seismograms.

8.1 Methodology

In Chapter 3 a methodology was devised to perform SRI over multiple length scales. These length scales were determined by the distance between a backbone array of seismometers and the new target sensors on which we wish to construct the new earthquake seismograms. Furthermore, these length scales were important as they defined the distance over which the earthquake energy had to be projected, i.e., from the location of the backbone seismometers on which the earthquake energy was actually recorded, to the location of the target sensors. This projection happens via the SRI propagators - the inter-receiver Green's functions constructed between backbone seismometer-target sensor pairs using noise interferometry (Equation (2.14)).

A set of spatial criteria was defined to best implement the SRI theory in practice. For any given earthquake, this spatial criteria defined the orientation of the backbone array seismometers and the target sensors with respect to the earthquake epicentre: the backbone array should lie approximately perpendicularly (at a local intersection angle of 70° - 110°) to a great circle path that propagates from the earthquake epicentre and also intersects the target sensors. Theoretically the backbone array represents a boundary of receivers which, according to the stationary phase approximation (Snieder, 2004), need not be a full, complete boundary providing the receivers (seismometers) that do exist occupy those regions of the boundary that provide a stationary phase contribution to the interferometric integrals. This spatial criteria thus aims to invoke the stationary phase approach for any practical application of SRI.

Furthermore, the values of the integrands in Equations (2.31) and (2.32), constructed for all backbone seismometers at locations $\mathbf{x}$, were interpolated to points within Voronoi cells. This interpolation aimed to regularise the distribution of the measurements made on the backbone seismometers, such that where seismometers (and thus data) were missing, the measurements on surrounding seismometers were interpolated into the data-less space. A 2D cosine taper was then applied to the interpolated values to ensure that those values associated with seismometers located close to the centre of the array, and therefore approximately within the stationary phase region of the receiver boundary, contributed the most to the final integration (summation) over the whole array.

Finally, the spatial criteria defined one optimum length scale over which to perform SRI using USArray seismometer networks, the station spacing of which is $\sim$ 70 km. Here we showed that when the inter-station distances between backbone seismometer-target sensor pairs were between approximately 210 km and 540 km, SRI seismograms were successfully constructed on the target sensors using correlation-correlation SRI. For the spatial distributions of seismometers within the USArray network, these backbone seismometers thus occupied two approximately parallel lines of seismometers. This leads us to the 'ideal' receiver geometry for SRI.

8.1.1 Experimental Design: The 'ideal' receiver geometry for SRI

For the SRI methodology to compliment earthquakes originating from any region we reiterate the ideal receiver geometry proposed by Curtis et al. (2012) and adapted here in Figure 8.1. The geometry comprises a cross-shaped backbone array of permanent seismometers with roving target sensors (seismometers) deployed in

temporary, spatially distributed locations (Figure 8.1A) at which we wish to establish a measurement capability. For ambient noise interferometric studies as demonstrated herein, the temporary, target sensors need only be deployed for six months (Lin et al., 2007). During this time, estimates of the inter-receiver Green's functions between each target sensor and each backbone seismometer can be constructed using Equation (2.14). The target sensors are then moved on to the next set of regularly spaced locations, and one maintains the measurement capability at the locations previously occupied (Figure 8.1B). Alternatively, one could replace the roving receiver array with a roving source array (Figure 8.1C). In this case, shots would be fired sequentially from the temporary source locations and the resulting energy would be recorded on the backbone seismometers: one would then actively measure the Green's functions between these locations. The source array would then be moved on to new locations and one would maintain the ability to perform SRI at the locations previously occupied. Thus, at any time after an earthquake has occurred, the Green's functions constructed between the backbone array and any previously occupied temporary, target location can be used to project the earthquake recordings from the backbone seismometers to that target location. This location thus becomes that of a "virtual" receiver at which a new, novel seismogram of the event can be constructed.

The cross-shaped backbone array ensures the stationary phase approximation is invoked correctly for earthquake signals propagating from any azimuth. It also allows for both correlation-correlation SRI and correlation-convolution SRI to be performed. For example, for an earthquake whose energy propagates towards the backbone array from the northwest, correlation-correlation SRI would be used to construct SRI seismograms at the temporary, target locations in A and B, i.e., at locations closer to the earthquake epicentre than the locations of seismometers within the backbone array, whilst correlation-convolution SRI would be used to construct the SRI seismograms beyond the backbone seismometer locations at the temporary source locations in C.

Furthermore, the regularly spaced backbone and temporary, target sensor arrays displayed in Figure 8.1 would eliminate the need to interpolate the integrands of Equations (2.31) and (2.32) to points within Voronoi cells. Instead, Equations (2.31) and (2.32) would be evaluated correctly by simply integrating (summing) over all values of the integrands. A cosine taper could still be applied to weight the values of the integrands according to the locations of their corresponding backbone seismometers within the array. This would ensure that those seismometers occupying the stationary phase points of the receiver boundary contribute the most to the final integration.

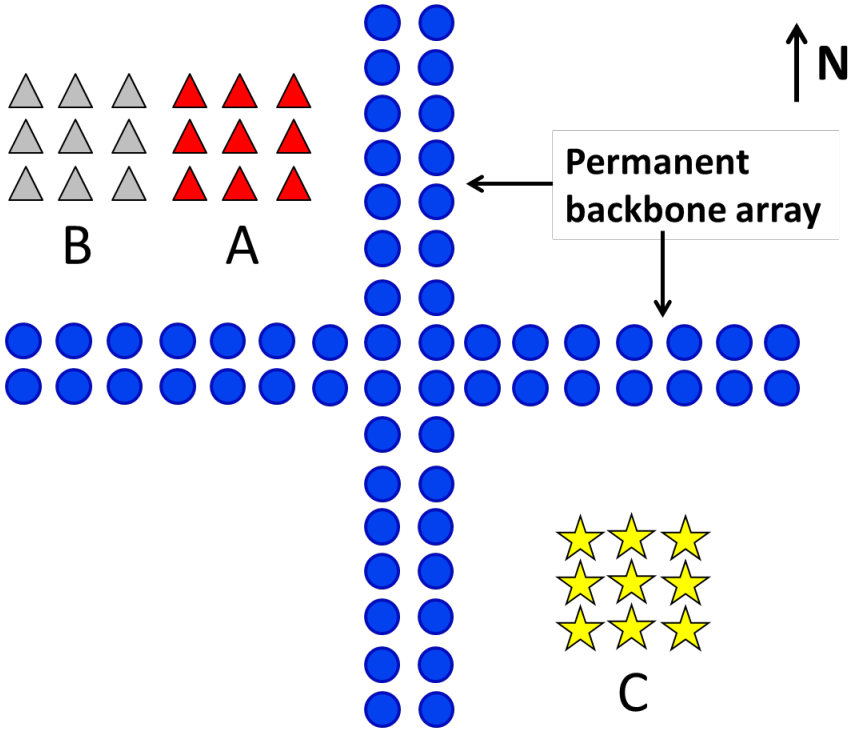

Figure 8.1: A schematic diagram outlining how receiver arrays may be designed to best compliment the SRI methodologies described herein, adapted from Curtis et al. (2012). Permanent seismometers are deployed in a cross-shaped backbone array (circles) and roving, target sensors (triangles) are deployed at temporary locations (A) for a period long enough to approximate the inter-receiver Green's functions between the target sensors and backbone seismometers. The temporary array can then be moved on to a new location. (B) Locations previously occupied by the temporary array that would represent the locations of the target sensors introduced within this study. SRI can thus be performed to construct new SRI seismograms at these locations at a time after the temporary receiver array has moved on to a new location. (C) An alternative to the theory discussed herein whereby a roving source array is used to actively measure the Green's functions between each source location and each backbone receiver. The Green's functions can then be used as herein to project the real earthquake energy recorded on the backbone array to the temporary source locations.

Also, by designing the backbone array to consist of two parallel lines of permanent seismometers both monopole and dipole sources can be estimated on this receiver boundary S. Currently, we assume Sommerfield radiation conditions on this boundary such that the dipole responses are approximated by $n_i \partial_i G \approx \pm jkG$. However, two regularly spaced, parallel lines of backbone seismometers, as shown in Figure 8.1, would allow one to estimate the dipole responses across the two lines, and the exact SRI integrals (such as that in Equation (2.25)) could be evaluated, thus eliminating some of the assumptions made herein.

Unfortunately, the geometry shown in Figure 8.1 was not the design of the deployment strategy used by USArray. The USArray 'Reference Array', which would satisfy our requirements of a fixed, permanent backbone array, is located irregularly throughout the United States (see Figure 8.2). The larger USArray 'Transportable Array' is, on most occasions, dense and regularly spaced but these seismometers are only deployed for up to two years before being moved to new locations. These seismometers are thus not suitable for a long-term, fixed backbone array but would provide good roving measurement locations, if a suitable backbone seismometer array could be established.

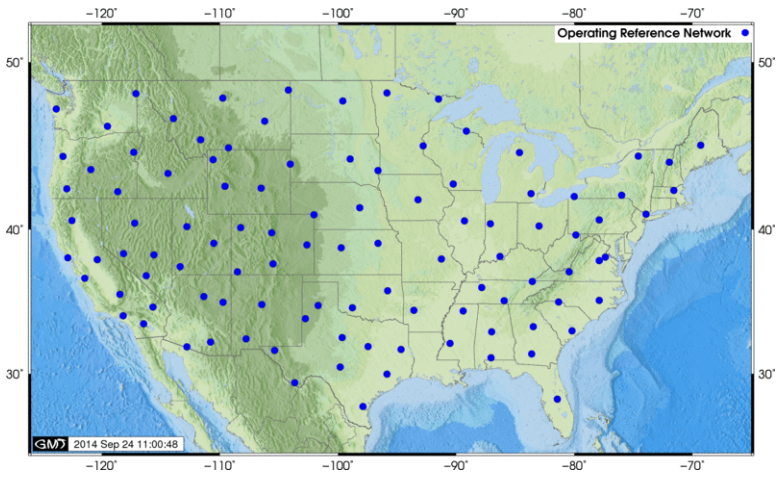

Figure 8.2: A map of the USArray Reference Network (circles) - a permanently deployed network of seismometers distributed irregularly throughout the United States. Source: `www.iris.edu/earthscope/usarray/_US-REF.gif`

To summarise, USArray seismometers have enabled the SRI methodologies to be thoroughly trialled throughout this thesis. However, they do not provide the optimum receiver distributions for future, continental-scale applications of SRI if the method is to be used in almost real-time to construct new earthquake seismogram data in the

hours after an event has occurred. Until these optimum receiver distributions for SRI can be created, we propose to construct the inter-receiver Green's functions between all possible pairs of USArray seismometers. This would create an archive of the projection operators for SRI that could then be inserted into Equation (2.31) or Equation (2.32) when an earthquake occurred. The project is well suited for the Terracorrelator - a large data computing facility at the University of Edinburgh that is currently being trialled to perform large-scale cross-correlations of ambient seismic noise data.

8.1.2 Source phase analysis

Curtis et al. (2012) showed that, in theory, the phase of the source time function t could be obtained if one had the correct source and receiver geometries. In Section 4.6 we explained that only if receivers were located around both stationary phase regions of the receiver boundary S, could t be determined. These stationary phase regions are regions along a source-to-receiver line that provide the stationary phase contributions to the interferometric integrals, which interfere constructively in the final integration (summation) over the receiver boundary S (Snieder, 2004).

Thus, obtaining the phase of the source time function of any given earthquake involves adding an extra condition to the spatial criteria in Section 3.6.1: the backbone array seismometers should occupy both stationary phase regions of the theoretical receiver boundary S. This geometry is illustrated again in Figure 8.3. Unfortunately the backbone seismometer arrays used herein did not fulfil this criterion.

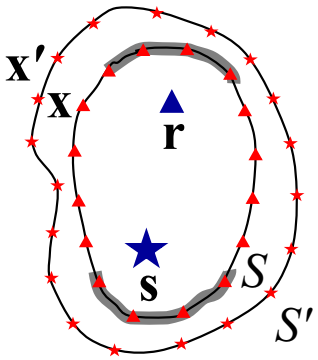

Figure 8.3: An illustration of the source and receiver geometry required to obtain the phase of the source time function t. Stars are sources, triangles are receivers. The grey shaded regions highlight schematically the stationary phase regions of the receiver boundary S. Importantly, *both* stationary phase regions must be occupied by the backbone seismometers at locations $\mathbf{x}$ in order to estimate t.

Ensuring seismometers occupy both stationary phase regions of the receiver boundary S significantly reduces the number of practical situations within which SRI can be performed. The ideal receiver geometry for SRI outlined in Figure 8.1 for example would not be suitable. Instead, a larger, gridded backbone array of permanently deployed seismometers would be required. This would consist of multiple cross-shaped arrays that are linked together to form a grid structure of seismometers, thus requiring far more seismometers within the permanent array.

Furthermore, when the earthquake source at $\mathbf{s}$ is a large, teleseismic event, the backbone arrays would need to be employed worldwide. This would ensure that earthquake energy propagating from any azimuth is recorded on the backbone seismometers and subsequently that those backbone seismometers occupy both stationary phase regions of a theoretical receiver boundary S.

Thus, whilst in theory the phase of the source function t can be obtained, in practice it relies heavily on dense, regularly spaced seismometer networks located worldwide. We first propose to test the method by finding a suitable, smaller-scale geometry using the USArray seismometer network and real earthquake data.

8.2 The Success of SRI in Constructing Earthquake Seismograms Retrospectively

In Chapters 4 and 5 we reviewed the success of correlation-correlation SRI and correlation-convolution SRI in constructing seismograms over three different length scales. An engineering or exploration seismology example was used to define the smallest length scale: six target sensors were located up to ~ 60 m from a regularly distributed line of receivers. Two backbone seismometer arrays were then utilised to define the two larger earthquake seismology length scales: one array orientated East-West in New Mexico located between 210 km and 540 km from eight target sensors, and one array orientated North-South in the centre of the United States located up to 2420 km from an additional eight target sensors.

Section 4.4.1 demonstrated the success of SRI in a small-scale engineering seismology example. The seismograms of an active weight-drop source were constructed on six target sensors using correlation-correlation SRI, and the results compared to the real recordings of the source on those same sensors. The match between the real and SRI seismograms was very good, but still not perfect despite the controlled conditions under which the correlation-correlation SRI method was

performed, i.e. controlled seismic sources were recorded on a line of regularly distributed geophones. These imperfections were likely caused by a combination of the power spectrum of the weight-drop source being multiplied into the SRI seismograms, and a breakdown of the assumption in correlational interferometry that the medium is non-attenuating.

The removal of ground roll from seismic shot gathers is one application of interferometry on an exploration seismology scale that has already been documented (Curtis et al., 2006; Halliday et al., 2007, 2010; Duguid et al., 2011). A new application could be in monitoring and locating micro-seismic events during well production. Thus, consider the schematic illustrations in Figure 8.4 which outline the geometries for monitoring a reservoir during well production: (A) Active seismic sources (stars) at locations such as $\mathbf{x}'$ are fired from a towed streamer, for example, and the responses $G(\mathbf{x}, \mathbf{x}')$ and $G(\mathbf{r}, \mathbf{x}')$ are recorded on ocean bottom receivers at locations $\mathbf{x}$ (filled triangles), and receivers located within the well at locations $\mathbf{r}$ (unfilled triangles), respectively. (B) Cross-correlations of these responses constructs the inter-receiver Green's functions $G(\mathbf{x}, \mathbf{r})$ between the well-based receivers and the permanently deployed receivers on the ocean bottom. These are the SRI propagators and the receiver locations in the well have become virtual source locations (unfilled stars). (C) The towed streamer and the well receivers are then removed prior to production, leaving behind a set of 'ghost' measurement locations within the well (circles) to which the SRI propagators have been constructed. (D) During well production, a micro-seismic event occurs within the well at location $\mathbf{s}$ (explosion) and is recorded on the ocean bottom receivers, $G(\mathbf{x}, \mathbf{s})$. (E) Using SRI as in Equation (2.28) the seismograms of the micro-seismic event can be constructed at the previously occupied receiver locations $\mathbf{r}$ within the well, $G(\mathbf{r}, \mathbf{s})$, thus creating virtual receivers within the well (unfilled triangles), that are located close to the event epicentre. Since the SRI seismograms $G(\mathbf{r}, \mathbf{s})$ are constructed over much shorter distances than the seismograms $G(\mathbf{x}, \mathbf{s})$ recorded on the ocean bottom receivers, SRI has the potential to more accurately locate micro-seismic events than when using only the event signals recorded on the permanently deployed ocean bottom receivers. We note however that this would require the use and construction of body waves, not surface waves as presented throughout this thesis. In order to develop the SRI methodologies described herein for other wave types (e.g. P- and S-waves, and also Love waves) the full Green's tensor would need to be constructed by cross-correlating both vertical and horizontal component data. Throughout this thesis we have only considered vertical component

data and thus only constructed surface wave estimates.

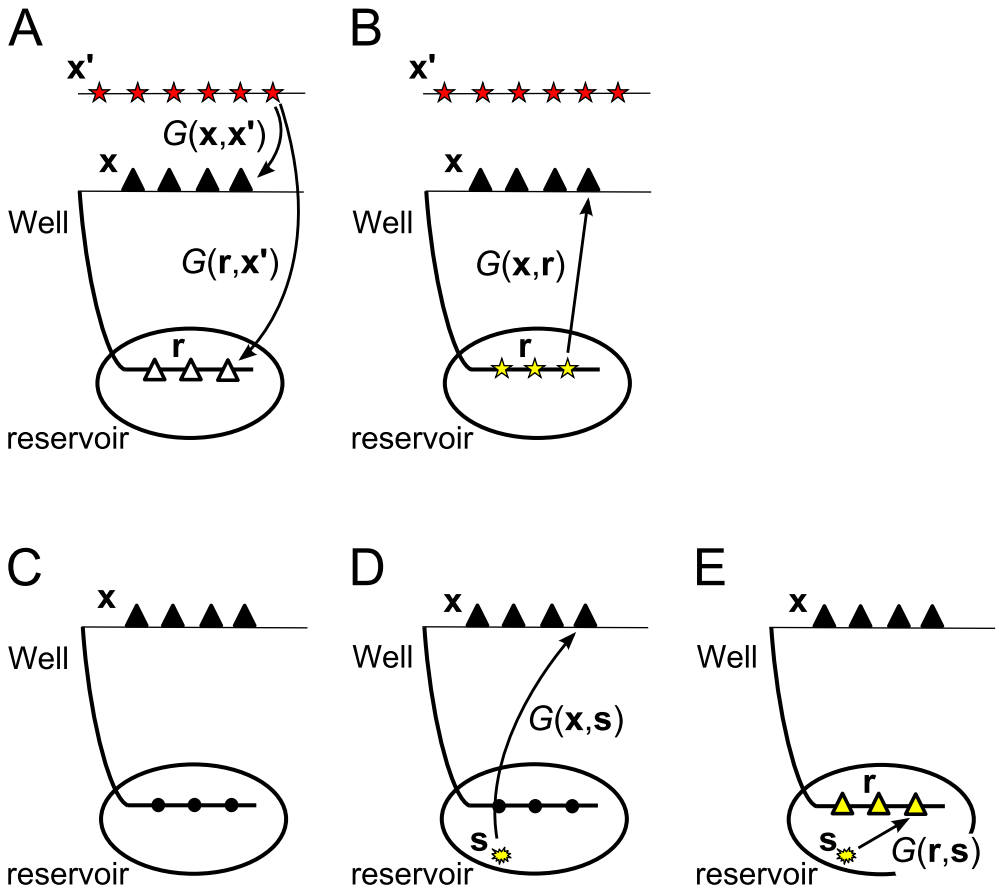

Figure 8.4: An illustration outlining the application of SRI to potentially locate microseismic events that occur in reservoirs during well production (e.g., the explosion at location $\mathbf{s}$ in (D)). The underlying processes are discussed in the text. Stars are sources, triangles are receivers, circles are virtual source locations at which we have established a measurement capability by inter-receiver interferometry. Curved arrows represent observed wavefields, straight arrows represent those wavefields constructed and thus estimated by interferometric processes. Terms such as $G(\mathbf{x}, \mathbf{r})$ are the Green's functions constructed, in this case, between a virtual source at $\mathbf{r}$ and the receiver at $\mathbf{x}$ (in (B)).

In Section 4.5.2 we performed SRI over a relatively small earthquake seismology scale: the East-West aligned array and correlation-correlation SRI were used to construct the earthquake seismograms of a M 5.8 earthquake that occurred in 2009 in Guerrero, Mexico, on eight target sensors. We then applied correlation-convolution SRI to construct the same earthquake seismograms on four of those same target sensors. This allowed a direct comparison to be made between the results of both SRI methods. Seven of the eight target sensors were actively recording data when the earthquake occurred, which allowed the virtual SRI seismograms to be compared with those actually recorded on the target sensors. The quality of the match between the real and SRI seismograms was quantified by calculating the correlation coefficient along the lengths of the traces.

Both SRI methods were successful at constructing new, novel seismograms of the M 5.8 Guerrero earthquake on target sensors located up to 540 km from the East-West aligned backbone array. Furthermore, correlation-convolution SRI allowed the discrimination of physical and non-physical arrivals in the seismograms constructed using correlation-correlation SRI. We attributed these non-physical arrivals to a breakdown in one of the underlying assumptions of correlation-type interferometry that the medium should be non-attenuative, and also to limited aperture in the backbone array of seismometers.

According to the stationary phase approximation (Snieder, 2004), the backbone seismometers should theoretically occupy those points of the receiver boundary that provide a stationary phase contribution to the interferometric integrals. We found that when backbone array seismometers were irregularly distributed, and thus when some stationary phase points were unoccupied, non-physical arrivals were constructed in the final SRI seismograms. The interpolation of existing data into Voronoi cells did however help to reduce the effects of these spatial irregularities. This was demonstrated in Section 4.6 when the SRI seismograms were constructed without interpolation of the integrands into Voronoi cells, and large amplitude artefacts were consequently constructed.

The North-South aligned array was then used in Section 4.5.3 to apply SRI over much larger inter-station distances and to thus really test the SRI methods. SRI seismograms of a M 6.5 earthquake that occurred off the coast of California were constructed on four target sensors located up to $\sim$ 1920 km west of the backbone array using correlation-correlation SRI. Correlation-convolution SRI was then used to extend the geometry to target sensors located up to 2420 km to the east of the backbone

array and over 4000 km from the earthquake epicentre.

Here we saw a discernible difference in the quality of the SRI seismograms constructed on target sensors located up to 1200 km from the North-South aligned backbone array compared to those located at larger inter-station distances. In Section 3.3 we provided a review of the inter-receiver Green's functions constructed between all backbone seismometer-target sensor pairs using noise interferometry, and found that those estimated Green's functions constructed over the largest inter-station distances were poorly constructed (low signal-to-noise ratios and root-mean-square values for the constructed surface wave arrivals), whilst those constructed over distances up to 1200 km exhibited much clearer surface wave arrivals. The theory of noise interferometry invokes processes of cross-correlation which have an underlying assumption of zero attenuation. Over these largest length scales we cannot assume the medium is non-attenuating. This is likely to induce non-physical arrivals into the estimated Green's functions which act to obscure the expected surface wave arrivals. Estimated Green's functions constructed with poor (low) signal-to-noise ratios were found to be less successful at projecting earthquake energy from the backbone seismometers to the target sensors.

Following these initial applications of correlation-correlation SRI and correlation-convolution SRI, Chapter 6 then provided an extensive review of the methods. Here we studied a total of 87 earthquakes, the seismograms of which we wished to construct using SRI. These earthquakes were chosen as they obeyed the spatial criteria defined in Section 3.6.1. Furthermore, the earthquakes sampled multiple magnitude scales, from M 2.4 to M 7.8, and were located at varying epicentral distances from the backbone seismometer arrays, from within 2000 km to up to 11,000 km. Thus, the earthquake energy was recorded on the backbone array seismometers with varying levels of quality (a quantity determined by the signal-to-noise ratio of the first arriving surface waves). We invoked the same two backbone arrays used in Chapters 4 and 5 to sample the same inter-station length scales.

The seismograms of 32 earthquakes were constructed on up to eight target sensors located up to 540 km from the East-West aligned array using both correlation-correlation and correlation-convolution SRI. The seismograms of earthquakes of M 5.5 and greater were constructed exceptionally well using SRI. We have since used a selection of these SRI seismograms constructed on target sensor 226A to create a catalogue of "virtual seismograms" of past earthquakes. Target sensor 226A was not deployed when the earthquakes occurred, thus 226A is a virtual seismometer on

which the SRI seismograms constructed are novel earthquake seismograms. These virtual seismograms are available in .SAC format and can be downloaded from `www.geos.ed.ac.uk/homes/s0679665/Catalogue.html`. The catalogue will be extended as and when new data becomes available. We plan to expand the available dataset by considering new backbone seismometer arrays that obey the same spatial criteria as those introduced herein. This will allow us to increase the azimuths from which earthquakes can originate, and will also identify new virtual seismometer locations, thus providing new seismogram data from a range of stations distributed throughout the United States. We propose that such virtual seismograms can be used alongside real earthquake data in future earthquake seismology studies e.g. for surface wave tomography.

The seismograms of the remaining 55 earthquakes were then constructed on eight target sensors located up to 2420 km from the North-South aligned array using either correlation-correlation SRI or correlation-convolution SRI. Here, the success of SRI in constructing accurate earthquake seismograms was dependent on the azimuth from which the earthquake originated. The seismograms of earthquakes that originated to the west of the North-South aligned array, from the Cascadia subduction zone or from further afield in Japan or New Zealand, were reconstructed poorly using SRI. The seismograms of earthquakes that originated to the east of the array however, particularly from within the northern Caribbean, were constructed well using SRI as clear surface waves could be identified, even in the SRI seismograms constructed over the largest length scales. In Section 6.5 we concluded that these azimuthal variations in the success of SRI were a consequence of the underlying geology of the United States. The geologic structure of the United States can be split into two main regions: the tectonically active and strongly heterogeneous western province, which extends from the Pacific Ocean to the Rocky Mountains, and the structurally stable, cratonic eastern province, which extends from the Rocky Mountains to the Atlantic coast. When earthquakes have originated to the west of the array, the subsurface complexities associated with the western province significantly reduce the quality of SRI seismograms constructed on target sensors located within the western province. This follows from the attenuation of earthquake energy that has propagated through this structurally complex region. When earthquakes have originated to the east of the North-South aligned backbone array however, the earthquake energy arrives at the backbone array seismometers having propagated through the structurally stable eastern province. This region is less attenuative than the western province and the earthquake

surface wave arrivals are recorded on the backbone array seismometers with high signal-to-noise ratios. These high quality earthquake recordings are then cross-correlated/convolved with the SRI propagators and high quality SRI seismograms of the events are subsequently constructed.

The success with which SRI constructs new earthquake seismograms retrospectively was also determined in Chapter 6. To analyse the quality of the match between the real recordings and the SRI seismograms quantitatively we studied the three individual components that comprise the SRI seismograms. These include: 1) The inter-receiver Green's functions constructed by noise interferometry. These are the SRI propagators that project the real earthquake signals recorded on the backbone array seismometers to the locations of the new target sensors. 2) The earthquake signals recorded on the backbone seismometers. 3) The individual correlation/convolution functions constructed between a target sensor and each backbone seismometer via processes of correlation or convolution. Summation over all correlation/convolution functions constructs the final SRI seismogram at the location of the target sensor.

A quantitative analysis of the average signal-to-noise ratios (SNRs) and average root-mean-square values (RMS) of these three components identified trends that related the quality of these individual components to the quality of their corresponding SRI seismogram. We found that the quality of the SRI propagators largely governed the outcome of SRI. When constructed over short to intermediate length scales (up to $\sim$ 1200 km) the inter-receiver Green's functions were constructed well using noise interferometry: average SNR values were typically > 25 and average RMS values were always > 0.7, and close to the maximum value of 1.0 for inter-receiver length scales between 210 km and 540 km. As the inter-station distance increased however, the quality of the SRI propagators deteriorated significantly, such that when constructed over distances up to 2420 km, the average SNR value was as low as 6.19 and the average RMS value was only 0.31. Noise interferometry involves processes of cross-correlation and as the inter-station distance increases to these larger length scales we cannot assume the medium is non-attenuating. This introduces significant artefacts into the SRI propagators that mask the surface wave arrivals and thus lower the average SNR and average RMS values. Such poorly constructed SRI propagators were found to be less successful at projecting the earthquake energy to the locations of the target sensors. This resulted in inaccurate SRI seismograms.

The average SNR value of the earthquake energy was also important to the outcome of SRI. This quantity determined the quality with which the earthquake

surface wave arrivals were recorded on the backbone array seismometers. It is this energy that is redatumed, both spatially and temporally, to the locations of the target sensors via the SRI propagators. Earthquakes that obeyed the spatial criteria defined in Chapter 3 but were of low magnitudes (between M 3.0 and M 4.0) were typically poorly recorded on the backbone seismometers: the average SNR values of such events were typically < 3.0. Earthquakes of M 5.5 and greater however were recorded well on the backbone seismometers: the average SNR values were typically between 8.0 and 10.0 but reached values greater than 15.0 on a number of occasions. When the spatial criteria were not obeyed, and a GCP from the earthquake epicentre did not intersect the backbone array approximately perpendicularly, even large magnitude events ($>$ M 6.0) were recorded on the backbone seismometers with average SNR values < 3.0. The seismograms of such events were subsequently constructed poorly using SRI, thus showing that even slight deviations from the spatial criteria outlined in Chapter 3 significantly effected the outcome of SRI. However, we also note that on occasion, even poorly recorded earthquake signals were projected to the locations of the target sensors successfully. This was only possible if the SRI propagators were constructed, and thus required to operate, over small inter-station distances (< 1200 km).

The correlation/convolution functions were constructed by either cross-correlating or convolving the SRI propagators and the earthquake signals recorded on the backbone array. The average SNR values of the correlation/convolution functions are thus a combination of the average SNR values of the other two SRI components and provide no new qualitative information. They do however estimate the quality with which the final SRI seismograms will be constructed.

Where real recordings of the earthquakes were available on the target sensors, the quality of the SRI seismograms constructed on those same sensors was determined by the correlation coefficient. This quantified the match between the real and SRI seismograms. We found that when the individual components of the SRI seismograms exhibited high SNR values and high RMS values (where applicable), the correlation coefficient of the final SRI seismogram was also typically high (> 0.6). To construct earthquake seismograms retrospectively by SRI, we thus propose that the quantitative analysis of the three components of SRI is a vital preliminary study. For example, a calculation of the SNR values of the earthquake recordings on the backbone array allows one to determine whether or not to perform SRI for that event.

Currently, we place less confidence in the earthquake seismograms constructed by SRI over the larger length scales presented in this thesis. This follows from the

poor quality inter-receiver Green's functions that are constructed over these distances and are thus less successful at projecting earthquake energy to new seismometer locations. These inter-receiver Green's functions are one of the main limitations of SRI in large, continental-scale applications. However, if the optimum receiver distributions described above and illustrated in Figure 8.1 are invoked, permanent backbone seismometer arrays can be deployed such that these larger inter-station distances are eliminated and higher quality Green's functions are constructed.

Given the varied success of correlation-based noise interferometry in constructing estimates of the Green's functions over the larger distances presented in this thesis, an alternative method to Green's function estimation was presented in Chapter 7. We shall now discuss the implications of this work for SRI.

8.3 Multidimensional Deconvolution (MDD)

In Chapter 7 we presented an example of Green's function estimation by multidimensional deconvolution (MDD). This was an attractive method as MDD is valid even in lossless (attenuative) media and it does not rely on a regular source distribution. Instead, we used 15 earthquake sources of variable magnitude that were distributed irregularly throughout the western United States and off the coast of California. The energy from each earthquake was recorded on backbone seismometers from within the North-South aligned array (at locations $\mathbf{x}$) and on four target sensors located to the east of the array (at $\mathbf{x_B}$). We did not separate the recorded wavefields into their inwards- and outwards-propagating components. Instead we assumed that all earthquake energy propagated across the backbone array and that back-scattering was weak across this receiver boundary. These earthquake recordings were then used to perform MDD and to thus estimate the Green's functions between each backbone seismometer-target sensor pair. The results of MDD were compared with the results of noise interferometry used extensively throughout this thesis.

On some occasions, the results of MDD were comparable with those of noise interferometry, despite far fewer data being used for MDD. We did however observe a strong bias in the quality of the MDD results that was dependent on the locations of the seismometers within the backbone array. This was a consequence of the distribution of the 15 earthquakes, the energies from which were used to construct the correlation functions C and the point-spread functions Γ. Although the source distribution can be irregular for MDD, the sources must illuminate the backbone seismometer array

sufficiently (Wapenaar et al., 2011). Here we proposed that only a selection of backbone seismometers were illuminated well. These seismometers were located close to where the great circle paths propagating from the earthquake epicentres intersected the backbone array approximately perpendicularly.

8.3.1 Further work

The initial results from this preliminary study are promising. Thus, we intend to perform a more comprehensive review of Green's function estimation by MDD. We will begin by increasing the number of earthquake sources used to construct the correlation functions C and the point-spread functions Γ. More earthquake sources should help to illuminate the backbone array sufficiently and this should improve the rank of the matrix $\mathbf{\Gamma}$. We then expect the inversion of $\mathbf{\Gamma}$ to be more stable and the inter-receiver Green's functions to be estimated more accurately.

Furthermore, we will extend the receiver boundary to include more seismometers. This will be beneficial when the inter-station distance is large, e.g., when constructing the estimated Green's functions between the backbone seismometers and target sensor GOGA. Over these large inter-station distances, the length of the backbone array used herein is too short to accurately span the stationary phase region of the convolution boundary on which MDD is based.

As we have discussed throughout this thesis, the inter-receiver Green's functions constructed between target sensor-backbone seismometer pairs are used as the propagators for SRI - they project the earthquake signals recorded on the backbone seismometers to the locations of the target sensors. Thus, we now introduce two forms of SRI that use MDD to construct the SRI propagators $G(\mathbf{x}, \mathbf{r})$. The geometries for deconvolution-correlation SRI and deconvolution-convolution SRI are illustrated in Figure 8.5A and B, respectively. Since MDD does not require a regular source distribution, the geometries for SRI by MDD do not utilise full boundaries of sources and receivers like the geometries illustrated earlier for the theoretical derivations of SRI by processes of correlation and convolution only. Our illustrations in Figure 8.5 thus show schematically the distributions of sources and receivers required for the practical application of SRI by MDD for an earthquake source at $\mathbf{s}$ and a target sensor at $\mathbf{r}$.

The source at $\mathbf{s}$, the seismograms of which we wish to construct by SRI, can be located on either side of the receiver boundary S. It is the location of this source that determines whether to perform correlation or convolution in the inter-source interferometry step of SRI (Equation (2.31) or Equation (2.32)). Importantly, the target

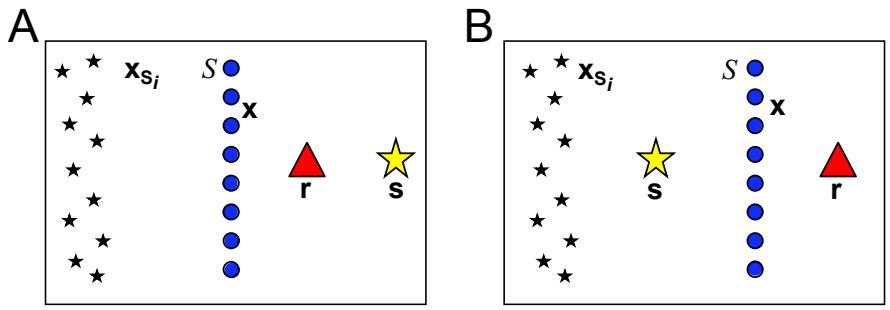

Figure 8.5: Two possible geometries for performing SRI using (A) deconvolution-correlation SRI, and (B) deconvolution-convolution SRI. In both cases, MDD constructs the inter-receiver Green's functions $G(\mathbf{x}, \mathbf{r})$ between the backbone seismometers at locations $\mathbf{x}$ (circles) on boundary S and the target sensor at location $\mathbf{r}$ (triangle). MDD requires the responses from sources at locations such as $\mathbf{x}_{\mathbf{S}_i}$ (small stars) to be recorded on the backbone seismometers and on the target sensor to construct the point-spread function Γ and the correlation function C. In (A), correlation as in Equation (2.31) is then used to estimate $G(\mathbf{r}, \mathbf{s})$, whilst in (B), convolution as in Equation (2.32) is used to estimate $G(\mathbf{r}, \mathbf{s})$. These processes thus construct the response from a source at $\mathbf{s}$ (large star) recorded on the target sensor at $\mathbf{r}$.

sensor at $\mathbf{r}$ must lie on the opposite side of the receiver boundary S to the irregularly distributed sources at locations such as $\mathbf{x}_{\mathbf{S}_i}$ (Wapenaar et al., 2011). We note that the geometries in Figure 8.5 are similar to the geometries used in the practical applications of correlation-correlation SRI and correlation-convolution SRI. The only differences are the locations of the sources at $\mathbf{x}_{\mathbf{S}_i}$ which are not completely surrounding the receivers and thus the energy from them is not assumed to be propagating isotropically. This is one assumption that can be relaxed by MDD theory without inducing non-physical arrivals, thus making it attractive in real data applications.

To perform the MDD and SRI methodologies for larger datasets we will use the Terracorrelator at the University of Edinburgh. This should allow larger matrices for Γ and C to be constructed, and subsequently larger matrix inversions to be executed.

8.4 Summary

Here we have reviewed the SRI methodologies and results presented throughout this thesis and their potential future implications in earthquake and engineering/exploration seismology.

We have used the information from Chapter 3 and the development of SRI methodologies to propose an 'ideal' receiver geometry for future applications of SRI.

This geometry also allows for the estimation of monopole *and* dipole sources on the backbone receiver boundary S. Furthermore, the geometry could be significantly extended to allow the calculation of the phase of the source time signature; however, to satisfy earthquake energy propagating from any azimuth, this would require far larger backbone seismometer arrays located worldwide.

From the results of Chapters 4 to 6 we have determined the success with which SRI constructs earthquake seismograms retrospectively, and the confidence that we can place in those SRI reconstructions. The SRI seismograms of earthquakes of magnitude 5.5 and greater were constructed exceptionally well on target sensors located close (up to ~ 540 km) to backbone seismometer arrays. Some of these SRI reconstructions have since been added to an on-line catalogue of "virtual" seismograms of past earthquakes. We propose that such virtual SRI seismograms could be used alongside real earthquake seismograms in future earthquake seismology studies. When target sensors are located further from the backbone seismometer arrays however (at distances > 1200 km), we place less confidence in the ability of SRI to construct earthquake seismograms on those target sensors. This is a consequence of poorly constructed SRI propagators by noise interferometry over these large inter-receiver distances. These SRI propagators are thus less able to successfully project real earthquake energy from the backbone seismometers to the locations of the target sensors.

In an attempt to improve these SRI propagators, we considered multidimensional deconvolution (MDD) as an alternative approach to noise interferometry in Chapter 7. This preliminary study has become the motivation of a much larger data application, within which we will use MDD to derive two new SRI methodologies: deconvolution-correlation SRI and deconvolution-convolution SRI. Since MDD can be applied in lossless (attenuative) media, deconvolutional approaches to SRI have the potential to improve the SRI seismograms constructed over the larger inter-receiver distances in Chapters 4 to 6, especially when the SRI propagators are required to operate throughout the strongly attenuating western United States.

Bibliography

Curtis, A., P. G. Gerstoft, H. Sato, R. Snieder, and K. Wapenaar (2006), Seismic interferometry; turning noise into signal, Leading Edge (Tulsa, OK), 25(9), 1082–1092, doi:{10.1190/1.2349814}, n/a.

Curtis, A., Y. Behr, E. Entwistle, E. Galetti, J. Townend, and S. Bannister (2012), The benefit of hindsight in observational science: Retrospective seismological observations, Earth and Planetary Science Letters, 345, doi:{DI10.1016/j.epsl.2012.06.008}.

Duguid, C., D. Halliday, and A. Curtis (2011), Source-receiver interferometry for seismic wavefield construction and ground-roll removal, The Leading Edge, 30(8), 838–843, doi:{10.1190/1.3626489}.

Halliday, D. F., A. Curtis, J. O. A. Robertsson, and D.-J. van Manen (2007), Interferometric surface-wave isolation and removal, Geophysics, 72(5), A69–A73, doi:{10.1190/1.2761967}.

Halliday, D. F., A. Curtis, P. Vermeer, C. Strobbia, A. Glushchenko, D. van Manen, and J. O. A. Robertsson (2010), Interferometric ground-roll removal: Attenuation of scattered surface waves in single-sensor data, Geophysics, 75(2), SA15–SA25, doi:{10.1190/1.3360948}.

Lin, F., M. H. Ritzwoller, J. Townend, S. Bannister, and M. K. Savage (2007), Ambient noise Rayleigh wave tomography of new Zealand, Geophysical Journal International, 170(2), 649–666, doi:{10.1111/j.1365-246X.2007.03414.x}.

Snieder, R. (2004), Extracting the Green's function from the correlation of coda waves: A derivation based on stationary phase, Physical Review E, 69(4, 2), doi:{10.1103/PhysRevE.69.046610}.

Wapenaar, K., J. van der Neut, E. Ruigrok, D. Draganov, J. Hunziker, E. Slob, J. Thorbecke, and R. Snieder (2011), Seismic interferometry by crosscorrelation and by multidimensional deconvolution: a systematic comparison, Geophysical Journal International, 185(3), 1335–1364, doi:{10.1111/j.1365-246X.2011.05007.x}.

Appendices

APPENDIX A

Earthquake List

Here we provide a list of the 87 earthquakes used throughout Chapter 6. They are grouped according to the backbone arrays on which they are recorded: Table A.1 lists the 32 earthquakes recorded on the East-West aligned array located in New Mexico, Table A.2 lists the 55 earthquakes recorded on the North-South aligned array located in the centre of the United States. Event magnitude, epicentre (description and latitude/longitude coordinates), date, time, and depth information is provided.

Table A.1: A list of the 32 earthquakes recorded on the East-West aligned backbone seismometer array located in New Mexico.

Magnitude	Location	Latitude	Longitude	Date	Time (hh:mm:ss)	Depth (km)
3.8	Offshore Colima, Mexico	18.812	-104.034	14.02.2009	05:08:38	5
3.8	Oaxaca, Mexico	16.803	-94.802	14.01.2009	11:10:18	114
3.8	Offshore Guerrero, Mexico	17.927	-101.867	25.01.2009	12:38:40	23
3.9	Veracruz, Mexico	17.809	-95.616	12.01.2009	19:13:20	26.7
3.9	Hidalgo,Mexico	20.35	-98.9	20.05.2010	21:11:03	5
4.0	Guerrero, Mexico	18.449	-101.254	28.09.2009	06:25:15	69.5
5.5	Mexico	18.18	-100.37	15.08.2009	13:22:43	56
5.6	Puebla, Mexico	18.114	-98.457	22.05.2009	19:24:18	62.3
5.6	Off the coast of Jalisco, Mexico	18.083	-105.597	23.11.2009	06:08:39	34.8
5.6	Revilla Gigedo Islands region	19.553	-109.165	03.06.2009	21:37:37	6
5.7	Offshore Veracruz, Mexico	18.911	-95.538	29.10.2009	10:52:56	16.4
5.8	Guerrero, Mexico	17.032	-99.446	27.04.2009	16:46:28	35
6.2	Off the coast of Jalisco, Mexico	18.795	-107.193	24.08.2010	02:11:59	10
6.3	Oaxaca, Mexico	16.396	-97.782	30.06.2010	07:22:27	20
6.4	Off the coast of Jalisco, Mexico	18.829	-107.339	24.09.2009	07:16:20	13

Magnitude	Location	Latitude	Longitude	Date	Time (hh:mm:ss)	Depth (km)
5.6	East Central Pacific Ocean	8.268	-110.357	21.01.2010	08:03:23	12
5.6	Central East Pacific Rise	-4.05	-103.969	24.05.2009	09:57:11	6
5.7	Pacific-Antarctic Ridge	-56.504	-143.181	31.07.2009	10:09:46	10
5.7	Central East Pacific Rise	-4.533	-104.912	06.10.2009	01:59:39	10
5.8	Galapagos Islands	2.429	-95.124	15.03.2009	03:14:31	10
6.0	Pacific-Antarctic Ridge	-54.843	-135.398	19.05.2010	10:51:03	10
6.0	Southern East Pacific Rise	-56.476	-122.321	03.12.2009	06:12:32	10
6.0	Southeast of East Island	-36.004	-102.686	08.07.2009	19:23:37	12
6.0	Galapagos Triple Junction	3.272	-103.823	15.10.2009	17:48:21	10
6.1	Southern East Pacific Rise	-56.234	-124.296	01.08.2009	13:33:29	10
6.2	Easter Island region	-29.144	-112.267	17.09.2009	23:21:38	10
6.3	Southern East Pacific Rise	-16.236	-115.296	07.03.2010	07:05:24	18
6.3	Guatemala	14.546	-91.143	03.05.2009	16:21:45	108
7.3	Offshore Honduras	16.731	-86.217	28.05.2009	08:24:46	19
5.7	Off the coast of northern Peru	-8.469	-80.471	04.07.2010	06:57:44	28.7
6.0	Off the coast of northern Peru	-6.567	-81.15	09.02.2009	15:09:02	15
6.1	Off the coast of northern Peru	-5.854	-80.891	15.02.2009	11:04:49	21

Table A.2: A list of the 55 earthquakes recorded on the North-South aligned backbone seismometer array located in the centre of the United States.

Magnitude	Location	Latitude	Longitude	Date	Time (hh:mm:ss)	Depth (km)
2.4	Northern California	40.292	-121.544	15.04.2010	11:52:15	5.9
2.6	Off the coast of California	40.621	-124.376	15.01.2010	07:03:24	14
2.8	Northern California	39.852	-121.659	11.03.2010	21:56:56	12.6
2.8	Northern California	40.639	-123.247	25.11.2010	10:01:00	32.4
3.0	Northern California	39.187	-120.46	04.08.2010	02:47:40	0.8
3.7	Northern California	40.544	-123.868	24.12.2010	12:59:19	25.3
3.8	Northern California	40.425	-123.568	10.07.2010	16:04:30	31.9
2.8	Nevada	39.705	-115.484	06.12.2009	21:11:49	5
3.0	Nevada	40.105	-117.571	12.12.2010	12:01:03	5
3.2	Nevada	40.769	-119.311	12.02.2010	04:37:32	10.2
3.4	Nevada	41.373	-119.893	01.10.2010	12:31:03	0
3.8	Nevada	41.056	-117.142	02.04.2009	03:52:20	5.1
3.1	Puerto Rico	17.521	-67.428	18.09.2010	07:47:35	43.6
3.2	Haiti	18.499	-72.475	08.04.2010	06:27:29	10
3.5	Virgin Islands	18.027	-64.742	04.12.2010	15:34:35	32.3
3.6	Haiti	18.274	-73.015	20.09.2010	11:22:26	10
3.7	Dominican Republic	19.326	-68.694	18.01.2010	17:22:41	38.9
4.0	Haiti	18.418	-72.044	27.01.2010	22:26:10	10

Magnitude	Location	Latitude	Longitude	Date	Time (hh:mm:ss)	Depth (km)
4.0	Off the coast of California	40.355	-127.071	29.05.2009	03:35:15	10
4.0	Northern California	39.777	-123.338	22.12.2009	23:40:43	9.7
4.1	Off the coast of California	40.438	-125.324	23.03.2009	01:24:24	10.6
4.1	Northern California	40.277	-123.868	04.01.2010	14:24:54	30.7
4.2	Nevada	40.076	-119.622	20.07.2010	21:48:29	11.7
4.2	Off the coast of California	40.462	-125.66	04.11.2009	02:16:56	15.5
4.2	Off the coast of California	40.395	-125.464	05.06.2010	09:05:26	26.2
4.2	Off the coast of California	40.876	-127.319	27.11.2010	21:02:54	10
4.4	Off the coast of California	40.771	-125.147	16.08.2010	12:05:17	23.3
4.5	Off the coast of California	40.327	-124.705	06.03.2010	08:46:24	12.4
4.5	Off the coast of California	40.392	-127.205	17.04.2010	04:22:13	10
4.5	Off the coast of California	40.27	-125.765	15.04.2010	08:36:06	29.5
4.7	Off the coast of California	40.487	-126.507	02.10.2009	09:17	10
5.0	Off the coast of California	40.31	-124.637	07.08.2009	10:49:34	16.9
5.1	Central California	36.388	-117.858	01.10.2009	10:01:24	5.6
6.5	Off the coast of California	40.65	-124.69	10.01.2010	00:27	29
5.0	Trinidad and Tobago	10.734	-61.635	27.12.2010	01:00:14	54.3
5.4	Dominican Republic	15.692	-68.541	13.11.2010	04:35:39	94.6
5.7	El Salvador	12.995	-88.64	20.12.2010	17:21:26	72.3
5.8	Puerto Rico	18.4	-67.07	16.05.2010	05:16:10	113
5.9	Offshore El Salvador	13.728	-90.132	18.01.2010	15:40:26	54.7
5.9	Offshore El Salvador	13.514	-89.907	26.11.2009	19:08:11	56.8
5.9	Central Peru	-8.498	-74.466	25.01.2010	22:52:46	147.7
5.9	Cayman Islands	19.004	-80.804	19.01.2010	14:23:38	10
5.9	Haiti	18.423	-72.823	20.01.2010	11:03:43	10.5

Magnitude	Location	Latitude	Longitude	Date	Time (hh:mm:ss)	Depth (km)
6.0	Malawi	-10.108	33.818	19.12.2009	23:19:15	6
7.0	Ryukyu Islands, Japan	25.93	128.425	26.02.2010	20:31:26	25
7.1	South coast of Honshu, Japan	33.167	137.944	09.08.2009	10:55:55	292
7.2	Northern Sumatra, Indonesia	3.748	96.018	09.05.2010	05:59:41	38
7.3	Fiji	-17.239	178.331	09.11.2009	10:44:55	595
7.4	East of the Kuril Islands	46.857	155.154	15.01.2009	17:49:39	36
7.6	Southern Sumatra, Indonesia	-0.79	99.96	30.09.2009	10:16:09	80
7.8	Off the west coast of the South Island, NZ	-45.762	166.562	15.07.2009	09:22:29	12
6.0	Northern Mid-Atlantic Ridge	23.864	-46.105	06.06.2009	20:33:28	14
6.0	Haiti	18.387	-72.784	12.01.2010	22:00:41	10
6.4	Offshore Carabobo, Venezuela	10.709	-67.927	12.09.2009	20:06:25	14
7.0	Haiti	18.443	-72.571	12.01.2010	21:53:10	13

APPENDIX B

RMS and SNR Analyses of Event Recordings

B.1 Introduction

In order to assess the quality of the SRI seismograms reconstructed at target sensors, we deconstructed the SRI seismograms into there 3 components: 1) the estimated Green's functions, 2) the recordings of the earthquakes on backbone array seismometers, and 3) the correlation/convolution functions. Here we calculate the average root-mean-square (RMS) values and average signal-to-noise ratios (SNR) of the earthquake seismograms recorded on the backbone arrays of seismometers. The RMS value is calculated within a 500 s time window within which we expect the first surface waves to arrive. The SNR of this signal window to a 500 s noise window is then calculated. The noise window directly follows the signal window temporally. Average RMS and SNR values are representative of all seismometers within the arrays.

B.2 Earthquakes recorded on the East-West aligned array

Table B.1 provides a list of the 32 earthquakes recorded on the East-West aligned array, whose seismograms were reconstructed on target sensors Z27A, 127A, 227A, 327A, 427A, 527A, 627A and 226A using SRI. The RMS values and SNR values of the event seismograms recorded on all backbone array seismometers were calculated and averaged over the whole array to give the values in the table.

Table B.1: Magnitudes and locations of the 32 earthquakes recorded on the East-West aligned backbone seismometer array. The average root-mean-square (RMS) values and average signal-to-noise ratios (SNRs) of these event seismograms recorded on the backbone array seismometers are calculated. Earthquakes are grouped by the 3 magnitude scales (groups) invoked in Chapter 6.

Magnitude	Location	Average RMS signal	Average SNR
3.8	Offshore Colima, Mexico	1.64E-08	2.58
3.8	Oaxaca, Mexico	1.08E-08	2.93
3.8	Offshore Guerrero, Mexico	1.94E-08	2.72
3.9	Veracruz, Mexico	1.69E-08	2.68
3.9	Hidalgo,Mexico	1.01E-08	2.34
4.0	Guerrero, Mexico	1.36E-08	2.38
5.5	Mexico	4.63E-07	17.48
5.6	Puebla, Mexico	5.97E-07	21.25
5.6	Off the coast of Jalisco, Mexico	7.34E-07	10.93
5.6	Revilla Gigedo Islands region	2.15E-06	17.63
5.7	Offshore Veracruz, Mexico	5.12E-07	2.37
5.8	Guerrero, Mexico	5.02E-06	42.54
6.2	Off the coast of Jalisco, Mexico	2.18E-06	8.82
6.3	Oaxaca, Mexico	4.96E-06	10.31
6.4	Off the coast of Jalisco, Mexico	1.81E-05	11.91
5.6	East Central Pacific Ocean	5.45E-07	8.20
5.6	Central East Pacific Rise	3.76E-07	15.24
5.7	Pacific-Antarctic Ridge	6.78E-08	5.00
5.7	Central East Pacific Rise	9.08E-07	15.82
5.8	Galapagos Islands	3.80E-06	20.52
6.0	Pacific-Antarctic Ridge	2.48E-07	4.01
6.0	Southern East Pacific Rise	2.23E-07	4.31
6.0	Southeast of East Island	1.80E-07	7.58
6.0	Galapagos Triple Junction	1.09E-06	6.47
6.1	Southern East Pacific Rise	9.53E-08	5.08
6.2	Easter Island region	6.46E-07	6.03
6.3	Southern East Pacific Rise	6.95E-07	10.52
6.3	Guatemala	1.04E-06	9.49
7.3	Offshore Honduras	5.94E-05	2.09
5.7	Off the coast of northern Peru	1.36E-07	2.55
6.0	Off the coast of northern Peru	2.03E-07	3.18
6.1	Off the coast of northern Peru	1.20E-07	2.88

B.3 Earthquakes recorded on the North-South aligned array

Table B.2 provides a list of the 55 earthquakes recorded on the North-South aligned array, whose seismograms were reconstructed on target sensors WDC, BMN, DUG, R29A, R30A, R31A, GOGA and P21A using SRI. The RMS values and SNR values of the event seismograms recorded on all backbone array seismometers were calculated and then averaged over the whole array to give the values in the table.

Earthquakes are grouped by the three magnitude scales (groups) described in Chapter 6 and by the direction from which the earthquake energy propagates towards the North-South aligned array. Thus, those earthquakes whose energy propagated towards the array from East to West are separated from those whose energy propagated towards the array from West to East. The former typically originate from within the Caribbean.

Table B.2: Magnitudes and locations of the 55 earthquakes recorded on the North-South aligned backbone seismometer array. The average root-mean-square (RMS) values and average signal-to-noise ratios (SNRs) of these event seismograms recorded on the backbone array seismometers are calculated.

Magnitude	Location	Average RMS	Average SNR
2.4	Northern California	1.38E-08	2.51
2.6	Off the coast of California	2.54E-08	2.79
2.8	Northern California	4.71E-08	2.75
2.8	Northern California	2.83E-08	2.67
3.0	Northern California	5.96E-09	2.59
3.7	Northern California	5.44E-08	2.66
3.8	Northern California	7.28E-09	3.03
2.8	Nevada	2.17E-08	2.08
3.0	Nevada	6.32E-09	2.49
3.2	Nevada	2.98E-08	2.51
3.4	Nevada	1.76E-08	2.44
3.8	Nevada	1.08E-08	2.19
3.1	Puerto Rico	3.55E-08	2.92
3.2	Haiti	2.76E-08	2.74
3.5	Virgin Islands	2.60E-08	3.06
3.6	Haiti	4.40E-08	3.09
3.7	Dominican Republic	1.42E-06	2.92
4.0	Haiti	4.53E-08	3.05
4.0	Off the coast of California	8.73E-09	3.26
4.0	Northern California	3.71E-08	2.80
4.1	Off the coast of California	1.24E-08	2.22
4.1	Northern California	4.37E-08	3.06
4.2	Nevada	5.68E-08	2.65
4.2	Off the coast of California	1.86E-08	3.78
4.2	Off the coast of California	1.37E-08	5.97
4.2	Off the coast of California	8.04E-08	3.05
4.4	Off the coast of California	2.58E-08	10.33
4.5	Off the coast of California	3.99E-08	5.19
4.5	Off the coast of California	8.20E-07	12.62
4.5	Off the coast of California	2.89E-08	5.99
4.7	Off the coast of California	3.73E-08	9.65
5.0	Off the coast of California	1.11E-07	20.18
5.1	Central California	2.18E-07	10.77
6.5	Off the coast of California	1.63E-05	22.00

Magnitude	Location	Average RMS	Average SNR
6.0	Malawi	6.20E-07	5.28
7.0	Ryukyu Islands, Japan	4.17E-06	2.13
7.1	South coast of Honshu, Japan	1.56E-06	3.67
7.2	Northern Sumatra, Indonesia	7.96E-06	1.84
7.3	Fiji	6.71E-07	3.14
7.4	East of the Kuril Islands	3.52E-05	4.51
7.6	Southern Sumatra, Indonesia	1.46E-05	3.10
7.8	Off the west coast of South Island, NZ	2.31E-05	2.20
5.0	Trinidad and Tobago	1.10E-07	3.21
5.4	Dominican Republic	1.10E-07	3.39
5.7	El Salvador	2.89E-07	3.45
5.8	Puerto Rico	4.83E-07	4.37
5.9	Offshore El Salvador	4.89E-07	4.46
5.9	Offshore El Salvador	5.09E-07	2.79
5.9	Central Peru	1.44E-07	3.68
5.9	Cayman Islands	1.34E-06	5.72
5.9	Haiti	2.60E-06	7.06
6.0	Northern Mid-Atlantic Ridge	1.01E-06	4.48
6.0	Haiti	8.50E-05	10.12
6.4	Offshore Carabobo, Venezuela	1.18E-05	4.07
7.0	Haiti	1.47E-04	10.82